ANALYSIS OF THE EQUIANGULAR SPIRAL ANTENNA

A Thesis
Presented to
The Academic Faculty

by

Michael McFadden

In Partial Fulfillment
of the Requirements for the Degree
Doctor of Philosophy in the
School of Electrical and Computer Engineering

Georgia Institute of Technology
December 2009

ANALYSIS OF THE EQUIANGULAR SPIRAL ANTENNA

Approved by:

Waymond R. Scott, Jr., Advisor
School of Electrical and Computer Engineering
Georgia Institute of Technology

Mary A. Ingram
School of Electrical and Computer Engineering
Georgia Institute of Technology

Glenn S. Smith
School of Electrical and Computer Engineering
Georgia Institute of Technology

Owen J. Eslinger
US Army Engineer Research and Development Center
US Army Corps of Engineers

Andrew F. Peterson
School of Electrical and Computer Engineering
Georgia Institute of Technology

Date Approved: October 30 2009

ACKNOWLEDGEMENTS

I would like to thank my advisor, Dr. Waymond Scott, for proposing the research topic and helping with the problems that I've encountered both working through the ideas in this thesis and putting them down on paper. I also appreciate the help of my dissertation committee members: Dr. Glenn Smith, Dr. Andrew Peterson, Dr. Mary Ingram, and Dr. Owen Eslinger. Their thoughtful advice while reviewing this thesis has been useful.

I've been privileged to know and work with a great group of people in the electromagnetics student office. I've used a lot of neat FDTD implementation ideas from Todd Lee. David Reid was always ready to help me with anything that needed to be done. I also appreciate the suggestions on problems or papers that I have gotten from everyone else in the office: Ilker Capoglu, Pelham Norville, Ricardo Lopez, Mu-Hsin Wei, and James Sustman.

A number of people outside of work have helped me to stay grounded over the last few years. Most notably, my wife, Kate, has listened to whining, equations, and often whining about equations. Many of these equations are in this document and I appreciate her patience and peanut butter sandwiches. My friends, Josh and Ryan, have done a great job keeping me from taking myself and my work too seriously over the past several years. My parents, Chris and Donna, have always been supportive of whatever I was up to, and it's a shame that my dad couldn't see me reach this pinnacle of nerdiness.

Several other people here at Georgia Tech have been really helpful during my thesis work. I'd like to thank the network administrators for allowing us to manage our own Beowulf cluster. Bob House milled the spiral antennas analyzed in Chapters 2 and 3 and we also made use of the Van Leer machine shop extensively to build the GPR system.

This work was supported by the U.S. Army Engineer Research and Development Center (ERDC), Geotechnical and Structures Laboratory (GSL) under Contract 912HZ-07-C-0026 and by the U.S. Army Research Office under Contract DAAD19-02-1-0252.

TABLE OF CONTENTS

LIST OF TABLES

LIST OF FIGURES

SUMMARY

This thesis presents an analysis of the behavior of an equiangular spiral antenna using a mixture of numerical and measurement techniques. The antenna is studied as an isolated element and as a part of a spiral-based ground-penetrating radar (GPR) detection system. The intention is to isolate the effect of varying different geometrical parameters that define the spiral element or the spiral GPR system. With some notion of each parameter's effect, systems that use the spiral antenna can be more easily designed.

In the isolated spiral element work, prototype antennas are constructed and measured for characteristic impedance and boresight gain. In addition, a numerical model based on the finite-difference time-domain method is constructed for studying the spirals. The measurements closely agree with numerical models for the antennas. Next, the models are used to construct design graphs that relate the geometry of the antenna to the characteristic impedance in the operating band and the lower-frequency cutoff of the operating band. Additional features of the boresight gain and patterns are studied.

The prototype antennas are incorporated into a full GPR system. The system has two spiral antennas that can be used as a bistatic or monostatic radar and each antenna is backed with an absorbing can. The system is tested in a sand box using several buried scattering objects. The numerical model is also extended to incorporate all relevant features. Good agreement is shown between measurements of the system and the model.

To characterize the system using the model directly required too much computing time, so two techniques to extrapolate the performance of the system were explored. First, reciprocity and the planar symmetry of the ground could be used to extrapolate the radar response of a scatterer located at different positions from the fields induced in the ground by the antennas. Second, the antennas could be characterized in terms of their plane-wave spectrum, which could then be used to calculate the fields in different ground types from

the field on a surface in front of the antennas when they radiate into free-space. Aspects of both techniques are explored in this thesis, but only the first is applied to the spiral system.

The reciprocity model described is developed and shown to agree well with measurements for sufficiently small scatterers. The model is then used to characterize the GPR system's ability to detect scatterers with different types of geometries. It is found that the bistatic pair is much less efficient than the monostatic antenna. In addition, the monostatic antenna is far more sensitive to scatterers very near the air-ground interface than away from it. This could make the monostatic system much less useful when dealing with clutter.

In addition, the claim that the circular polarization of the spiral antenna is useful for identifying the geometry of a target in the ground is examined. Because circular polarization is a far-field concept, some redefinition of the term is required to study it in the near-field under the ground. In this work, the question of whether circular polarization exists in the ground under the antennas is replaced with the equivalent question of whether a symmetric scatterer is rejected by the antennas. This symmetric-scatterer rejection is well-defined even directly next to the antennas, and it is found that symmetric-scatterer rejection occurs well into the near-field, however for grounds with high permittivity, the angular width of the region where rejection occurs becomes smaller.

The use of the plane-wave spectrum for characterizing the GPR system was found to have two difficulties. The first difficulty is that the calculation of the plane-wave spectrum from some finite plane of field data can only be done accurately when the antenna under test is highly directive in the direction normal to the sampling plane. The second difficulty is that the plane-wave spectrum can only be used to predict the fields in the ground when the antenna under test has a small scattering cross-section. The spiral antennas in this work are not particularly directive and they have a fairly large scattering cross-section, so the technique was not coupled with the reciprocity model. However, the problem of calculating the plane-wave spectrum of a low-directivity antenna was looked into extensively, and a technique for improving this calculation is presented as the final part of this thesis.

CHAPTER I

INTRODUCTION

The equiangular spiral antenna, which was first proposed in 1957, was originally a slot cut out of a metal sheet [1]. In the decade after its introduction, a number of analyses of this structure, isolated in free space, were attempted with varying success. Since this period, practical spiral elements have changed significantly with the introduction of the dielectric substrate necessary for printed circuit fabrication and the absorbing can that is necessary to create a unidirectional pattern. In addition, today the antenna is often placed near a large dielectric body when it is used in detection systems such as ground-penetrating or through-wall radar systems.

It is the intention of this work to examine the issues introduced by these changes through the use of numerical models and experiment. Design graphs are provided for relevant parameters and an attempt is made whenever possible to develop an understanding of phenomena observed in design graph studies. The spiral is studied in the context of a spiral-based ground-penetrating radar detection system that is built and modeled over the course of the work.

In the following section, the reasoning behind the design of the spiral is explored, and some of the models for its operation are discussed. In addition, the historical development of the understanding of the antenna is described, and references are given that show its use in detection systems. In chapter two, a discussion of the finite-difference time-domain (FDTD) numerical model used in this work along with the details of the measurements that verified the model's proper operation are presented. In chapter three, an FDTD-based analysis of the spiral antenna operating on a dielectric substrate is presented including its characteristics in the operating band and the frequency limitations of the operating band. In chapter four, the modeling and verification of the complete spiral-based GPR system is described. The complete system modeled consists of an absorbing can with absorber for

each of the two spiral elements used, a mount for the two spirals, a model for the ground, and any scatterer of interest. In chapter five, an analysis of the two-spiral GPR system is presented in terms of its interaction with electrically small scatterers. Finally, in chapter six, some work on the plane-wave spectrum and its application to the understanding of a GPR system are presented.

1.1 The Frequency-Independent Antenna Problem

In many applications, it is desirable that an antenna have the ability to radiate efficiently over a broad range of frequencies. For instance, in a communication system, a broadband antenna can increase the amount of information sent at one time by transmitting on several separate regions of the spectrum. In radar systems, it is desirable to send a pulse that is abrupt and localized in time in order to distinguish reflections from material interfaces from one another. Since the abruptness of a signal in the time domain is limited by the bandwidth of that signal as represented in the frequency domain, an antenna with no bandwidth constraints would also be ideal for radar systems.

While unable to achieve complete frequency independence, V. H. Rumsey outlined two requirements for an antenna to behave equally well at all frequencies within an arbitrarily wide band [2]. The first requirement imposed on the geometry of the antenna is related to the scaling principle of electromagnetics. The second requirement is known as the truncation principle and is imposed by the necessity that the antenna be finite in size. In this chapter, both properties are described. Afterwards, it is shown that the equiangular spiral antenna, the subject of this work, approximately satisfies the conditions Rumsey proposed. The chapter concludes with an overview of the published research that has been performed on the antenna.

1.2 The Scaling Principle

One may calculate the input impedance and directivity of a half-wavelength dipole without any information as to its physical length or its frequency of operation. [1] This is possible because of the scaling principle of electromagnetics, which generally states that the impedance and directivity of a lossless antenna are only a function of its geometry as described in wavelengths. This principle is shown using Maxwell's equations in this section. Consider Maxwell's equations in a simple non-conductive medium described by a permittivity $\epsilon_a(\overrightarrow{r})$ and a permeability $\mu_a(\overrightarrow{r})$, both functions of position. The equations satisfied by the electric and magnetic fields $\overrightarrow{\mathcal{E}}_a(\overrightarrow{r},t)$ and $\overrightarrow{\mathcal{H}}_a(\overrightarrow{r},t)$ are

$$\nabla \times \overrightarrow{\mathcal{E}}_a(\overrightarrow{r},t) = -\mu_a(\overrightarrow{r})\frac{\partial \overrightarrow{\mathcal{H}}_a(\overrightarrow{r},t)}{\partial t} \qquad \nabla \cdot \Big(\epsilon_a(\overrightarrow{r})\overrightarrow{\mathcal{E}}_a(\overrightarrow{r},t)\Big) = 0$$
$$\nabla \times \overrightarrow{\mathcal{H}}_a(\overrightarrow{r},t) = \epsilon_a(\overrightarrow{r})\frac{\partial \overrightarrow{\mathcal{E}}_a(\overrightarrow{r},t)}{\partial t} \qquad \nabla \cdot \Big(\mu_a(\overrightarrow{r})\overrightarrow{\mathcal{H}}_a(\overrightarrow{r},t)\Big) = 0,$$

for all $\overrightarrow{r}$ in $\mathbb{R}^3$ except on some surface S, where a boundary condition is imposed.

One may simplify these equations by Fourier transforming [2] each side along the time dimension. When doing so, the transformed quantities, $\overrightarrow{\mathcal{E}}_a(\overrightarrow{r},\omega_a)$ and $\overrightarrow{\mathcal{H}}_a(\overrightarrow{r},\omega_a)$ represent the portion of the solution that oscillates with a time dependence of $e^{j\omega_a t}$. The value of the transformed quantities at the fixed frequency ω_a are represented in bold-face. The equations satisfied by those quantities are shown below

$$\nabla \times \vec{\mathbf{E}}_{\mathbf{a}}(\overrightarrow{r}) = -j\omega_a\mu_a(\overrightarrow{r})\vec{\mathbf{H}}_{\mathbf{a}}(\overrightarrow{r}) \qquad \nabla \cdot \Big(\epsilon_a(\overrightarrow{r})\vec{\mathbf{E}}_{\mathbf{a}}(\overrightarrow{r})\Big) = 0 \qquad (1.1)$$
$$\nabla \times \vec{\mathbf{H}}_{\mathbf{a}}(\overrightarrow{r}) = j\omega_a\epsilon_a(\overrightarrow{r})\vec{\mathbf{E}}_{\mathbf{a}}(\overrightarrow{r}) \qquad \nabla \cdot \Big(\mu_a(\overrightarrow{r})\vec{\mathbf{H}}_{\mathbf{a}}(\overrightarrow{r})\Big) = 0, \qquad (1.2)$$

for all $\overrightarrow{r}$ in $\mathbb{R}^3$ except on some surface S.

On S, a boundary condition is imposed on $\vec{\mathbf{E}}_{\mathbf{a}}(\overrightarrow{r})$ or $\vec{\mathbf{H}}_{\mathbf{a}}(\overrightarrow{r})$. This surface could be the surface of an ideal metal conductor with the imposition that the tangential electric field remain zero, or it could be part of an antenna feed where the electric field is set to excite the antenna at the frequency ω_a. Now consider the functions defined by scaling the solutions

[1] This is true for an ideal half-wavelength dipole that is assumed to be thin and lossless.

[2] The Fourier transform of some function f(t) is defined in this thesis to be $F(\omega) = \int f(t)e^{-j\omega t}dt$ with inverse transform $f(t) = \frac{1}{2\pi}\int F(\omega)e^{j\omega t}d\omega$. The choice of Fourier transform normalization will not change any results in this section.

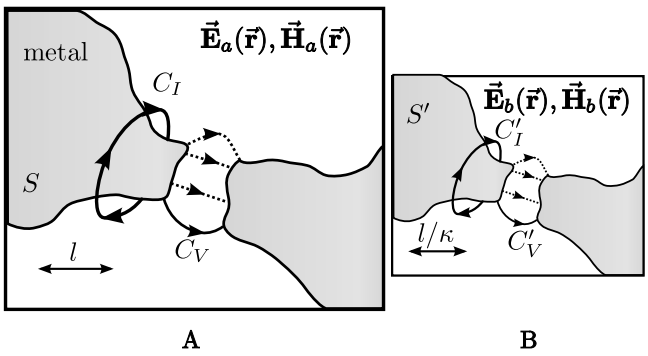

Figure 1.1: Possible boundary conditions for an antenna problem prior to and after scaling by a factor κ. C_I and C_V are contours that could be used to calculate the voltage and current being fed into the antenna. C_V has parameterization $\vec{r}_a(s)$. C'_V has parameterization $\vec{r}_b(s)$. In the transformation shown, $\kappa > 1$.

as well as the geometry of the space

$$\vec{\mathbf{E}}_\mathbf{b}(\overrightarrow{r}) = \vec{\mathbf{E}}_\mathbf{a}(\kappa\overrightarrow{r}) \qquad \vec{\mathbf{H}}_\mathbf{b}(\overrightarrow{r}) = \vec{\mathbf{H}}_\mathbf{a}(\kappa\overrightarrow{r}) \tag{1.3}$$

$$\epsilon_b(\overrightarrow{r}) = \epsilon_a(\kappa\overrightarrow{r}) \qquad \mu_b(\overrightarrow{r}) = \mu_a(\kappa\overrightarrow{r}). \tag{1.4}$$

See Fig. 1.1 for a diagram of the initial and transformed spaces. Note that when the scale factor κ is applied, distances measured in the transformed space are a factor of $1/\kappa$ times the original distance. By applying the chain rule for differentiation [3] to $\nabla \times \vec{\mathbf{E}}_\mathbf{b}$ and $\nabla \cdot \left(\epsilon_b \vec{\mathbf{E}}_\mathbf{b}\right)$, one can show that these functions satisfy Maxwell's equations for the scaled geometry $\epsilon_b(\overrightarrow{r})$ and $\mu_b(\overrightarrow{r})$ at a frequency $\omega_b = \kappa\omega_a$

$$\begin{aligned}
\nabla \times \vec{\mathbf{E}}_\mathbf{b}\Big|_{\overrightarrow{r}} &= \kappa \nabla \times \vec{\mathbf{E}}_\mathbf{a}\Big|_{\kappa\overrightarrow{r}} \\
&= -\kappa j\omega_a\mu_a(\kappa\overrightarrow{r})\vec{\mathbf{H}}_\mathbf{a}(\kappa\overrightarrow{r}) && \text{by Faraday's law (1.1)} \\
&= -j\omega_b\mu_b(\overrightarrow{r})\vec{\mathbf{H}}_\mathbf{b}(\overrightarrow{r}) && \text{using (1.3) and (1.4)} \\
\nabla \cdot \left(\epsilon_b \vec{\mathbf{E}}_\mathbf{b}\right)\Big|_{\overrightarrow{r}} &= \kappa\, \nabla \cdot \left(\epsilon_a \vec{\mathbf{E}}_\mathbf{a}\right)\Big|_{\kappa\overrightarrow{r}} \\
&= 0.
\end{aligned}$$

A similar procedure yields the formulas in (1.2). Since the original solution satisfies some boundary condition on the surface S, it must also be true that the new solution satisfies a

[3] In the notation used below, $\nabla \times \overrightarrow{E}\Big|_{\vec{\mathbf{r}}} = \nabla \times \overrightarrow{E}(\vec{\mathbf{r}})$. This is intended to emphasize that the curl or divergence operator is with respect to the standard coordinates $\vec{\mathbf{r}}$. It is applied first and then the resulting vector field is evaluated at $\vec{\mathbf{r}}$.

scaled boundary condition $\vec{\mathbf{E_b}}(\overrightarrow{r}) = \vec{\mathbf{E_a}}(\kappa\overrightarrow{r})$ on $S' = \{\overrightarrow{r}|\kappa\overrightarrow{r} \in S\}$.

To summarize, whenever a solution to Maxwell's equations for a harmonic excitation at frequency ω_a is known, one can automatically obtain another solution to Maxwell's equations where all dimensions have been scaled down by a factor of κ and the harmonic excitation has been scaled up to $\kappa\omega_a$. Where the original surface S was a perfect conductor, there is now a scaled conductor κ times smaller in the new solution. Where there was once an antenna feed, there is now a scaled down feed.

One can obtain the impedance of the antenna by taking the ratio of the voltage to current at the antenna feed. By checking this parameter in the scaled and unscaled spaces one may show that the impedance remains unchanged. In order to compute the voltages V_b and V_a in the scaled and unscaled spaces, consider the contour, C_V, and a parameterization, $\overrightarrow{r}_a(s) : [0,1] \to \mathbb{R}^3$, along with the scaled contour, C'_V, and its parameterization, $\overrightarrow{r}_b(s) : [0,1] \to \mathbb{R}^3$. Noting that $\overrightarrow{r}_a(s) = \kappa\overrightarrow{r}_b(s)$, one finds

$$\begin{aligned} V_b &= \int_{\mathcal{C}'_\mathcal{V}} \vec{\mathbf{E_b}}(\overrightarrow{r}_b) \cdot d\overrightarrow{r}_b \\ &= \int_0^1 \vec{\mathbf{E_a}}(\kappa\overrightarrow{r}_b(s)) \cdot \overrightarrow{r'}_b(s)ds \qquad \text{using (1.3)} \\ &= (1/\kappa)\int_0^1 \vec{\mathbf{E_a}}(\overrightarrow{r}_a(s)) \cdot \overrightarrow{r'}_a(s)ds \\ &= V_a/\kappa, \end{aligned}$$

where $\overrightarrow{r'}_a(s)$ and $\overrightarrow{r'}_b(s)$ refer to derivatives with respect to s.

An identical calculation will show that the current, I_b, obtained by integrating the magnetic field around C_I, will be I_a/κ, leaving the impedance, V_b/I_b, unchanged. In fact, through a similar calculation one can show that the directivity of the antenna in any given direction also remains the same after the scaling.

This property of Maxwell's equations is known as the scaling principle. It may be stated in a way that is useful to an antenna engineer as follows: an antenna's operating impedance and radiation characteristics are a function of its geometry as described in wavelengths. In Rumsey's work on frequency independence, he remarked that an antenna with a geometry that did not change when scaled would show the same impedance and radiation

characteristics at all frequencies. This observation is of primary importance in frequency-independent antenna design. In this document, a geometry satisfying this property is called scale-independent.

1.3 The Truncation Principle

Geometries that satisfy Rumsey's requirement of scale independence must be infinitely large. However, finite approximations to these antennas may still have arbitrarily large bandwidths if the finite antenna radiates in the same way as the infinite one. A scale-independent geometry can be truncated without effect at a particular frequency only if the majority of the current on the structure is concentrated in a finite region. Rumsey referred to this necessity as the truncation principle and called the finite region where radiation occurs the active region.

One might note at this point that the two principles taken together guarantee that any physically realizable antenna cannot actually be frequency independent. If the antenna has an active region of radiation, then scaling down to lower frequencies will scale the size of this active region larger until it can no longer fit on the antenna. Likewise, scaling up to higher frequencies will scale the size of the active region so small that the desired geometry cannot be fabricated accurately. Because of this fact, the name "frequency-independent antenna" was a point of contention in a set of correspondences from the early 1960s [3]. While possibly misnamed, it is important to realize that the two principles described do provide a formal guideline for designing an antenna with an arbitrarily wide bandwidth. To set the lower-frequency cutoff, the outer truncation of the antenna is adjusted. To set the upper frequency cutoff the inner truncation of the antenna is adjusted.

1.4 The Spiral Geometry and Frequency Independence

The class of geometries that are identical after a scaling transformation consists of angular and conic sections such as infinitely large biconical antennas or bow-ties. The currents on these antennas tend to decay slowly and require a resistive termination for broadband use. This addition of loss makes them no longer satisfy the scaling principle as described above. To obtain a practical frequency-independent geometry, Rumsey proposed a relaxation of

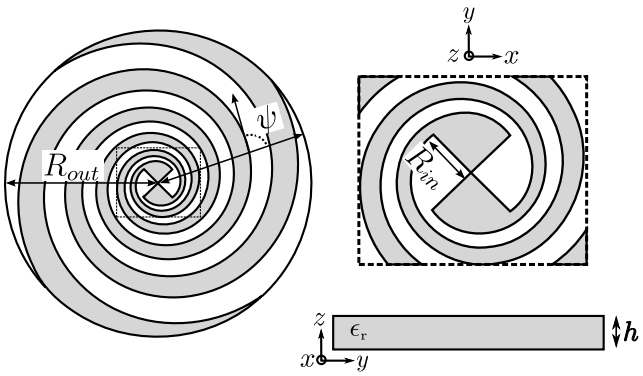

Figure 1.2: Geometry of a truncated two-arm equiangular spiral antenna

the requirements. He allowed scaling to modify the antenna's geometry, but only by a rotation. This clearly would leave the impedance properties of the antenna the same. If, in addition, the radiation pattern of the antenna were rotationally symmetric, then true frequency independence could be achieved.

In [2], Rumsey derives a curve that satisfies the property that a scaling is equivalent to a rotation. This curve is written in polar coordinates as

$$r(\theta) = e^{a\theta+b}, \tag{1.5}$$

where the constant a determines the rate of wrapping and the constant b scales the curve. This scaling is also equivalent to a rotation. By scaling the curve by a factor κ one finds

$$\kappa r(\theta) = \kappa e^{a\theta+b} = e^{a(\theta+\log(\kappa)/a)+b} = r(\theta + \log(\kappa)/a). \tag{1.6}$$

In words, the curve has been rotated by an angle of $\log(\kappa)/a$ radians.

The curve, called the equiangular spiral, has the property that at any two points the angles between the tangent and radial vectors are equal. In fact this angle is frequently used to describe the spiral's geometry instead of a. The angle, here denoted ψ, can be related to a by $\tan(\psi) = 1/a$.

When this curve is repeatedly rotated by 90°, it forms the edges of a two-armed self-complementary structure as shown in Fig. 1.2. The exterior of the antenna may be truncated in a number of ways. The truncation used in Fig. 1.2 was introduced by Dyson in [4] because it maximizes the number of turns for a given outer radius.

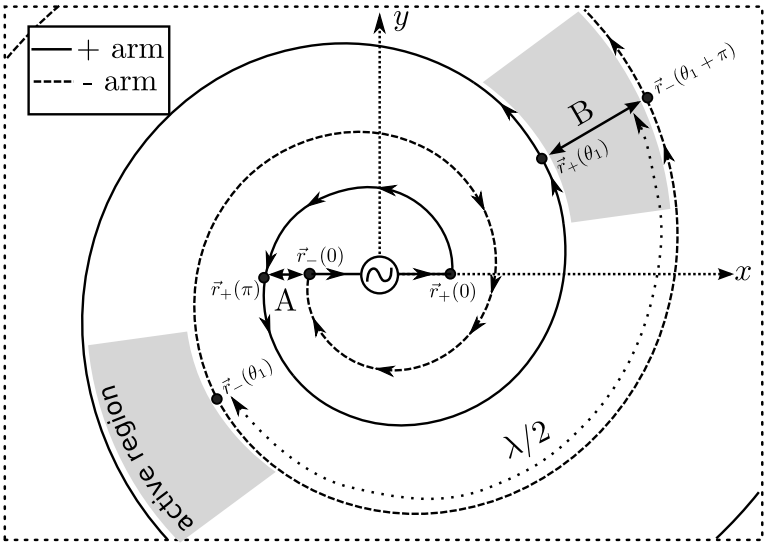

Figure 1.3: Transmission line theory of operation. At A, the currents in the two arms are approximately in antiphase, their radiations canceling. At B, the currents in the two arms are now approximately in phase, their radiations summing. The region near B and the region adjacent to it (shown in gray) are known as the active region of the antenna.

If the geometry is defined so that the spiral arms become close enough together to directly connect to a waveguide, no additional feed section is necessary at the inner truncation. However, because of fabrication tolerances this is often not possible. In this work, a bow-tie section is used directly at the feed of the antenna, as shown in Fig. 1.2.

Since the spiral curve was defined to equate rotation with scaling, it is clearly scale-independent in the sense used by Rumsey. To establish that the spiral antenna is frequency independent, it is necessary to determine if it also satisfies the truncation principle. If the current distribution on the spiral antenna were known to decay rapidly as a function of arm length, this would be sufficient proof. As discussed in the literature review below, this has been shown to be the case experimentally and to a certain degree numerically [4–7].

In this section, a description of the radiation mechanism and why the spiral radiates in a distinct, finite region is discussed. It is a slightly modified version of a model proposed by Julius Kaiser for the Archimedean spiral [8]. The Archimedean spiral is similar to the equiangular spiral but is defined by the curve $r(\theta) = a\theta$. It does not possess scale-independence. It does, however, tend to show essentially the same broadband characteristics seen in the equiangular spiral when designed properly.

The premise of the model Kaiser proposed is that the spiral antenna can be considered a transmission line that, by the nature of the wrapping of its arms, is transformed into a radiating structure. In Kaiser's model, the width of the spiral arms is ignored. In Fig. 1.3, a spiral is shown that is composed of two contours described by equation (1.5). Before describing the mechanism, the coordinate used to describe the position along the spiral arms must be defined. Let $\vec{r}_+(\theta)$ be the position vector for the first spiral arm. The vector points from the origin to the point $(r(\theta), \theta)$, where standard polar coordinates are used and $r(\theta)$ is defined by (1.5) for $b = 0$. The curve that describes the second spiral is then

$$\vec{r}_-(\theta) = -\vec{r}_+(\theta).$$

Suppose that the current source, shown connecting the two arms at $\vec{r}_+(0)$ and $\vec{r}_-(0)$, provides a time harmonic excitation of the spiral. Then, the steady-state current in the entire spiral will have the same time variation within a phase shift. Using the convention that a harmonic signal may be represented by a complex exponential multiplied by a phasor, the current at the point $\vec{r}_\pm(\theta)$ is described by

$$I_\pm(\theta, t) = i_\pm(\theta)e^{j\omega t}, \tag{1.7}$$

where $i_\pm(\theta)$ is a complex valued function of θ. The actual current is always the real part of $I_\pm(\theta, t)$, and that real part has a positive sign when it is directed outward.

Since the spiral is modeled with no outer truncation, the current may be assumed to consist of an outward traveling wave only. If the phase velocity of the wave is assumed to be a constant, v_p, one may describe the phase of the current on the spiral by the travel time from the origin, denoted here as t_d. This travel time is $s_\pm(\theta)/v_p$, where $s_\pm(\theta)$ is the distance along the spiral path from the origin to the point $\vec{r}_\pm(\theta)$. One may obtain this distance

$$\begin{aligned} s_\pm(\theta) - s_\pm(0) &= \int_0^\theta \left| \frac{d\vec{r}_\pm(\theta)}{d\theta} \right| d\theta \\ &= \int_0^\theta \sqrt{\left(\frac{dr(\theta)}{d\theta}\right)^2 + \left(r\frac{d\theta}{d\theta}\right)^2}\, d\theta \\ &= (e^{a\theta} - 1)\sqrt{1 + \frac{1}{a^2}}. \end{aligned} \tag{1.8}$$

One then finds that the phase of the current on the spiral is

$$\begin{aligned}
\angle I_{\pm}(\theta,t) &= \angle I_{\pm}(0,t-t_d) && \text{where } t_d \text{ is the time delay} \\
&= \angle i_{\pm}(0)e^{j\omega t} + \angle e^{-j\omega t_d} && \text{where (1.7) is used} \\
&= \angle I_{\pm}(0,t) - \frac{2\pi f s_{\pm}(\theta)}{v_p} && \text{because } t_d = s^{\pm}(\theta)/v_p \\
&= \angle I_{\pm}(0,t) - \frac{2\pi s_{\pm}(\theta)}{\lambda} && \text{because } \lambda f = v_p. \qquad (1.9)
\end{aligned}$$

If one assumes that the feed diameter is a very small fraction of a wavelength, the fact that the antenna is fed in a balanced mode implies that the currents shown at location A in Fig. 1.3 are in antiphase. This is written as

$$\angle I_{+}(\pi,t) - \angle I_{-}(0,t) \approx \angle I_{+}(0,t) - \angle I_{-}(0,t) = \pi. \qquad (1.10)$$

Since the two adjacent currents at location A are so close to one another, their contributions to radiation cancel. The cancellation continues as long as the path length traveled by both currents is electrically small. As θ increases, there comes a point, $\vec{r}_{-}(\theta_1)$, where

$$s_{-}(\theta_1+\pi) - s_{-}(\theta_1) = \lambda/2. \qquad (1.11)$$

From (1.8), one may calculate the point explicitly. It occurs when

$$\theta_1 = \frac{1}{a}\log\left(\frac{\lambda}{2(e^{a\pi}-1)\sqrt{1+a^{-2}}}\right). \qquad (1.12)$$

At this point and the arm adjacent to it, shown as location B in Fig. 1.3, one finds

$$\angle I_{-}(\theta_1+\pi,t) - \angle I_{+}(\theta_1,t) = \left(\angle I_{-}(\theta_1+\pi,t) - \angle I_{-}(\theta_1,t)\right) + \left(\angle I_{-}(\theta_1,t) - \angle I_{+}(\theta_1,t)\right).$$

The first term is evaluated explicitly

$$\begin{aligned}
\angle I_{-}(\theta_1+\pi,t) - \angle I_{-}(\theta_1,t) &= \angle I_{-}(0,t) - \angle I_{-}(0,t) - \frac{2\pi(s_{-}(\theta_1+\pi) - s_{-}(\theta_1))}{\lambda} \quad \text{by (1.9)} \\
&= \pi.
\end{aligned}$$

Since both currents in the second term are evaluated at the same distance from the origin but on opposite arms, (1.9) implies that these currents are still in antiphase. Then, summing

the two $\pm\pi$ terms, one finds that the currents at location B are in phase. Therefore their radiation contributions sum.

This description will show that the same condition occurs at the same value of θ_1 along the opposite arm, $r_+(\theta)$. The region of the spiral near point B and that adjacent to it is referred to as the active region of the antenna (shown in gray). Higher-order active regions occur when $\lambda/2$ in (1.11) is replaced with $k\lambda + \lambda/2$ for integer k. However, at each of these regions the radiation reduces the power in the outward traveling wave so that higher-order active regions may often be ignored in an analysis.

For spirals with a sufficiently tight wrapping, the active region may be described in a simpler way. From (1.5), it is apparent that reducing the magnitude of the parameter a corresponds to increasing the wrapping tightness. Therefore, letting a tend to zero, one obtains an approximate radiation condition from (1.12) and (1.5)

$$\begin{aligned} r(\theta_1) &= e^{a\theta_1} \\ &= \frac{a\lambda}{2(-1+e^{a\pi})\sqrt{1+a^2}} \\ &\approx \frac{a\lambda}{2(-1+1+a\pi+...)1} \\ &\approx \lambda/(2\pi) \\ 2\pi r(\theta_1) &= \lambda. \end{aligned}$$

In words, a tightly wrapped spiral will radiate in a circular band of circumference λ. This condition is identical to that obtained by Kaiser for the Archimedean spiral. This may be part of the reason that ideas developed for the Archimedean spiral sometimes apply to the equiangular.

The essentials of this derivation can be captured visually by drawing the phase of the current onto the spiral arms. In Fig. 1.4, the phase of the current at a fixed time, $t = 0$, on a tightly wrapped spiral, $a = 0.05$, is shown. The phase is indicated using a color map and the traveling wave on the arms is driven so that the wavelength is 1 m. At the inner truncation of the spiral, it can be seen that the two arms are driven in anti-phase, with the right arm driven at 0 radians while the left is driven at π radians. Noting that the arm

that is driven with a negative current is cross-hatched, one can see that near the center of the spiral, the two arms are consistently in anti-phase of one another, meaning their contributions to radiation will cancel. The phase difference becomes less significant nearer the active region, which approximately occurs at a radius, r, satisfying $2\pi r = 1$ m. This is indicated with a black band that surrounds the circle $2\pi r = 1$ m. At the active region for the spiral, however, adjacent arms are in phase. The arms stay in phase for a full two turns, and they stay in phase longer for tighter wrappings, but outside of the active region, they return to an out of phase condition. In Fig. 1.5, the same situation can be seen for $\lambda = 1.5$ m. Here, the active region occurs when $2\pi r = 1.5$ m.

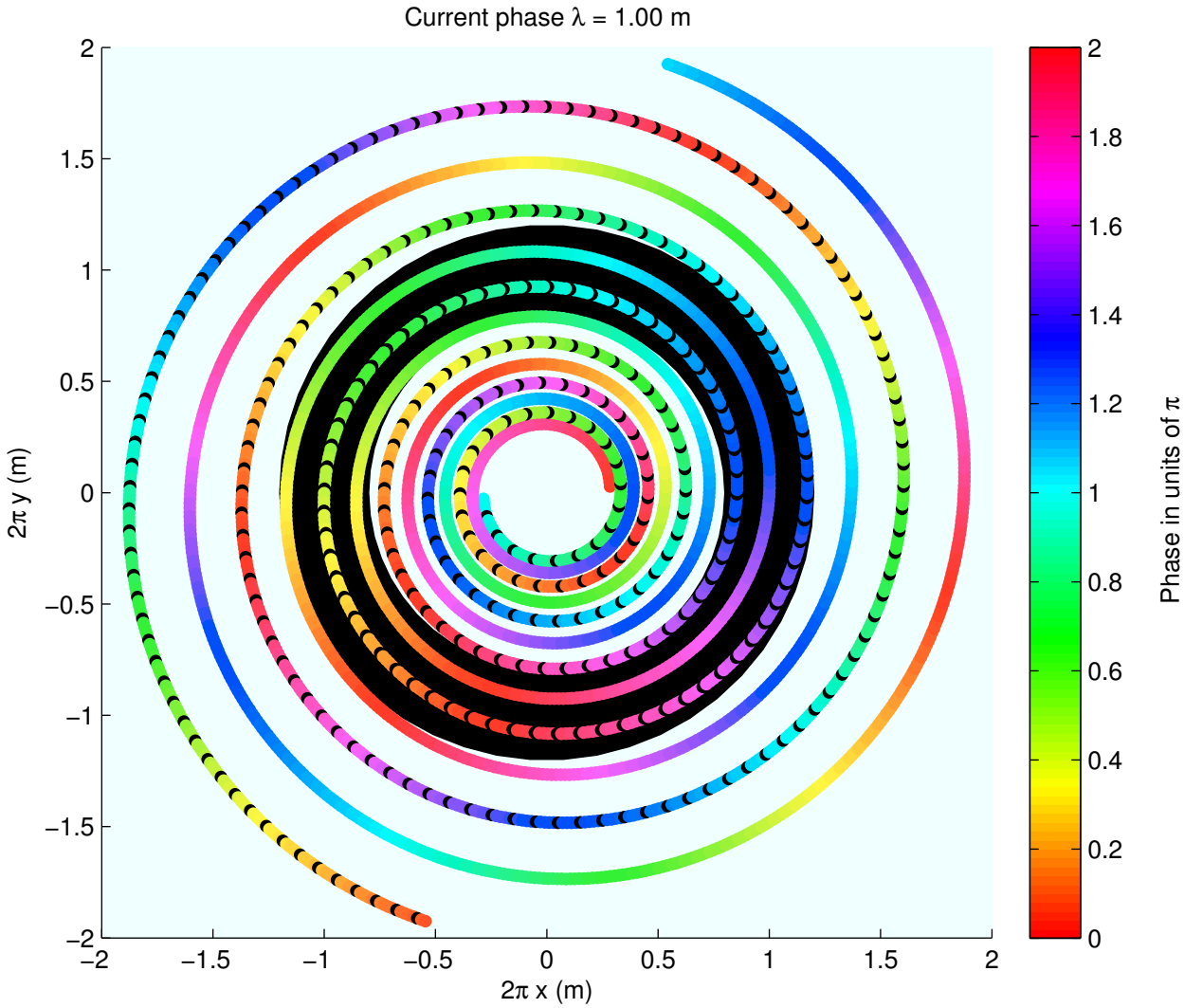

Figure 1.4: Transmission line theory of operation. At the center, the currents in the two arms are approximately in antiphase and their radiations cancel. At the active region, shown as a black band, the currents in the two arms are approximately in phase, and their radiations sum.

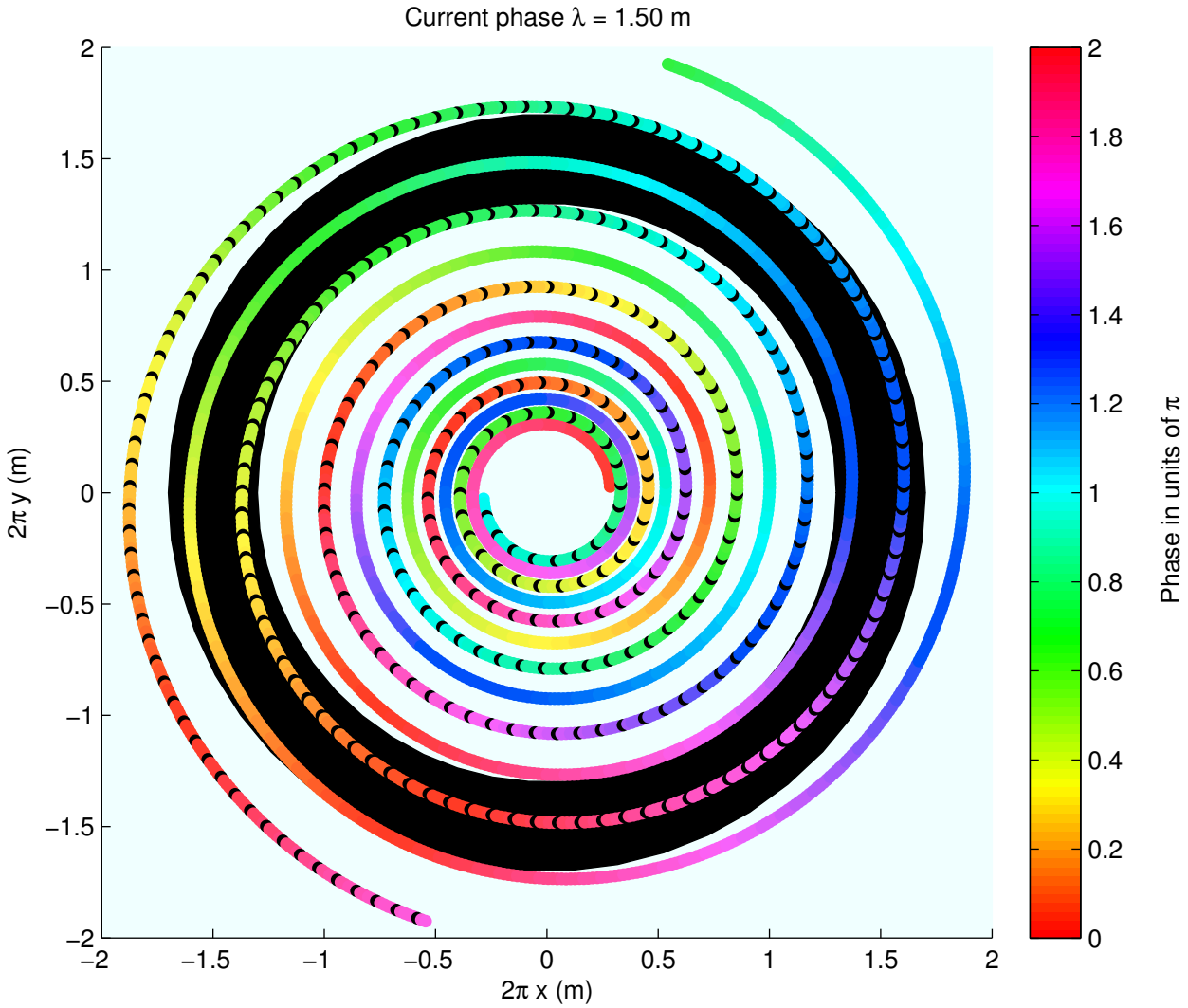

Figure 1.5: Transmission line theory of operation. At the center, the currents in the two arms are approximately in antiphase and their radiations cancel. At the active region, shown as a black band, the currents in the two arms are approximately in phase, and their radiations sum.

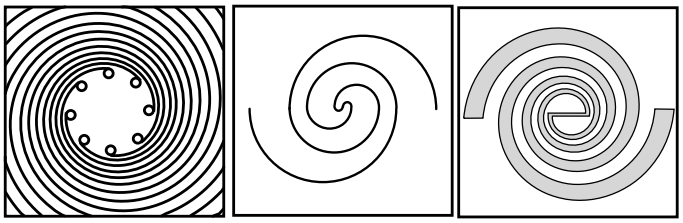

Figure 1.6: (a) Rumsey's infinite arm spiral was in some sense the limit as the number of spiral arms tended to infinity. (b) Curtis's semi-circle spiral is composed of semicircles attached at the ends. (c) Wentworth and Rao's equiangular spiral analysis was fed with a line source.

1.5 Previous Work on the Spiral Antenna

The application of the equiangular spiral antenna in radar detection, direction-finding, and communication systems [9–12] causes it to appear in a wide variety of works, but it is rarely the focus of the work. Most journal publications that include an equiangular spiral will reference the original sources. These are Dyson's 1957 thesis, the paper on the same work, and Rumsey's book on frequency independence [1, 2, 4]. However, many studies that primarily focus on the Archimedean spiral also provide some conclusions about the equiangular spiral. One of the first published attempts at analyzing the spiral was by Curtis in 1959 [13]. There, the two-arm spiral was approximated by a series of connected thin-wire semicircles. The model showed good agreement with experimental results when the antennas were made in the same semi-circular shape. In 1961, Cheo, Rumsey, and Welch published an analytical work in which the spiral element was approximated with an "infinite arm" spiral [14]. While not physical, the solution did show a current that dropped off rapidly, suggesting an active region for the antenna. Both approximations to the spiral geometry may be seen in Fig. 1.6. In 1963, Sivan-Sussman showed experimentally that two-arm, four-arm, and six-arm spiral radiation patterns show some of the characteristics seen in the infinite spiral solution when fed in a similar way [15].

Some of the earliest purely experimental works on the spiral were by Bawer and Wolfe [16, 17]. They consisted of papers in 1960 and 1961 that described the design of spiral antennas on printed circuit boards and the use of an absorbing can to create a unidirectional

pattern. This appears to be the first work to propose the use of a dielectric backing material for the spiral. Prior works formed the spiral shape by cutting slots out of thick metal sheets. Bawer and Wolfe's papers were criticized by Dyson for lumping the Archimedean spiral in with the equiangular spiral in [3]. However, from a design point of view the equiangular spiral does appear to share a great deal with the Archimedean spiral. Another notable experimental work was by Weir and Robinson in 1973 [18]. The report focused only on the equiangular spiral designed on a printed circuit board and shows the dramatic changes in the operating-band impedance that can be caused by the introduction of the substrate. The focus of the report was to determine the effect of various building materials on the impedance of the antenna measured from the feed. It contained the guideline that the antenna's impedance could be predicted by applying Booker's relation for an effective dielectric, as described later in this document [19].

The spiral has been a subject of a number of numerical works, but is often presented as a verification for a numerical technique rather than the subject of the work itself. A very early computerized application of the method of moments by Mei in 1964 [20] used the spiral as an example problem. Here the current on a thin-wire equiangular spiral was computed as an example of the utility of the method. Another example is an early application of the finite-difference time-domain (FDTD) method to antennas in 1994 by Luebbers. He analyzed two spiral antennas over an absorbing can, but again the focus of the work was on the accuracy of the FDTD method [21]. A work by Wentworth and Rao broke this mold somewhat in 1995 with a method-of-moments analysis of the equiangular spiral element without a dielectric backing [22]. Here a number of parameterized design graphs are shown for the axial ratio. Impedance is shown as a function of the geometric parameters of the spiral, also. One notable result obtained in this paper was that the self-complementary antenna's impedance did not appear to satisfy Booker's relation [19]. Finite-difference time-domain simulations performed in the work for this thesis have shown that this result was at least partially a consequence of the feed chosen in the paper, depicted in Fig. 1.6, which was not self-complementary. When modeled with the line feed, the impedance measured tends to be a strong function of the exact feed geometry unless the feed is made electrically small.

On the other hand, modeling the spiral with an extremely small feed attached to a self-complementary bow-tie tends to show the predicted value for the impedance. A notable numerical work is a 2005 finite-volume time domain analysis of an Archimedean spiral on dielectric in a can containing a honey-comb absorber [23]. The numerical model is compared with experimental data and shows good agreement. The paper continues with an extensive study of the current distribution on the spiral.

While not directly addressed in this thesis, one active area of research regarding the spiral antenna is in making the antenna pattern unidirectional. This is typically achieved by attaching an absorbing can to the back of the antenna, but this wastes half of the energy inserted into the spiral and requires a significant amount of space. Because of this, a number of authors have proposed methods to reflect the radiation. This has generally been achieved by placing some type of planar reflector behind the spiral [24, 25]. In recent work by Nakano, two reflectors are described. In a 2008 paper, he shows a PEC backing to an equiangular spiral antenna with very little effect over a fairly wide band. The axial ratio is kept fairly low by attaching a resistive ring around the edges of the spiral. This ring is very effective at absorbing the outgoing wave and provides good evidence that the equiangular spiral can be resistively truncated just as well as an Archimedean [26]. A 2009 paper describes the use of a PCB reflector with a periodic array of metal squares on it that are not electrically bound together. This configuration is referred to as an electronic band gap reflector in the paper. The electronic band gap material reflects waves with the opposite sign of a normal PEC conductor over a narrow band of frequencies. This allows the reflector to be placed very close to the antenna without canceling its radiation, but inherently reduces the bandwidth of the antenna to that of the band gap. The paper shows that the technique can be made to work with some optimization [27].

The spiral appeared as a subject in some detection-system work, although these papers were often not focused on the spiral itself, but rather some aspect of the detection problem. A prototype spiral for a GPR system is shown in a 2002 paper by Su with the cited benefits that the circular polarization properties of the antenna could be expected to reject ground reflections [28]. The subject of circularly polarized radiation is considered less important

in a land mine detection scenario by Paolino. He noted in a 2002 paper that a monostatic circularly polarized antenna would also be expected to reject a land mine due to symmetry considerations [29]. The main reasons for interest in the spiral for detection systems cited in Paolino's work are its inherent real-valued impedance in the range of $100 - 200\Omega$ for typical microwave substrates, and its frequency independence. He chooses an Archimedean spiral over an equiangular spiral because of the ease with which the Archimedean spiral can be resistively terminated. In a 2002 paper by Lacko, a comparison of the Archimedean spiral and the equiangular spiral is undertaken by fabricating and measuring four test antennas, two of each type, one of each with a balun and arm terminations and one of each without. The conclusions of the paper are that the Archimedean spiral is a better candidate for a GPR system based on its well-defined dispersion relation [30]. In a 2004 conference paper by Bradley, an array of Archimedean spirals is described for use mounted on a truck in a forward-looking detection system [31]. In 2005, a paper by Thaysen provided experimental results for a prototype equiangular spiral antenna intended for use in a GPR system. The advantages of the spiral antenna for the GPR problem stated were the invariance of its properties with frequency, its circular polarization, and its flat profile [32].

In addition, the equiangular spiral is used as a radiating element in a number of patented detection systems. The system described in [33] uses a large four-armed equiangular spiral in a monostatic configuration to detect pipes. This makes use of the monostatic system's rejection of symmetric scatterers. A more recent set of patents from 2007-2008 show an on-going interest in using the equiangular spiral for a detection system. In [34], a system is described that would assist in airport luggage scanning that uses a set of equiangular spiral elements. In [35], a system that would allow imaging through a wall for use in surveillance is described that uses a transmit and receive pair of equiangular spiral antennas.

Overall, there is evidence that the equiangular spiral is often considered as a candidate antenna in detection system problems, and its frequency independence is overwhelmingly considered to be its main strong-point. Despite this, the equiangular spiral is often substituted with an Archimedean spiral. Given that the equiangular spiral satisfies Rumsey's scaling principle described in this section while the Archimedean spiral does not, this choice

may seem unreasonable, except in a realistic detection system the equiangular spiral would radiate in the presence of additional elements that make it no longer satisfy the scaling principle. In this thesis, several such elements are included, such as the dielectric substrate, the absorbing can, or the ground. Throughout the work, it is seen that the equiangular spiral does not become significantly less broadband as these elements are included in the model. This may suggest that the antenna is very versatile or it may suggest that satisfying the scaling principle is not terribly important for an antenna to be broadband. It is likely that in most cases the Archimedean spiral is a suitable substitute for the equiangular spiral, and that much of the analysis in this thesis could be applied equally well to an Archimedean-based system.

CHAPTER II

MODELING AND VERIFICATION OF THE SPIRAL ELEMENT

To begin the study of the spiral, a set of software tools for full-wave simulation were developed to implement the finite-difference time-domain (FDTD) algorithm. For completeness, this section presents a basic outline of the finite difference method. A brief description of a ballooned mesh, and a convolutional perfectly matched layer is given. The numerical feed for an antenna problem is discussed and finally the verification of the model using measurements of fabricated spiral antennas is presented. Further details on the FDTD method can be found in [36].

2.1 The Finite Difference Time Domain Method

The finite-difference time-domain (FDTD) method was implemented for use in all of the modeling efforts in this project. The code was written primarily in C using the open-MPI library for message passing on a computing cluster. The FDTD method provides an approximate solution to the vector fields $\overrightarrow{\mathcal{E}}, \overrightarrow{\mathcal{H}}, \overrightarrow{\mathcal{D}}$, and $\overrightarrow{\mathcal{B}}$ in Maxwell's equations

$$\nabla \times \overrightarrow{\mathcal{H}} = \overrightarrow{\mathcal{J}} + \frac{\partial \overrightarrow{\mathcal{D}}}{\partial t} \tag{2.1}$$

$$\nabla \times \overrightarrow{\mathcal{E}} = -\frac{\partial \overrightarrow{\mathcal{B}}}{\partial t} \tag{2.2}$$

$$\nabla \cdot \overrightarrow{\mathcal{B}} = 0 \tag{2.3}$$

$$\nabla \cdot \overrightarrow{\mathcal{D}} = \rho, \tag{2.4}$$

on a discrete grid of points that extend throughout the space of interest. In addition to Maxwell's equations, some constitutive relations hold in the space. These state that $\overrightarrow{\mathcal{E}}$ may be written as a function of $\overrightarrow{\mathcal{D}}$ and that $\overrightarrow{\mathcal{H}}$ may be written as a function of $\overrightarrow{\mathcal{B}}$. The solution is obtained as a discrete function of time and all fields have initial values of zero throughout the grid. The FDTD method also solves a type of boundary value problem in that arbitrary

perfectly conductive bodies, which enforce a zero tangential $\overrightarrow{\mathcal{E}}$ on a given surface, may be placed in the simulation space.

FDTD allows the constitutive relations to be very general. The relationship between $\overrightarrow{\mathcal{D}}$ and $\overrightarrow{\mathcal{E}}$ or $\overrightarrow{\mathcal{H}}$ and $\overrightarrow{\mathcal{B}}$ may vary as a function of position or frequency. The code implemented for this project allows for arbitrary simple materials where $\overrightarrow{\mathcal{D}} = \epsilon\overrightarrow{\mathcal{E}}$ and dispersive materials where $\overrightarrow{\mathcal{D}}$ can also depend on past values of $\overrightarrow{\mathcal{E}}$.

The FDTD method consists of approximating each partial derivative in Maxwell's equations with a finite difference in order to derive an explicit update from the fields at one discrete time to the next. These finite difference expressions come from a Taylor expansion of the function being differentiated. One form of Taylor's theorem states that a function with $n+1$ continuous derivatives may be approximated by a polynomial of order n near some point z,

$$f(z+\Delta) = \sum_{k=0}^{n} f^{(k)}(z)\frac{\Delta^k}{k!} + O(\Delta^{k+1}). \tag{2.5}$$

When replacing a partial derivative with a finite difference, the Taylor approximation may be used repeatedly to give an arbitrarily accurate approximation to the derivative. For example, taking only a single term, one obtains the first-order approximation

$$\begin{aligned} f(z+\Delta) &= f(z) + \Delta f'(z) + O(\Delta^2) \\ \Rightarrow f'(z) &= \frac{f(z+\Delta) - f(z)}{\Delta} + O(\Delta). \end{aligned}$$

In the FDTD method, two values of $f(z)$ are used to obtain a more accurate approximation to the derivative. This is referred to as the central-difference approximation.

$$\begin{aligned} f(z+\Delta) &= f(z) + \Delta f'(z) + \frac{\Delta^2}{2} f''(z) + O(\Delta^3) \\ f(z-\Delta) &= f(z) - \Delta f'(z) + \frac{\Delta^2}{2} f''(z) + O(\Delta^3) \\ \Rightarrow f'(z) &= \frac{f(z+\Delta) - f(z-\Delta)}{2\Delta} + O(\Delta^2). \end{aligned}$$

This is more commonly written as

$$f'(z) = \frac{f(z+\frac{\Delta}{2}) - f(z-\frac{\Delta}{2})}{\Delta} + O(\Delta^2). \tag{2.6}$$

With the central-difference approximation, the FDTD algorithm may be obtained directly from Maxwell's curl equations. Consider the x-component of (2.1),

$$\frac{\partial D_x}{\partial t} = -J_x + \frac{\partial H_z}{\partial y} - \frac{\partial H_y}{\partial z}. \tag{2.7}$$

The other two components of (2.1) may be obtained by the substitutions $(x, y, z) \rightarrow (y, z, x)$ and $(x, y, z) \rightarrow (z, x, y)$. To emphasize this, the components in this section are written as (α, β, γ) where it is assumed that (α, β, γ) is one of $(x, y, z), (y, z, x)$, or (z, x, y). For simplicity, it is also assumed that $\overrightarrow{\mathcal{D}} = \epsilon(\vec{\mathbf{r}})\overrightarrow{\mathcal{E}}$ and $\overrightarrow{\mathcal{B}} = \mu(\vec{\mathbf{r}})\overrightarrow{\mathcal{H}}$ in this section.

Applying the central-difference approximations for step sizes of $(\Delta_x, \Delta_y, \Delta_z, \Delta_t)$ along each dimension in (2.1), one obtains

$$\begin{aligned}\epsilon(\vec{\mathbf{r}})\frac{E_\alpha(\vec{\mathbf{r}}, t - \frac{\Delta_t}{2}) - E_\alpha(\vec{\mathbf{r}}, t - \frac{\Delta_t}{2})}{\Delta_t} = -J_\alpha(\vec{\mathbf{r}}, t) + \frac{H_\gamma(\vec{\mathbf{r}} + \hat{\beta}\frac{\Delta_\beta}{2}, t) - H_\gamma(\vec{\mathbf{r}} - \hat{\beta}\frac{\Delta_\beta}{2}, t)}{\Delta_\beta} \\ - \frac{H_\beta(\vec{\mathbf{r}} + \hat{\gamma}\frac{\Delta_\gamma}{2}, t) - H_\beta(\vec{\mathbf{r}} - \hat{\gamma}\frac{\Delta_\gamma}{2}, t)}{\Delta_\gamma}.\end{aligned} \tag{2.8}$$

Doing the same to the components of (2.2) yields

$$\begin{aligned}\mu(\vec{\mathbf{r}})\frac{H_\alpha(\vec{\mathbf{r}}, t - \frac{\Delta_t}{2}) - H_\alpha(\vec{\mathbf{r}}, t - \frac{\Delta_t}{2})}{\Delta_t} = -\frac{E_\gamma(\vec{\mathbf{r}} + \hat{\beta}\frac{\Delta_\beta}{2}, t) - E_\gamma(\vec{\mathbf{r}} - \hat{\beta}\frac{\Delta_\beta}{2}, t)}{\Delta_\beta} \\ + \frac{E_\beta(\vec{\mathbf{r}} + \hat{\gamma}\frac{\Delta_\gamma}{2}, t) - E_\beta(\vec{\mathbf{r}} - \hat{\gamma}\frac{\Delta_\gamma}{2}, t)}{\Delta_\gamma}.\end{aligned} \tag{2.9}$$

One can then obtain update equations

$$\begin{aligned}E_\alpha\left(\vec{\mathbf{r}}, t + \frac{\Delta_t}{2}\right) &= E_\alpha\left(\vec{\mathbf{r}}, t - \frac{\Delta_t}{2}\right) - \frac{\Delta_t}{\epsilon(\vec{\mathbf{r}})}J_\alpha(\vec{\mathbf{r}}, t) \\ &+ \frac{\Delta_t}{\epsilon(\vec{\mathbf{r}})\Delta_\beta}\left[H_\gamma\left(\vec{\mathbf{r}} + \hat{\beta}\frac{\Delta_\beta}{2}, t\right) - H_\gamma\left(\vec{\mathbf{r}} - \hat{\beta}\frac{\Delta_\beta}{2}, t\right)\right], \\ &- \frac{\Delta_t}{\epsilon(\vec{\mathbf{r}})\Delta_\gamma}\left[H_\beta\left(\vec{\mathbf{r}} + \hat{\gamma}\frac{\Delta_\gamma}{2}, t\right) - H_\beta\left(\vec{\mathbf{r}} - \hat{\gamma}\frac{\Delta_\gamma}{2}, t\right)\right]\end{aligned} \tag{2.10}$$

$$\begin{aligned}H_\alpha\left(\vec{\mathbf{r}}, t + \frac{\Delta_t}{2}\right) &= H_\alpha\left(\vec{\mathbf{r}}, t - \frac{\Delta_t}{2}\right) \\ &- \frac{\Delta_t}{\mu(\vec{\mathbf{r}})\Delta_\beta}\left[E_\gamma\left(\vec{\mathbf{r}} + \hat{\beta}\frac{\Delta_\beta}{2}, t\right) - E_\gamma\left(\vec{\mathbf{r}} - \hat{\beta}\frac{\Delta_\beta}{2}, t\right)\right]. \\ &+ \frac{\Delta_t}{\mu(\vec{\mathbf{r}})\Delta_\gamma}\left[E_\beta\left(\vec{\mathbf{r}} + \hat{\gamma}\frac{\Delta_\gamma}{2}, t\right) - E_\beta\left(\vec{\mathbf{r}} - \hat{\gamma}\frac{\Delta_\gamma}{2}, t\right)\right]\end{aligned} \tag{2.11}$$

The update equations obtained show that each new E component is calculated from its previous value and a set of H components that circulate around the E component. The

same can be said of each H component. A picture of this situation is shown in Fig. 2.1a. If the grid contains the required neighboring components for every E and H field stored, a periodic array of E and H vectors is formed. One choice of unit-cell for this periodic array is shown in Fig. 2.1c. This structure is often called a Yee grid after K.S. Yee [37]. The unit-cell chosen is not unique, but it should be noted that the choice of placing the E components on the edges of the cell makes it possible to enforce a PEC boundary on the faces of the Yee cell rather than in the middle, which can be more intuitive when meshing.

Using the unit cell chosen in Fig. 2.1c, the samples required can be placed into arrays for evaluation on a computer. Choosing the samples so that each (i, j, k) refers to a particular Yee cell and each time step, n, refers to a successive iteration of the update equations, the samples of the array refer to the locations and times described in Table 1. Below, the arrays use the notation $E_\alpha|^n_{(i,j,k)}$ where (i, j, k) is considered to be a vector with integer coordinates, so that for example

$$E_\alpha|^n_{(i,j,k)-\hat{\mathbf{x}}} = E_\alpha|^n_{(i-1,j,k)}\,. \tag{2.12}$$

In the stated notation, the E_α samples are placed so that

$$E_\alpha|^n_{(i,j,k)} = E_\alpha(\hat{\alpha}\Delta_\alpha/2 + i\Delta_x\hat{\mathbf{x}} + j\Delta_y\hat{\mathbf{y}} + k\Delta_z\hat{\mathbf{z}}, n\Delta_t - \Delta_t/2). \tag{2.13}$$

while the H_α samples are placed so that

$$H_\alpha|^n_{(i,j,k)} = H_\alpha(i\Delta_x\hat{\mathbf{x}} + j\Delta_y\hat{\mathbf{y}} + k\Delta_z\hat{\mathbf{z}} + \hat{\beta}\Delta_\beta/2 + \hat{\gamma}\Delta_\gamma/2, (n-1)\Delta_t) \tag{2.14}$$

The final update equations as implemented in a computer program may now be obtained. Substituting $\hat{\mathbf{r}} = \hat{\alpha}\Delta_\alpha/2 + i\Delta_x\hat{\mathbf{x}} + j\Delta_y\hat{\mathbf{y}} + k\Delta_z\hat{\mathbf{z}}$ and $t = n\Delta_t - \Delta_t/2$ into (2.10), one obtains

$$\begin{aligned} E_\alpha|^n_{(i,j,k)} = {} & E_\alpha|^{n-1}_{(i,j,k)} - \frac{\Delta_t}{\epsilon(\vec{\mathbf{r}})} J_\alpha(\vec{\mathbf{r}}, n\Delta_t) \\ & + \frac{\Delta_t}{\epsilon(\vec{\mathbf{r}})\Delta_\beta}\left[H_\gamma|^n_{(i,j,k)} - H_\gamma|^n_{(i,j,k)-\hat{\beta}}\right]. \\ & - \frac{\Delta_t}{\epsilon(\vec{\mathbf{r}})\Delta_\gamma}\left[H_\beta|^n_{(i,j,k)} - H_\beta|^n_{(i,j,k)-\hat{\gamma}}\right] \end{aligned} \tag{2.15}$$

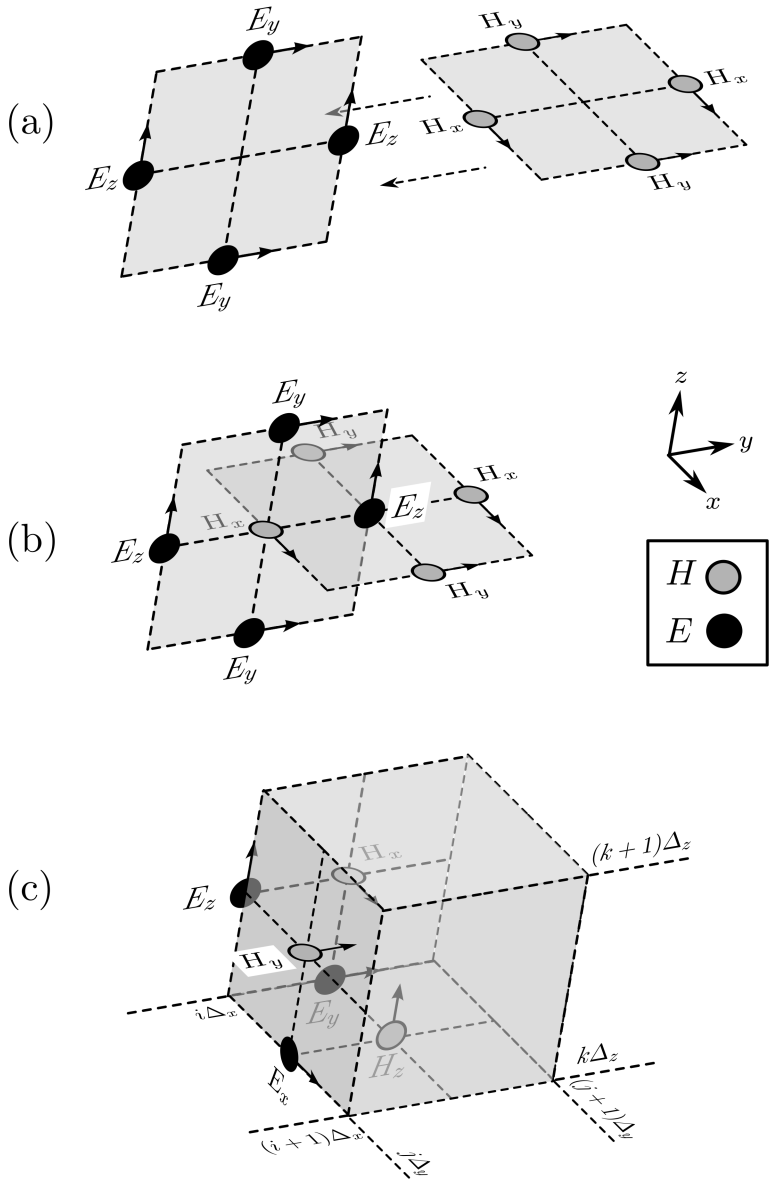

Figure 2.1: Formation of the Yee cell. In (a), the components that would neighbor an H_x component are shown next to the components that would neighbor an E_z component. In (b), the components are shown interlocking so that both components have all of their neighbors. If every component has the set of circulating neighbors required, a periodic array with the unit cell shown in (c) is created. This is an example of a Yee unit cell.

Table 1: Positioning of the field components in the (i, j, k) Yee cell.

	x	y	z	t
$E_x\|^n_{(i,j,k)}$	$(i+\frac{1}{2})\Delta_x$	$j\Delta_y$	$k\Delta_z$	$n\Delta_t$
$E_y\|^n_{(i,j,k)}$	$i\Delta_x$	$(j+\frac{1}{2})\Delta_y$	$k\Delta_z$	$n\Delta_t$
$E_z\|^n_{(i,j,k)}$	$i\Delta_x$	$j\Delta_y$	$(k+\frac{1}{2})\Delta_z$	$n\Delta_t$
$H_x\|^n_{(i,j,k)}$	$i\Delta_x$	$(j+\frac{1}{2})\Delta_y$	$(k+\frac{1}{2})\Delta_z$	$(n-\frac{1}{2})\Delta_t$
$H_y\|^n_{(i,j,k)}$	$(i+\frac{1}{2})\Delta_x$	$j\Delta_y$	$(k+\frac{1}{2})\Delta_z$	$(n-\frac{1}{2})\Delta_t$
$H_x\|^n_{(i,j,k)}$	$(i+\frac{1}{2})\Delta_x$	$(j+\frac{1}{2})\Delta_y$	$k\Delta_z$	$(n-\frac{1}{2})\Delta_t$

Substituting $\hat{\mathbf{r}} = i\Delta_x\hat{\mathbf{x}} + j\Delta_y\hat{\mathbf{y}} + k\Delta_z\hat{\mathbf{z}} + \hat{\beta}\Delta_\beta/2 + \hat{\gamma}\Delta_\gamma/2$ and $t = (n-1)\Delta_t$ into (2.11), one obtains

$$\begin{aligned} H_\alpha|^n_{(i,j,k)} = {} & H_\alpha|^{n-1}_{(i,j,k)} \\ & - \frac{\Delta_t}{\mu(\vec{\mathbf{r}})\Delta_\beta}\left[E_\gamma|^{n-1}_{(i,j,k)+\hat{\beta}} - E_\gamma|^{n-1}_{(i,j,k)}\right]. \\ & + \frac{\Delta_t}{\mu(\vec{\mathbf{r}})\Delta_\gamma}\left[E_\beta|^{n-1}_{(i,j,k)+\hat{\gamma}} - E_\beta|^{n-1}_{(i,j,k)}\right] \end{aligned} \tag{2.16}$$

The arrays E_α and H_α are initialized to zero at some times $t = -\Delta_t/2$ and $t = 0$ respectively. E_α is then updated from the current E_α arrays and the H_α arrays using (2.15) to the time $t = \Delta_t/2$. Note that the source term, J_α, is assumed to be a known function of space and time, so this computation can be performed with just that information. After completion, the H_α arrays are updated to time $t = \Delta_t$ using (2.16). In this fashion, both sets of arrays can be updated forward in time indefinitely. Because the updates only depend on the most recent time, they can be performed in-place. This method of updating is called a leap-frogging scheme because the point in time represented by the E and H arrays jump $\Delta_t/2$ past one another as the updating process continues.

It can be shown that the E and H fields obtained from this procedure naturally satisfy the divergence equations (2.4) and (2.3) [36]. One issue that has been avoided in this description is that of numerical stability. The equations as derived will, for small cell sizes, approximately solve Maxwell's equations, but there must also be a relationship held between the time step Δ_t and the spatial steps, Δ_α. This relationship is called the Courant condition

and is

$$\Delta_t \leq \frac{1}{c\sqrt{\frac{1}{(\Delta_x)^2} + \frac{1}{(\Delta_y)^2} + \frac{1}{(\Delta_z)^2}}}, \tag{2.17}$$

where c is the speed of light in the region [36]. If Δ_t is chosen larger than the Courant condition, the solution will grow without bound with each update and will not converge to a solution to the equations for small cell sizes. Since one generally wants a solution over the largest span of time possible using the fewest number of updates, Δ_t is generally chosen very close to the upper bound.

When FDTD is implemented on a computer, the E and H arrays are truncated to some box and zero field values are assumed at the edge. This effectively means that the FDTD method simulates sources placed in a metal box. For an antenna problem it is generally preferable that the FDTD simulation have the appearance of operating in free-space. Solutions to this problem are discussed in Section 2.3. First the use of a varying cell size is discussed.

2.2 The Use of a Varying Cell Size

It was noted in the previous section that the FDTD method with a cell size Δ enforces Maxwell's equations at each point in the grid within an error on the order of Δ^2. Using this as a rule of thumb, in some general sense at least, whatever error is present in a given FDTD simulation will also decrease as the square of the cell size. This is generally the case, but one sometimes encounters situations where the error in a simulation is occurring primarily because the cell-size is too large to accurately represent the geometry being modeled. In these situations, the error may decrease with cell size at a slower rate. An example of this type of error occurs when a spiral antenna is modeled with an extremely fine arm width near the center of the feed. The PEC boundary condition that must be applied on the arms is enforced by zeroing out the E-field components that lie on the arms after each update. The effect of this method of enforcing the condition is that the apparent object being modeled is composed of square cells. An example of a stair-stepped mesh is shown in Fig. 2.2.

In this situation, the spiral arms may become so thin near the feed that they fail to be continuously connected. This can introduce large errors into the fields near the feed of

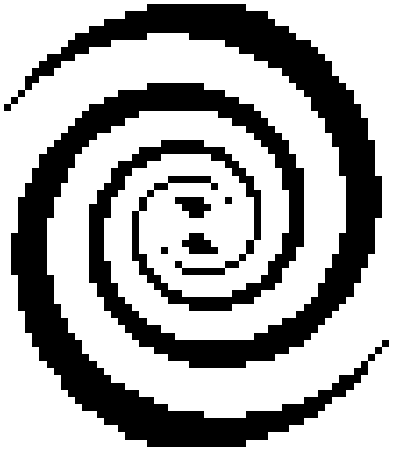

Figure 2.2: Mesh of a spiral antenna with $R_{\text{out}} = 25$ cm and $R_{\text{in}} = 8$ mm. Severe stair-stepping errors can be seen near the spiral's feed. The cell size choice of $\Delta = 2$ mm would need to be reduced to properly model that the arms are continuous wires.

the antenna, causing the measured impedance to be incorrect. If the arms are connected, the zig-zag effect may cause the apparent length of the arms to be longer than the curved version. In order to model this spiral with a very thin inner arm in a traditional FDTD code, one must model the entire grid with a uniformly smaller cell size. This can be very costly computationally, so a number of techniques for giving a more accurate representation of the geometry near small features have been proposed. Among them are conformal subcell techniques where the exact geometry of the small feature is handled with a special update as in [38] or [39].

By far the simplest technique for dealing with structures with vastly different feature sizes like the spiral is the ballooned mesh technique, which has been described in [40]. Here the cell size is made smaller near regions with fine geometrical features and is increased in size away from the fine features. If this is done by gradually changing the cell size from field component to field component, the errors introduced can be controlled. An example of a ballooned mesh for the spiral antenna is shown in Fig. 3(a). The fields simulated in the ballooned grid are transformed in the same way that the mesh is, so an inverse transform is necessary to view the physical solution. Since regions without fine geometrical features

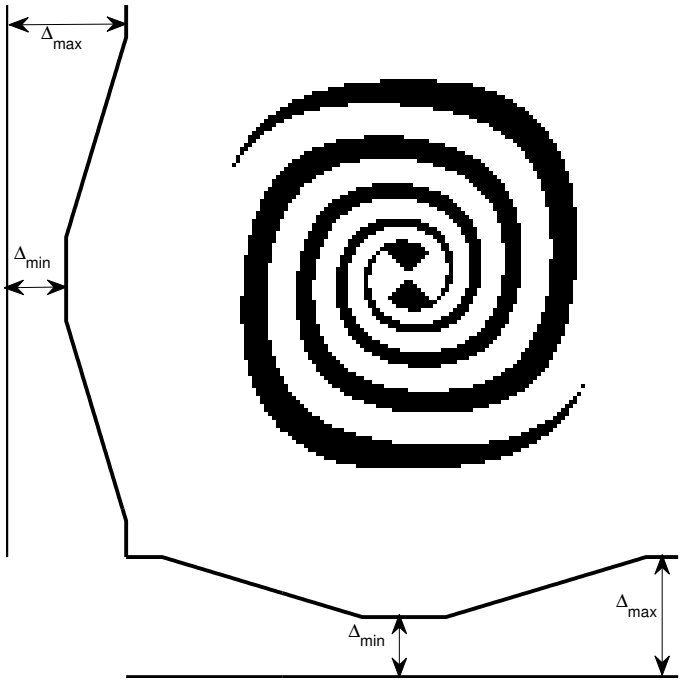

(a) Ballooned spiral mesh.

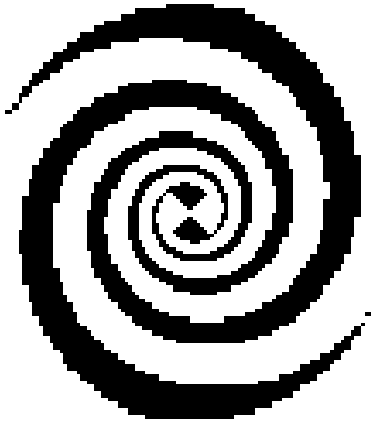

(b) Ballooned mesh through a coordinate transform.

Figure 2.3: (a) Bars show the cell size used as a function of position. The mesh shown is ballooned to give a smaller cell size near the feed. This is the actual simulated mesh. (b) shows the equivalent mesh to (a) through the coordinate transform. Here, Δ ranges from 1 mm to 2 mm. It can be seen that the smaller cell size near the center allows the continuity of the arms to be resolved.

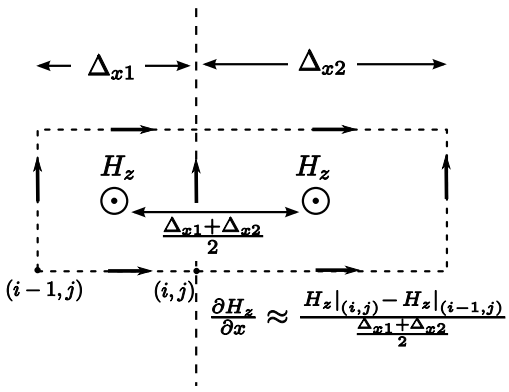

Figure 2.4: The interface between a region with cell size Δ_{x1} and Δ_{x2} is shown. To calculate a derivative for the field-update exactly at the interface, the average cell size is used. It can be seen here that this is an appropriate length, but because the field is not located half-way between the two H_z components, Δ^2 accuracy is not ensured.

can be modeled with a larger cell size, the simulation space can be kept much smaller. Unfortunately, to preserve the stability of the method, the time step must be set with respect to the smallest spatial step in the grid. This is also true of other subcell methods, excepting recent work by Liu [39].

The implementation of a variable cell size is almost identical to the original FDTD method. The update equations (2.10) and (2.11) are exactly the same except the cell size used for Δ_i is now a function of the position, with Δ_x a function of x, Δ_y, a function of y, and Δ_z a function of z. When a derivative is required at the interface between two cell sizes as in Fig. 2.4, the average cell size may be used. Because the second-order accuracy of the finite difference taken at the interface depends on the derivative being located half of the way between the two H_z components in Fig. 2.4, an error will be introduced as a reflected wave. Because this error depends on the difference between the two cell sizes, smoothly varying the cell size will ensure these reflections are small.

2.3 The Perfectly Matched Layer

The problem of determining the properties of an antenna operating in an infinite space using an antenna operating in a finite amount of space is not unique to FDTD. The solutions proposed for the FDTD method fall into three general categories. First, the error introduced by the truncation of the grid may be time-gated out of any simulated field of interest

provided the grid is large enough. Second, the field at the edge of the grid may be estimated from the fields inside of the grid and fields at the boundary can be updated as if they neighbor the estimated fields. These techniques are called absorbing boundary conditions or radiation boundary conditions and are discussed in [36]. Finally, the edges of the simulation space may be lined with an absorbing material much like an anechoic chamber. Since one is not restricted to physically realizable materials in a simulation, the last technique has been much more effective than its physical counterpart. Well-tuned numerical absorbers often show reflection coefficients 70dB-120dB below the incident field. These numerical absorbers are often called "Perfectly Matched Layers" (PML).

In this work, only the PML method has been employed. The complex frequency shifted PML, described by [41] was implemented using the recursive convolution technique described in [42]. This PML has better performance near metal interfaces than a standard PML, which allows the spiral antenna to be placed very close to the edge of the simulation space. A complete description of the CPML is available in [36].

2.4 Feeding the Antenna in an FDTD Simulation

In the previous sections, the method of updating the fields in a region of space has been discussed with very little details on where the energy comes from. In many antenna problems, a full 3-D model of the transmission line that feeds the antenna is not possible. Instead, the feed of the antenna is approximated. This approximate feed may be a circuit element like a current or voltage source, or a transmission line with a circuit element attached to it.

When energy is fed into the grid using the current source term present in (2.10), the effect is that of a current source circuit element being placed between the ends of the region of current. This is because the presence of the current is completely independent of any voltage across the extent of the source, showing that the impedance of the source is infinite.

Alternately, if a set of E components are set to a specific value after each E update, a fixed voltage is inserted into the grid. Because the voltage introduced is independent of the current flowing out of the source, the apparent impedance of the source is zero. A picture of the circuit equivalents of these two types of sources are shown in Fig. 5(a) and 5(b).

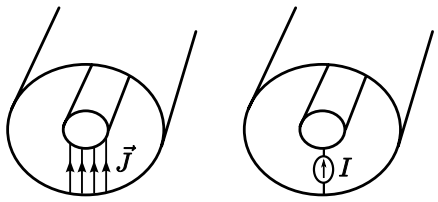

(a) Ideal current source.

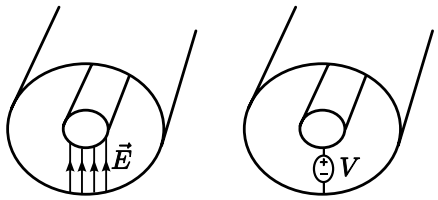

(b) Ideal voltage source.

Figure 2.5: (a) shows an ideal current source implemented as a non-zero current density term between the conductors of a transmission line structure in the 3-D grid. (b) shows the equivalent ideal voltage source, implemented as enforced E-field values.

While these two extremes of impedance may be suitable for feeding an antenna that has no well-defined impedance to match to, for an antenna like the spiral that has a clearly defined resistance over a broad band of frequencies, feeding the antenna using these sources leads to a considerable amount of unnecessary ringing due to mismatch. Feeding the spiral with a source that has a short or open impedance will cause currents to run along the arms of the antenna, reflect at the ends, and then reflect back onto the arms at the feed. All energy on the spiral arms must be lost to radiation before the end of the simulation. This leads to unnecessarily long computations to obtain quantities like the gain or impedance as a function of frequency.

While to fix this problem, one need only implement some source with a fixed finite impedance such as that described in [43], in this work a slightly more complex transmission line model described in [36] is implemented. This allows the reflection from the antennas to be taken directly without any signal processing. The idea of the transmission line model is to run a one-dimensional FDTD simulation of the transmission line equations in parallel with the FDTD code. At one end of the line a one-way injector creates an incident voltage wave. At the opposite end of the line, the voltage is inserted into the grid and the current measured in the grid is inserted back into the 1-D simulation. The reflected voltage, v_{refl},

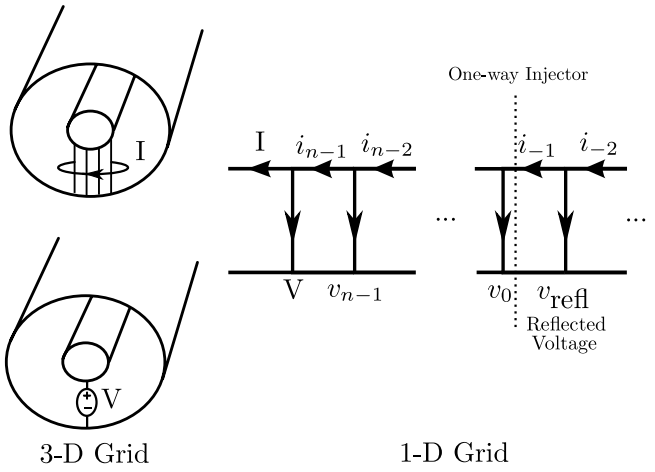

Figure 2.6: A 1-D field simulation is used to model a transmission line. The 1-D grid is connected to the 3-D grid through the current and voltage at the end of the lines. A one-way injector divides the voltages in the line into a total and scattered field region, allowing the reflected voltage to be read from the area behind the injector.

can be read off the voltage in the line behind the one-way injector. A picture of this situation is shown in Fig. 2.6.

When a spiral is modeled with this feed, the impedance of the line in the simulation is set to that of the transmission line used in measurements. This gives the finite source impedance necessary to reduce the ringing time for the spiral, and the direct simulation of the incident and reflected voltages simplifies the signal processing involved in calculating the reflection coefficient for the antenna.

2.5 Modeling the Spiral Element

The initial match to measured data and work on the nature of the operating band was all done using uniform cell simulations. After the publication of the paper on this subject, graded cell sizes were introduced to increase the accuracy of the simulation. The work on the lower-frequency cutoff of the spiral in Chapter 3 was the first work in this thesis done using a graded cell size, and the remainder of the thesis is done using a graded mesh.

The transmission line model described in the previous section was used to feed all spiral antennas in the numerical work. The CPML was used in all simulations to truncate the grid. In addition to the numerical methods described in this chapter, a time-domain near-field to far-field transformer (NFFT) was implemented for calculating the far-field radiation

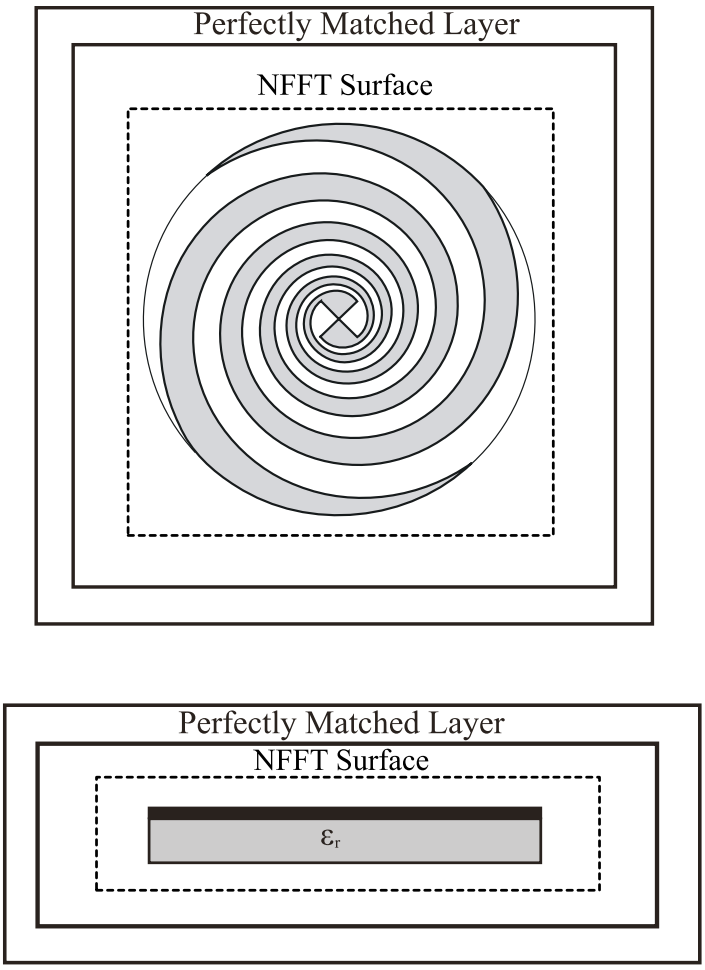

Figure 2.7: Numerical geometry for FDTD simulations of the spiral antenna.

of antennas simulated in the FDTD grid. The details of this implementation are found in [36]. A diagram of the simulation space used for the spiral antennas in the initial phase of this work is shown in Fig. 2.7.

2.6 Initial Verification of the Numerical Model

Before beginning a study of the operating-band performance of the spiral, the FDTD model was verified. Additional verification of the FDTD model is provided in Chapter 4 relating to the additional components of the spiral GPR system, but here only the spiral element is modeled. Two spirals were fabricated for verification. Using parameters defined in Fig. 1.2, the geometry of the spirals was $\psi = 79°$, $R_{in} = 3$ mm and $R_{out} = 0.114$ m. The first was made on Arlon Foamclad R/F 100 with a thickness of approximately 1 mm. Foamclad

is a composite dielectric with a thin layer of polyester film, $\epsilon_r = 3.2$, on top of a foam layer ($\epsilon_r \approx 1$). For the second, Rogers RO3006 substrate was used with a thickness of 1.27 mm and $\epsilon_r = 6.15 \pm 0.15$. The spirals constructed are shown in Fig. 8(a) and 8(b).

The stated parameters were inserted into the FDTD model described in Section 2.5 for the verification. A uniform cell size of 0.2 mm was used and the space was tightly enclosed around the antenna. The numerical grid was on the order of $1200 \times 1200 \times z$ cells where z varied from 24 to 50 cells depending on the thickness required by the spiral substrate. The code was executed on a cluster with 64 CPU's and generally took two to three hours to simulate a complete pulsed excitation, corresponding to 6 ns of simulation time. An example of the spiral mesh used in this work is shown in Fig. 2.9.

The impedance and gain measurements of the spirals were obtained using an HP8720D network analyzer. The outer conductors of two lengths of 085 semi-rigid coax were electrically bound together with conducting tape to form a balanced transmission line. The line was attached at one end to a Picosecond Pulse Labs 5315 balun. At the opposite end, the outer conductor was removed and the inner conductors of the coax were stripped of their dielectric casing.

Since a set of balanced transmission line calibration standards were not available, removable calibration standards were constructed to perform the match-open-short calibration procedure described in [44]. The calibration standards consisted of a small connector piece built from two SMB connector contacts and a disk of polycarbonate. A match (100 Ω chip resistor), open, and short (copper disk) as well as the spiral antenna were soldered to the connector pieces. These calibration standards are shown in Fig. 2.10.

The two spirals were simulated in the finite-difference model. The Rogers substrate was modeled as a uniform dielectric with $\epsilon_r = 6.15$. The Foamclad substrate was modeled as a 0.1 mm layer of polyester and the foam layer was approximated with air. Comparisons between the measured and simulated impedances for the Foamclad and Rogers spirals are shown in Fig. 2.11 and Fig. 2.12. The experimental and simulated data show good agreement. The curves show a region of relatively flat behavior, but resonant peaks occur below a certain frequency. The imaginary impedance on both curves settles to a value of

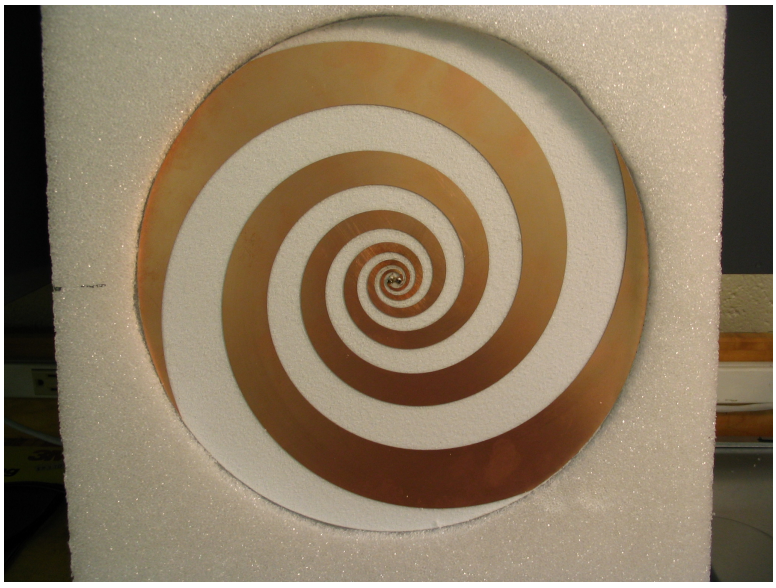

(a) Foamclad substrate spiral.

(b) Rogers substrate spiral.

Figure 2.8: Constructed spiral antennas used for verifying the numerical model.

Figure 2.9: Numerical mesh used for verification of the FDTD model. This mesh has a uniform cell size of 0.2 mm and is $1184 \times 1184 \times 25$ cells. Obtaining a suitable impulse response from the antenna required 6 ns of simulation time for the excitation used and required 2 hours of computer time on the 64 node cluster available at the time.

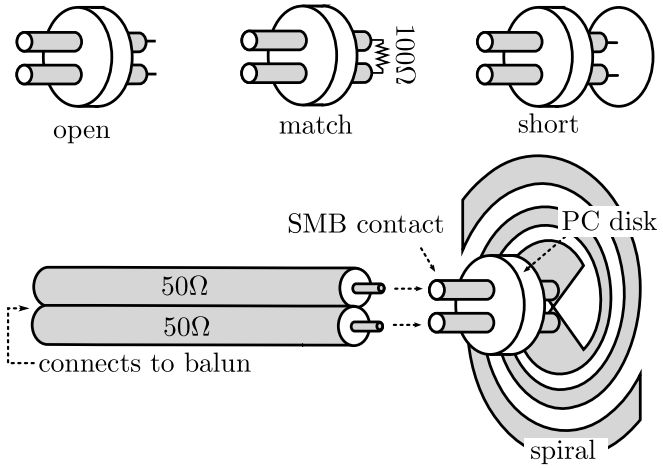

Figure 2.10: Calibration standards used in impedance measurements.

zero above 1 GHz. The real impedance of the substrate-free spiral is near the expected 188Ω, while the spiral on Rogers substrate shows a much lower impedance near 100Ω. The cause of the resonant peaks and the relationship between the substrate and the impedance will be discussed in Chapter 3.

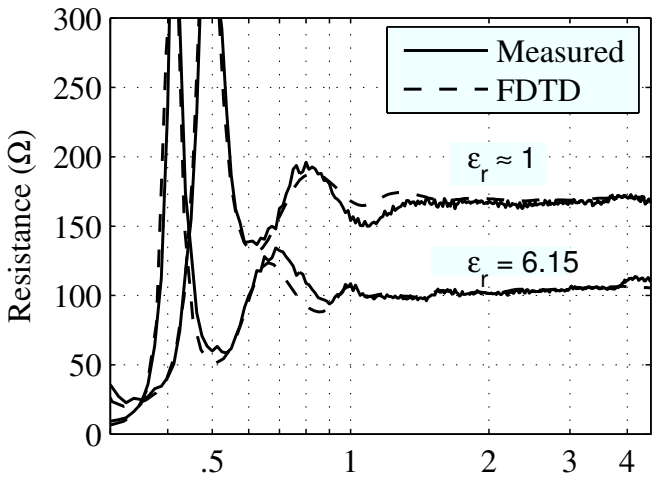

Figure 2.11: Comparison of measured and FDTD resistance for the Foamclad and Rogers substrate with design parameters $\psi = 79°$, $R_{in} = 3$ mm and $R_{out} = 0.114$ m.

Bore-sight gain measurements were also taken for the two spirals. These were performed using the two-antenna method [45]. In order to perform these measurements, the antenna was placed on a table made of low dielectric constant foam 1 m from any scatterers. The gain measurements were time-gated to remove reflections from objects in the test area. The measured and simulated curves for the bore-sight gain of the two spirals are shown in Fig. 2.14 and Fig. 2.15. A picture of the gain measurement setup for the two-antenna method is shown in Fig. 2.13.

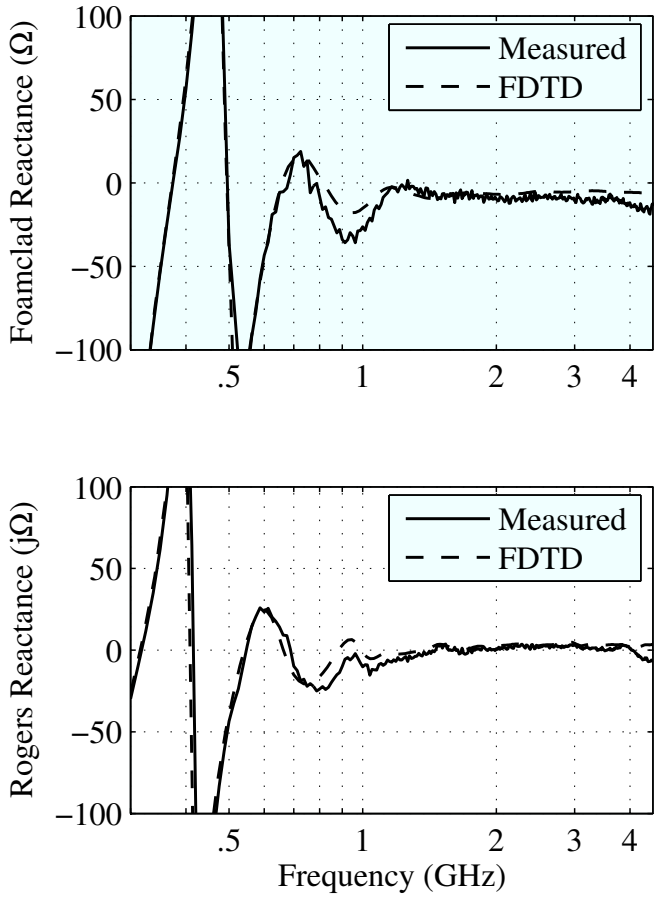

Figure 2.12: Comparison of measured and FDTD reactance for the Foamclad and Rogers substrate with design parameters $\psi = 79°$, $R_{in} = 3$ mm and $R_{out} = 0.114$ m.

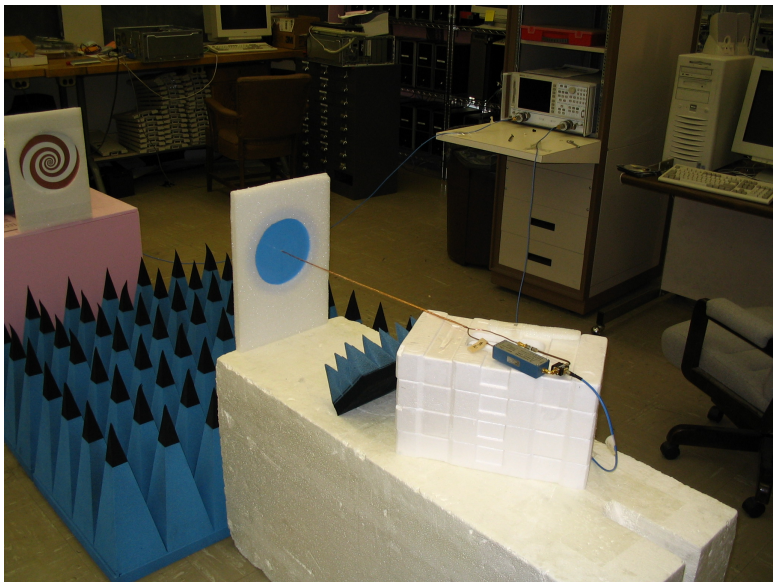

Figure 2.13: In the two-antenna measurement for gain, two identical antennas are placed face-to-face in the far-field and the S_{21} parameter is measured. Prior to obtaining S_{21}, the scattering from objects in the room was time-gated out. The gain can be calculated from the magnitude of this parameter if the distance between the two antennas is known.

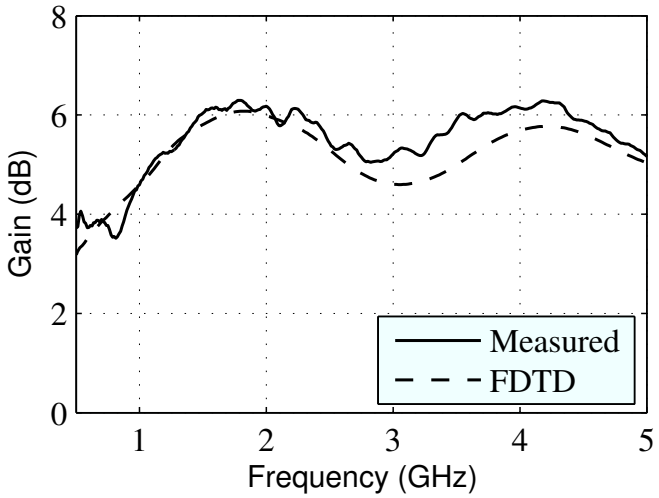

Figure 2.14: Comparison of measured and FDTD gain results for the Foamclad substrate with design parameters $\psi = 79°$, $R_{in} = 3$ mm and $R_{out} = 0.114$ m.

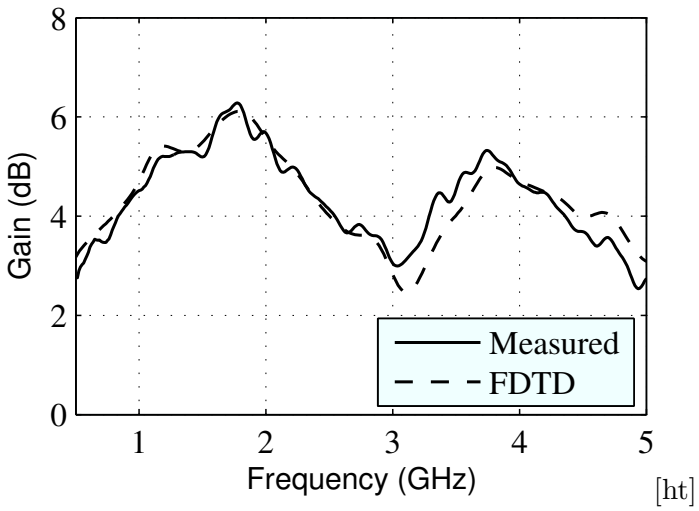

[ht]

Figure 2.15: Comparison of measured and FDTD gain results for the Rogers substrate with design parameters $\psi = 79°$, $R_{in} = 3$ mm and $R_{out} = 0.114$ m.

CHAPTER III

ANALYSIS OF THE SPIRAL ELEMENT

With the numerical model of the element verified for dielectric substrates throughout the range of interest for a design study, an analysis of the behavior of the spiral is undertaken using the numerical model. In the first subsection, the performance of the antenna in the operating band is studied, including the impedance, bore-sight gain and pattern. A design graph is constructed for relating the relevant parameters of the spiral element to the characteristic impedance of the antenna. It is shown that the gain of the spiral antenna would have a theoretical value that is independent of frequency but that the introduction of the substrate adds a frequency dependence to the expression. In addition, a ripple in the gain as a function of frequency is shown and a simple model that might cause this feature of the gain is proposed. Finally, the pattern of the antenna is shown to vary significantly as a result of this gain ripple with frequency. A designer could use the design graph in this section to estimate the best substrate for a required characteristic impedance, but as evidenced by the remainder of the subsection, high dielectric substrates can lead to a drastic frequency-dependent gain deterioration.

In the second subsection, the lower-frequency cutoff of the operating band is studied. It is shown that the lower-frequency cutoff is not significantly affected by the use of a high dielectric substrate for reasonable substrate geometries and spirals with a wrapping tightness of $\psi \leq 82°$. Next, design graphs that relate the lower-frequency cutoff to the significant geometry features are constructed in terms of a number of metrics. A designer could use the design graphs in this chapter to make initial estimates on a suitable spiral geometry based on criterion of frequency bandwidth and gain, axial ratio, or VSWR constraints.

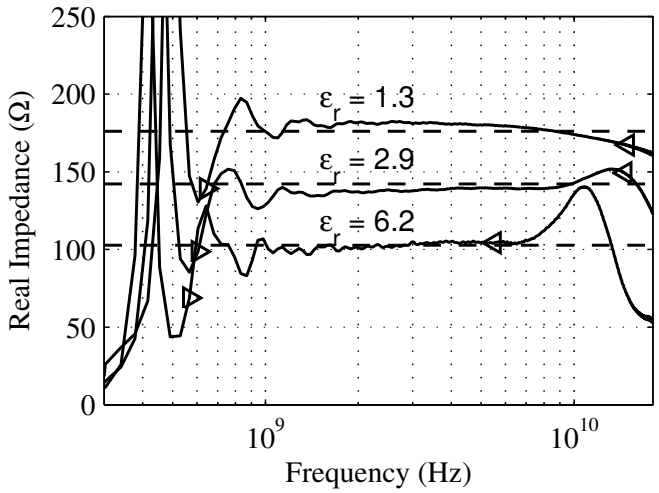

Figure 3.1: Real impedance curves for spirals designed to be (top to bottom): $188\Omega, 148\Omega$, and 108Ω. The triangular markers denote the edges of the operating band. The dashed lines show the calculated characteristic impedance, defined here to be the average in the operating band.

3.1 Operating Band Performance

3.1.1 Impedance Curves

Spiral antenna impedance curves tend to show three distinct regions of behavior. The lower frequencies are dominated by the outer truncation, the upper frequency behavior relates to the inner truncation, and the behavior in the intermediate frequencies is determined by the shape of the spiral curve itself. Portions of the traveling wave model proposed by J. Kaiser for the Archimedean spiral are used to explain the form of the curves in a manner similar to [18].

Using the auxiliary one-dimensional transmission line and the FDTD model described in Chapter 2, impedance curves as a function of frequency were calculated for the spiral on the substrates of interest. The real parts of some of these curves are shown in Fig. 3.1. The imaginary portions are very similar but have an average value of zero regardless of the dielectric.

The spirals used in Fig. 3.1 had the geometrical parameters $\psi = 79°$, $R_{in} = 3$ mm, and $R_{out} = 0.114$ m. Each parameter is defined in Fig. 1.2. Each spiral shown had a 1.27 mm thick substrate with dielectric constants $\epsilon_r = 1.3, 2.9$, and 6.2 from top to bottom. These values were chosen to progressively decrease the impedance by about 40 Ω. The

spiral impedance curves show three important features that are present in all impedance curves seen in this study: The lower-frequency region of the impedance is dominated by a series of resonant peaks, the middle frequencies are approximately constant, and the upper frequencies contain either a resonant peak or a region where the real impedance decreases with frequency.

The low-frequency peaks arise from the portion of the energy inserted onto the spiral arms that travels to the end of the spiral and reflects back to the feed without radiating. On an infinitely large spiral, a traveling wave at any particular frequency propagates along the spiral arms until it reaches a circular active region with a circumference equal to one wavelength. At this point, the majority of the energy in the wave is converted to radiation. However, when the spiral is truncated at a given outer radius, all frequencies low enough to have active regions outside the chosen truncation point will reach the edge of the spiral and reflect back to the feed. The reflection causes ripples that take the form of a series of peaks because the current at the feed point consists of the initial feed current, I, summed with a delayed reflected current, $\Gamma I e^{-j\omega t_d}$, where ω is the particular angular frequency of interest, Γ is a reflection coefficient, and t_d is the delay time necessary for the wave to propagate to the end of the spiral arms and back. This sum has a variation that is roughly periodic as a function of frequency. The amplitude of the ripple decreases rapidly as frequency increases and more of the active region for a particular frequency fits onto the antenna. All spirals shown in Fig. 3.1 will have an outer circumference of one free-space wavelength at 419 MHz. The frequency at which this occurs is typically taken to be the low-frequency cutoff of the spiral.

In the region between the erratic behavior at the upper and lower frequencies, a band of nearly constant impedance is seen. Because this is the expected behavior of a frequency-independent antenna, this region is referred to as the "operating band". Since the spiral arm structure is self-complementary, a spiral lodged in a homogeneous dielectric has an operating-band impedance of

$$Z = \frac{\eta}{2} = \frac{1}{2}\sqrt{\frac{\mu}{\epsilon}} = \frac{1}{2}\sqrt{\frac{\mu_0}{\epsilon_r \epsilon_0}}, \tag{3.1}$$

by Booker's relation [19]. In free-space this impedance is approximately 188Ω.

In the non-homogeneous case, (3.1) may still be used, but the ϵ_r value must be replaced with an equivalent dielectric constant, typically denoted ϵ_{EFF}, which may be thought of as an average of the dielectric constants in the region weighted in some way by the magnitude of the electric field in a given region of space. The value ϵ_{EFF} is the equivalent homogeneous dielectric constant that would be required to match the phase velocity of the traveling wave on the dielectric backed spiral arms. A wave traveling down the spiral arms will have a different effective permittivity value because the arms become wider with respect to the substrate thickness. In the operating band, the effective permittivity near the inner truncation appears to determine the impedance of the spiral. When the inner truncation is sufficiently small compared to the substrate thickness, the impedance can be approximated by evaluating Booker's relation in a half-space of dielectric. This approximation and others appear in [18, 46, 47].

$$\epsilon_{\text{EFF}} = \frac{\epsilon_r + 1}{2} \tag{3.2}$$

$$Z = \frac{\eta_0}{2\sqrt{\epsilon_{\text{EFF}}}}. \tag{3.3}$$

In Fig. 3.1 the dashed lines are a computed average value for the operating-band impedance and these show a fair agreement with (3.2) and (3.3). It may be noted that while the effective permittivity near the feed does predict the operating-band impedance with some accuracy, it does not predict the minimum operating frequency very well.

The impedance in the operating band ends with a resonant peak for the thicker, higher dielectric constant substrates, and a downward trend in the impedance otherwise. This upper frequency behavior is caused by the the reflection at the discontinuity between the spiral arms and the bow-tie structure. The peak may be made more severe by increasing the wrapping angle, ψ.

3.1.2 Impedance Design Graphs

The impedance of the feed line to the spiral should be matched to the nearly constant value in the operating band seen in Fig. 3.1. This value is referred to as the characteristic impedance of the spiral, Z_c. To obtain this value for a particular spiral's impedance plot,

$Z(f)$, the interval over which the impedance remained approximately constant was required. This was defined to be the largest interval, $[f_{min}, f_{max}]$, over which the standard deviation of the impedance in the interval was less than a fixed value. Z_c was then defined as the average value of $Z(f)$ on this interval. The intervals chosen for the curves in Fig. 3.1 are denoted by the marker arrows and the average values taken are the dashed lines. In this figure and all subsequent figures that make use of the calculation, the maximum standard deviation was set to 7 Ω.

In the description of the spiral in which the conductor thickness is assumed to be zero, five parameters define the spiral. R_{in}, R_{out}, and ψ are defined in Fig. 1.2. ϵ_r is the dielectric constant of the substrate, and h is the thickness of the dielectric substrate. The intention of the design graphs is to relate the characteristic impedance, Z_c, to these parameters. The graphs should show the function $Z_c(R_{in}, h, R_{out}, \psi, \epsilon_r)$ over some restriction of its domain. In the course of this work, it was noted that, when the averaging process is taken into account, the impedance can be reduced to a function of only two related variables: h/R_{in} and ϵ_r.

Since the average value taken to be the characteristic impedance begins at a frequency high enough to essentially ignore the reflection from the outer truncation, the parameter R_{out} may be neglected as long as the value is large enough to obtain a well-defined operating band. In this study, this was seen to occur when $R_{out} > 20R_{in}$. In addition, it was observed that the function Z_c remained approximately constant as the thickness or inner truncation were varied as long as the ratio h/R_{in} remained constant. This can be related to the scaling principle. It was also found through simulations that the parameter ψ has a very minimal effect on the characteristic impedance of the antenna. Instead, ψ changes the impedance plot near the edges of the operating band, leaving the average value the same. This may be seen in Fig. 3.2 where a spiral's characteristic impedance is evaluated with parameters $R_{out} = 0.114$ m, $R_{in} = 3$ mm, $h = 1.27$ mm, and various ϵ_r over a range of ψ.

This allows one to define the function $Z_c(h/R_{in}, \epsilon_r)$ and plot the effect of the substrate on a single graph. The impedance of the spiral was evaluated numerically over the range $0.1 < h/R_{in} < 1$ for $1 < \epsilon_r < 7$ in Fig. 3.3. Here the data was taken from a spiral with a

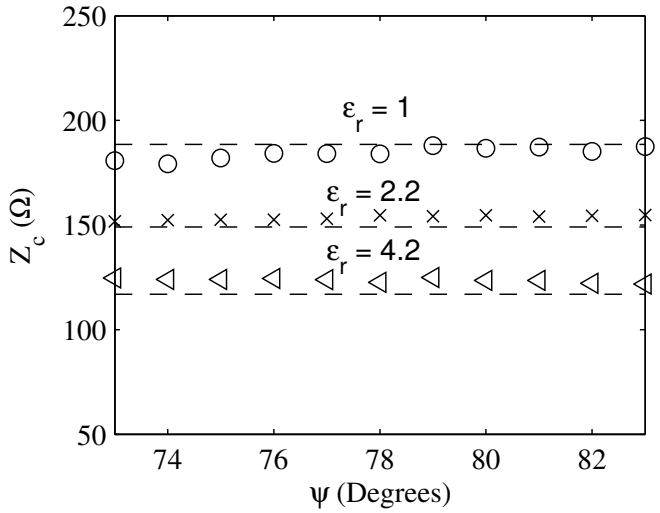

Figure 3.2: Z_c as a function of ψ, $R_{out} = 0.1143$ m, $R_{in} = 3$ mm, $h = 1.27$ mm. Dashed values show the impedance estimate in (3.2) and (3.3).

geometry of $\psi = 79°, R_{out} = 0.12$ m, $R_{in} = 3$ mm for various h and ϵ_r.

As seen in Fig. 3.3, the impedance tends towards the half-space value in (3.2) and (3.3) as $h/R_{in} \to \infty$ and towards the free-space value of $\eta_0/2$ as $h/R_{in} \to 0$. In the interior region, it is seen that for a moderately thick dielectric ($h/R_{in} > 0.4$ for instance), the impedance is a strong function of the dielectric constant and a very weak function of the parameter h/R_{in}. Only for a thin dielectric does h/R_{in} show a strong effect on the impedance value.

3.1.3 Theoretical Bore-sight Gain on a Substrate

In this section, a simple model of the operation of the spiral is described that shows the same qualitative behavior as the gain curves. Referring to the model proposed by J. Kaiser described above, the energy on the spiral arms can be thought of as a traveling wave on a transmission line. The energy is fed from the center of the line and travels outwards in a spiral path towards an active region where it is radiated away. Since, unlike the Archimedean spiral, the equiangular spiral arms expand, the ratio of the gap width of this transmission line to the height of the substrate becomes larger as the wave travels along the arms, causing the effective dielectric constant on the line to approach that of free space. Using the expression (3.3), which appears to describe the impedance of this transmission line at the feed point, one can write the impedance of the transmission line as a function of

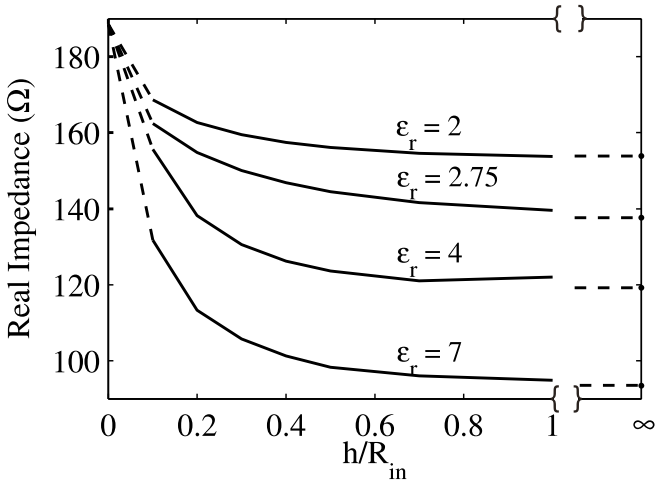

Figure 3.3: $Z_c(R_{in}/h, \epsilon_r)$ with $\psi = 79°, R_{in} = 3$ mm, $R_{out} = 0.12$ m. The solid lines are interpolated numerical values. The dashed lines trace the edge of each curve towards its value for no substrate (left) and an infinitely thick substrate (right).

s, the distance along the line as

$$Z(s) = \frac{\eta_0}{2\sqrt{\epsilon_{\text{EFF}}(s)}}, \tag{3.4}$$

where η_0 is the impedance of free space and $\epsilon_{\text{EFF}}(s)$ is the effective permittivity at the location s. While this implies the impedance is always changing along the line, this is an extremely slow variation and it can be assumed that along the ring that constitutes the active region, $Z(s)$ remains constant at some value Z_{act}. Since the transmission lines, like the spiral arms, are assumed lossless, the power in the wave remains constant. Therefore the current in this region remains constant as well.

This then implies that the radiation from the spiral will be that from a traveling ring of current with circumference λ (here λ is the wavelength of the traveling wave in the active region and is distinguished from the free-space wavelength, λ_0). The radiation from a harmonically varying current distribution of angular frequency ω is well-known and the details of the integration necessary for a traveling ring of current can be found in [48]. For a ring of circumference λ, one obtains a radiated field

$$E^r(r, \phi, \theta = 0, \omega) \quad = \quad e^{-jkr}\frac{\omega\mu_0\lambda I_{act}(\hat{x} - j\hat{y})}{8\pi r}, \tag{3.5}$$

where E^r is the radiated field in phasor form with an assumed $e^{j\omega t}$ time dependence, k is the free-space propagation constant, defined $k = \frac{2\pi}{\lambda_0}$, and I_{act} is the magnitude of the traveling ring of current in the active region. Equation (3.5) shows the expected result that the radiated wave at bore-sight is circularly polarized. If the current and impedance at the feed point are denoted I_{in} and Z_{in} respectively, and the effective permittivity in the active region ring is denoted ϵ_{act}, one may use (3.5) to write the gain G in terms of the known radiated power per unit area on bore-sight, $P_{rad}(r, \phi, 0, \omega)$, and the power inserted into the spiral, P_{in}

$$\begin{aligned} P_{rad}(r,\phi,0,\omega) &= \frac{|E^r(r,\phi,0,\omega)|^2}{2\eta_0} \\ &= \frac{(\omega\mu_0\lambda I_{act})^2}{(8\pi r)^2\eta_0} \qquad (3.6) \\ P_{in} &= \frac{I_{in}^2 Z_{in}}{2} \qquad (3.7) \end{aligned}$$

$$G = 4\pi\frac{P_{rad}}{P_{in}} = \frac{\pi\eta_0 I_{act}^2}{2\epsilon_{act} I_{in}^2 Z_{in}}. \qquad (3.8)$$

Assuming that, prior to reaching the ring, there was no loss in the traveling wave one may write

$$\begin{aligned} \frac{P_{act}}{P_{in}} &= 1 \qquad (3.9) \\ \Rightarrow \left(\frac{I_{act}}{I_{in}}\right)^2 &= \frac{Z_{in}}{Z_{act}} \qquad (3.10) \\ G &= \frac{\pi}{\sqrt{\epsilon_{act}}}, \qquad (3.11) \end{aligned}$$

where P_{act} is the power in the wave at the active region and (3.4) is used in the derivation of (3.11).

This means that the spiral without substrate should radiate a constant gain of π at all frequencies. However, for a spiral on a dielectric substrate, the gain can be expected to monotonically decrease as the frequency increases, moving the active region inward toward the feed. As this occurs, ϵ_{act} moves upwards towards its value near the feed of approximately $\frac{\epsilon_r+1}{2}$.

Some effort was put into finding a relationship between ϵ_{act} and the frequency f in order to obtain a functional form for the gain using a transmission line approximation,

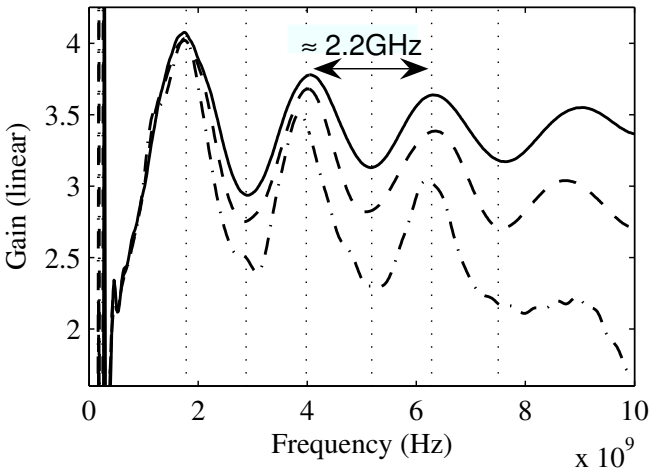

Figure 3.4: Simulated gain for a spiral with $\psi = 79°$, $R_{out} = 0.12$ m, $R_{in} = 2.5$ mm with ϵ_r from highest to lowest: 1, 2.2, and 4.2. Dotted lines denote the minima and maxima of the gain ripple.

but aside from the limiting values discussed above, the match was unsatisfactory. The effect on the gain is directly related to the failure of the antenna to truly satisfy Rumsey's scaling principle. If the dielectric thickness were to increase as the wave moved outward, the ϵ_{act} could conceivably be kept constant and this would imply that the gain would remain constant. The data shown in Fig. 2.14 and Fig. 2.15 show this decreasing behavior with a rate of descent that becomes steeper with a higher dielectric constant. This is again seen in Fig. 3.4, here with simulated data. In addition to the decreasing gain, a gain ripple is observed with an amplitude of approximately 1 to 2 dB. It is shown in the next section that this ripple is related to the outer truncation of the spiral.

3.1.4 Bore-sight Gain Ripple

In Fig. 3.4, a sequence of gain curves is shown for various dielectric constants with $\psi = 79°$, $R_{out} = 0.12$ m and $R_{in} = 2.5$ mm. The simulated gain curves can be seen to ripple approximately at the same rate as a function of frequency. The ripples seen in Fig. 3.4, 2.14, and 2.15 are also present in all FDTD simulations of the bore-sight gain in this study. In this section, the ripple seen is analyzed with a simple model and FDTD simulations.

Ripples in the frequency domain are often the result of an echo in the time-domain, as noted in section 3.1.1. Here the radiated field takes the form of some initial pulse

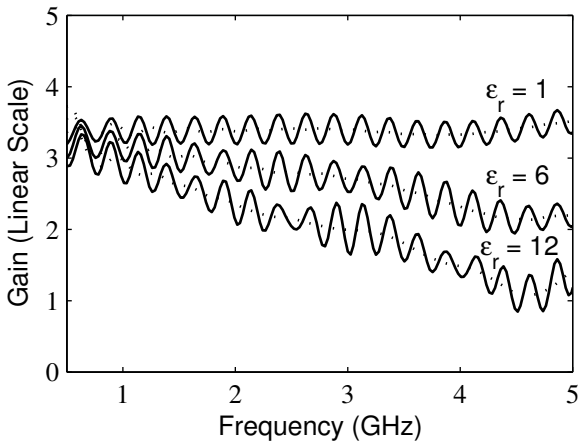

Figure 3.5: Simulated gain for three 1.2 m radius spirals (top to bottom): $\epsilon_r = 1, 6, 11$. Time gated gain is shown dotted.

$h(t)$ and a delayed scattered pulse $\Gamma h(t - t_d)$. This gives a Fourier transform of the form $\mathcal{F}\{h\}(\omega)(1 + e^{-j\omega t_d}\Gamma)$. The magnitude of this function shows a periodic ripple on top of the original response with a period in the frequency domain of $\frac{1}{t_d}$. In Fig. 3.4 all three plotted gain functions show a ripple with a period of approximately 2.2 GHz, which corresponds to a time delay of 0.45 ns. The fact that each of the gain curves shows the same ripple period makes it unlikely that the secondary radiation is the result of the traveling wave in the spiral, since the phase velocity of the traveling wave is a stronger function of the dielectric than the shown variation in the period.

Instead, it would appear that the initial pulse is radiated into free space and the second pulse is the result of some scattering that occurs at a distance of $c(0.45 \times 10^{-9}s) \approx 13.5$ cm. The truncation of the spiral occurs 12 cm from the feed, and after running a number of simulations with various radii for the spirals it became apparent that the time delay that causes the ripple tends to be approximately R/c, where R is the radius of the spiral. In order to verify that the ripple is related to the truncation of the spiral, a large spiral was modeled in FDTD so that the secondary ripple could be seen separated from the initial radiated pulse. In Fig. 3.5 and 3.6, three spirals with differing dielectric constants and a radius of 1.2 m are shown in the frequency domain and time domain.

The time-domain plots in Fig. 3.6 show an initial radiation with a peak around 0 ns and a secondary radiation with a peak around 4 ns. The delay is the expected transit time

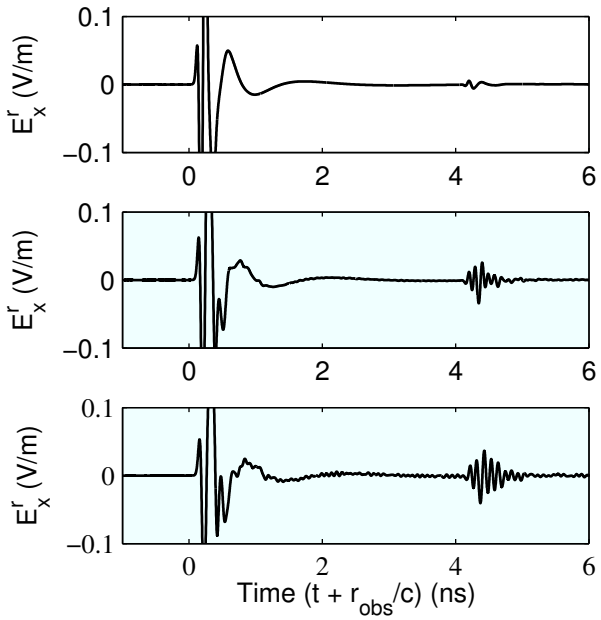

Figure 3.6: Time domain response for 1.2 m radius spirals (Top to bottom): $\epsilon_r = 1, 6, 11$. Here r_{obs} refers to the distance from the center of the spiral to an observer in the far-field.

for a spiral of this size. With the two pulses separated, the effect of the secondary radiation can be removed by time-gating. This is seen in Fig. 3.5 as the dotted line. It should be noted that both peaks in the time plot show a chirping property with high frequencies being radiated earlier than low frequencies. This is most easily seen in the $\epsilon_r = 1$ case. The fact that this chirping appears in both pulses suggests that the delayed pulse is a scattering from the radiation in the active region. If the initial pulse were radiated at the feed point then the scattered pulse would be a delayed version of the excitation (a differentiated Gaussian pulse in this case). Instead, each frequency is believed to be radiated at its active region where $r = \lambda/2\pi$. The signal travels to the outer radius and scatters as depicted in Fig. 3.7. Since the time delay between the two pulses is

$$\begin{aligned} t_d &= (R - \lambda/2\pi)/c \\ &= R/c - v_p/(2\pi f c) \\ &= R/c - 1/(\sqrt{\epsilon_{\text{EFF}}}\omega). \end{aligned}$$

The effect of this delay on the transform of $h(t)$ can be approximately written as

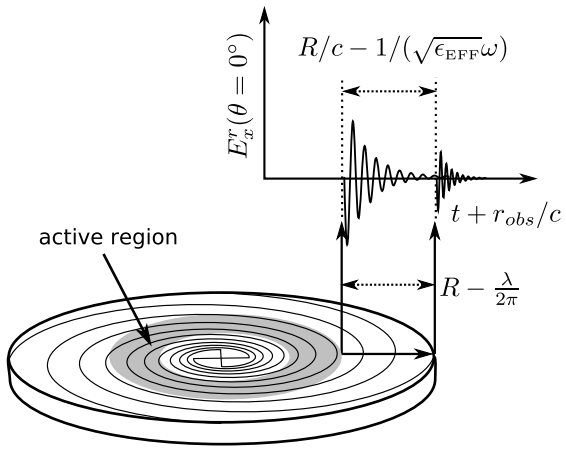

Figure 3.7: Diagram of the radiation of a narrow-band pulse of angular frequency ω. The time scale shown includes the delay to a far-field observer at r_{obs} from the antenna's center.

$$\mathcal{F}\{h\}(\omega)(1 + e^{-j\omega t_d}\Gamma) \quad = \quad \mathcal{F}\{h\}(\omega)(1 + e^{-j\omega R/c}e^{-j/\sqrt{\epsilon_{\text{EFF}}}}\Gamma), \tag{3.12}$$

which has the periodic variation R/c that is typically observed. It should be noted that this scattering occurs even when the dielectric is not present and only at the outer truncation point of the spiral, not at each successive arm of the spiral that the radiated wave encounters.

3.1.5 Radiation Patterns

Since the antenna is modeled as lossless here, the power radiated must still be the power inserted at the feed. Because of this, it may be of interest where the energy that is deflected from bore-sight is radiated. This can be determined by constructing a radiation pattern of the antenna. Since the lower hemisphere is almost identical to the upper hemisphere, only the upper hemisphere is shown here. Figure 3.8 shows the gain as a function of angle for the upper hemisphere of the antennas in Fig. 3.4 at the dielectric constants 4.2 and 1.

In Fig. 3.8 it can be seen that the scattered pulse acts to alternately expand and contract the pattern along the z-axis in the free-space case. These expansions correspond with the maxima of the gain ripple observed. In the dielectric case the pattern becomes more complicated at the higher frequencies with more radiated power deflected into side-lobes, but the same behavior is still observed.

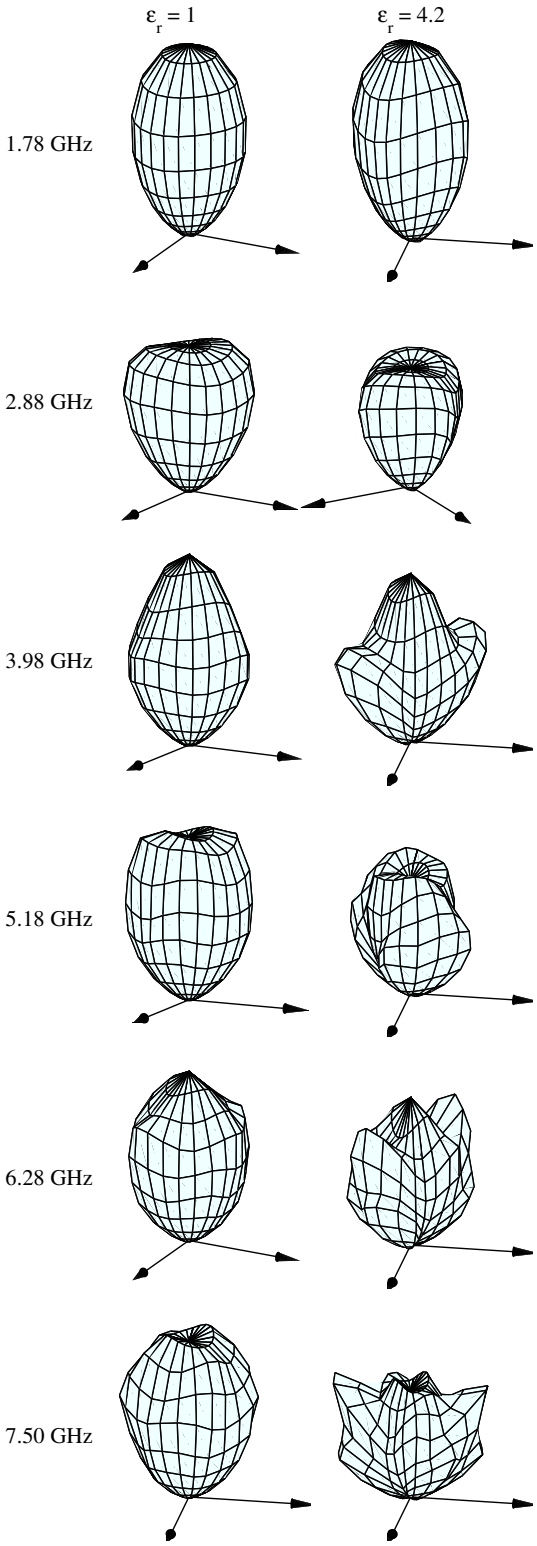

Figure 3.8: Radiation patterns for the upper and lower gain curves at the respective minima and maxima denoted in Fig. 3.4 by dotted vertical lines.

The introduction of the absorbing can that is typically used with the spiral antenna could be expected to change the nature of the scattering at the truncation point since there would be an additional scattering off of the can edge. Also, many designers truncate the outer radius of the spiral with absorber to reduce the reflected traveling wave. This may have the added side effect of absorbing the radiated wave described here.

3.1.6 Conclusions

An FDTD model of the spiral element was constructed and compared against measured data. This model was then used to study the effects of the dielectric backing on the spiral's behavior in the operating band. These effects consist of a decrease in the impedance over the operating band that becomes more severe as the dielectric constant and substrate thickness are increased. The behavior of the bore-sight gain in the operating band was described, and the source of a ripple in the gain as a function of frequency was analyzed. Simple models for some of these effects have been presented or summarized from other work. Questions remain as to the nature of the wave that generates the scattered radiation and why it appears to travel radially outward through the spiral arms without scattering, only to scatter at the truncation point. In the next section, the cutoff frequencies of the operating-band are discussed and the effect of the spiral's geometry on the lower cutoff is analyzed.

3.2 Operating Bandwidth

With a general discussion of the characteristics of the spiral element in its operating band presented, the range of frequencies where this analysis may be applied is examined. This question has a number of answers depending on which operating-band characteristics are most important for a particular design. Because the majority of the current on a spiral at the highest frequencies is concentrated near the feed region, the exact nature of the feed used by the spiral typically determines the upper frequency limitation of the spiral. Because of this, it is difficult to make general statements about the upper frequency limit with much more specificity than that made by Bawer and Wolfe that the spiral operates in a frequency-independent manner while the active region fits on the antenna [17]. However, the lower frequency limit is determined by currents at the exterior region of the spiral,

which is entirely a property of the spiral element. In this section, the determination of the lowest frequency of operation for a fixed geometry, or the equivalent problem of finding the smallest spiral antenna that can operate at a given frequency is examined.

In Dyson's original paper on the equiangular spiral, he provides a design graph that relates the geometry of the antenna to the lowest frequency at which the antenna effectively emits circularly-polarized radiation [1]. This work is summarized in [22] for the self-complementary spiral with the guideline that the length of the antenna arms must exceed one wavelength at the lowest frequency of operation. Both studies were based on Dyson's original slot spiral and consequently do not include the effect of a substrate. In addition, each defines proper operation only in terms of the axial ratio of the antenna.

In this chapter, the low-frequency performance of the equiangular spiral is examined in a parametric study using a numerical model of the antenna. The lowest frequency of operation is defined in terms of three metrics: boresight axial ratio, boresight circularly polarized gain, and voltage standing wave ratio (VSWR). Graphs that show the effect of relevant antenna parameters on the lowest frequency are presented. In addition, the off-angle gain and axial ratio are examined.

3.2.1 Defining the Low-Frequency Cutoff

The equiangular spiral's lower cutoff frequency is sometimes stated to occur when the length of the arms reaches approximately one wavelength. The length, L, of the arms can be related to the geometry given in Fig. 1.2 by the equation,

$$L = \sqrt{1 + (\tan\psi)^2}\,(R_{out} - R_{in})\,. \tag{3.13}$$

While approximately true for smaller ψ, this guideline must fail when the spiral is tightly wrapped because $L \to \infty$ as $\psi \to 90^\circ$. If the lower cutoff frequency were only a function of the length of the antenna, and not the truncation diameter, then an antenna of any size could be made to operate at an arbitrarily low frequency by wrapping the antenna tighter. An equiangular spiral curve with ψ near 90° closely approximates an Archimedean spiral, as noted in [3]. Since the Archimedean spiral has an alternative guideline for the lower

cutoff frequency that is independent of the wrapping tightness, this second cutoff condition must eventually take precedence. In this paper, the Archimedean-style model of [17] and [5] is used as a starting point and is modified by a factor that is a function of the spiral geometry.

According to this model, the antenna's radiation primarily comes from an annular "active region" with a circumference of approximately one wavelength [8]. The design rule that is typically inferred from this model is that the antenna will operate properly when the active region fits on the spiral [17]. To be more precise, the antenna could be said to work properly at some frequency, f, when its circumference, $C = 2\pi R_{out}$, is larger than one wavelength, λ, where $\lambda = c/f$ and c is the speed of light. This rule is approximately true, but there is no abrupt change in the antenna parameters when the ratio C/λ reaches unity. To pick a particular ratio C/λ that corresponds to the lower cutoff frequency, the designer must specify a definition of proper operation.

To illustrate some possibilities, the three metrics used to define proper operation in this work are shown for some typical spiral antennas in Fig. 3.9. These include the VSWR, the boresight circularly polarized gain, and the boresight axial ratio. For each metric, there is a region of low frequencies where the metric has an undesirable value, and a region of higher frequencies where the metric stays relatively constant near a desirable value. The latter region of frequencies is referred to as the operating band. To determine the lower cutoff frequency of the operating band, a cutoff value is chosen that indicates the worst acceptable performance of the antenna for a given metric. The frequency that corresponds to this cutoff is taken to be the minimum frequency of operation and is shown as a vertical line on each graph in Fig. 3.9.

In order to obtain cutoff frequencies over a wide range of spiral antenna geometries, FDTD simulations for various R_{in}, R_{out}, h, ψ, and ϵ_r were run. It was found that the effect of R_{in} was negligible on the lower cutoff frequency. R_{out} had the inverse relationship to the lower cutoff frequency predicted by the active region concept. The variation of ψ was determined to be of interest for parameterization. Finally, the substrate parameters ϵ_r and h were seen to have an erratic and usually minimal effect on the cutoff. The design graphs

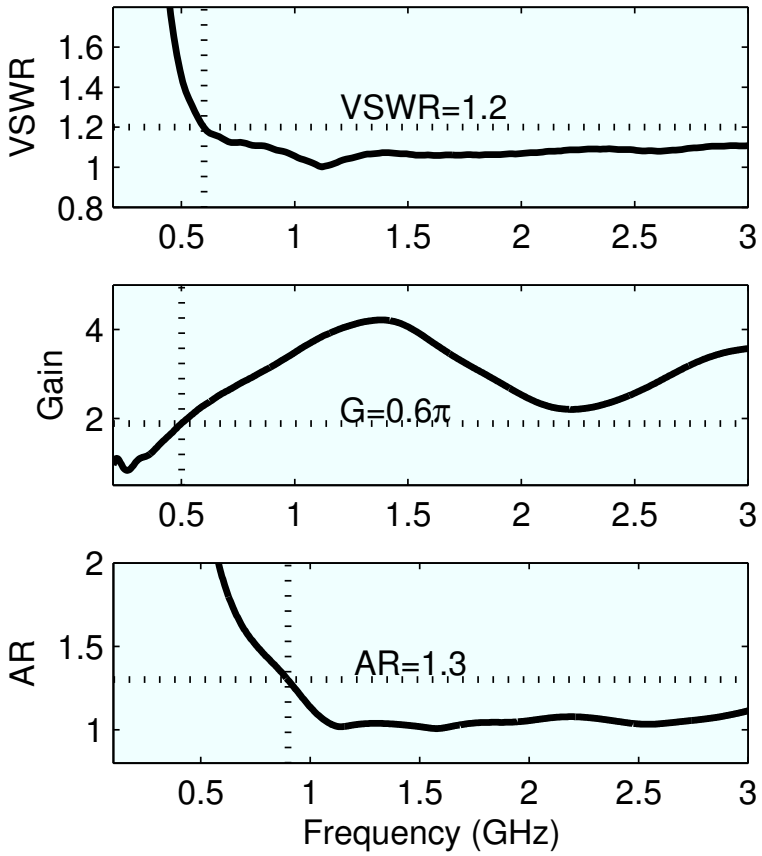

Figure 3.9: Examples of the performance of the spiral antenna with the corresponding lower cutoff frequency of operation represented by a vertical dotted line.

give the range of cutoffs associated with each dielectric simulated. Additional information on the effect of the substrate on the cutoff is provided in Section 3.2.2.

With the relevant parameters established, the ranges were determined by the available computational resources. The value of R_{in} was held constant at 7 mm. The dielectric constant, ϵ_r, was allowed to vary from 1.0 to 6.0 in 0.5 increments. The substrate thickness, h, was held constant at 1.8 mm. The value of R_{out} was held constant at 15.24 cm. The parameter ψ was varied from 71° to 82° in 0.5° increments. This required 253 separate simulations of the spiral antenna. Due to its wide availability, an additional FR4 substrate with $\epsilon_r = 4.2$ was also simulated over the same ranges.

3.2.2 Effect of the Substrate

Substrates that have a thicker and higher dielectric constant tend to slow the phase velocity of the currents traveling on the spiral arms when the arms are sufficiently close to one another. Because of this, a sufficiently thick substrate will reduce the wavelength for a given frequency and allow the antenna to operate at a lower frequency than it would without a substrate present. This observation is exploited to minimize the size of an Archimedean spiral in [49].

The equiangular spiral, however, has the property that the distance between the spiral arms increases linearly as a function of distance from the feed. Because of this, the substrate will often have a large effect on currents near the feed, but considerably less effect near the outer truncation of the spiral. An example of this can be seen in Fig. 3.10 where the simulated right-handed circularly-polarized (RHCP) gain of a fixed spiral geometry is shown for substrate thicknesses that vary from 0 mm to an impractically thick 10 mm. Here, $\psi = 82°$, $\epsilon_r = 6.0$, $R_{in} = 1.4$ cm and $R_{out} = 15.24$ cm.

While the thick substrates have an extremely detrimental effect in the operating band of the antenna, the lower frequencies are almost unaffected. The worst effects seen in Fig. 3.10 occur for the substrates with electrical thicknesses that are a large fraction of a wavelength. For instance, the 10 mm substrate has an electrical thickness of $\lambda/4$ at 3GHz, where the response is especially erratic.

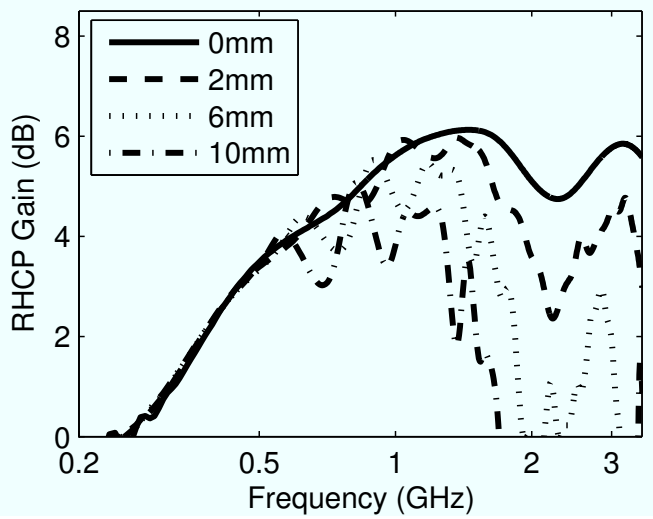

Figure 3.10: Right-handed circularly polarized gain on boresight of a spiral antenna with a fixed geometry of $\psi = 82°$, $\epsilon_r = 6.0$, $R_{in} = 1.4$ cm, $R_{out} = 15.24$ cm, and a varying substrate thickness. The plot shows the relatively minor effect of the substrate on the lower frequencies of operation and the degeneration of the operating band for electrically thick substrates.

Because spirals with electrically thick substrates often do not have identifiable operating bands, this study focuses only on spirals with an electrically thin substrate. When the substrate is electrically thin, it can only have an effect on the lower cutoff frequency if the spiral is wrapped very tightly, meaning $\psi \approx 90°$. Because the results shown in Fig. 3.10 are for the most tightly wrapped spirals in this study, the substrate will not play a large role in the lower-frequency cutoff for the spirals modeled in this work. The minor variation in the Section 3.2.3 design graphs that is due to the dielectric is shown as a gray band that represents the range of values over all dielectrics studied.

It may be possible to reduce the cutoff frequency of an equiangular spiral on an electrically thin substrate by wrapping it so tightly that the arm width at the truncation point is smaller than the substrate thickness. Because spirals of this type still satisfy the condition that the arm thickness varies linearly with distance from the center, they require an extremely fine resolution near the feed to be modeled properly. Spirals of this wrapping tightness could not be modeled with the computational resources available for this study and therefore the results of this work should only be applied for relatively loosely wrapped spirals with $\psi < 82°$.

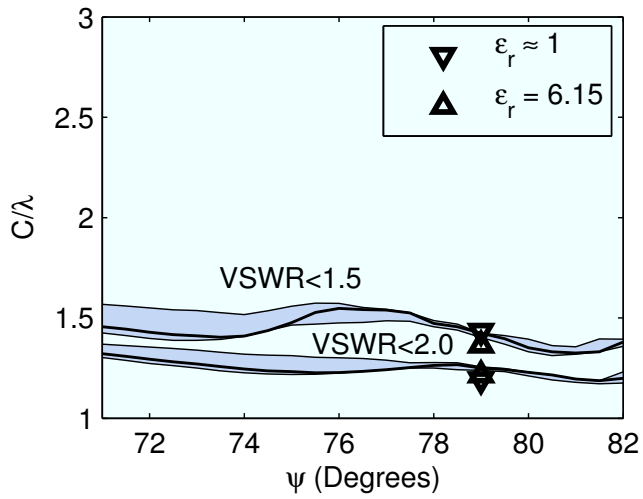

Figure 3.11: C/λ at cutoff defined by the VSWR of the antenna as a function of ψ. The gray bands represent the range of cutoff frequencies for the substrates simulated. FR4 ($\epsilon_r = 4.2$) is shown as the solid black line. Experimental data from the antennas shown in Fig. 8(a) and 8(b) are shown as triangles for each cutoff condition.

3.2.3 C/λ Ratios at Cutoff

To characterize the impedance bandwidth, a metric is desired that defines how close the impedance at a given frequency is to the operating-band impedance. To do this, the VSWR is chosen. This is the ratio of the maximum to minimum standing wave amplitude on the transmission line that feeds the antenna, and may be related to the reflection coefficient, Γ, by

$$VSWR = \frac{1 + |\Gamma|}{1 - |\Gamma|}. \tag{3.14}$$

The value is always greater than one and approaches unity for a perfectly matched antenna. Since the impedance of a spiral antenna is essentially constant in its operating band, a properly driven spiral antenna will have a VSWR very near unity for a wide region of frequencies.

To generate design graphs based on the VSWR, the antennas were fed with their operating-band impedance as interpolated from Fig. 3.3. The values for C/λ for two different VSWR cutoff values were computed for the range of spiral antennas simulated and the results are shown in Fig. 3.11 as a function of ψ.

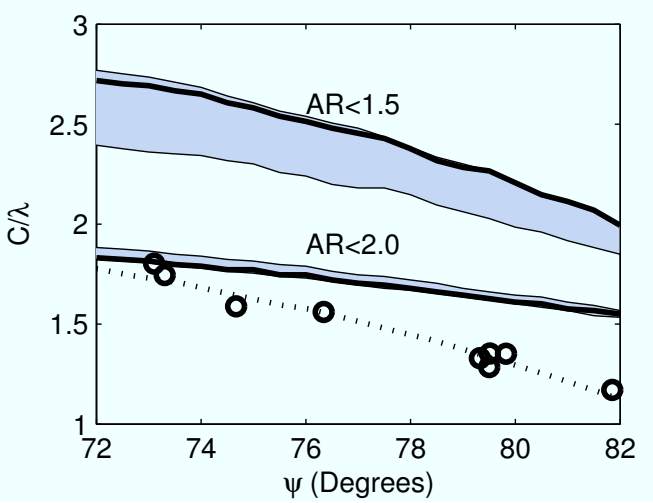

Figure 3.12: C/λ at cutoff defined by the boresight axial ratio of the antenna as a function of ψ. The gray bands represent the range of cutoff frequencies for the substrates simulated. FR4 ($\epsilon_r = 4.2$) is shown as the solid black line. The results of Dyson's slot-spiral study are shown in the dashed line. Circles mark the individual data points of his study. Note that the region above $\psi = 78.6°$ in Dyson's data is extrapolated from more loosely wrapped spirals.

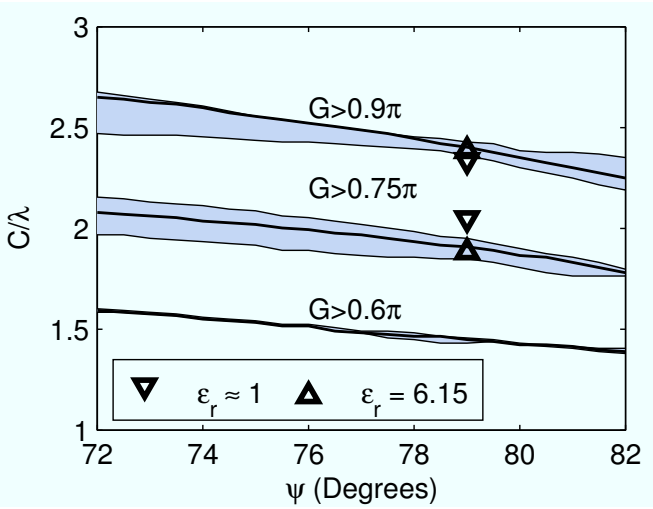

Figure 3.13: C/λ at cutoff defined by the boresight circularly polarized gain of the antenna as a function of ψ. The gray bands represent the range of cutoff frequencies for the substrates simulated. FR4 ($\epsilon_r = 4.2$) is shown as the solid black line. Experimental data from the antennas shown in Fig. 8(a) and 8(b) are shown as triangles for the two higher frequency cutoff conditions.

Experimental VSWR results from the antennas shown in Fig. 8(a) and 8(b) are included on the plot. These are for two antennas with $\psi = 79°$, $R_{in} = 3$ mm, and $R_{out} = 11.4$ cm. The substrates were chosen at the outer edges of the dielectric values in this study. A Foamclad substrate was used to emulate air and a Rogers RO3006 substrate with $h = 1.27$ mm and $\epsilon_r = 6.15$ was used for the high dielectric value. The experimental results show good agreement with the simulation.

To describe the polarization properties of the antenna, the boresight axial ratio metric is used. It is defined to be the ratio of the major axis over the minor axis of the polarization ellipse. Therefore, a linearly polarized antenna will have a large axial ratio while a circularly-polarized antenna will have an axial ratio near unity. A plot of C/λ for two boresight axial-ratio cutoff values as a function is shown in Fig. 3.12.

For reference, the results of Dyson's slot-spiral bandwidth study are presented in Fig. 3.12. Dyson's cutoff value was chosen at an axial ratio of 2.0. His ψ values range from 65.8° to 78.6°. It should be noted that his study was not restricted to self-complementary antennas. His data are given in terms of a composite parameter that he calls the angular width factor. This angular width factor is a function of ψ and a second parameter that describes the degree to which the antenna is not self-complementary. The data above 78.6° shown in Fig. 3.12 were extrapolated by Dyson from non-self-complementary spirals with a ψ less than the stated value.

To describe the power radiated by the antenna, the circularly-polarized boresight gain of the antenna was used as a metric. The antennas in this work radiated RHCP in the direction away from the substrate, but had the antennas been inverted, there would likely be no effect on the graphs. The RHCP gain of an antenna is defined to be the ratio of the RHCP power in a given direction radiated by the antenna to the power radiated in any direction by a perfectly isotropic radiator when each antenna is fed by a matched transmission line. This can be expressed as

$$G(\theta, \phi) = \frac{4\pi P_{\mathrm{RAD}}}{P_{\mathrm{IN}}}, \tag{3.15}$$

where G is the gain, θ is the decline from boresight, ϕ is the azimuthal angle, P_{RAD} is the

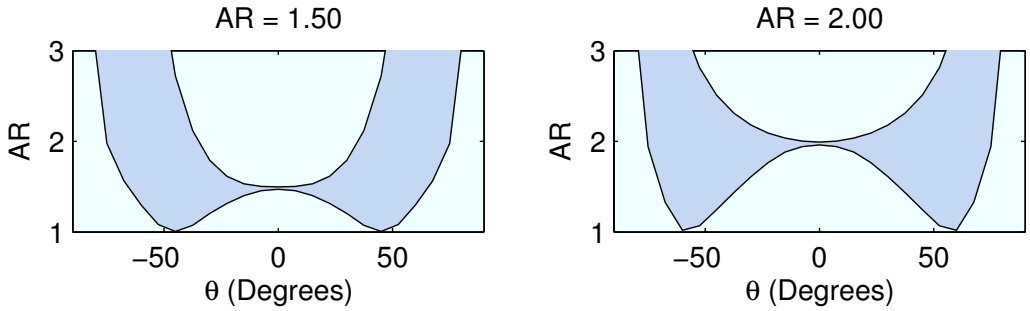

Figure 3.14: The shaded region shows the composite axial ratio of the equiangular spiral antenna at the cutoff frequency. The composite contains all angles of ψ and each antenna used in the design study.

radiated RHCP power density in watts per steradian as a function of angle, and P_{IN} is the power inserted into the antenna. A plot of C/λ for three cutoff values of the circularly-polarized gain as a function of ψ is shown in Fig. 3.13. As with the VSWR, experimental results from the antennas shown in Fig. 8(a) and 8(b) have been included in the plot. The lowest frequency cutoff value fell below the frequency where a far-field assumption was valid in our test range and therefore only the two higher frequency cutoff bands are shown.

In Figs. 3.11, 3.12, and 3.13, one observes a general trend that increasing the parameter ψ yields a slightly better minimum frequency cutoff. This corresponds to wrapping the spiral more tightly, and agrees with observations made by Dyson in [1]. The graphs also show the degree to which reducing the restriction on a given parameter allows one to reduce the size of the antenna. For instance, reducing the restriction on the VSWR from 1.5 to 2.0 has a negligible effect on the antenna's size, while reducing the restriction on the gain from 0.9π to 0.75π can reduce the antenna's circumference by half a wavelength at the lowest frequency of operation. As a final note, the degree to which the gray bands of the plots are thin, as well as the corresponding experimental data, suggest that the substrate may be ignored when calculating the lower-frequency cutoff of an equiangular spiral on an electrically thin substrate for the range of studied.

3.2.4 Off-angle Performance

One limitation of the design graphs shown above is that the definitions of the operating band based on axial ratio and gain depend only on the boresight radiation. This was chosen

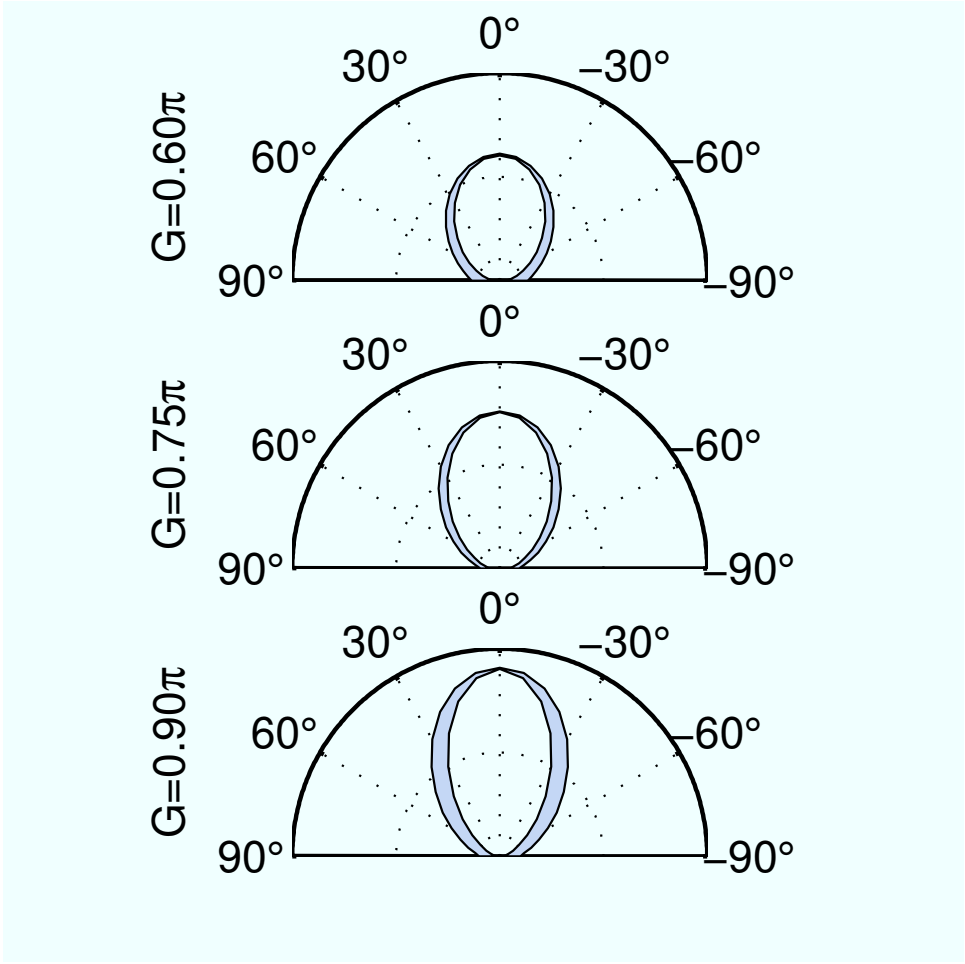

Figure 3.15: The shaded region shows the composite pattern of the equiangular spiral antenna at the cutoff frequency. Composites contain all angles of ϕ and each antenna used in the design study. Radial units range from 0 to π.

because the boresight radiation tends to be the best performance for the antenna. However, in most situations it is necessary to know the behavior off of boresight as well. It was found in this work that the off-angle performance of this antenna is very stable at low frequencies.

In order to present this, two graphs showing the composite performance of the antenna are shown. For each antenna in the design study above, the far-field radiation in every direction at the cutoff frequency was recorded using a near-field-to-far-field transformer [36]. For the related far-field parameters, axial ratio and circularly polarized gain, a maximum and minimum value were taken over all antennas simulated. In addition, since this antenna has a great deal of rotational symmetry at low frequencies, each ϕ cut was included in the minimization and maximization. The minimum and maximum values of a parameter over all ϕ and ϵ_r form the outline of a composite parameter for the antennas studied in Fig. 3.12 and Fig. 3.13. In Fig. 3.14, the composite axial ratio at cutoff is shown for each cutoff value used in Fig. 3.12. In Fig. 3.15, the composite gain pattern at cutoff is shown for the circularly polarized gain of the antenna given each cutoff value used in Fig. 3.13.

Since the frequencies used in the plots were selected based on the boresight performance, each plot shows no variation at $\theta = 0°$. On the axial ratio plots, one sees relatively little variation until near $\theta = 50°$, where the AR varies from nearly 1 to 3. Beyond this point, the polarization becomes increasingly linear, but this region may be seen to have low relative gain from the pattern plots.

3.2.5 Conclusion

Design graphs showing the lower cutoff frequency of the equiangular spiral antenna over a wide region of design parameters have been shown. The general trend observed in each graph, that increasing the arm wrapping tightness tends to lead to better performance, agrees with the original work of Dyson [1]. Additionally, the graphs show that for spirals that are not wrapped extremely tightly, the substrate may be ignored when calculating the lower cutoff. The design graphs provide a quantitative correction to the standard rule for calculating the lower-frequency cutoff and may be used either to determine the minimum usable frequency of operation available for a given antenna size, or to determine the absolute

minimum antenna size possible to operate at a given frequency.

This work also examines the off-angle performance of the antenna and finds it extremely well-behaved with very little change observed in the shape of the pattern or off-angle axial ratio over all substrates simulated. A designer may assume that over the parameterization region given, these variables will not strongly affect the nature of the off-angle performance.

CHAPTER IV

MODELING AND VERIFICATION OF THE TWO-SPIRAL GPR SYSTEM

After completing the study of the spiral element on a dielectric substrate, a two-spiral GPR system was constructed and verified against the FDTD model. In this chapter, the construction, calibration, measurement and modeling efforts are described. Care is taken as each additional component of the system is added to verify that the model and measurements agree.

4.1 Spiral Element Prototype Design and Modeling

While the spiral element described in the previous chapter had already been modeled, some improvements to the element and the measurement procedure were made before introducing additional complexity. The first change to the procedure dealt with calibration. The use of hand-made calibration standards and slip-on connectors during calibration was prone to breakage and would not have been suitable for operation in a field measurement system. Instead, the center conductors of two 0.141" semi-rigid lines were directly soldered to the spiral antenna arms.

The second change dealt with the balun. In order to drive the antenna in a balanced mode using the two lines that feed the spiral arms, it would generally be necessary to use a balun and phase-match the lines. This would also require an adequate characterization of the balun to make accurate measurements of the spiral's response. To avoid errors in the balun characterization and phase matching, the balanced signal was applied virtually using the principle of superposition. A technique similar to this is described in [50], but a simplified description is given below.

To characterize a system that consists of the center conductors of two coax lines attached to an antenna, one must account for non-standard modes that propagate on the coax lines. These modes consist of the common modes of each line as well as modes that travel between

the two coax lines' outer conductors. To simplify the analysis, the outer conductors of the coax lines were bonded to one another, and the outer conductor was wrapped with an absorbing material at some distance from the antenna to reduce the effect of any common modes produced. This is shown in Fig. 4.1. A schematic of the situation is shown in Fig. 4.2. With an absorber on the outer conductors at a sufficient distance away from the spiral, there will not be a voltage wave between the outer conductor and the ground, so it is considered to be grounded. The measurements the network analyzer takes are then the amplitudes of the voltages v_1 and v_2 with respect to ground.

The two lines are attached to a network analyzer through an SMA connector and a full set of two-port network parameters are measured, S'_{ij} at the ports $1'$ and $2'$. If the lengths and losses of the coax lines and the effect of the SMA connector are characterized prior to the measurement, the transfer function across the line is known. It takes the form $\tau e^{-j\beta l}$, where τ represents the transmission across the SMA connector of the line, β is the wave number in the line, and l is the length of the line. This will, in general, take the form e^{af+b} as a function of frequency, f, for some complex a and b. The S-parameters of the spiral antenna attached to the lines can then be related to the S-parameters of the antenna using the signal flow-diagram for the situation, shown in Fig. 4.3,

$$
\begin{aligned}
S'_{11} &= S_{11}e^{-2(a_1 f+b_1)} \\
S'_{22} &= S_{22}e^{-2(a_2 f+b_2)} \\
S'_{12} &= S_{12}e^{-(a_1+a_2)f-(b_1+b_2)} \\
S'_{21} &= S_{21}e^{-(a_1+a_2)f-(b_1+b_2)}.
\end{aligned}
$$

This allows the spiral antenna to be characterized as a two-port network with two 50 Ω ports. While this characterization is useful for calibration purposes, the spiral antenna operates in a balanced mode and no modeling of its behavior when driven single-endedly has been performed for this work. It is shown below that the two-port network defined can be related to a one-port network with two possible modes of excitation, a common mode and a differential mode. The differential mode of excitation creates the balanced response of the spiral antenna that is desired. The transmission-line configuration for the coax lines

Figure 4.1: Semi-rigid line feed for the spiral antennas. The two semi-rigid lines are wrapped in electrically conductive tape and inserted into a rectangular metal tube. The two lines are shown attached to the back of the spiral element. Electrical absorber is placed on the outside of the tube to absorb any common-mode signal that may affect the measurements.

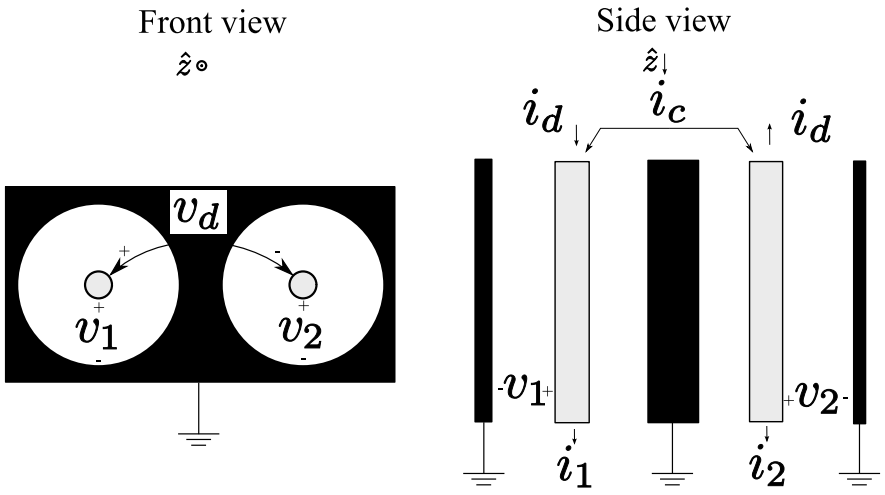

Figure 4.2: Close view of the two semi-rigid coax lines. The outer conductor is bound to earth ground at the network analyzer and absorber near the antenna keeps a voltage wave from traveling along this mode, so sufficiently far from the spiral antenna one may assume the outer conductor of the coaxes are grounded. This allows the system to be treated as a two-port network or as a balanced pair.

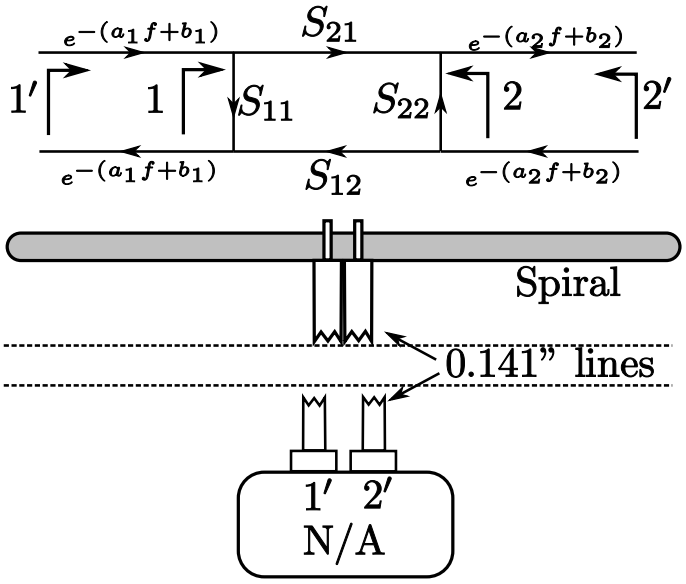

Figure 4.3: Signal flow graph approximation to the spiral system.

is shown in Fig. 4.2. The voltages v_1 and v_2 are the voltages on the inner-conductors with respect to ground. Assuming the distance along the line is measured by the coordinate z, the voltages and currents at a position z on the coax lines 1 and 2 are

$$v_k(z) = v_k^+ e^{-j\beta z} + v_k^- e^{j\beta z} \tag{4.1}$$

$$i_k(z) = \frac{v_k^+}{Z} e^{-j\beta z} - \frac{v_k^-}{Z} e^{j\beta z}. \tag{4.2}$$

where $v_k^{+/-}$ is the amplitude of the forward or backward traveling wave, k is the line, 1 or 2, and Z is the impedance of the line.

These waves can be divided into differential and common modes. The differential voltage and current on the balanced line will be called v_d and i_d, while the common-mode voltage and current will be v_c and i_c. Like the waves on each coax line, the $v_{d,c}$ and $i_{d,c}$ waves will consist of a forward and backward traveling wave, $v_{d,c}^{+/-}$ and $i_{d,c}^{+/-}$. Currents and voltages will be related by the differential and common-mode impedances, Z_d and Z_c. The differential voltage is the total voltage between the lines.

$$v_d(z) = v_1(z) - v_2(z) = v_d^+ e^{-j\beta z} + v_d^- e^{j\beta z}. \tag{4.3}$$

The common-mode current is the total current flowing toward the device, and it is assumed

to be equal in each line

$$i_c(z) = i_1(z) + i_2(z) = \frac{v_c^+}{Z_c} e^{-j\beta z} - \frac{v_c^-}{Z_c} e^{j\beta z}. \tag{4.4}$$

(4.3) and (4.4) define the other modes on the line. The common-mode voltage is the common part of the voltage on each line,

$$v_1(z) = v_c(z) + v_d(z)/2$$
$$v_2(z) = v_c(z) - v_d(z)/2,$$

from which it can be seen that

$$v_c(z) = \frac{v_1(z) + v_2(z)}{2} = v_c^+ e^{-j\beta z} + v_c^- e^{j\beta z}. \tag{4.5}$$

The differential-mode current is the portion of the current that travels in opposite directions,

$$i_1(z) = \frac{i_c(z)}{2} + i_d(z)$$
$$i_2(z) = \frac{i_c(z)}{2} - i_d(z),$$

from which it can be seen that

$$i_d(z) = \frac{i_1(z) - i_2(z)}{2} = \frac{v_d^+}{Z_d} e^{-j\beta z} - \frac{v_d^-}{Z_d} e^{j\beta z}. \tag{4.6}$$

With the common and differential modes defined at each point, they can be related to the waves on the coax lines,

$$v_d^\pm = v_1^\pm - v_2^\pm$$
$$v_c^\pm = \frac{v_1^\pm + v_2^\pm}{2}$$
$$i_d^\pm = \frac{v_1^\pm - v_2^\pm}{2Z}$$
$$i_c^\pm = \frac{v_1^\pm + v_2^\pm}{Z}. \tag{4.7}$$

Equations (4.7) allow the characteristic impedances for the differential and common modes to be expressed,

$$Z_d = \frac{v_d^+}{i_d^+} = 2Z \tag{4.8}$$

$$Z_c = \frac{v_c^+}{i_c^+} = Z/2. \tag{4.9}$$

This work will diverge from [50] here. There, a full set of scattering parameters are derived that include the common modes produced by differential modes and vice versa. Here, only the differential response to a differential excitation on the one-port is derived, and this can be done directly without the use of generalized scattering parameters. The reflection from the spiral antenna is called $S_{dd,11}$ here, and it can be calculated by applying $v_1^+ = -v_2^+ = v$,

$$S_{dd,11} = \frac{v_d^-}{v_d^+} = \frac{v_1^- - v_2^-}{v_1^+ - v_2^+} = \frac{S_{11}v + S_{12}(-v) + S_{21}v + S_{22}(-v)}{2v} = \frac{S_{11} + S_{22} - (S_{12} + S_{21})}{2}. \quad (4.10)$$

This measurement will be taken with respect to a characteristic impedance of 100Ω according to (4.8).

To compute the balanced scattering response, one must accurately characterize the lengths and losses of the two semi-rigid lines that drive each spiral arm. To measure a characteristic length for each line, only a single reflection measurement is required with a known calibration standard. A simple short-circuit calibration standard that does not damage the line can be made by attaching a brass shim to the end of the coax line and smearing a conductive epoxy over the interface. When the epoxy is allowed to dry, it creates a solid conductive surface at the end of the line that approximates a perfect reflector. A picture of the two semi-rigid lines, electrically bonded together with the short calibration standard attached to the end is shown in Fig. 4.4.

A standard short-open-load (SOL) calibration for a 3.5 mm connector is used at the reference plane for the line. The recorded reflection response, $\Gamma(f)$ is then assumed to be of the form

$$\Gamma(f) = -e^{-2(af+b)}, \quad (4.11)$$

where a and b are complex numbers and f is the frequency of operation. This form is almost the same as assuming the transfer function through the line is nothing more than a delay and a loss, but allows for an additional degree of freedom. The best-fit linear approximation to the log of the $\Gamma(f)$ response is calculated and the a and b responses recorded are used

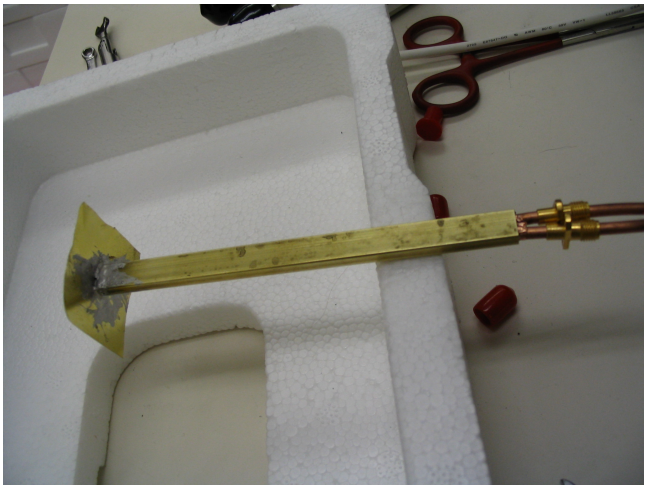

Figure 4.4: Conductive epoxy short-circuit used to characterize each semi-rigid line prior to attachment to the spiral antennas.

to adjust all future measurements made with the line. The branch choice made in the logarithm is arbitrarily chosen to minimize $|b|$ at the lowest frequencies measured.

In addition to changing the feed structure for the antennas, a new spiral element was used in the GPR system. The element was chosen to have the largest possible diameter given constraints on price and weight. The element has an operating band that spans 1-4 GHz with good performance. It was fabricated on 1.8 mm thick Rogers RT 5870 dielectric substrate ($\epsilon_r \approx 2.33$). Using the geometry parameters described in the previous section, the parameters of the spiral were $R_{\text{out}} = 9.5$ cm, $R_{\text{in}} = 4$ mm, $\psi = 81°$. The modeling of the element was unchanged.

Because the GPR system will be primarily analyzed in the time-domain, most verification for the system will be done in the time-domain. The FDTD model was fed with a differentiated Gaussian pulse with a center frequency of 1.5 GHz of the form

$$\begin{aligned} V_{inc}(t) &= -\left(\frac{t-t_d}{\tau}\right) e^{-\frac{1}{2}\left(\frac{t-t_d}{\tau}\right)^2} \text{ V} \\ \tau &= \frac{1}{2\pi 1.5 \text{ GHz}} \\ t_d &= 0.5 \text{ ns}. \end{aligned} \tag{4.12}$$

This pulse can be seen in Fig. 4.5 and has peak values of ± 0.606 V. The response from the antenna element was calculated as a function of time using FDTD. In addition, the

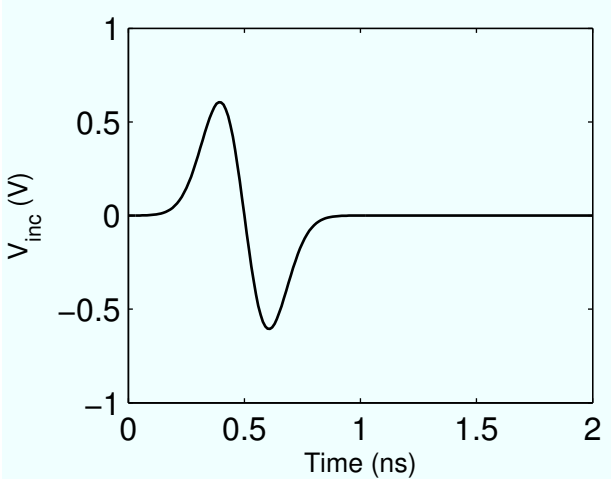

Figure 4.5: Differentiated Gaussian pulse used for excitation of the spiral in this work.

S_{11} response as a function of frequency was obtained from the prototype antenna using the superposition method described above. After inverse Fourier transforming and convolving with this pulse, the measured time-domain response of the antenna was obtained. The comparison of the measurement and model is shown in Fig. 4.6.

The discrepancy in the initial reflected pulse near 1 ns was a concern for future matching efforts. The FDTD model shows a symmetric pulse with height ± 0.125 V while the measurement shows an asymmetric pulse with heights 0.107 V and -0.095 V. It was decided to investigate the difference in order to ensure that it was not caused by a problem with the superposition method of measurement. The eventual cause was found to be in the method of feeding the antenna used in the FDTD simulations. By constructing a more complete numerical model of the feed, a better match was obtained. In the new feed model, the semi-rigid lines were constructed and fed from the simple feed line. The interface between the simple feed and the fully modeled semi-rigid lines was not ideal, and had to be characterized prior to running a simulation with the lines. This calibration was performed numerically just as it would be in the measurement scenario, using an SOL calibration with the numerical standards shown in Fig. 4.7.

Using the fully modeled feed, the scattered response from the antenna showed a much better match to the measurements. The response is shown in Fig. 4.8. Here, the worst

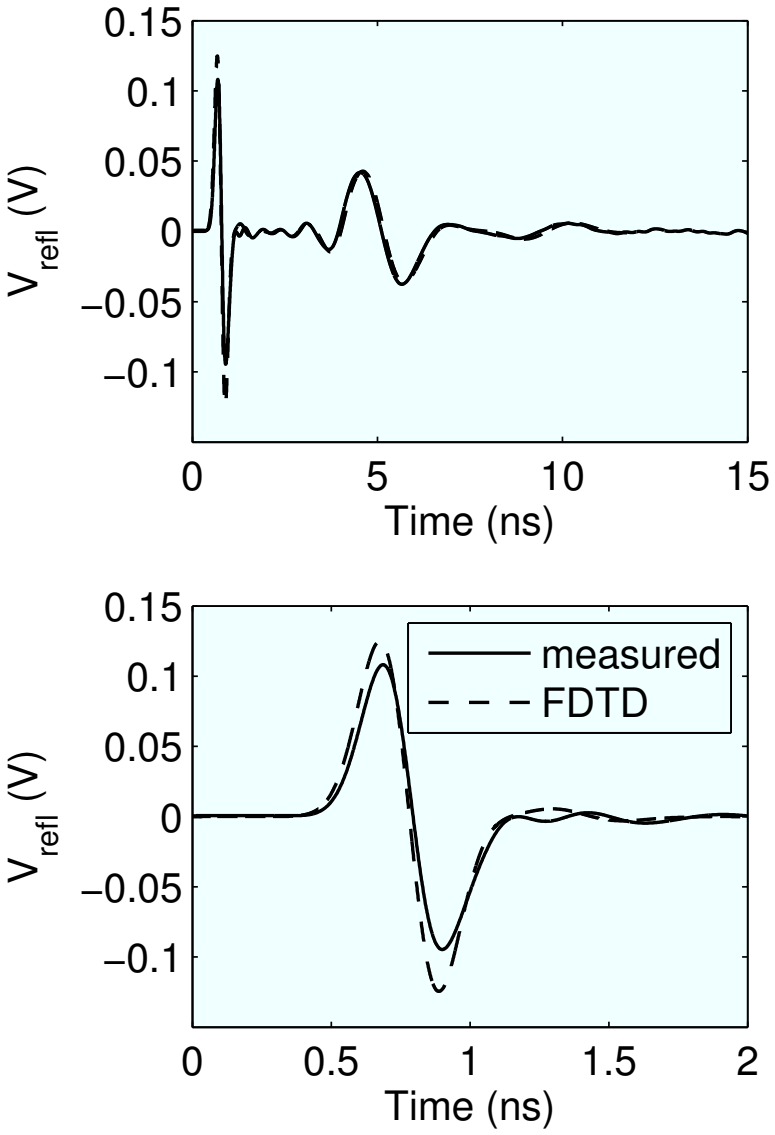

Figure 4.6: Comparison of model and measurement for the spiral element fed using the simple FDTD feed model and the superposition method for measurement. The second subfigure shows a closer look at the initial pulse.

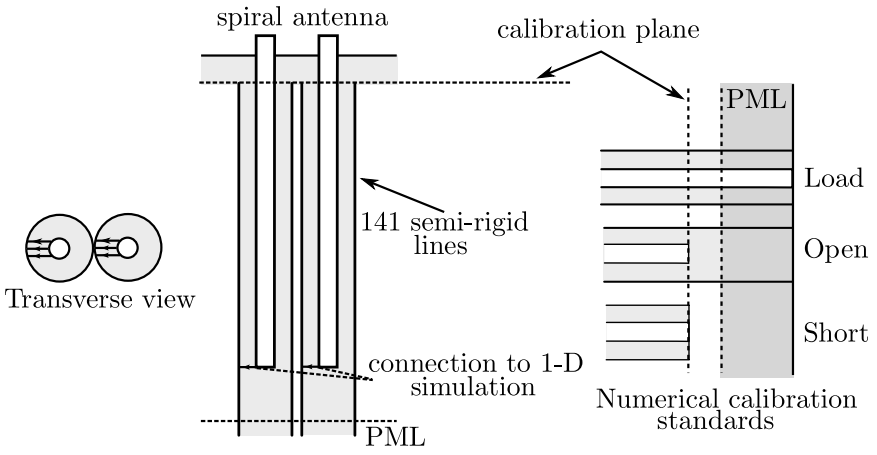

Figure 4.7: The connection between the simple transmission line and the fully modeled semi-rigid lines is shown on the left. On the right, the numerical SOL calibration standards used to remove the effect of the transition from the response are shown.

discrepancy seen is a very minor delay error, but overall the match is very good. Unfortunately, the full feed model requires three additional calibration simulations for a given feed geometry and a much finer cell-size resolution to obtain this match. In addition, the numerical calibration simulations required to handle two antennas fed in this way would be even more time-consuming. These issues would make most of the simulations in the remainder of this work impractical given computational resources, and so it was decided to keep the simple feed, remaining aware of a discrepancy in this transmit-antenna scattered peak height that may result in slightly less power entering the FDTD grid than may occur in reality.

With the numerical model of the element re-verified for the new feed method, the first addition to the model was to introduce the absorbing can for the spirals. A picture of the spiral in the can is shown in Fig. 4.9. This was initially modeled without the absorbing material present. The cans are 14 cm tall, with inner diameter of 20 cm and outer diameter of 20.3 cm. 20.3 cm is also the diameter of the spiral substrate used. The spiral element was attached to the empty can and driven with the differentiated Gaussian pulse (4.12). In Fig. 4.10, the scattered voltage received in the measurement is shown and is compared with the predicted result from the FDTD model. The initial reflection occurs at approximately 1 ns and is caused by the transition from the coax lines to the spiral arms. The second

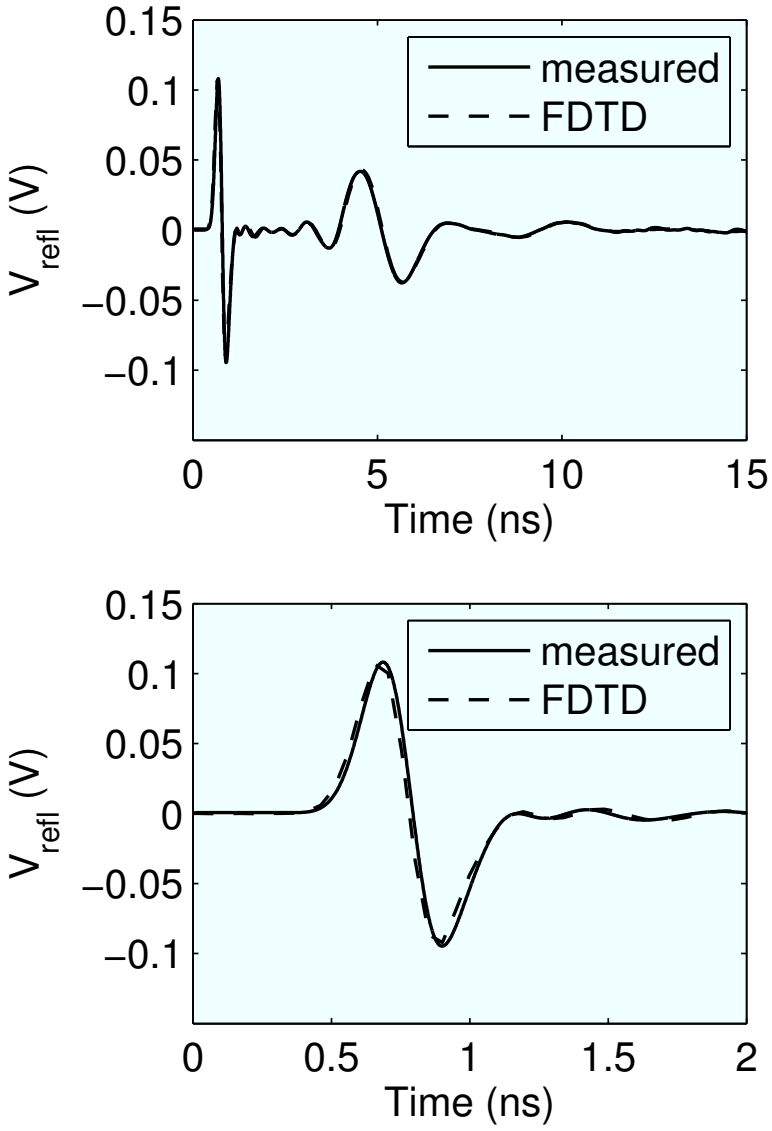

Figure 4.8: Comparison of model and measurement for the spiral element fed using the complete FDTD feed model and the superposition method for measurement. The second subfigure shows a closer look at the initial pulse.

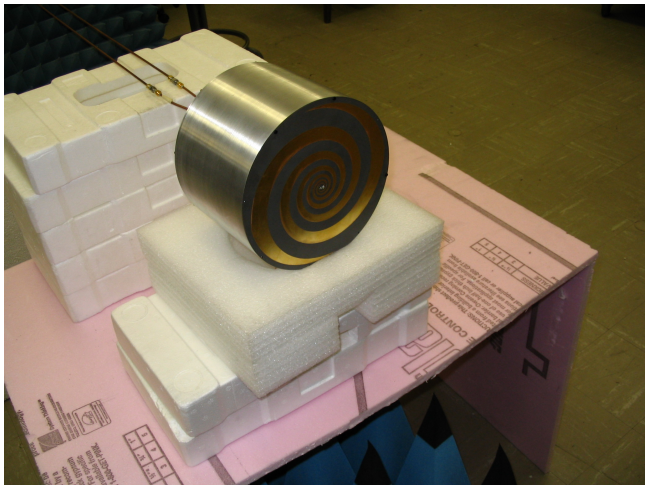

Figure 4.9: Spiral antenna in absorbing can, connected to the semi-rigid lines.

reflection occurs from approximately 4 ns to 15 ns. This is a combination of two signals. The first is related to current that reaches the end of the spiral arms and returns to the feed. The second is a ringing inside of the can. The primary difference between the measured and modeled response is in the size of the initial reflection, which was also seen in the previous measurements. To dampen this ringing, the absorber was added to the prototype and model.

4.2 Absorber Material Measurements

Prior to including the absorber in the FDTD model, it was necessary to obtain its electrical parameters. Modeling the absorber in FDTD requires the conductivity, dielectric constant, and possibly Debye relaxations. When the conductivity is non-zero or a relaxation is present in the modeled frequencies, a different update equation is required, as described in [36]. AN-79 absorber, shown in Fig. 4.11, consists of six layers of polyurethane foam. Each layer is loaded with a different density of carbon to adjust the loss in the layer. The AN-79 absorber was cut to form a cylinder that was inserted into the can taking up 11 cm of the 14 cm available inside.

To obtain material properties for the absorber layers used in the absorbing can, samples of each layer were cut from the AN-79 sheets and measured separately. Initially, it was assumed that the carbon-loaded foam would have a near-unity dielectric constant with

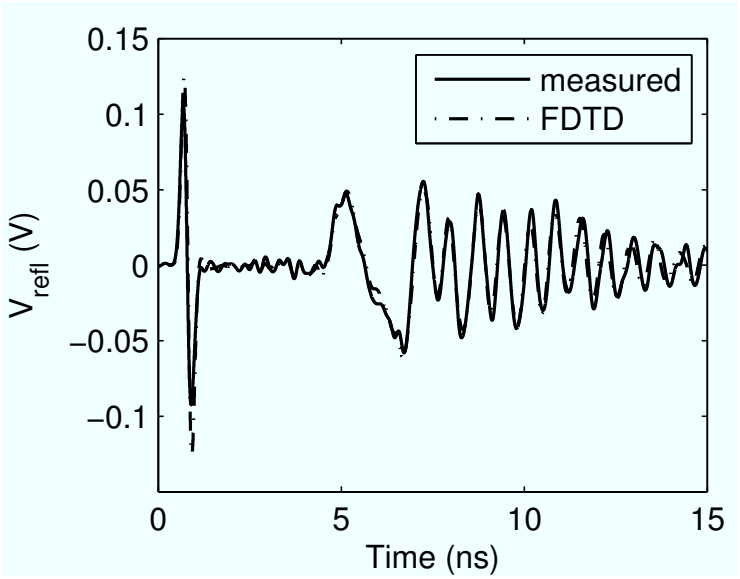

Figure 4.10: V_{refl} measured and modeled for the spiral antenna element with an empty can.

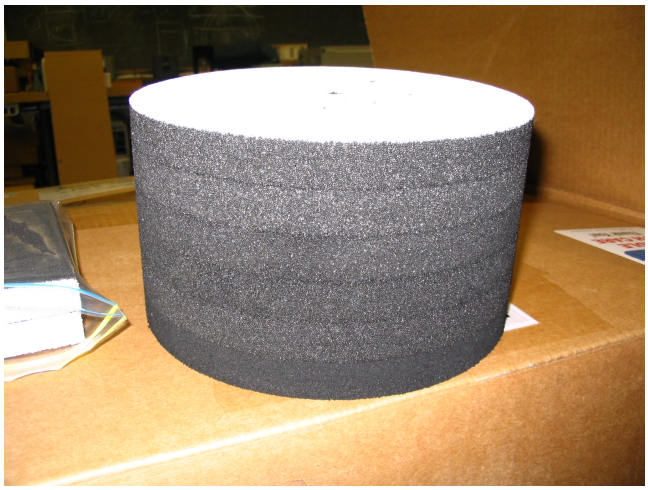

Figure 4.11: AN-79 absorber consists of six layers of carbon-loaded foam. Each layer from top to bottom has a higher carbon density to create a conductivity gradient for absorbing an incoming wave.

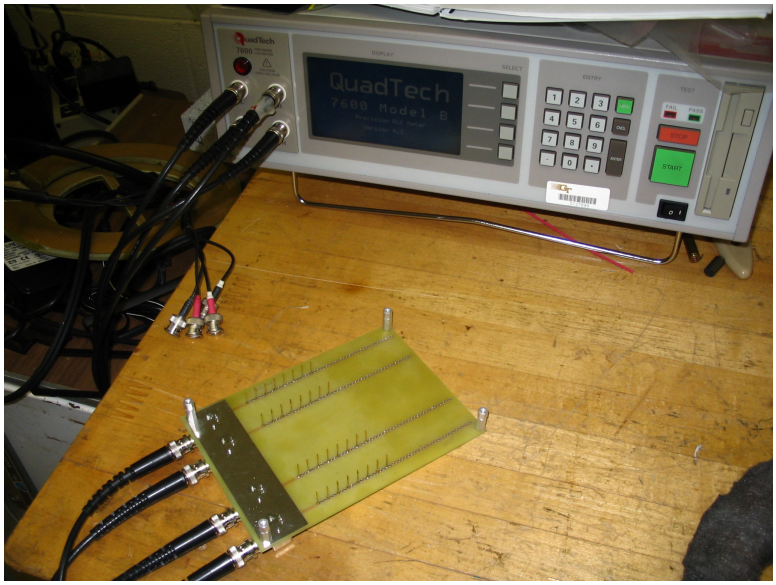

Figure 4.12: DC resistance fixture for the four-point probe.

some conductivity. A four-terminal resistance meter was used to measure the conductivity. Each electrode for the resistance meter was attached to a fixture with a distributed line of probes that were inserted into a rectangular slab of the absorber. The fixture is shown in Fig. 4.12 and a schematic of a four-terminal resistance probe is shown in Fig. 4.13.

The current enters the sample through the outer probes. By distributing the connection into the sample throughout a line, a more uniform current distribution is created in the sample's interior. The inner probes are attached to a high-resistance volt-meter. By distributing the connection to the volt-meter across a line in the sample, the current drawn should not drastically affect the uniformity of the current distribution. If the current is actually uniform within the extent of the sample, and the material properties of the sample are uniform, the current density, $\vec{\mathbf{J}}$, will be

$$|\vec{\mathbf{J}}| = \sigma|\vec{\mathbf{E}}| = \sigma\frac{V_m}{l},$$

where $\vec{\mathbf{E}}$ is the electric field, σ is the conductivity of the sample, V_m is the measured voltage, and it is assumed that the current flow and electric field vectors point along the direction indicated in Fig. 4.13. This will cause the measured resistance, R, to be

$$R = \frac{V_m}{I} = \frac{V_m}{|\vec{\mathbf{J}}|A} = \frac{l}{\sigma A},$$

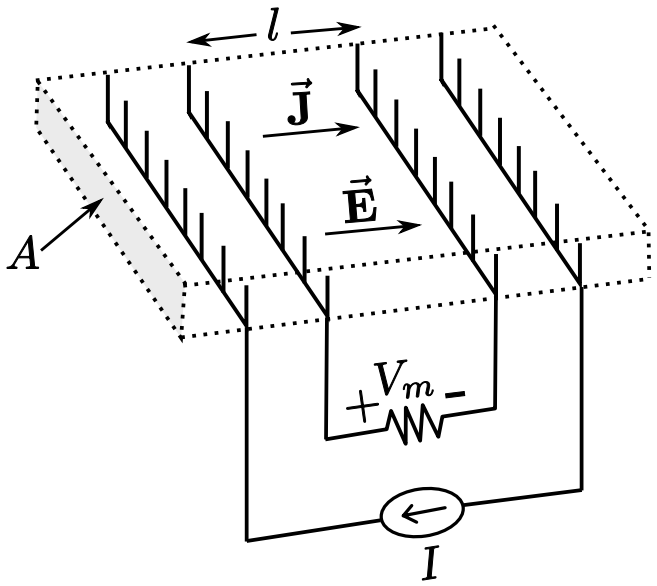

Figure 4.13: A current I is driven through a sample of cross-sectional area A via the outer probes. A high-resistance volt-meter attached to the inner probes draws a small amount of current, creating the voltage drop between the inner probes, V_m. The probes are a distance l apart. It is assumed that the current sampled is sufficiently small that the current between the inner probes is approximately uniform, allowing the conductivity to be taken from the resistance measured.

where I is the total current in the sample, A is the cross-sectional area, and l is the length between the inner probes.

The QuadTech 7600 LCR meter was used to obtain the impedance measurements. This is a four-terminal impedance meter for use at frequencies below 2 MHz. The low-frequency measurements were used to calculate the conductivity of the sample for the six slabs of AN-79 absorber. The meter failed to show a resistance for the four slabs with the least carbon loading. One possible explanation for this could be that the less densely loaded absorbers do not have a direct path for current flow at DC but appear like a series RC circuit, with spaces in the foam acting like capacitors that take on lower impedances at higher frequencies, allowing for loss. The two slabs with the highest carbon density did read a resistance, but this was highly variable and showed a dependence on the method of insertion, the number of times the slab had been measured, as well as the amount of time since insertion. The measured conductivities with their associated variability are shown in the σ_{DC} column in Table 2.

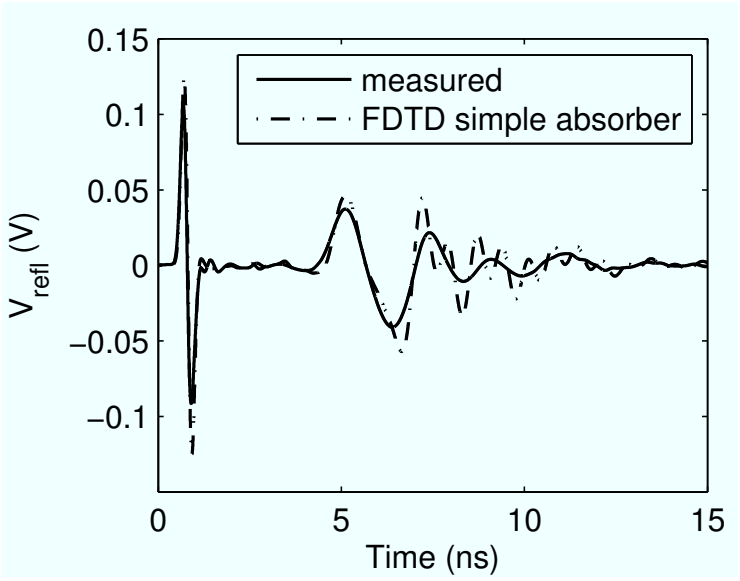

Figure 4.14: V_{refl} measured and modeled for the spiral antenna element using the simple absorber model. Each absorber slab is modeled with $\epsilon_r = 1$ and the conductivity measured using the DC resistance fixture. The poor match between the measurement and the model suggests that measuring the material properties at the frequencies of interest may improve the results.

These conductivities were inserted into the last two slabs in the FDTD model and compared against measurements of the absorber-backed spiral. These comparisons are shown in Fig. 4.14. While the absorber model based on the low-frequency measurements do show the absorbing can's reflection decreased significantly from that seen in Fig. 4.10, the presence of higher frequency ripples in the response that do not appear in the measurement suggest that this model is inaccurate at higher frequencies.

To obtain a better match, the complex ϵ_r values at the frequencies of operation of the spiral GPR system were measured. These dielectric values were measured using a slightly modified version of that described in [51]. In this measurement, a coaxial air-line of known length is partially filled with the sample material and the S-parameters are obtained. A picture of the measurement setup is shown in Fig. 4.15. A GR-900 airline is used, which is sexless to provide for a well-defined calibration plane, and has very large connectors to allow a suitable sample size to be inserted into the line. Pieces of the absorber were cut to fit inside the airline using a computer-controlled milling machine. To assist in making a clean cut, the absorber was frozen in dry ice.

Figure 4.15: Measurement setup for the Baker-Jarvis dielectric measurements. A GR900 airline is used with a cut-out of the absorber placed on the center conductor. Because the calculation of ϵ_r used only requires the S_{21} parameter, the exact distance to the beginning of the sample is not required. Only the length of the sample is needed.

Because a full set of GR-900 calibration standards were not available and the measurements were only required over a limited region of frequencies, a TRL calibration was performed. In this calibration, only a through, reflect (a connector with some reflection coefficient of unity magnitude near ± 1) and line (any delay with a phase length known within $\lambda/4$ at the center frequency of calibration) are required to solve for the S-parameters of the two-port network. The solution has a singularity for certain electrical lengths of the delay line, so this calibration technique can only work over a limited range of frequencies. The details of the TRL calibration are provided in [52, 53].

The calibrated S_{21} measurement was taken over the frequency range from 300 MHz to 1.7 GHz for an air-line partially filled with the absorber sample. A schematic and signal flow diagram of this scenario are shown in Fig. 4.16. Because the length of the air-line is known precisely and the length of the sample can be measured, the reference plane of the S-parameters can be easily moved to the interface of the sample. The old and new reference planes are shown in the upper part of Fig. 4.16. The S_{21} parameter at the interface can be read from the signal flow diagram. For a simple graph, like that in Fig. 4.16, the

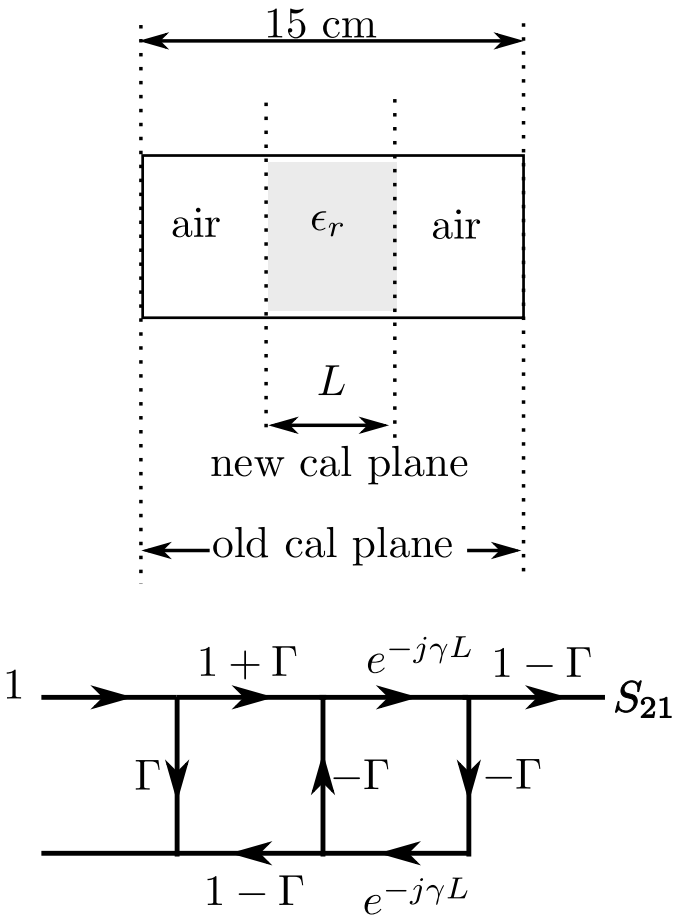

Figure 4.16: Measurement schematic and signal flow diagram for the partially filled coaxial measurement. The S_{21} parameter for the partially filled coax may be used to calculate ϵ_r.

transmission S_{21} can be read by summing the contributions along every path that reaches S_{21}, obtaining

$$\begin{aligned} S_{21} &= (1+\Gamma)e^{-j\gamma L}(1-\Gamma)(1+(\Gamma e^{-j\gamma L})^2+(\Gamma e^{-j\gamma L})^4+...) \\ &= (1-\Gamma^2)e^{-j\gamma L}\Sigma_{k=0}^{\infty}(\Gamma e^{-j\gamma L})^{2k} \\ &= \frac{(1-\Gamma^2)e^{-j\gamma L}}{1-(\Gamma e^{-j\gamma L})^2}, \end{aligned} \tag{4.13}$$

where in the last line the geometric series is replaced with its rational form. With an expression for S_{21}, the assumption is made that $\mu_r = 1$. This allows S_{21} to be written exclusively as a function of ϵ_r by substituting the relations,

$$\Gamma = \frac{1 - \sqrt{\epsilon_r}}{1 + \sqrt{\epsilon_r}}$$
$$\gamma = \frac{\omega\sqrt{\epsilon_r}}{c}, \tag{4.14}$$

into (4.13).

For a particular measured value of S_{21}, denoted here by S'_{21}, ϵ_r can be solved using any nonlinear minimizer by minimizing the function $|S'_{21} - S_{21}(\epsilon_r)|$ over all possible ϵ_r where $S_{21}(\epsilon_r)$ is defined by (4.13) and (4.14). After measuring S'_{21} over the frequencies of interest, ϵ_r was computed for each frequency using the built-in MATLAB implementation of the Nelder-Mead method for minimizing a nonlinear function, fminsearch. The ϵ_r curves showed a significant non-unity dielectric constant that tended to decrease with frequency. In addition, all curves showed some degree of loss. The simplest material model that has these properties is a single-pole Debye model with a conductivity term. This material model has complex ϵ_r as a function of frequency,

$$\epsilon_{\text{guess}}(\omega) = \epsilon_{r,\infty} + \frac{\epsilon_{r,s} - \epsilon_{r,\infty}}{1 + j\omega\tau} + \frac{\sigma}{j\omega\epsilon_0}.$$

Using the same technique as above, the best-fit set of coefficients $\epsilon_{r,s}, \epsilon_{r,\infty}, \tau$, and σ were fit to the calculated ϵ_r values above by minimizing the function,

$$\sum_{\omega} \left|\epsilon_r(\omega) - \epsilon_{\text{guess}}(\omega, \epsilon_{r,s}, \epsilon_{r,\infty}, \tau, \sigma)\right|^2. \tag{4.15}$$

The measured $\epsilon_r(\omega)$ and the best-fit Debye models, ϵ_{guess}, are shown in Fig. 4.17. These plots show the measured ϵ_r data as roughly linear, but have a reasonable fit to the Debye model. The most deviation from the Debye model occurs at the lowest frequencies because there are fewer data points at these frequencies. By weighting the point as a function of frequency, the best-fit curves can be forced to have a better match at the lower frequencies at the expense of the higher frequency match, but this was not preferred. Using the same technique, the curves can also be matched to a purely conductive model and a purely dispersive model, but each match showed a greater residual than the dispersive and conductive model shown. The coefficients for the best-fit Debye models are shown in Table 2. These

Table 2: Measured material parameters for the six foam layers in Eccosorb AN-79. Layers are ordered by increasing carbon filling density. $\epsilon_{r,s}, \epsilon_{r,\infty}$, and τ define the Debye single pole model for the material [36]. σ is the conductivity used in the Debye model, and σ_{DC} is the conductivity measured using the resistance meter.

Layer #	$\epsilon_{r,s}$	$\epsilon_{r,\infty}$	τ (ns)	σ (S/m)	σ_{DC} (S/m)
1	1.29	1.15	0.174	0.0023	-
2	1.50	1.23	0.177	0.0047	-
3	1.56	1.27	0.169	0.0046	-
4	1.83	1.32	0.175	0.011	-
5	2.71	1.47	0.229	0.031	0.003 ± 0.001
6	16.7	3.24	0.294	0.43	0.4 ± 0.1

coefficients were inserted into the FDTD model and compared with the measurement. The scattered voltages for the FDTD model and measurement are shown in Fig. 4.18. This material model showed a substantially better match to the measured data than the original low-frequency measurements.

4.3 Two-antenna System Measurements

With a match to the element model obtained, the second antenna was constructed and placed in the configuration shown on the right in Fig. 4.19. The use of the virtual balun in the two antenna case is essentially the same as in Section 4.1. The antenna system may now be considered to be a four-port network, with a 4×4 matrix of S-parameters that are obtained through a change of reference plane as before. Now the system is re-interpreted as a two-port network with balanced lines like that shown in Fig. 4.20. Using a derivation similar to that shown in Section 4.1, it can be shown that the differential-to-differential response from the first antenna to the second, called here $S_{dd,21}$, is

$$S_{dd,21} = \frac{S_{31} - S_{32} - S_{41} + S_{42}}{2}. \tag{4.16}$$

The monostatic system is not significantly changed by the introduction of a second antenna element. To verify the bistatic performance of the system, measurements were initially taken in free-space. The antenna pair was placed facing a PEC sphere mounted on a foam block attached to a positioner. This configuration is shown in Fig. 4.21. The T antenna was driven with a differentiated Gaussian pulse and the response was recorded

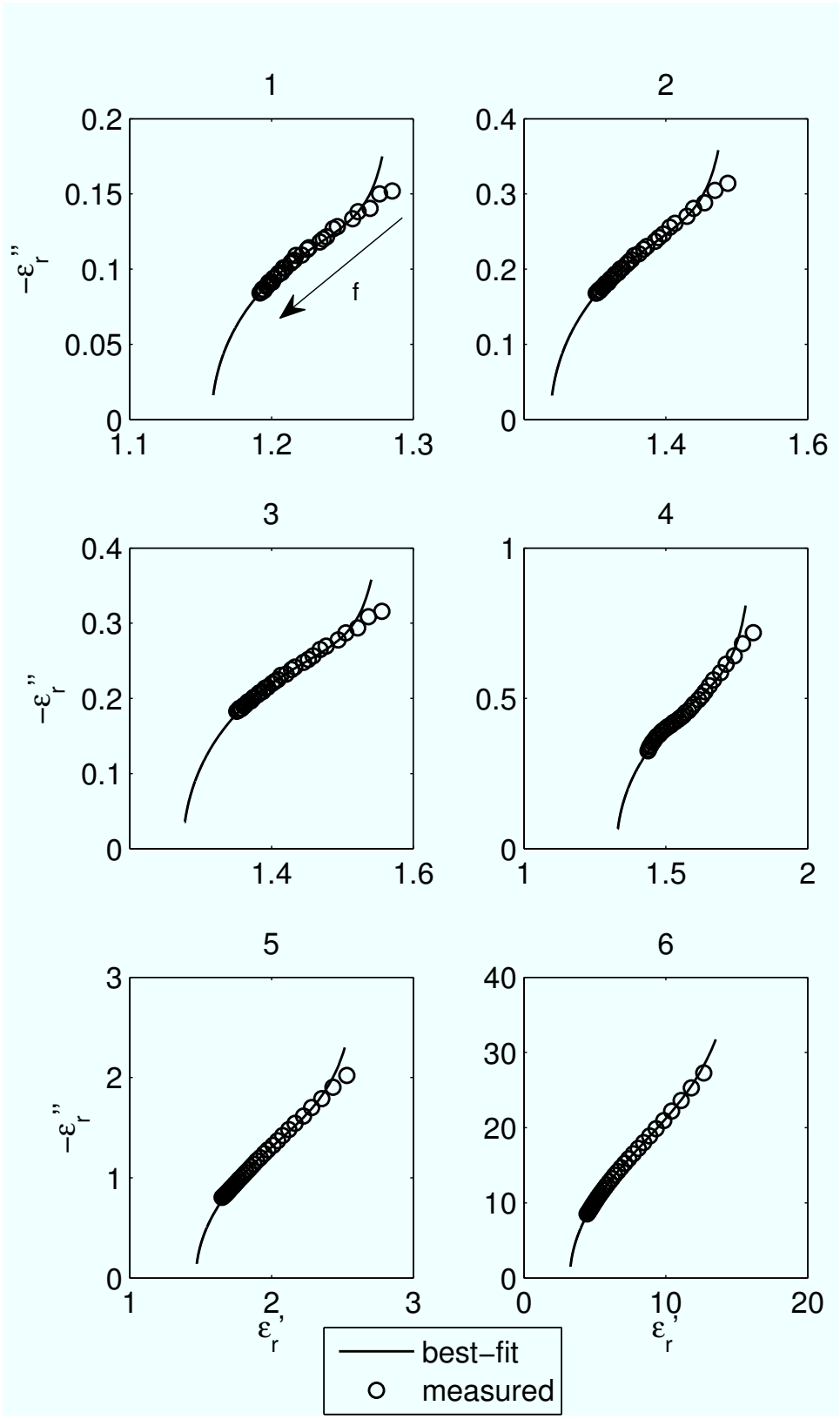

Figure 4.17: Measurements of $\epsilon_r = \epsilon_r' + j\epsilon_r''$, the complex dielectric constant of the carbon-loaded absorbers. The slabs are numbered in order of increasing carbon loading. The arrow labeled f shows the direction of increasing frequency.

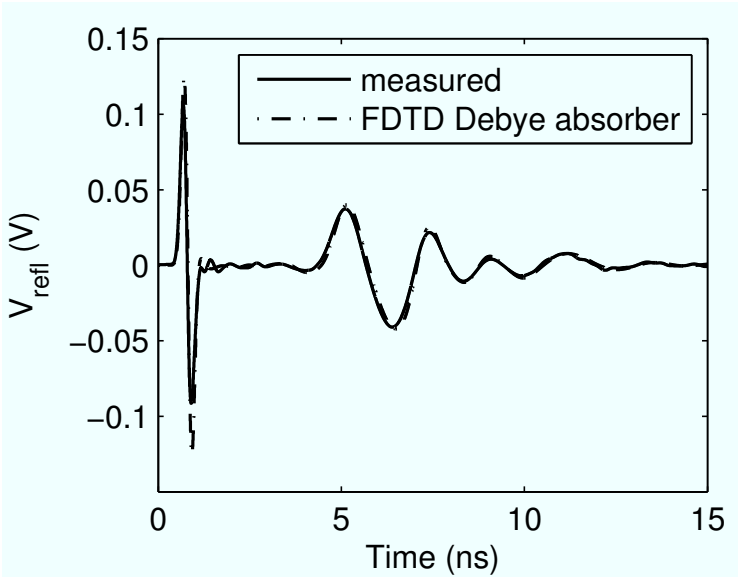

Figure 4.18: V_{refl} measured and modeled for the spiral antenna element with the absorber. The FDTD Debye absorber curve is the predicted response using the best-fit Debye models obtained from the Baker-Jarvis material measurements.

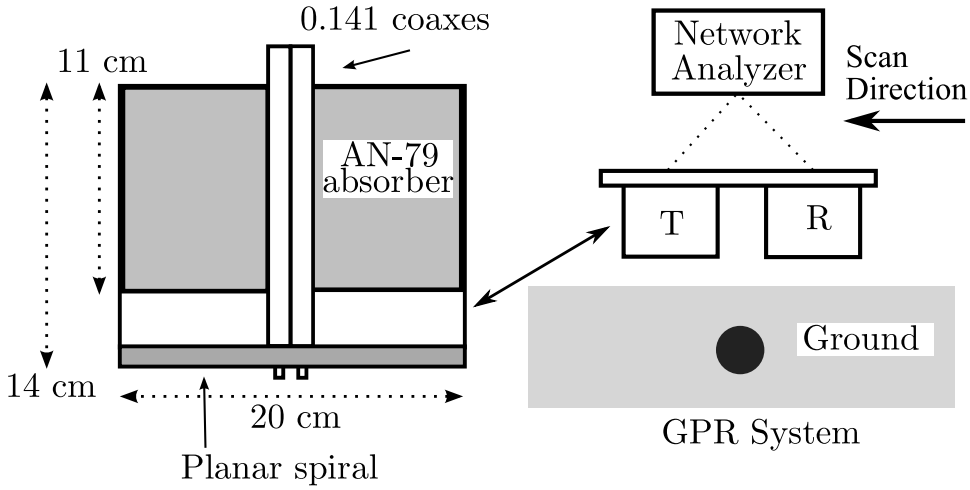

Figure 4.19: Geometry of the spiral element and the bistatic GPR system.

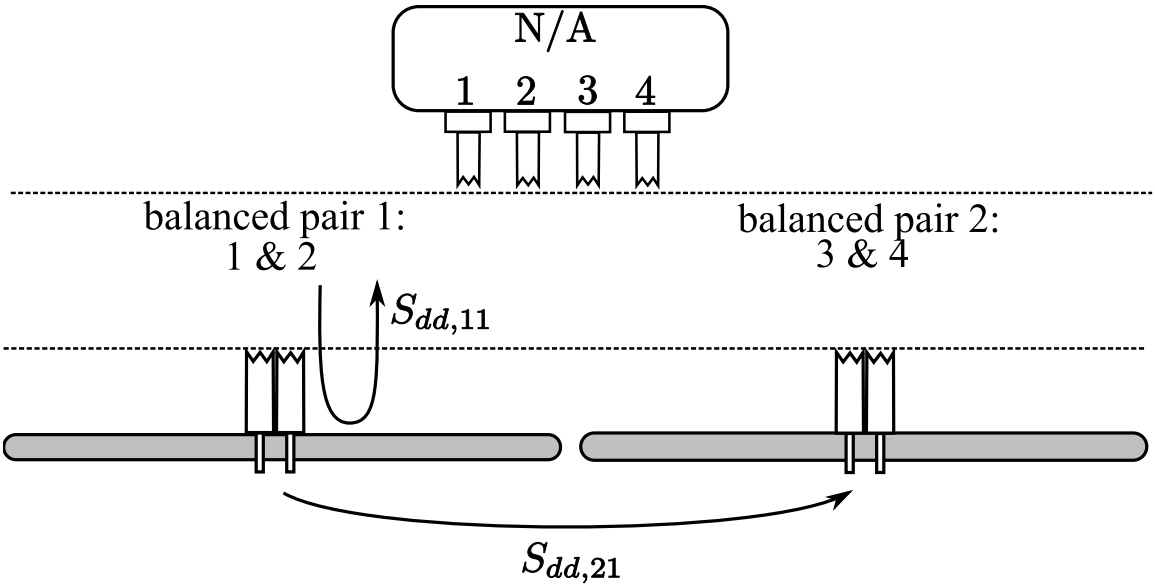

Figure 4.20: The connection of the 4-port network analyzer to the spiral antennas and the equivalent 2-port balanced network parameters, $S_{dd,11}$ and $S_{dd,21}$.

on the R antenna. Spurious reflections and direct coupling between the antennas were removed from the measured signal by repeating the measurement with the sphere absent. The simulated response for the sphere's scattering was obtained using the same technique. The measured and modeled sphere scattering for spheres placed at different distances away from the antenna is shown in Fig. 4.22. An additional delay of around 3 ns can be seen from the 4 cm to 44 cm distance, which correlates well with the expected additional transit time of of 0.8 m/3 $\times$ 10^8 m/s = 2.66 ns. It should be noted that for the 1.5 GHz pulse used, these show a good agreement well into the near-field. Because the GPR system often interacts with the ground in the near-field, this match was considered to be important.

Additional measurements were taken with the sphere at angles off of boresight. The sphere was scanned in the direction indicated in Fig. 4.19. It was maintained at a constant distance of 14 cm from the spiral plane and the scattering from the sphere was recorded as above. The comparison of the measurement and model is shown in Fig. 4.23.

4.4 Modeling the Ground Response

Having verified the model's behavior for scattering in free-space, the direct-coupling and ground bounce was measured for various distances from the ground. To calculate the ground

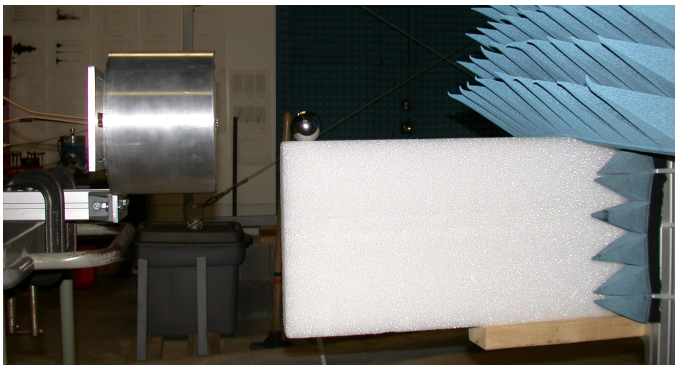

Figure 4.21: The antenna pair faces a foam mount that is attached to a positioner. To remove spurious reflections from the measurement area, the difference between the measurement with the sphere present and absent is recorded.

bounce using the FDTD model, the material properties of the sand used are required. A sample of sand was taken from the sandbox at several depths. The sand was measured by weight before and after allowing its water content to evaporate. Fig. 4.24 shows the measured water content by weight as a function of depth.

Previous material measurements of the complex dielectric constant as a function of frequency were provided by Dr. Waymond Scott. The dielectric curves were fit to a single-pole Debye model with the relaxation constant fixed at that of water, 9 ps, in accord with [54]. The best-fit curves were obtained using the same method described in Section 4.2. The best-fit Debye parameters $\epsilon_{r,s}$ and $\epsilon_{r,\infty}$ for frequencies between DC and 3 GHz are shown in Fig. 4.25. Because the moisture measurements stayed below 4 percent at the deepest level, and the data points showed very little dispersion at the lowest water content levels, a simple dielectric of $\epsilon_r = 2.35$ was chosen to model the sand in the sandbox.

The antenna pair was placed on a 3-D positioner and scanned over a flattened sand-bed. While the sand-bed was made as flat as possible, slight variations in the distance to the surface caused the measurements at a particular point to sometimes vary. To match to the FDTD model, which did not include these variations, the average response over the full extent of the sandbox was used, a region approximately 1 m by 1 m. The FDTD model consisted of the antennas above a flat half-space of dielectric $\epsilon_r = 2.35$. These average values are shown in Fig. 4.26 compared with the FDTD modeled response for distances to the ground ranging from 2 cm to 10 cm. The modeled responses match the averaged

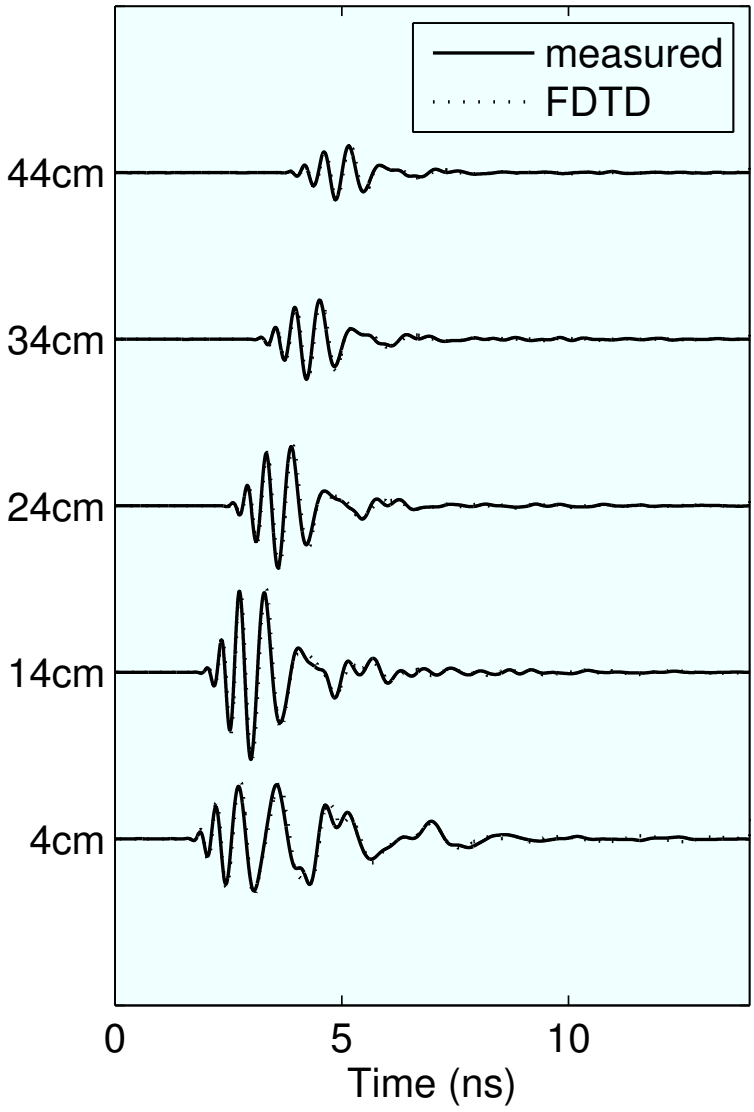

Figure 4.22: Bistatic time-domain reflections from a PEC sphere placed on boresight for the two antenna system, modeled and measured. The sphere distance ranges from 4 cm to 44 cm in 10 cm increments.

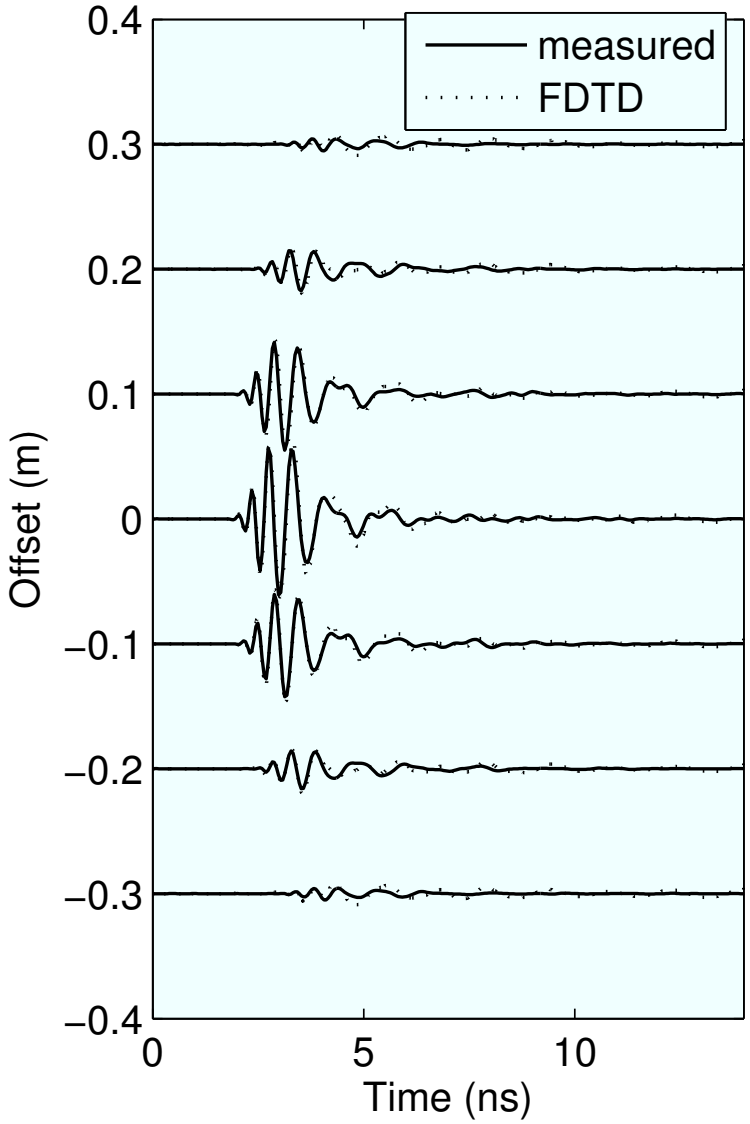

Figure 4.23: Reflections from a PEC sphere 14 cm from the plane of the antennas, as the antennas are scanned across, modeled and measured.

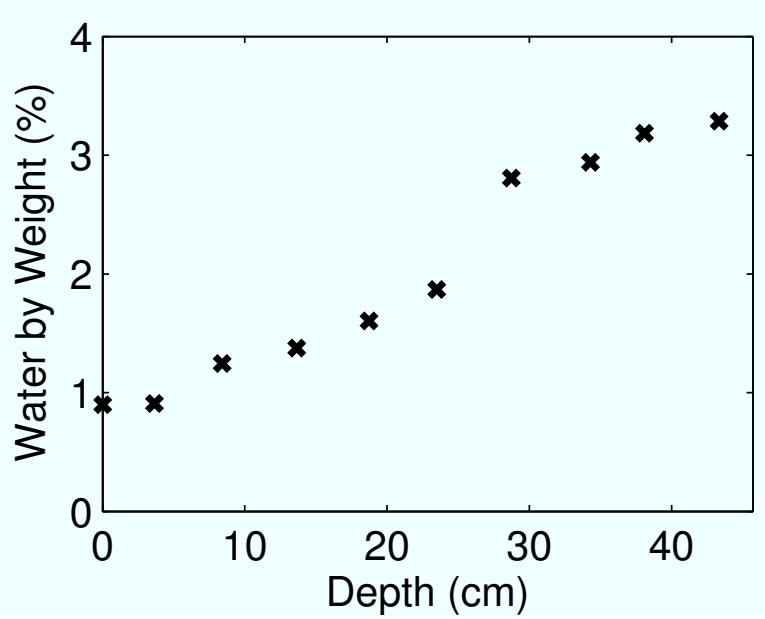

Figure 4.24: Water content in the sandbox as a function of depth. The measurement was obtained by taking sand samples at different depths in the sandbox. Samples were weighed before and after the water content had evaporated. The percentage of the original weight consisting of water is shown.

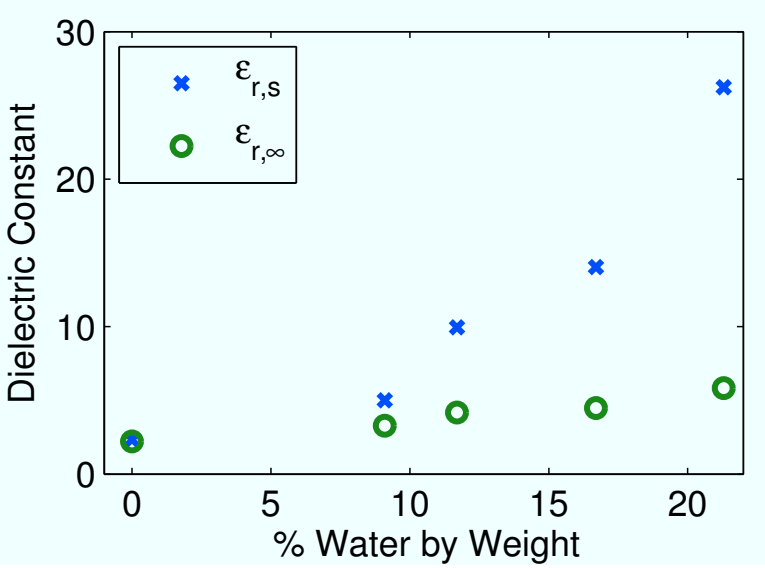

Figure 4.25: Previous dielectric constant measurements of the sand in the sandbox as a function of water content by weight were taken and matched to a single-pole Debye model. The data points show that dry sand is essentially non-dispersive but wet sand becomes very dispersive.

measurements fairly well.

4.5 Full System Modeling

Finally, the measurement and model were compared for a complete GPR interaction. In the GPR work, the antenna's excitation is changed to make the responses easier to interpret. As may be seen in Fig. 4.18, much of the low-frequency energy inserted into the spiral is reflected back to the terminals with a significant delay. The ringing caused by these low frequencies can distort the response to a scatterer and can be difficult to correct for. Therefore, a slightly higher-frequency pulse was used in the full system measurements. Here, a modulated Gaussian pulse with a center frequency of 1.4 GHz and frequency content from about 1 GHz to 1.8 GHz was used. The pulse is shown in Fig. 4.27. The functional form is given by

$$V_{inc}(t) = \cos\left(2\pi f_{mod}(t - t_d)\right) e^{-\left(\frac{t-t_d}{\tau}\right)^2} \text{ V} \tag{4.17}$$

$$f_{mod} = 1.4 \text{ GHz}$$

$$\tau = 0.5 \text{ ns}$$

$$t_d = 2 \text{ ns}.$$

A metal sphere with a radius of 6 cm was buried in the sand below the bistatic pair. A picture of the situation is shown in Fig. 4.28. After burial, the ground was leveled to the extent possible. The measured distance to the ground from the spiral antenna plane was 4.5 ± 0.5 cm and the measured distance from the ground to the center of the sphere was 21.7 ± 0.5 cm, with the error in the measurement due to variations in the height of the ground. Because of uncertainties in the geometry, the model was run for a number of different depths and heights to see the best match. The match occurs for a height of 4.5 cm and a depth of 22.8 cm, which is just beyond the stated tolerance for the ground measurement. The time response directly above the sphere is shown in Fig. 4.29 and as a function of position in Fig. 4.30. It can be seen that the features of the response agree fairly well.

It may be noted that in all of the verification measurements for the system shown, only

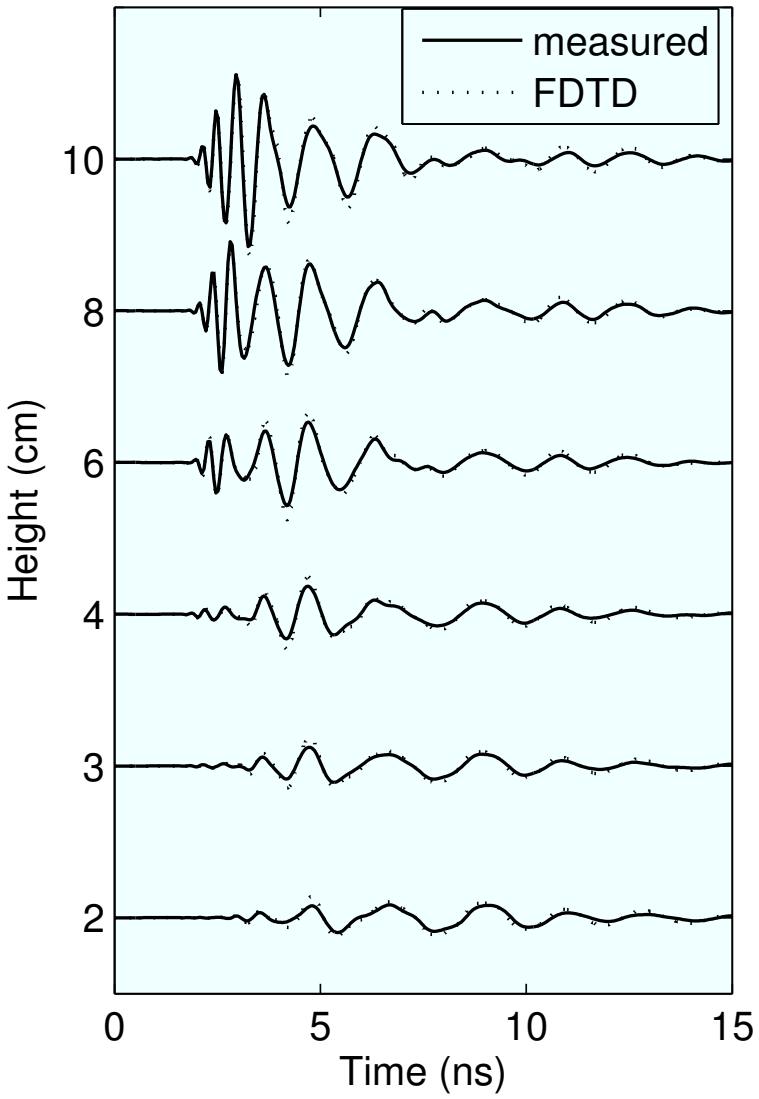

Figure 4.26: Reflection from the ground on the receive antenna for various heights from the ground, modeled and measured.

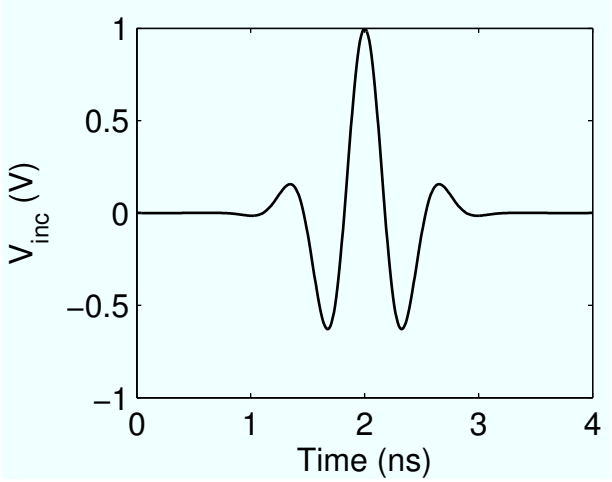

Figure 4.27: Modulated Gaussian pulse used for excitation of the spiral in this work.

the bistatic data is used even though the monostatic data is also recorded. This is because even with some of the lower frequencies removed, the monostatic data contains a very large reflection from the antennas that overwhelms the scattering response from objects in the vicinity of the antennas. When looking at the monostatic data, it is useful to take a training segment of the data where there are no known scatterers and average over that region to obtain a base value. The difference from this base value at each scan position will then show scatterers in the ground more clearly. Using the same configuration as that shown in Fig. 4.30, Fig. 4.31 shows the monostatic response, modeled and measured, where the average value of the region between $x = 30$ cm and $x = 40$ cm has been used to train the response.

The clearest difference seen in Fig. 4.31 is that the monostatic response occurs almost 3 ns later than the bistatic response. The reason for this difference is discussed in Chapter 5. In addition, it can be seen that the region where the training data was taken has a significantly lower noise signal than near the target. This is an artifact of the training window used and it may be reduced by using a larger training window. However, larger windows do not significantly change the response near the scattered signal from the sphere.

Figure 4.28: The bistatic pair is attached to a positioner facing toward the sand. A 6 cm radius metal sphere is placed in the ground. After burial, the sphere is 22 ± 0.5 cm below the ground surface.

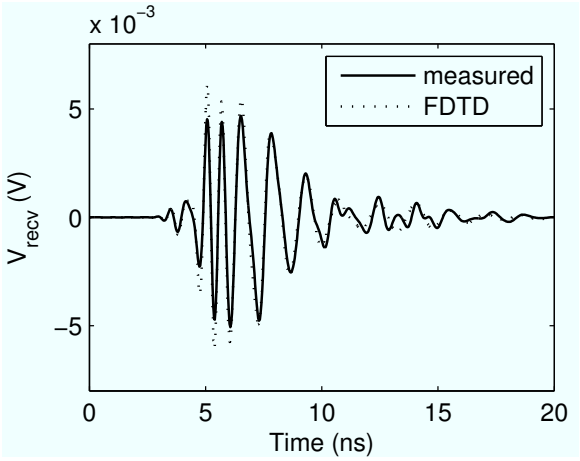

Figure 4.29: The bistatic time-domain response when the two antennas are directly above the sphere.

4.6 Dispersion Removal

The radiated pulse, (4.17), used in Fig. 4.31 and Fig. 4.30, extends over about 2 ns. Because the responses seen in the figures extend over 5 ns for the bistatic and 7 ns for the monostatic, the process of radiating the pulse must also disperse it. The dispersion in a spiral antenna occurs because different frequencies radiate from different locations on the spiral at different times. The process of dispersion removal takes account of the delays in each frequency component caused by this fact and removes the delays for each frequency.

The delay applied to each frequency radiated from the spiral can be estimated using the transmission-line model of operation discussed in Section 1.4. There, the antenna is modeled as a transmission-line structure that only radiates in roughly circular sections of the spiral arms that satisfy the radiation condition (1.11). In this section, this simple model of the spiral's radiation is used to obtain the dispersion properties of the equiangular spiral. The argument is not substantially different from that proposed for the conical spiral in [55]. It is found that this model does not predict the exact dispersion relation of the antenna, but does provide the functional form of the dispersion relation, which will allow a dispersion-removal filter to be designed for the spiral used in this work.

In Section 1.4, the equiangular spiral is modeled as two wires formed into equiangular spiral curves. The first arm takes the polar-coordinate form, $r(\theta) = e^{a\theta}$ and the second

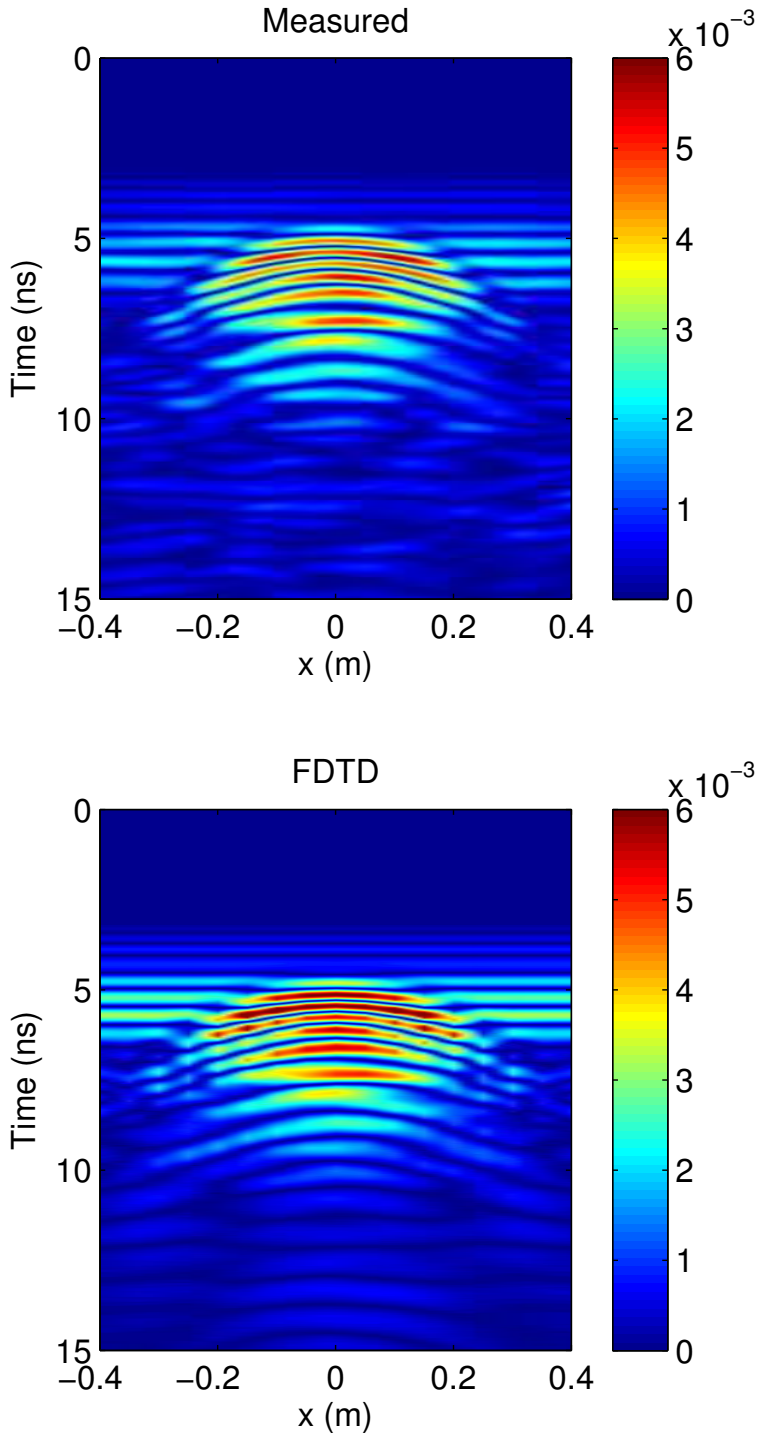

Figure 4.30: The bistatic time-domain response of the sphere as a function of the position of the antennas. At $x = 0$ the antennas are directly above the sphere.

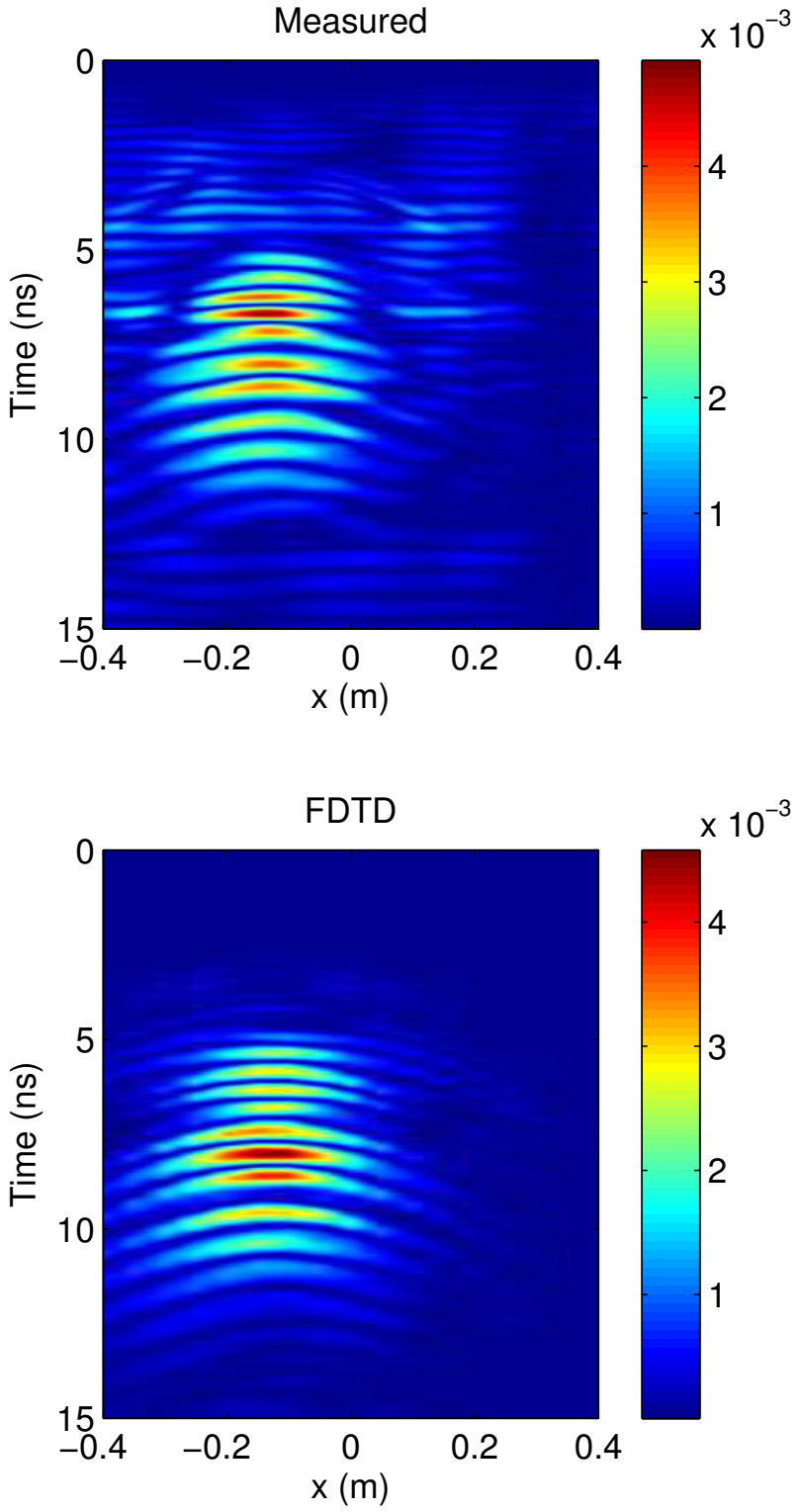

Figure 4.31: The monostatic time-domain response of the sphere as a function of the position of the antennas. At $x = 0$ the antennas are directly above the sphere.

is the same curve but rotated π radians. The radiation from the spiral occurs when the length of one arc of the spiral passing through π radians is equal to $\lambda/2$ for the frequency of interest. This condition is (1.11). In this section, the spiral is the same as that used in Section 1.4, except the polar coordinate curve used is $r(\theta) = R_{in}e^{a\theta}$. The equivalent radiation condition to (1.12) is then

$$\theta_1 = \frac{1}{a}\log\left(\frac{\lambda}{2R_{in}(\exp(a\pi)-1)\sqrt{1+a^{-2}}}\right), \tag{4.18}$$

or equivalently,

$$r(\theta_1) = \frac{\lambda}{2(e^{a\pi}-1)\sqrt{1+a^{-2}}}. \tag{4.19}$$

Proceeding as in (1.8), the distance traveled along a spiral with wrapping parameter a between the radii $r(\theta)$ and R_{in} may be calculated to be

$$L(\theta) = \sqrt{1+a^{-2}}\,(r(\theta) - R_{in})\,. \tag{4.20}$$

For a given angular frequency, ω, the total path length traveled to the active region, $p(\omega)$ is then the sum of the path length along the bow-tie antenna and the path-length along the spiral arms,

$$p(\omega) = R_{in} + \sqrt{1+a^{-2}}\,(r(\theta_1) - R_{in}) \tag{4.21}$$

$$= \frac{\lambda(\omega)}{2\,(e^{a\pi}-1)} + R_{in}\left(1 - \sqrt{1+a^{-2}}\right). \tag{4.22}$$

Suppose that a narrow-band pulse with frequency content near ω is fed onto the arms of the spiral. Assuming that the substrate has little effect on the velocity of the pulse, one may calculate the time-delay for the pulse to leave the feed and reach the active region using the speed of light, c,

$$t_d(\omega) = \frac{\pi}{\omega\,(e^{a\pi}-1)} + \frac{R_{in}}{c}\left(1 - \sqrt{1+a^{-2}}\right). \tag{4.23}$$

Because the relationship between the radiation from the spiral and the voltage fed onto the spiral is linear and time-invariant, ignoring the vector nature of the radiated field, one can describe this relation by a transfer function, $H(\omega) = |H(\omega)|e^{j\Psi(\omega)}$.

Suppose a narrow-band pulse with Fourier transform $F(\omega)$ centered around some frequency ω_0 were applied to this system, then the response out of the system would be

$$|H(\omega)|e^{j\Psi(\omega)}F(\omega).$$

Because F is narrow-band around ω_0, the transfer function's phase relationship may be approximated fairly well with a first-order Taylor expansion,

$$|H(\omega_0)|e^{j\frac{\partial\Psi}{\partial\omega}\big|_{\omega_0}(\omega-\omega_0)+\Psi(\omega_0)}F(\omega). \tag{4.24}$$

This transfer function consists of multiplication by a complex constant and a time delay of $-\frac{\partial\Psi}{\partial\omega}\,|_{\omega_0}$. This derivative of the phase is typically called the transfer function's group delay at ω_0. By the argument given above, the effect of inserting a narrow-band pulse onto the spiral would be the radiation of that pulse with a time-delay described by (4.23). By comparing (4.23) and (4.24) one obtains a constraint on the derivative of the phase,

$$-\frac{\partial\Psi}{\partial\omega} = \frac{\pi}{\omega\left(e^{a\pi}-1\right)} + \frac{R_{in}}{c}\left(1-\sqrt{1+a^{-2}}\right). \tag{4.25}$$

The stated delay goes to infinity at DC. To correct this, the model is only applied over the operating region of the antenna, defined here to be frequencies where the active region fits on the spiral portion of the antenna,

$$\frac{\pi c}{R_{out}(e^{a\pi}-1)\sqrt{1+a^{-2}}} < \omega < \frac{\pi c}{R_{in}(e^{a\pi}-1)\sqrt{1+a^{-2}}}. \tag{4.26}$$

For frequencies outside of this region, the delay is kept constant and is set to be continuous with the delay in the operating region,

$$-\left.\frac{\partial\Psi}{\partial\omega}\right|_{\omega_0} = \begin{cases} \frac{(R_{out}-R_{in})\sqrt{1+a^{-2}}}{c} + \frac{R_{in}}{c} & \omega < \frac{\pi c}{R_{out}(e^{a\pi}-1)\sqrt{1+a^{-2}}} \\ \frac{R_{in}}{c} & \omega > \frac{\pi c}{R_{in}(e^{a\pi}-1)\sqrt{1+a^{-2}}} \\ \frac{\pi}{\omega(e^{a\pi}-1)} + \frac{R_{in}}{c}\left(1-\sqrt{1+a^{-2}}\right) & \text{otherwise.} \end{cases} \tag{4.27}$$

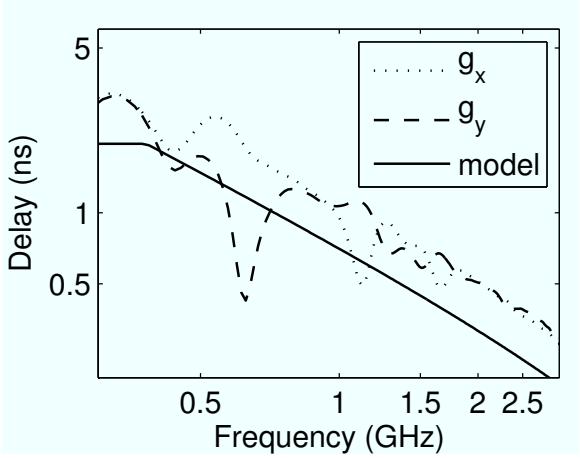

Figure 4.32: The group delay of the equiangular spiral on boresight for the x and y components. Here only the spiral element is modeled. No can or absorber is included. The delay prediction using the transmission-line model for the spiral is also shown.

This model can be verified by comparing it with the dispersion relation obtained using the FDTD model for the spiral antenna developed in this work. If the near-to-far-field transformer is applied to the boresight direction of the antenna, the transfer function between the voltage inserted onto the feed line and the far-field radiation in this direction can be obtained. In Fig. 4.32, the group delay of this transfer function is shown compared with the group delay predicted by the simple model proposed. For simplicity, the FDTD model did not include the spiral absorbing can. The two components, g_x and g_y, are the group delays for the E_x and E_y far-field components respectively, where the coordinate system is defined in Fig. 1.2. The "model" curve is the predicted group delay determined by (4.27).

While the simple model shows the same functional form as the dispersion relation obtained from the FDTD simulation, the match appears to be off by a fixed constant. This constant could be attributed to the slowing of the wave by the dielectric substrate, or any of the numerous approximations made in the simple model, such as the infinitesimally thin arms, the unrealistic assumption that the current travels exactly along a spiral path, or that all of the radiation for a given frequency is assumed to radiate simultaneously at the first active region.

The close similarity in the functional form seen in Fig. 4.32 does suggest that a very

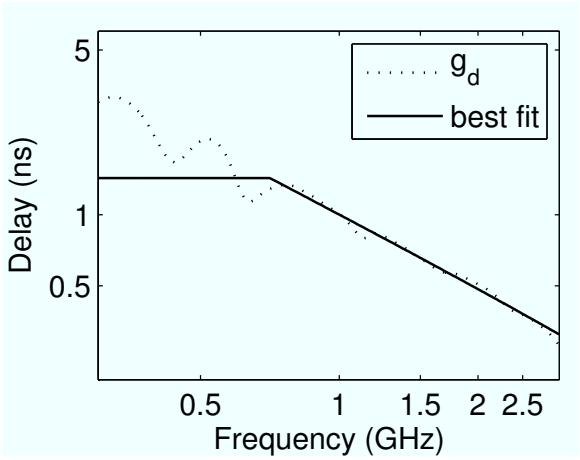

Figure 4.33: The averaged group delay of the equiangular spiral's x and y components with the best-fit curve of the form $a/\omega + b$. The best fit for the spiral used in this work was obtained for $a = 6.51, b = 34.5$ ps.

strong model could be obtained by fitting the dispersion curves obtained to the same functional form used in (4.27), namely $a/\omega + b$ for some real constants a and b. This best-fit can be calculated using a linear regression scheme. The group delays for each component above, g_x and g_y, are averaged to obtain one function for fitting, g_d. A linear regression is then applied to the variables g_d and $1/\omega$ over the frequencies of the operating band. The best-fit curve is shown in Fig. 4.33 along with the averaged group delay, g_d. The best-fit for the spiral used in the system was obtained at $a = 6.51$ and $b = 34.5$ ps.

As stated above, the phase of the transfer function as a function of frequency, $\Psi(\omega)$, relates to the group delay, $g_d(\omega)$ by

$$-\frac{\partial \Psi}{\partial \omega} = g_d(\omega). \tag{4.28}$$

Having obtained a good approximation to $g_d(\omega)$, the phase may be obtained within a constant by integration,

$$\Psi(\omega) - \Psi(\omega_{ref}) = \int_{\omega_{ref}}^{\omega} g_d(\omega) d\omega. \tag{4.29}$$

Because the exact transfer function is known as a function of frequency from the FDTD model, the unknown phase, $\Psi(\omega_{ref})$, may be obtained from any particular reference frequency. For this model, the phase was chosen at 1.5 GHz and taken from the boresight radiation's E_x component. With a reasonable model for the dispersion of the antenna,

the pulse radiated can be modified by passing the radiation through an all-pass filter that removes the delays introduced by the spiral. To remove the dispersion from the radiated pulse, the filter used is

$$H(\omega) = e^{-j\Psi(\omega)}. \tag{4.30}$$

To verify the proper functioning of the dispersion filter, the $\hat{\theta}$ and $\hat{\phi}$ components of the radiated field of the spiral antenna were computed using the near-to-far-field transformer. Here θ and ϕ are the standard spherical coordinates with $\theta = 0$ pointing along the z axis and $\hat{\theta}$ and $\hat{\phi}$ defined at $\theta = 0$ to be $\hat{\mathbf{x}}$ and $\hat{\mathbf{y}}$ respectively. The radiated pulses along several angles of θ off of bore-sight are shown in Fig. 4.34 and 4.35 along with the same signals passed through the filter.

The two most obvious effects of the filter are its time shift, and its phase shift. The time shift simply removes any delays during radiation from the spiral. The phase shift is caused by the choice of ω_{ref} used in 4.29. The effect of the phase shift can be observed by noting that the processed E_θ curve is similar to the transmitted pulse while the processed E_ϕ curve is similar to the unprocessed E_θ curve. Ignoring the phase shift effect, the most important feature is the increased symmetry of the processed pulse. The processed E_θ curve has a nearly even symmetry about its center at 2 ns while the processed E_ϕ curve has a nearly odd symmetry about its center at 2 ns. The original curves did not possess this symmetry with later parts of the pulses being slightly different shapes than earlier ones. This increased symmetry is caused by the removal of dispersion from the processed signal. Multiple angles in addition to boresight are shown in each figure and it can be seen that the spiral shows the same dispersion off of boresight.

While the effects of the dispersion on the radiated field are not substantial, the GPR data obtained has dispersion from both transmission and reception, doubling the amount of delay for each frequency component. To process the GPR data for dispersion, the filter, (4.30), is applied twice. In Fig. 4.36 and 4.37, the results of filtering the measured bistatic and monostatic responses are shown for the sphere in Fig. 4.28. The 2 ns delay present in

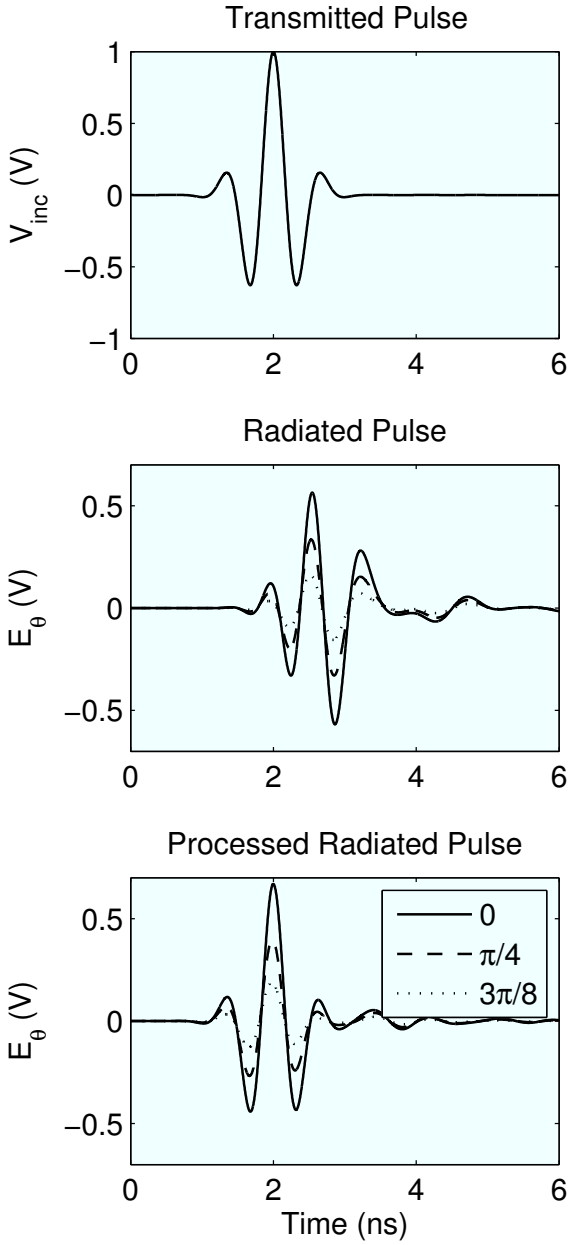

Figure 4.34: Comparisons of the radiated E_θ pulse for three values of θ before and after dispersion processing. The field at some observer located a distance r from the antennas in the given direction is $E_\theta\left(t - r/c\right)/r$. The processed pulse shows greater symmetry about its center than the original.

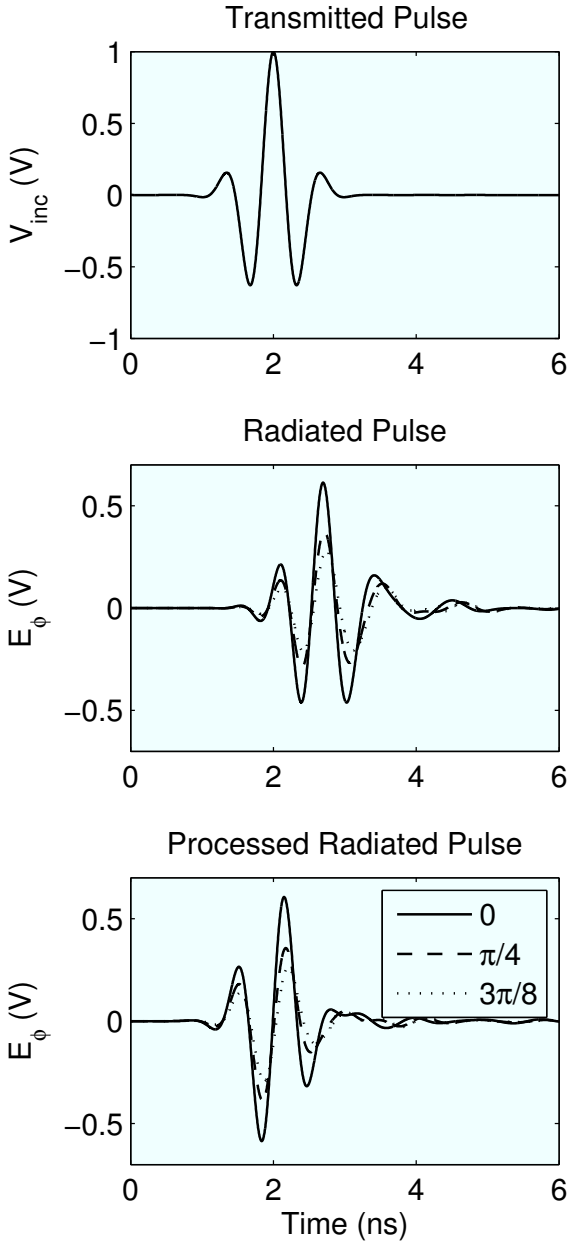

Figure 4.35: Comparisons of the radiated E_ϕ pulse for three values of θ before and after dispersion processing. The field at some observer located a distance r from the antennas in the given direction is $E_\phi\left(t - r/c\right)/r$. The processed pulse shows greater symmetry about its center than the original.

the modulated Gaussian pulse has been removed from the processed signals in order to make them more easily related to the distance of the scatterer. Looking at Fig. 4.37 in particular, one sees a significant effect from the dispersion removal. The monostatic response shown in Fig. 4.36 does not show a significant difference, and the reason for this is discussed in a later section.

4.7 Scatterer Symmetry

When the spiral antenna is proposed for use in a GPR system, it is often chosen because of its natural circular polarization (CP) on boresight [28, 32]. Possible advantages of CP in a GPR system are reported to be that the response to a linear scatterer is independent of its orientation, or that a CP wave's reflection off of the ground is rejected by an antenna with the same polarization properties. In [29], it is noted that this second property could be less useful in GPR land mine detection, since the symmetry of the mine would suggest that a CP wave will reject it. Since the polarization of a wave is defined in the far-field where the radiation has a clearly defined propagation vector, an interesting question is to what extent any reasoning about CP makes sense in the GPR problem, where interactions with scatterers typically take place in the near-field.

The spirals used in this work are driven with a four-port network analyzer. Because of this, the measurement process inherently takes both monostatic measurements with the transmit antenna and bistatic measurements with the antenna pair at the same time. Since the antennas are chosen with opposite polarizations, any scatterer that is rejected in the monostatic response because of its symmetry will appear in the bistatic response. This fact will allow the rejection that is said to be related to CP to be studied.

In this section, the argument that antennas that radiate CP do not detect symmetric scatterers is reviewed in the far-field where the statement is well-defined. This argument is a simplified version of that presented in Baum [56]. After establishing that symmetry could be important to understanding the GPR system, this chapter will conclude with a verification that the FDTD model properly predicts the response from both symmetric and asymmetric scatterers.

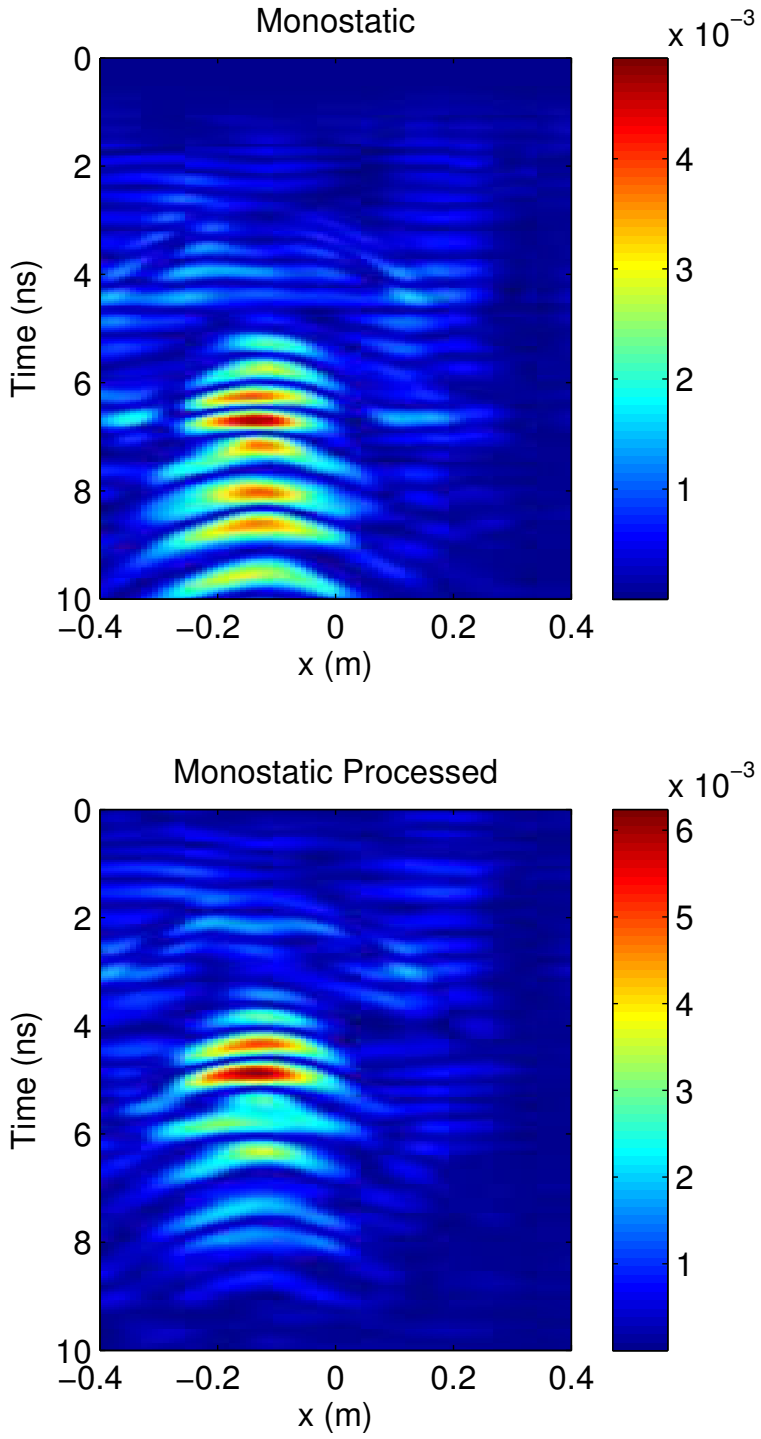

Figure 4.36: Comparison of the monostatic scattered response with mean removed of the 6 cm sphere with and without the application of the dispersion filter.

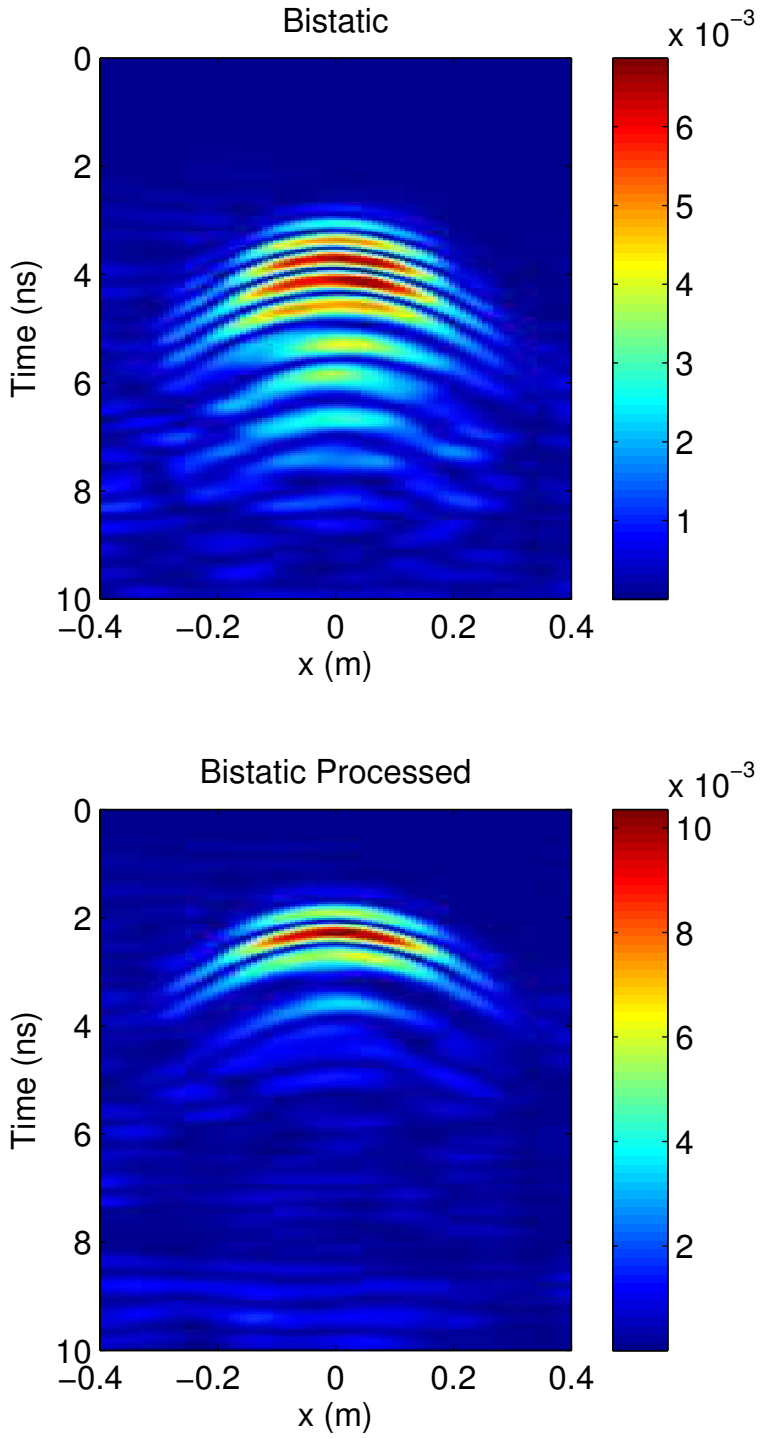

Figure 4.37: Comparison of the bistatic scattered response with mean removed of the 6 cm sphere with and without the application of the dispersion filter.

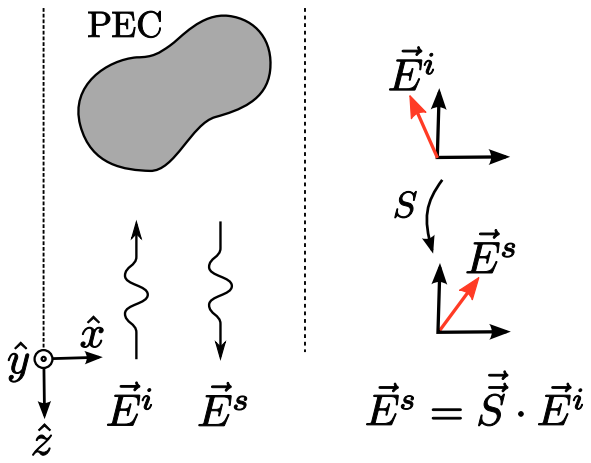

Figure 4.38: Incident and back-scattered plane-waves are shown in a far-field interaction with a PEC scatterer. The coordinate system is chosen so that the polarization vectors are both in the xy-plane. The two are related linearly by the matrix, S.

Consider a monostatic radar system, with a transmitting antenna illuminating a scatterer in the far-field. Near the scatterer, the radiation is approximately a plane-wave. Since the radar system is also in the far-field of the scattered radiation, the back-scattering is also a plane-wave. This system can be thought of as that shown in Fig. 4.38. Setting the coordinate system so that the incident plane-wave propagates in the direction $-\hat{\mathbf{z}}$, the plane-wave has a polarization vector in the xy-plane, $\vec{\mathbf{E}}^i$. The scattered plane-wave will propagate in the direction $\hat{\mathbf{z}}$ and will have a polarization vector in the xy-plane, $\vec{\mathbf{E}}^s$.

Because the relationship between the incident and scattered polarizations is linear, it can be expressed by a matrix, S

$$\begin{pmatrix} E_x^s \\ E_y^s \end{pmatrix} = \begin{pmatrix} S_{xx} & S_{xy} \\ S_{yx} & S_{yy} \end{pmatrix} \begin{pmatrix} E_x^i \\ E_y^i \end{pmatrix}. \tag{4.31}$$

Consider the same scattering problem except the target has been rotated by θ degrees in the xy-plane. This situation will have a scattering matrix S'. Since the entire geometry of the solution consists of the incident field and the scatterer, rotating the incident field and scatterer by θ degrees, the scattered field must be the same but also rotated by θ degrees.. If R_θ is the rotation matrix for a θ degree rotation, this statement can be written

$$S' R_\theta \vec{\mathbf{E}}^i = R_\theta \vec{\mathbf{E}}^s = R_\theta S \vec{\mathbf{E}}^i. \tag{4.32}$$

Since the statement is true for an arbitrary vector $\vec{\mathbf{E}}^i$, the prime and unprimed matrices are related by

$$S'R_\theta = R_\theta S. \tag{4.33}$$

Now suppose the scatterer has a rotational symmetry in the xy-plane, meaning the scatterer is equal to a version of itself rotated by θ about the z axis. This type of symmetry means the S and S' matrices must be equal,

$$SR_\theta = R_\theta S. \tag{4.34}$$

The fact that these two matrices commute will actually restrict the form of the S matrix a good deal. Recalling the form of a counter-clockwise rotation matrix for angle θ,

$$R_\theta = \begin{pmatrix} \cos(\theta) & -\sin(\theta) \\ \sin(\theta) & \cos(\theta) \end{pmatrix}. \tag{4.35}$$

Inserting this into (4.34), one obtains

$$\begin{aligned} SR_\theta &= \begin{pmatrix} \cos(\theta)S_{xx} + \sin(\theta)S_{xy} & -\sin(\theta)S_{xx} + \cos(\theta)S_{xy} \\ \cos(\theta)S_{yx} + \sin(\theta)S_{yy} & -\sin(\theta)S_{yx} + \cos(\theta)S_{yy} \end{pmatrix} \\ &= \cos(\theta)\begin{pmatrix} S_{xx} & S_{xy} \\ S_{yx} & S_{yy} \end{pmatrix} + \sin(\theta)\begin{pmatrix} S_{xy} & -S_{xx} \\ S_{yy} & -S_{yx} \end{pmatrix} \end{aligned} \tag{4.36}$$

$$\begin{aligned} R_\theta S &= \begin{pmatrix} \cos(\theta)S_{xx} - \sin(\theta)S_{yx} & \cos(\theta)S_{xy} - \sin(\theta)S_{yy} \\ \sin(\theta)S_{xx} + \cos(\theta)S_{yx} & \sin(\theta)S_{xy} + \cos(\theta)S_{yy} \end{pmatrix} \\ &= \cos(\theta)\begin{pmatrix} S_{xx} & S_{xy} \\ S_{yx} & S_{yy} \end{pmatrix} + \sin(\theta)\begin{pmatrix} -S_{yx} & -S_{yy} \\ S_{xx} & S_{xy} \end{pmatrix}. \end{aligned} \tag{4.37}$$

Equating (4.36) with (4.37), subtracting the identical $\cos(\theta)$ terms from each side, and assuming $\sin(\theta) \neq 0$, one obtains

$$\begin{pmatrix} S_{xy} & -S_{xx} \\ S_{yy} & -S_{yx} \end{pmatrix} = \begin{pmatrix} -S_{yx} & -S_{yy} \\ S_{xx} & S_{xy} \end{pmatrix}. \tag{4.38}$$

The equality of these matrices gives that diagonal terms in the S matrix are equal and off-diagonal terms are opposites. A general scatterer that stays the same under an arbitrary θ degree rotation in the xy-plane will have a scattering matrix of the form

$$S = \begin{pmatrix} S_{||} & S_{\perp} \\ -S_{\perp} & S_{||} \end{pmatrix}. \tag{4.39}$$

When a circularly polarized wave is incident on a scatterer of this type, the response is given by

$$S \begin{pmatrix} 1 \\ j \end{pmatrix} = (S_{||} + jS_{\perp}) \begin{pmatrix} 1 \\ j \end{pmatrix}. \tag{4.40}$$

In words, the circulation direction of the electric field vector is unchanged. Since the incident wave and scattered waves have opposite signed propagation vectors, the handedness of the wave has switched from initially LHCP to RHCP. Since a CP antenna will accept only one handedness and reject the other, symmetric scatterers should not have a monostatic response on boresight. It should be noted that the type of symmetry referred to here is much more general than a continuous symmetry about an axis. A shape that is invariant under a rotation of some particular non-zero angle $-\pi < \theta < \pi$ can have any of the shapes shown in Fig. 4.39. This argument would hold for a symmetric scatterer in a half-space of dielectric as well, but is not necessarily valid outside of the far-field assumptions made. The assumptions made above would apply to a GPR system if the antenna was in the far-field of the ground. This is not true for the GPR system in this work, but it is shown in this section and the following chapter that the monostatic radar can reject a symmetric scatterer well into the near-field under the proper conditions.

4.8 GPR Responses for PEC Scatterers with Different Shapes

Having established that symmetry may affect the radar system, it is shown that the effects are properly modeled in the FDTD simulation. Three PEC scatterers are chosen, shown in Fig. 4.40. A symmetric scatterer, a sphere, an asymmetric scatterer, a pipe, and a "nearly" symmetric scatterer, an oblong shell are used. It can be seen that the responses are more complex than is suggested by the far-field symmetry arguments, but a full analysis

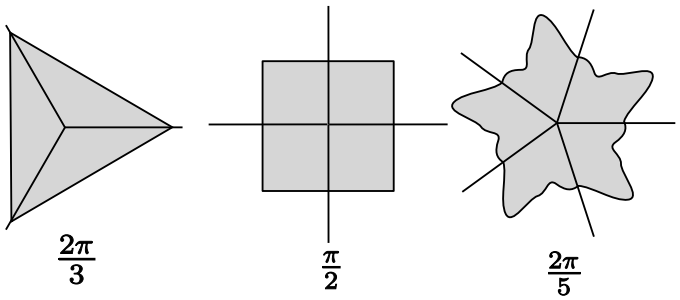

Figure 4.39: Shapes with rotational symmetry in the plane. Each of these could be extruded into the third dimension. The profile of the extrusion is also not important.

of the spiral-GPR system's ability to reject symmetric scatterers is postponed until the next chapter.

First, the sphere responses are shown again in Fig. 4.41, here side by side with the model. It can be seen that the bistatic response looks like a fairly sharp hyperbola that occurs at 2.5 ns. The monostatic response shows no sharp hyperbola at 2.5 ns, but does show a long ringing response that has a magnitude only half as large as the bistatic response. The cause of this delayed ringing is shown in the next chapter to be the spiral antenna itself, and not the scatterer. For the purposes of this verification chapter, it should simply be noted that both the bistatic and monostatic responses show a reasonably good agreement with the FDTD model.

The pipe shown in Fig. 4.40 was laid perpendicular to the direction of the scan at a depth of 20.5 cm. A scan was taken using the same method shown for the sphere. The monostatic and bistatic scans are shown in Fig. 4.42. This shows the expected response with both the bistatic and monostatic responses appearing as a thin hyperbola near 2.5 ns.

The 155 mm artillery shell shown in Fig. 4.40 was buried in the sand at a depth of 20.5 cm with its length placed parallel to the direction of the scan. A surface mesh for the shell was provided by ERDC and inserted into the FDTD grid. The scan lane measured and modeled is shown in Fig. 4.43. The bistatic response of the shell is as expected, with a thin response occurring with a delay profile that approximately fits the profile of the shell with a rapid drop off at the edges. The monostatic shell response shows features of both the sphere and the pipe scatterer. An initial thin response occurs near 2.5 ns and then a

Figure 4.40: Three scatterers, modeled as perfect electrical conductors are shown. From left to right they are a rectangular pipe, a 155 mm artillery shell, and a calibration sphere.

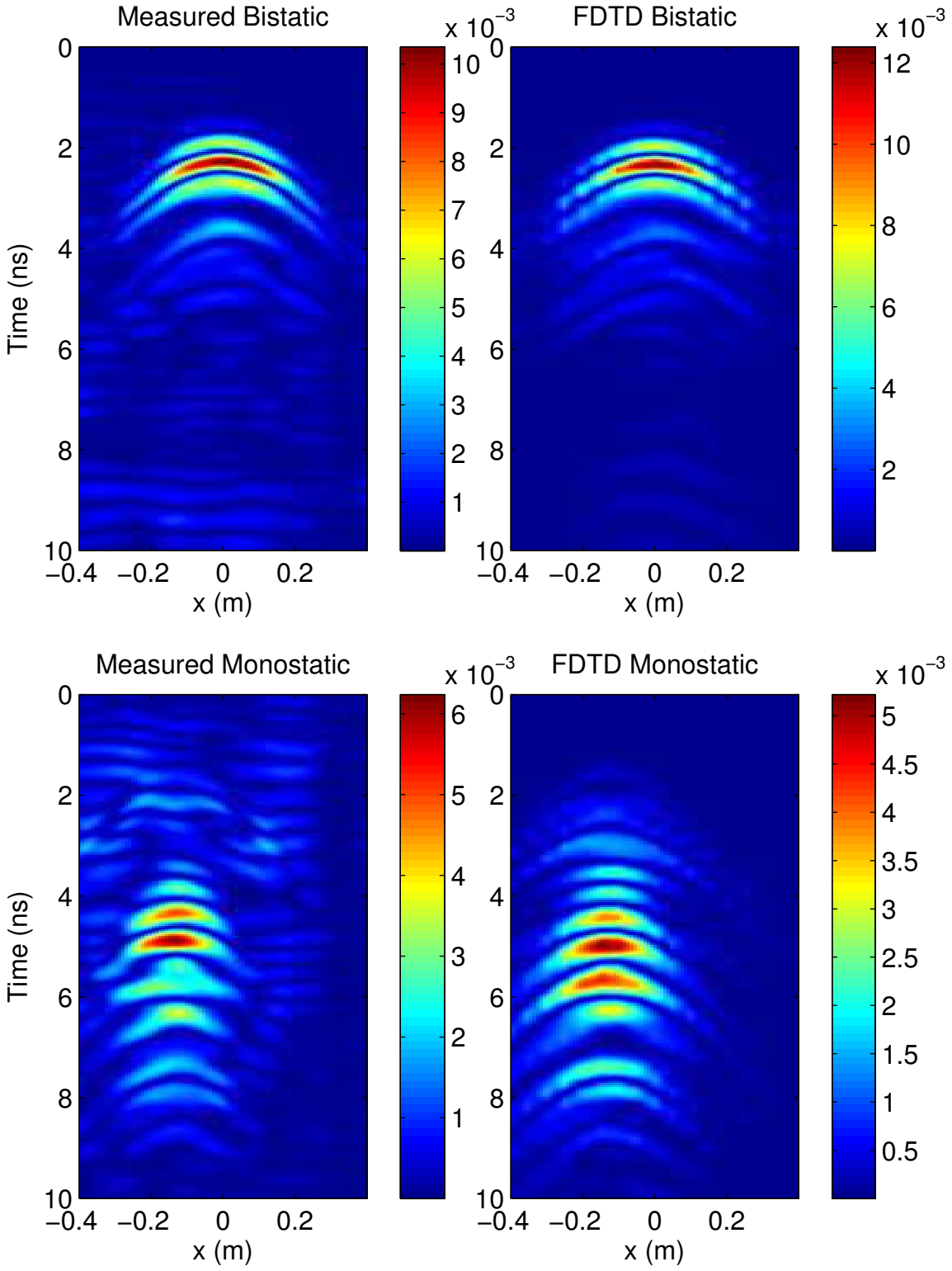

Figure 4.41: Comparison of the dispersion-removed responses of a 6 cm sphere, modeled and measured. Monostatic and bistatic responses are shown.

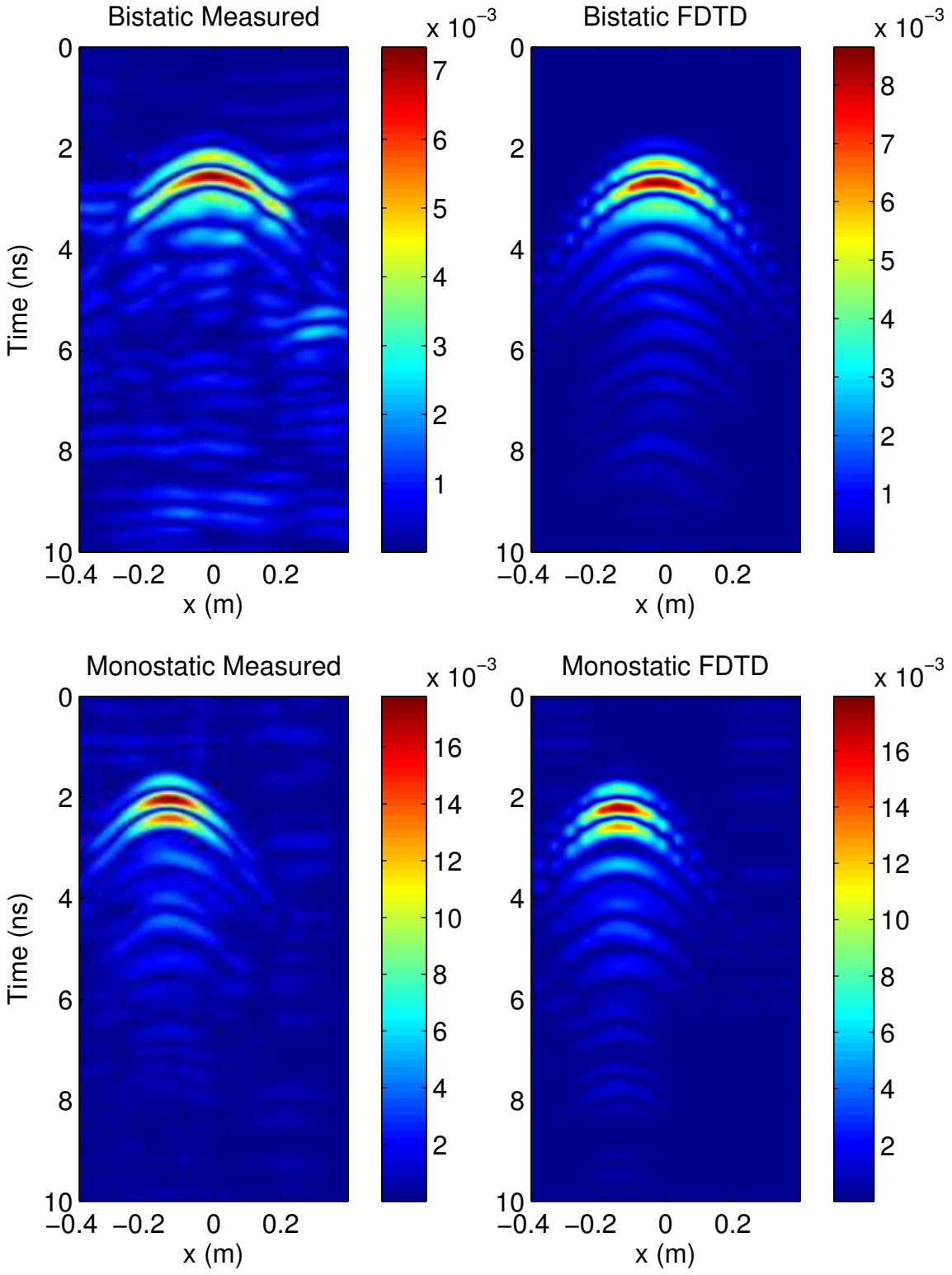

Figure 4.42: Comparison of the dispersion-removed responses of a thin rectangular pipe, 30 cm in length, modeled and measured. Monostatic and bistatic responses are shown.

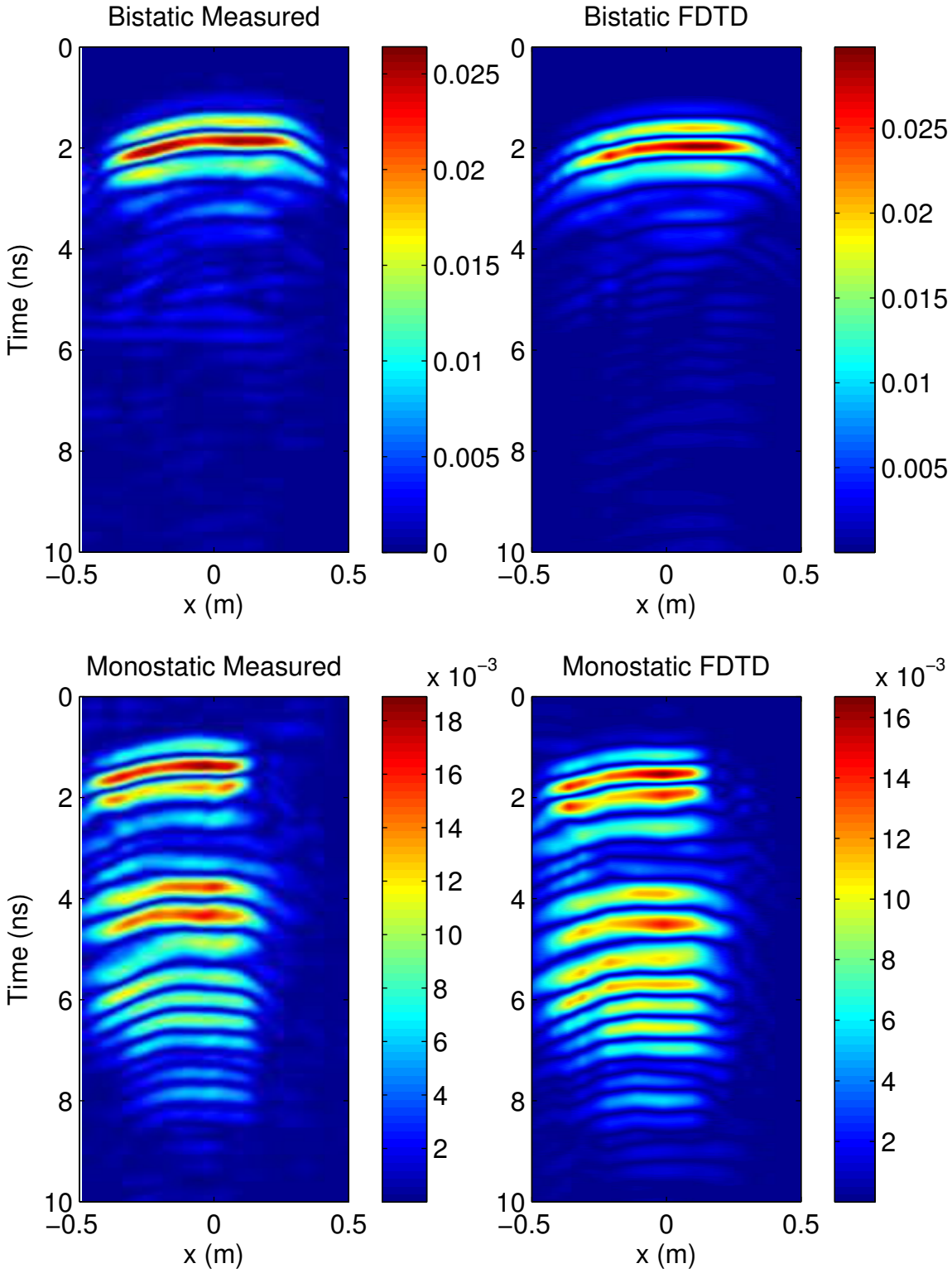

Figure 4.43: Comparison of the dispersion-removed responses of a 155 mm shell, modeled and measured. Monostatic and bistatic responses are shown.

delayed, ringing response occurs afterwards near 5 ns.

The three responses show that essentially the bistatic response behaves as expected, showing some signal for each scatterer type. In addition, the dispersion in the bistatic responses appears to be properly removed by the dispersion filter. The filter also appears to function properly for the pipe's monostatic response, but each of the monostatic responses for targets that have some degree of symmetry, the shell and sphere, show a significant amount of ringing at late times. In the next chapter it is shown that the monostatic response to a symmetric scatterer is mostly rejected by the antenna, but that the signal remaining is still large when compared with the bistatic response because the bistatic response is so weak. The reason that the error signal seen occurs at later times and is not substantially compressed by the dispersion filter is also discussed.

CHAPTER V

ANALYSIS OF THE GPR SYSTEM

Having verified the proper modeling of the GPR system for sand and air, some analysis of the system can be made. To reduce the complexity of the analysis, the antenna system itself is held constant and only analyzed over a scan lane. This leaves four parameters to study the GPR system's configuration, shown in Fig. 5.1. These are the height from the ground, h, the dielectric constant of the ground, ϵ_r, the depth of the buried scatterer, d, and the lateral distance from the center of the two antennas, x.

In the previous section, it was shown that in addition to the position, the response to a scatterer is a strong function of its shape. Therefore, to completely analyze the system would also require a set of simulations that varied the shape of the scatterer in some systematic way. To model a single scatterer located 5 to 25 cm below the ground using 128 processors currently requires approximately 8 hours of computation. This means a full scan lane computation requires on the order of a week and parameterizing scan lane responses with respect to ϵ_r and h could require many months. Upon completion, the analysis would still be restricted to a particular scatterer geometry and depth, d.

To provide an analysis despite these difficulties, a simplification of some aspect of the problem is required. Since the focus of this report has been primarily on the GPR system itself and not on the features of scatterers, the simplification was chosen to affect primarily the nature of the scatterer. In this section, a technique is described that allows the antennas' response to electrically small scatterers with an arbitrary shape placed at an arbitrary position in the ground to be characterized with only two FDTD simulations and some simple post-processing calculations. This will make it possible to characterize the system much more completely than before.

In the technique, the fields generated by the antennas when no scatterer is present are

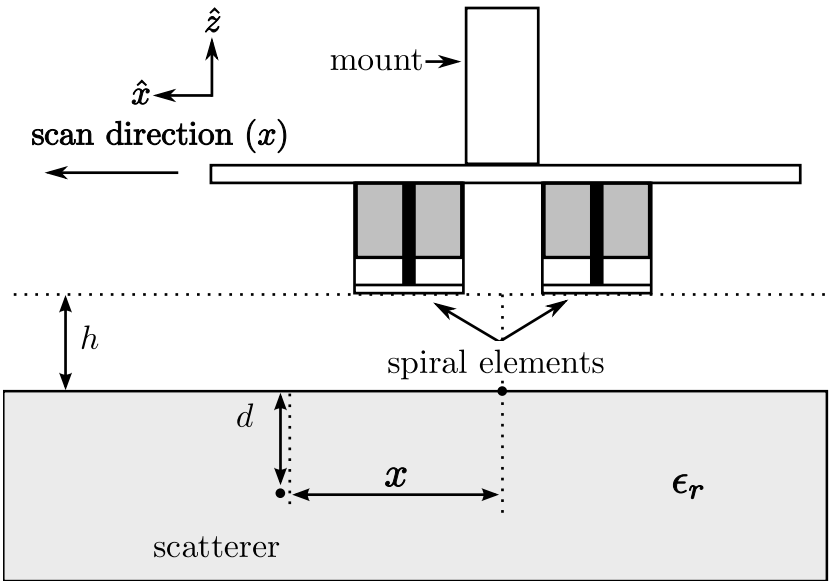

Figure 5.1: Geometry of the GPR system to be analyzed. Here the origin of the $x-z$ coordinate system is directly between the antennas at the interface between the air and the ground. The antennas are centered at $x = 0$ but during measurement the antennas are free to move along the x axis.

calculated at each point of interest in the ground while the transmitting antenna transmits. Next, the same simulation is repeated but with the receive antenna transmitting. A reciprocity relation with additional approximations may then be used to calculate the scattered voltage seen by the monostatic and bistatic system when an arbitrary small scatterer is placed at any point in the ground where the fields have been calculated. Since the FDTD method calculates the field at all points in the ground simultaneously, the scattered response for all x and at any depth, d, up to the edge of the simulation space can be computed with only two 8 hour long simulations.

The Lorentz reciprocity relation is used as a starting point to derive the relation between these field quantities and the radar responses obtained. The relation obtained is a form of the expression given in [57] but the derivation will take material inhomogeneities in the space into account. This is done using a treatment similar to the derivation in [48] for the relationship between an antenna's transmitting and receiving pattern. While the reciprocity relation itself is exact, it can only be used to calculate the scattered voltage seen on the antennas if one additionally knows the distribution of current on the scattering object. To

obtain a complete relation for the radar responses, an approximation is applied to obtain the current distributions.

For small scatterers, the currents and charges induced are similar to electric and magnetic dipoles. The linear relation between the incident field and the dipole moment induced is called the polarizability tensor, and using this the radar response can be calculated. The approximation involved in this small-scatterer assumption is discussed and the FDTD model is used to show that this is an accurate assumption for sufficiently small scatterers using a simple example where the polarizability tensor can be computed exactly. The technique of using a polarizability tensor to represent the geometry of the scatterer has been used extensively in quasi-static work by Baum in [58], and similar treatments have been used in the same work for the GPR problem dealing with characteristic resonances, but these treatments make assumptions about the antenna and scatterer interaction occurring in the far-field. In this work, it is shown that these analyses extend to the near-field as well and that the FDTD model can be used to provide the required expressions for the fields near the antenna.

Following the description of the small-scatterer model and its verification with FDTD data, a symmetry argument is made to show the relationship between the small scatterer's geometry and the tensor that encodes that geometry. It is shown that small symmetric scatterers are rejected by an antenna that has a condition similar to circular-polarization, even in the near-field. Next, measurements of two small scatterers, one with a plane of symmetry and one without, are compared to the results predicted by the small-scatterer model. It is shown that the symmetric scatterer has a similar response to the sphere response shown in Fig. 4.31.

With the general behavior of the small-scatterer model described and verified, the model is used to analyze the effect of the properties h and ϵ_r. The magnitude of the response to a linear scatterer at any given position is shown for various h and ϵ_r values. In addition, the symmetry rejection ability of the spiral GPR system is shown for different ϵ_r.

Finally, the late-time ringing seen in the symmetric scatterer responses shown is described using the small-scatterer model. It is shown that this is caused by the spiral antennas themselves and not any additional component of the model. An argument is made that this late-time ringing could be reduced by the introduction of resistive loading at the exterior of the spiral antennas.

5.1 Near-field Reciprocity Relation in the Ground

In this section, a reciprocity relation is shown that allows one to calculate the voltage induced on an antenna when an arbitrary current distribution is placed nearby. The calculation requires that the current distribution be known. In addition one must know the fields around the antenna when it transmits without the current present. The derivation accounts for an inhomogeneous ground. In the next section, an approximate relation is provided to compute the scattered currents on a small PEC from the incident fields on that scatterer. These two expressions will then be used to give a relationship between the scattered voltages measured on the antennas and the incident fields on the scatterers.

In deriving the reciprocity relation, a symmetric form of the time-harmonic Maxwell's equations are used. These introduce a fictitious magnetic charge and magnetic current term. The use of this form reduces to the standard Maxwell's equations when the magnetic sources are set to zero, but also will simplify the treatment of small current loops that can arise on a scatterer by allowing them to be approximated with a magnetic dipole. The relation between a small loop and a magnetic dipole is discussed in [59].

Being fictitious, there is no standard form for the introduced magnetic current and charge terms in Maxwell's equations. Formulations vary by a constant scale factor depending on the author with the two main forms being those described in [48] and those described in [60]. Here those used in [60] are chosen. The symmetric form of Maxwell's equations for harmonic time-dependence are

$$\nabla \times \vec{\mathbf{H}} = \vec{\mathbf{J}} + j\omega\vec{\mathbf{D}} \tag{5.1}$$

$$\nabla \times \vec{\mathbf{E}} = -j\omega\vec{\mathbf{B}} - \vec{\mathbf{M}} \tag{5.2}$$

$$\nabla \cdot \vec{\mathbf{B}} = \rho_m \tag{5.3}$$

$$\nabla \cdot \vec{\mathbf{D}} = \rho, \tag{5.4}$$

where $\vec{\mathbf{M}}$ is the magnetic current and ρ_m is the magnetic charge.

In a reciprocity relation, two solutions to the symmetric Maxwell's equations are given, $(\vec{\mathbf{E}}^a, \vec{\mathbf{H}}^a)$ and $(\vec{\mathbf{E}}^b, \vec{\mathbf{H}}^b)$, in a region with a common $\mu(\vec{\mathbf{r}})$ and $\epsilon(\vec{\mathbf{r}})$. [60] shows the steps necessary to convert the curl equations, (5.1) and (5.2), into a differential form of the Lorentz reciprocity relation. Integrating over an arbitrary volume, V, and applying the divergence theorem one obtains

$$\iiint_V \left(\vec{\mathbf{E}}^a \cdot \vec{\mathbf{J}}^b - \vec{\mathbf{H}}^a \cdot \vec{\mathbf{M}}^b\right) dV - \iiint_V \left(\vec{\mathbf{E}}^b \cdot \vec{\mathbf{J}}^a - \vec{\mathbf{H}}^b \cdot \vec{\mathbf{M}}^a\right) dV = - \iint_{\partial V} \left(\vec{\mathbf{E}}^a \times \vec{\mathbf{H}}^b - \vec{\mathbf{E}}^b \times \vec{\mathbf{H}}^a\right) \cdot \hat{\mathbf{n}} dS, \tag{5.5}$$

where $\hat{\mathbf{n}}$ is the outward facing normal everywhere on the boundary surface of V, ∂V. V is not necessarily assumed to be connected here, and when it is not, the surface integral term should be considered to be a sum of surface integrals over the boundary of each connected region.

To apply this reciprocity relation to the GPR problem, the situations for the A and B fields must be described. The materials in the space used are depicted in Fig. 5.2. The figure shows an antenna test bed in an anechoic chamber. An antenna radiates above an inhomogeneous body. The entire region is surrounded with conductive absorber and encased in a PEC. The results in this section can be extended to an unbounded region, but all measurements in this work are for a bounded region and the assumption of a bounded region is easier to work with.

The material configuration is constant in situations A and B. The materials are left intentionally unspecified. There exist permittivity, conductivity and permeability as a function of position, $\epsilon_r(\vec{\mathbf{r}})$, $\sigma(\vec{\mathbf{r}})$ and $\mu_r(\vec{\mathbf{r}})$. There also exist a set of closed surfaces S_k on which

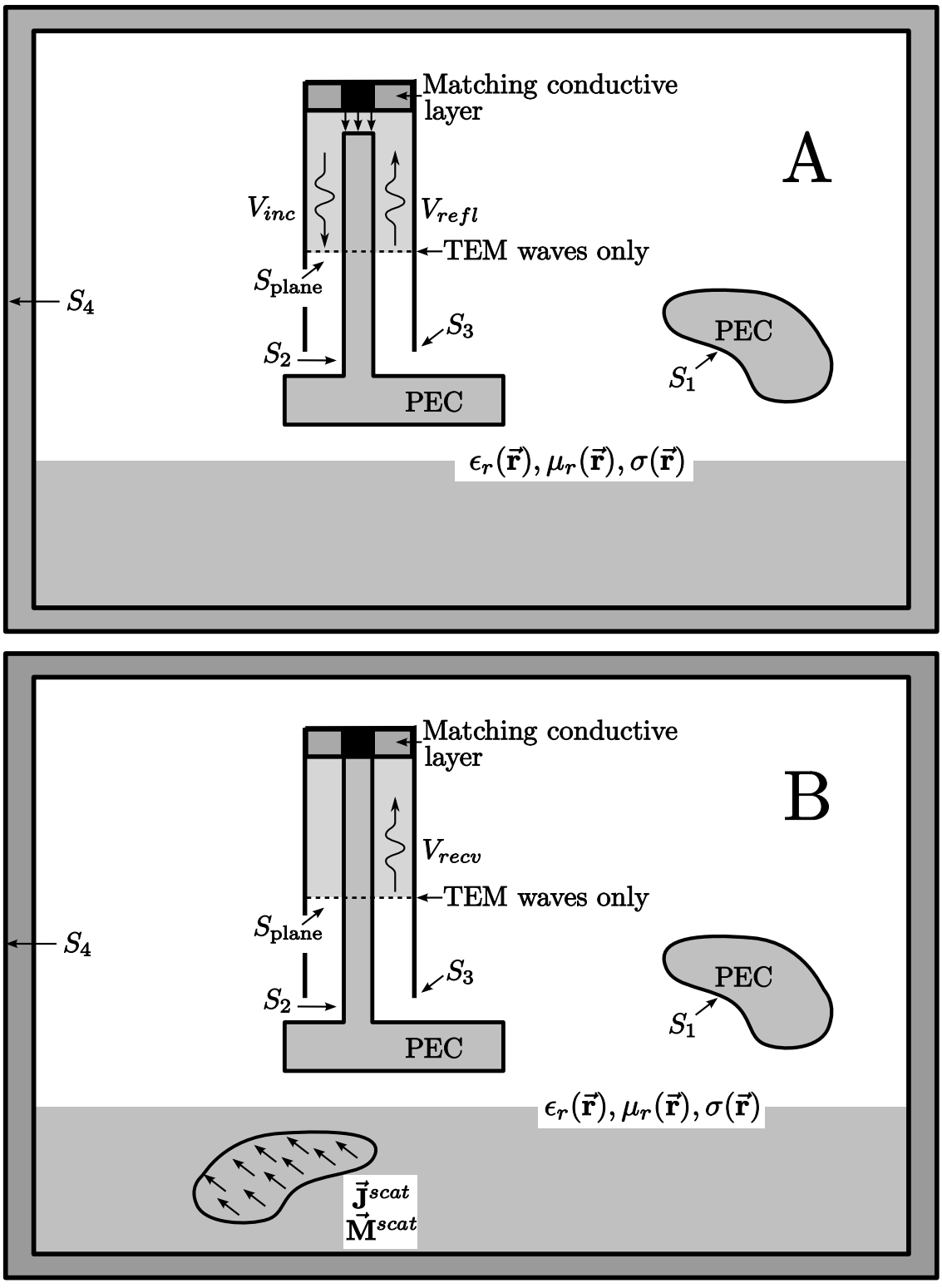

Figure 5.2: Two situations for the reciprocity relation. In situation A, the antenna is transmitting into a region of space. In situation B, the antenna is receiving while enforced currents radiate.

a PEC boundary condition is imposed. A generic monopole antenna is depicted, but the antenna's shape is arbitrary. The only important feature for this derivation is that it must be fed by a coax line that is attached to a perfectly matched source and on some planar surface, S_{plane}, in the coax line between the source and the connection to the antenna there are clearly defined forward and backward propagating TEM waves. The volume, V, in the reciprocity relation extends over the interior of the region except the areas contained inside of PEC surfaces and the shaded region of the coax line. This region is excluded to allow the TEM waves on S_{plane} to be used.

In situation A, a portion of the cylinder in the coax line is replaced with an enforced electric field oscillating with an $e^{j\omega t}$ time dependence to provide an idealized voltage source. The radiation from this source settles into a TEM wave before reaching the surface S_{plane} with a voltage of V_{inc}. The reflection from the antenna also creates a TEM wave at S_{plane} with voltage V_{refl} and the matching tab at the back of the coax line ensures that the only two waves at the surface are V_{inc} and V_{refl}. The fields in the space when the source is on are named $\vec{\mathbf{E}}^a$ and $\vec{\mathbf{H}}^a$. In regions of the space that have some conductivity $\sigma(\vec{\mathbf{r}})$, an induced current exists, $\vec{\mathbf{J}}^a$ where $\vec{\mathbf{J}}^a = \sigma\vec{\mathbf{E}}^a$.

In situation B, the source is set to zero while the matching tab at the back of the coax line is kept in place to ensure that only the wave V_{recv} exists at the surface, S_{plane}. A distribution of electric and magnetic current, $\vec{\mathbf{J}}^{scat}$ and $\vec{\mathbf{M}}^{scat}$, exists in front of the antennas in the ground. Radiation from these sources creates a set of corresponding fields in the space named $\vec{\mathbf{E}}^b$ and $\vec{\mathbf{H}}^b$. In addition to the enforced currents, $\vec{\mathbf{J}}^{scat}$ and $\vec{\mathbf{M}}^{scat}$, the electric field also induces conductive currents, $\vec{\mathbf{J}}^b$, where $\vec{\mathbf{J}}^b = \sigma\vec{\mathbf{E}}^b$. Applying (5.5) to the A and B situations gives

$$\iiint_V \left(\vec{\mathbf{E}}^a \cdot (\vec{\mathbf{J}}^b + \vec{\mathbf{J}}^{scat}) - \vec{\mathbf{H}}^a \cdot \vec{\mathbf{M}}^{scat}\right) dV - \iiint_V \left(\vec{\mathbf{E}}^b \cdot \vec{\mathbf{J}}^a\right) dV = - \iint_{\partial V} \left(\vec{\mathbf{E}}^a \times \vec{\mathbf{H}}^b - \vec{\mathbf{E}}^b \times \vec{\mathbf{H}}^a\right) \cdot \hat{\mathbf{n}} dS. \quad (5.6)$$

The left side of (5.6) can be reduced by applying the fact that the currents $\vec{\mathbf{J}}^a$ and $\vec{\mathbf{J}}^b$ are

conductive. This yields

$$\iiint_V \left(\vec{\mathbf{E}}^a \cdot (\vec{\mathbf{J}}^b + \vec{\mathbf{J}}^{scat}) - \vec{\mathbf{H}}^a \cdot \vec{\mathbf{M}}^{scat}\right) dV - \iiint_V \left(\vec{\mathbf{E}}^b \cdot \vec{\mathbf{J}}^a\right) dV =$$
$$\iiint_V \left(\sigma\vec{\mathbf{E}}^a \cdot \vec{\mathbf{E}}^b - \sigma\vec{\mathbf{E}}^b \cdot \vec{\mathbf{E}}^a\right) dV + \iiint_V \left(\vec{\mathbf{E}}^a \cdot \vec{\mathbf{J}}^{scat} - \vec{\mathbf{H}}^a \cdot \vec{\mathbf{M}}^{scat}\right) dV =$$
$$\iiint_V \left(\vec{\mathbf{E}}^a \cdot \vec{\mathbf{J}}^{scat} - \vec{\mathbf{H}}^a \cdot \vec{\mathbf{M}}^{scat}\right) dV. \quad (5.7)$$

The right side of (5.6) can be reduced by breaking the boundary up into its individual contributions. There are two types of surfaces in ∂V, as shown in Fig. 5.2. S_k are all set against PEC objects and S_{plane} is the surface in the coax line.

$$\iint_{\partial V} \left(\vec{\mathbf{E}}^a \times \vec{\mathbf{H}}^b - \vec{\mathbf{E}}^b \times \vec{\mathbf{H}}^a\right) \cdot \hat{\mathbf{n}} dS = \sum_k \iint_{S_k} \left(\vec{\mathbf{E}}^a \times \vec{\mathbf{H}}^b - \vec{\mathbf{E}}^b \times \vec{\mathbf{H}}^a\right) \cdot \hat{\mathbf{n}} dS$$
$$+ \iint_{S_{plane}} \left(\vec{\mathbf{E}}^a \times \vec{\mathbf{H}}^b - \vec{\mathbf{E}}^b \times \vec{\mathbf{H}}^a\right) \cdot \hat{\mathbf{n}} dS. \quad (5.8)$$

The fact that $\vec{\mathbf{E}}^a$ and $\vec{\mathbf{E}}^b$ are zero on the PEC surfaces, S_k, sets these integrals to zero. This gives

$$\iiint_V \left(\vec{\mathbf{E}}^a \cdot \vec{\mathbf{J}}^{scat} - \vec{\mathbf{H}}^a \cdot \vec{\mathbf{M}}^{scat}\right) dV \quad = \quad - \iint_{S_{plane}} \left(\vec{\mathbf{E}}^a \times \vec{\mathbf{H}}^b - \vec{\mathbf{E}}^b \times \vec{\mathbf{H}}^a\right) \cdot \hat{\mathbf{n}} dS. \quad (5.9)$$

The remaining surface integral can be evaluated by substituting the known fields for a TEM wave in a coax line. A closer view of the surface is shown in Fig. 5.3. A local coordinate system is defined on the surface and the fields for a voltage wave of magnitude V^+ and current I^+, both assumed complex, traveling in the $\hat{\mathbf{z}}$ direction and measured at the reference plane S_{plane} can be expressed in terms of the standard cylindrical coordinates in these variables [53],

$$\vec{\mathbf{E}} = \frac{V^+\hat{\rho}}{\rho \log(b/a)} \qquad a < \rho < b \quad (5.10)$$

$$\vec{\mathbf{H}} = \frac{I^+\hat{\phi}}{2\pi\rho} \qquad a < \rho < b. \quad (5.11)$$

The relationship between V^+ and I^+ is given by the line's geometry, but in this case it will only be necessary to define the impedance of the line, Z, by $V^+/I^+ = Z$. A wave traveling in the $-\hat{\mathbf{z}}$ direction with voltage magnitude V^-, and current magnitude I^- has

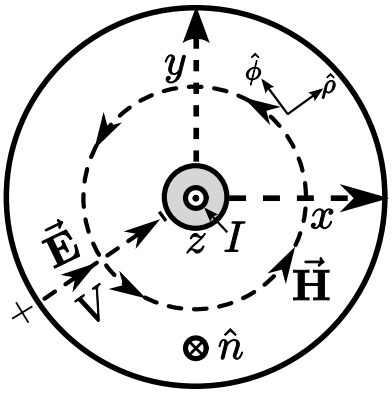

Figure 5.3: Close-up of coax surface, S_{plane}. Contours for measuring the voltage and current from the electric and magnetic fields are shown.

the same form, but the impedance relation is now $V^-/(-I^-) = Z$. The fields can be substituted into the right-hand integrands of (5.9) to obtain

$$\vec{\mathbf{E}}^a \times \vec{\mathbf{H}}^b = \left(\frac{V_{inc}\hat{\rho} + V_{refl}\hat{\rho}}{\rho \log(b/a)}\right) \times \frac{I_{recv}\hat{\phi}}{2\pi\rho} = -\frac{(V_{inc} + V_{refl})\, V_{recv}\hat{\mathbf{z}}}{\rho^2 \log(b/a) 2\pi Z}, \tag{5.12}$$

and

$$\vec{\mathbf{E}}^b \times \vec{\mathbf{H}}^a = \frac{V_{recv}\hat{\rho}}{\rho \log(b/a)} \times \frac{I_{inc}\hat{\phi} + I_{refl}\hat{\phi}}{2\pi\rho} = \frac{V_{recv}\,(V_{inc} - V_{refl})}{\rho^2 \log(b/a) 2\pi Z}\hat{\mathbf{z}}. \tag{5.13}$$

In these forms, the integrals can be evaluated as

$$\begin{aligned}\iint_{S_{plane}} \left(\vec{\mathbf{E}}^a \times \vec{\mathbf{H}}^b\right) \cdot \hat{\mathbf{n}} dS &= -\int_a^b \int_0^{2\pi} \frac{(V_{inc} + V_{refl})\, V_{recv}}{\rho^2 \log(b/a) 2\pi Z} \left(\hat{\mathbf{z}} \cdot \hat{\mathbf{n}}\right) \rho d\phi d\rho \\ &= \frac{(V_{inc} + V_{refl})\, V_{recv}}{Z}\end{aligned} \tag{5.14}$$

and

$$\begin{aligned}\iint_{S_{plane}} \left(\vec{\mathbf{E}}^b \times \vec{\mathbf{H}}^a\right) \cdot \hat{\mathbf{n}} dS &= \int_a^b \int_0^{2\pi} \frac{V_{recv}\,(V_{inc} - V_{refl})}{\rho^2 \log(b/a) 2\pi Z} \left(\hat{\mathbf{z}} \cdot \hat{\mathbf{n}}\right) \rho d\phi d\rho \\ &= \frac{V_{recv}\,(V_{refl} - V_{inc})}{Z}.\end{aligned} \tag{5.15}$$

Substituting these into (5.9) one obtains

$$\begin{aligned}\iiint_V \left(\vec{\mathbf{E}}^a \cdot \vec{\mathbf{J}}^{scat} - \vec{\mathbf{H}}^a \cdot \vec{\mathbf{M}}^{scat}\right) dV &= -\iint_{S_{plane}} \left(\vec{\mathbf{E}}^a \times \vec{\mathbf{H}}^b - \vec{\mathbf{E}}^b \times \vec{\mathbf{H}}^a\right) \cdot \hat{\mathbf{n}} dS \\ &= -\left(\frac{(V_{inc} + V_{refl})\, V_{recv}}{Z} + \frac{(V_{inc} - V_{refl})\, V_{recv}}{Z}\right) \\ &= -\frac{2V_{inc}V_{recv}}{Z},\end{aligned} \tag{5.16}$$

which gives the final form of this relation,

$$V_{recv} = -\frac{Z}{2V_{inc}} \iiint_V \left(\vec{\mathbf{E}}^a \cdot \vec{\mathbf{J}}^{scat} - \vec{\mathbf{H}}^a \cdot \vec{\mathbf{M}}^{scat} \right) dV. \tag{5.17}$$

5.2 Use of the Reciprocity Relation in the GPR System

In the previous section, it was shown that the received voltage on an antenna in the presence of a known current distribution can be calculated from the fields in the space when the antenna is transmitting in the absence of that distribution. In this section, this relation, (5.17), is applied to the radar system described in Chapter 4. While the relation derived in the previous section was exact, in this section, a series of approximations are made to allow for a simple relationship. Consider the diagram of the spiral antennas in Fig. 5.4. Note that the antennas are fed with a single coax line each through a balun. The derivation can also be made for the virtual balun, but is needlessly more complicated. Two coax lines feed the spiral antennas and an electrically-small closed surface, S, in front of the antennas is delineated. In this section, the scattered voltage received on one coax line, j, when another line, k, is excited in the presence of the PEC scatterer is determined. This scattered voltage will provide estimates of the monostatic and bistatic responses related to $S_{dd,11}$ and $S_{dd,21}$ when the cross-talk between the antennas is calibrated out.

Suppose an out-going time-harmonic wave with magnitude V_{inc} is transmitted on coax k and creates incident fields in the ground $(\vec{\mathbf{E}}^{i,k}, \vec{\mathbf{H}}^{i,k})$ when the scatterer is not present. If the scatterer is present in each situation, there are different fields, $(\vec{\mathbf{E}}^{t,k}, \vec{\mathbf{H}}^{t,k})$. Define the scattered fields to be

$$\vec{\mathbf{E}}^{s,k} = \vec{\mathbf{E}}^{t,k} - \vec{\mathbf{E}}^{i,k}. \tag{5.18}$$

These scattered fields are the result of the radiation of scattered currents and charges located on the surface of the PEC. For electrically small scatterers, the $\vec{\mathbf{E}}^i$ and $\vec{\mathbf{H}}^i$ fields are nearly constant over the PEC surface and the scattered currents and charges on different parts of the scatterer can interact quickly enough that they settle down to a static solution very quickly. This situation is called quasi-static because the charges and currents are static solutions that vary uniformly with a harmonic time dependence. In this situation, some

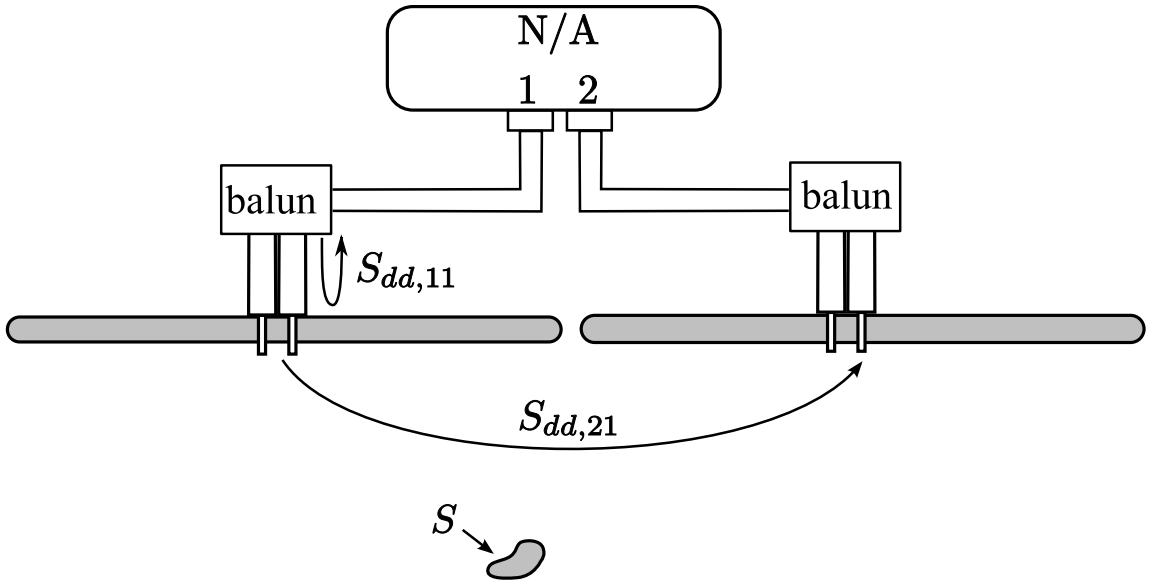

Figure 5.4: Two coax lines attached through baluns to the spiral antennas. The spirals radiate onto a small PEC scatterer.

general statements can be made about the approximate form of the scattered currents and charges.

In particular, no tangential $\vec{\mathbf{E}}$ field may exist on the PEC surface because this would imply an infinite current flow in the direction of the $\vec{\mathbf{E}}$ field. Consequently, the scatterer must produce a charge distribution that cancels the electric field along directions that the scatterer has tangent surfaces. For example, in Fig. 5.5, an incident field is shown being canceled by a distribution of charge on the scatterer. The charge distribution can be approximated with the dipole shown, and the electric current distribution can be derived from this charge distribution.

Similarly, no normal magnetic field (ignoring operation at DC) may exist on the surface of the scatterer, because an infinite current would be induced whenever the magnetic field changed according to Faraday's law. Consequently, the scatterer must produce a loop of current to cancel the magnetic field along any direction that the scatterer has a normal PEC. In Fig. 5.5, an incident magnetic field is shown being canceled by a distribution of current on the scatterer. The current distribution is similar to a loop and could be approximated with the magnetic dipole shown. With the magnetic dipole representing the magnetic charge distribution, the equivalent magnetic current distribution required can be

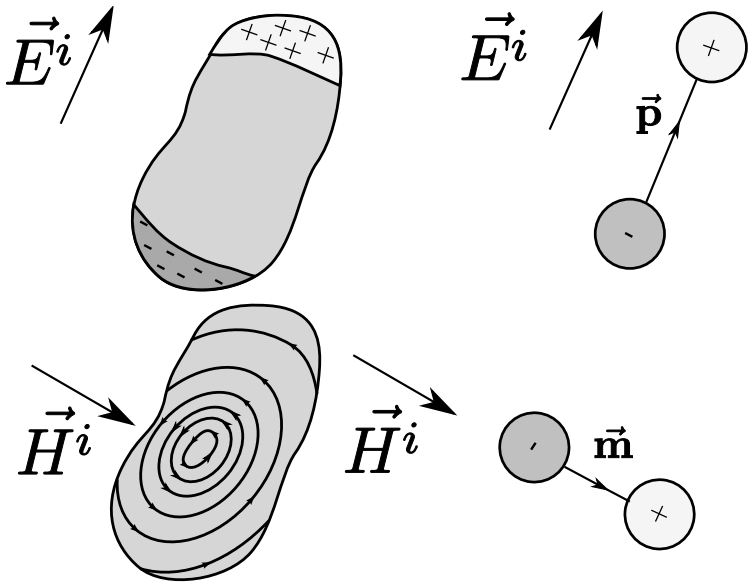

Figure 5.5: A small PEC's interaction with quasi-static fields. Above, an incident electric field induces charge on the PEC. The charge distribution can be approximated with an electric dipole. Below, varying magnetic field would create a tangential electric field on the PEC surface, which would cause current to flow until the normal component of the field was forced to zero. The circulating current can be approximated with a small loop, or equivalently a magnetic dipole.

calculated.

The distributions created are similar to an electric and magnetic dipoles. The current distribution for an oscillating dipole is simply a Dirac delta in the direction of the dipole moment. By the continuity equation, the current for an electric dipole moment $\vec{\mathbf{p}}$ and a magnetic dipole moment $\vec{\mathbf{m}}$ is concentrated at the center of the dipole, $\vec{\mathbf{r_0}}$,

$$\vec{\mathbf{J}} = j\omega\vec{\mathbf{p}}\delta(\vec{\mathbf{r}} - \vec{\mathbf{r_0}}) \tag{5.19}$$

$$\vec{\mathbf{M}} = j\omega\vec{\mathbf{m}}\delta(\vec{\mathbf{r}} - \vec{\mathbf{r_0}}). \tag{5.20}$$

Since the dipole moments induced on the scattering objects are linearly related to the incident fields, the relation can be written in terms of a matrix in a fixed basis, or basis-free as a tensor. The tensor that relates field to moment is typically called a polarizability tensor or dyad. Using the notation in [59], these are referred to as $\underline{\alpha_{\mathbf{e}}}$ and $\underline{\alpha_{\mathbf{m}}}$ respectively. When

the medium surrounding the scatterer has permittivity, ϵ, and permeability, μ, [1]

$$\vec{\mathbf{p}} = \epsilon \underline{\alpha_{\mathbf{e}}} \cdot \vec{\mathbf{E}}^i \tag{5.21}$$

$$\vec{\mathbf{m}} = \mu \underline{\alpha_{\mathbf{m}}} \cdot \vec{\mathbf{H}}^i. \tag{5.22}$$

A brief introduction to the dyadic notation and its generalization is available in [61], although no more than the first few sections are needed for anything used this chapter [2]. To avoid some subtlety in this chapter, dyads are always expressed in some real orthonormal basis [3], as elements of $\mathbf{R}^3$. In total then, the current distribution for the small scatterer is written as

$$\vec{\mathbf{J}} = j\omega \left(\epsilon \underline{\alpha_{\mathbf{e}}} \cdot \vec{\mathbf{E}}^i(\vec{\mathbf{r_0}}) \right) \delta(\vec{\mathbf{r}} - \vec{\mathbf{r_0}}) \tag{5.23}$$

$$\vec{\mathbf{M}} = j\omega \left(\mu \underline{\alpha_{\mathbf{m}}} \cdot \vec{\mathbf{H}}^i(\vec{\mathbf{r_0}}) \right) \delta(\vec{\mathbf{r}} - \vec{\mathbf{r_0}}). \tag{5.24}$$

One may then use (5.17) to calculate the received voltage on some coax j in the presence of the scattered currents induced when there is a V_{inc} wave on coax line k

$$V_{scat,jk} = -\frac{Z}{2V_{inc}} \iiint_V \left(\vec{\mathbf{E}}^{i,j} \cdot \vec{\mathbf{J}}^{scat} - \vec{\mathbf{H}}^{i,j} \cdot \vec{\mathbf{M}}^{scat} \right) dV = \\ - \frac{j\omega Z \left(\epsilon \vec{\mathbf{E}}^{i,j} \cdot \underline{\alpha_{\mathbf{e}}} \cdot \vec{\mathbf{E}}^{i,k} - \mu \vec{\mathbf{H}}^{i,j} \cdot \underline{\alpha_{\mathbf{m}}} \cdot \vec{\mathbf{H}}^{i,k} \right)}{2V_{inc}}. \tag{5.25}$$

Finally, by linearity, when V_{inc} is on the coax line k, the total voltage received on the line j must be the sum of the scattered voltage and whatever cross-talk voltage would exist if the scatterer were not present, $V_{cross,jk}$. Explicitly,

$$V_{recv,jk} = V_{cross,jk} + V_{scat,jk}. \tag{5.26}$$

[1] The definitions given here disagree with [59], but are set by the requirement that the SI units of α_e and α_m are m^3. Due to the choice of definition for the magnetic current used above, the magnetic moment has units of Wb m = Vsm. This requires the additional constant μ to obtain the proper units.

[2] For the purposes of this chapter, it is actually sufficient to think of a vector as a 3×1 matrix with complex entries. The dot product used, $\vec{\mathbf{a}} \cdot \vec{\mathbf{b}}$ is simply then the single component of the matrix, $\vec{\mathbf{a}}^T \vec{\mathbf{b}}$. The dyadic product $\vec{\mathbf{a}}\vec{\mathbf{b}}$ is the 3×3 matrix, $\vec{\mathbf{a}}\vec{\mathbf{b}}^T$. Dot products with a dyad generalize from the definition for the dot product of two vectors. For some dyad $\underline{\mathbf{S}}$, $\vec{\mathbf{a}} \cdot \underline{\mathbf{S}}$ is the 1×3 row vector (typically thought of as a dual vector, but the distinction can be ignored here, since a dyadic product will always be taken on the left or the left and right simultaneously here). Likewise, $\underline{\mathbf{S}} \cdot \vec{\mathbf{b}}$ is the 3×1 column vector, thought of as a vector.

[3] The use of a real orthonormal basis will allow one to say that $\hat{\mathbf{e}}_\mathbf{i} \cdot \hat{\mathbf{e}}_\mathbf{j} = \delta_{ij}$, where δ_{ij} is the Kronecker delta, 0 for $i \neq j$ and 1 otherwise. This is required for arguments in Section 5.4.

The response of the antennas will typically be calibrated against an additional measurement where no scatterer is present. When the ground is roughly uniform, this measurement can be approximated by taking an average measurement for the simulation or by finding an area where it is known there is no scatterer present. In either situation, the viewed response from the antennas will be just $V_{scat,jk}$ and expression (5.25) will provide an estimate of the response. Specifically, the calibrated monostatic response measured, V_{mono}, will be

$$V_{mono} = -\frac{j\omega Z\left(\epsilon\vec{\mathbf{E}}^{i,1}\cdot\underline{\alpha_{\mathbf{e}}}\cdot\vec{\mathbf{E}}^{i,1} - \mu\vec{\mathbf{H}}^{i,1}\cdot\underline{\alpha_{\mathbf{m}}}\cdot\vec{\mathbf{H}}^{i,1}\right)}{2V_{inc}}, \tag{5.27}$$

and the calibrated bistatic response measured, V_{bi}, will be

$$V_{bi} = -\frac{j\omega Z\left(\epsilon\vec{\mathbf{E}}^{i,2}\cdot\underline{\alpha_{\mathbf{e}}}\cdot\vec{\mathbf{E}}^{i,1} - \mu\vec{\mathbf{H}}^{i,2}\cdot\underline{\alpha_{\mathbf{m}}}\cdot\vec{\mathbf{H}}^{i,1}\right)}{2V_{inc}}. \tag{5.28}$$

5.3 Verification of the Small-Scatterer Model

In this section, the small-scatterer model described in the previous section is verified using the FDTD model. This is done for the geometry shown in Fig. 5.6 with $a = 0.8$ mm, and $h = 1$ cm. The small scatterer used here is a short thin wire. The radar response of a wire given the assumption that it is extremely thin is pursued in [62] using a complicated formulation, but in the work for this thesis, the simple response derived in [59] is sufficient for verifying the relation. In [59], the dipole moment of a thin wire pointing in the direction $\hat{\mathbf{n}}$ with geometry shown in Fig. 5.6 is a function of the incident field on that dipole, $\vec{\mathbf{E}}^{i}$, given by

$$\vec{\mathbf{p}} = \frac{4\pi h^3\epsilon\hat{\mathbf{n}}\hat{\mathbf{n}}}{3\left[\ln(2h/a)-1\right]}\cdot\vec{\mathbf{E}}^{i}. \tag{5.29}$$

This provides the polarizability tensors necessary to calculate the radar responses,

$$\begin{aligned}\underline{\alpha_{\mathbf{e}}} &= \frac{4\pi h^3\hat{\mathbf{n}}\hat{\mathbf{n}}}{3\left[\ln(2h/a)-1\right]}\\ \underline{\alpha_{\mathbf{m}}} &= 0.\end{aligned} \tag{5.30}$$

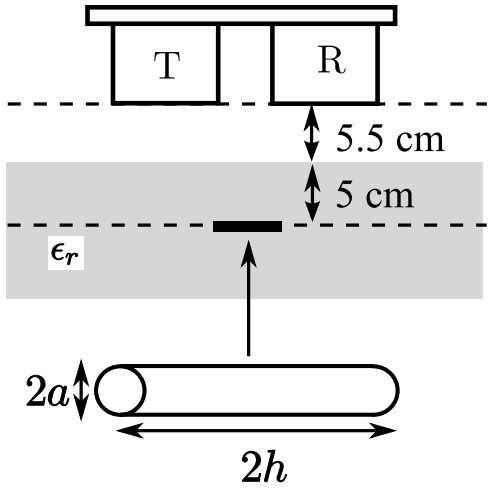

Figure 5.6: Geometry for the verification of the small-scatterer model using a short thin dipole. The dipole used in this verification has parameters $a = 0.8$ mm and $h = 1$ cm.

An FDTD simulation was run with no scatterer present for the transmit and receive antennas to obtain the fields $\vec{\mathbf{E}}^{i,k}$ for k = 1 and 2 respectively as a function of frequency. Then, (5.30), (5.27) and (5.28) were used to calculate the responses for a given excitation $V_{inc}(\omega)$,

$$V_{mono}(\omega) = -\frac{Z}{2V_{inc}(\omega)} \frac{(\vec{\mathbf{E}}^{i,1} \cdot \hat{\mathbf{n}})^2 j\omega 4\pi h^3 \epsilon}{3\left[\ln(2h/a) - 1\right]} \tag{5.31}$$

$$V_{bi}(\omega) = -\frac{Z}{2V_{inc}(\omega)} \frac{(\vec{\mathbf{E}}^{i,2} \cdot \hat{\mathbf{n}})(\vec{\mathbf{E}}^{i,1} \cdot \hat{\mathbf{n}}) j\omega 4\pi h^3 \epsilon}{3\left[\ln(2h/a) - 1\right]}. \tag{5.32}$$

where V_{inc} was the Fourier transform of the modulated Gaussian response used in (4.17).

Finally, these responses were inverse Fourier transformed to obtain a prediction for the dipole response. To verify the model, the FDTD code was run with the dipole included to calculate the scattered voltage induced. The entire calculation was performed once for $\epsilon_r = 1$ and again for $\epsilon_r = 2.35$, the dielectric constant of the sandbox used in measurements. The responses are shown in Fig. 5.7 and 5.8. They are very similar for the 2 cm dipole shown (near $\lambda/10$). Additional comparisons were made for larger dipoles, but these failed to show good agreement because a resonance became apparent in the response.

5.4 Symmetry Properties of Small Scatterers

It has been shown that when the GPR system interacts with a small scatterer, the details of the scattering object can be removed from the analysis and replaced with the 9 elements

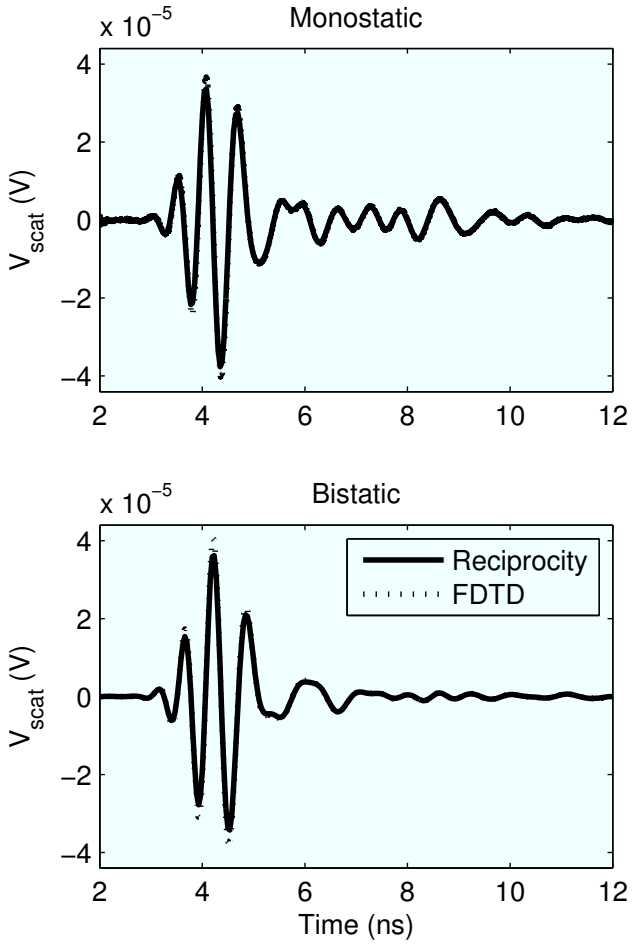

Figure 5.7: Reciprocity model prediction compared with the FDTD response for a 2 cm dipole in air ($\epsilon_r = 1$). The dipole is 10.5 cm from the antennas.

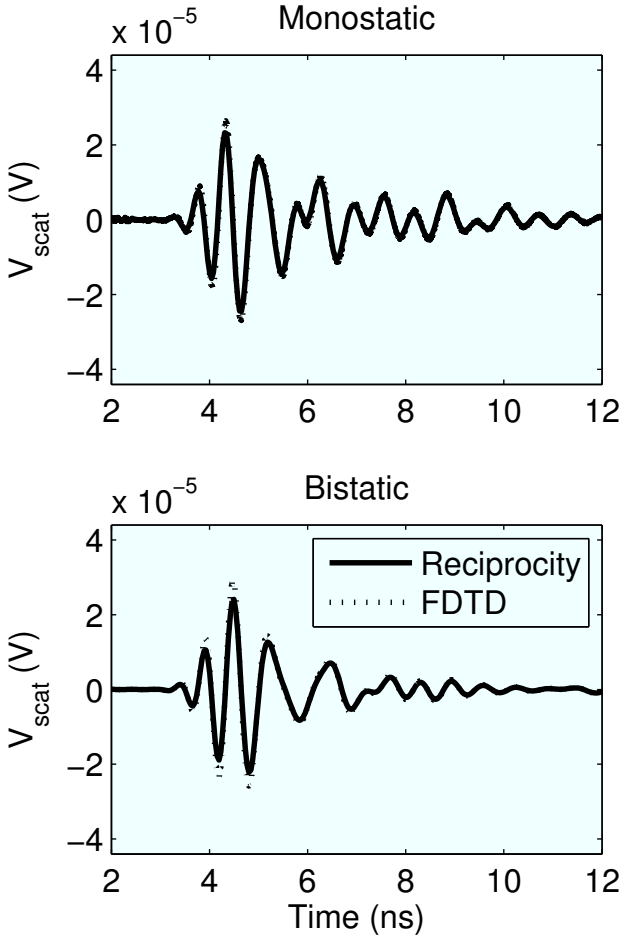

Figure 5.8: Reciprocity model prediction compared with the FDTD response for a 2 cm dipole in sand ($\epsilon_r = 2.35$). The antennas are 5.5 cm from the sand and the dipole is buried 5 cm underground.

of a 3×3 matrix that encodes the geometry of the scatterer. The verification shown so far has only compared simulation data with simulation data. To provided measurements that verify the model, the polarizability tensors are needed for a real scatterer. While the polarizability tensor can be measured, there are few situations where its form is analytically known. One example where the polarizability tensor is known analytically was shown in the previous section. However, the dipole must be very small to satisfy the expression used, and errors in the assumptions about the sand can easily overwhelm any attempt to verify using a small dipole.

The small-scatterer model derived can still be used without analytically known polarizability tensors. In this section, two symmetry arguments are made for the matrix that allow two classes of scatterers to be characterized within a single unknown constant. Scatterers from these classes will then be chosen that have a larger scattered response than the dipole. By normalizing the responses seen for GPR measurements of these scatterers to the maximum value, the single unknown can be solved and measured responses can be compared with the model. Both symmetry arguments are adopted to this framework from polarimetry work by Baum in [56]. First, the reciprocity of the scattering situation is taken advantage of, reducing the 9 component matrix to a 6 component symmetric matrix. Next, it is shown that if the scatterer has an axis of rotational symmetry, the 6 component symmetric matrix reduces to a 2 component form. Finally, some measured verification of the model is provided for two scatterers that can be characterized to within a single unknown.

5.4.1 Reciprocity

The polarizability tensor, $\underline{\alpha_{\mathbf{e}}}$, relates the main direction of dipole moment on the scatterer surface to the incident electric field, $\vec{\mathbf{E}}^i$. It is shown below that the polarizability tensor must be symmetric because otherwise a particular bistatic pair of antennas would not satisfy the reciprocity relation. To make the reciprocity argument in the simplest way possible, suppose that two antennas are used in a bistatic configuration similar to that shown in Fig. 5.1, but with different antennas. Since $\underline{\alpha_{\mathbf{e}}}$ is independent of frequency, the antennas can operate at sufficiently low frequencies that they do not create any magnetic fields, but

instead only create slowly varying electric fields. An example of such an antenna might be a dipole driven at such a low frequency that it essentially acts like a capacitor, and a second identical dipole rotated by 90 degrees. Let $\hat{\mathbf{e_1}}, \hat{\mathbf{e_2}}, \hat{\mathbf{e_3}}$ be an orthonormal basis specified by the fact that the first antenna produces an incident field of

$$\vec{\mathbf{E}}^{i,1} = E_1 \hat{\mathbf{e_1}}, \tag{5.33}$$

when transmitting, and the second produces an incident field of

$$\vec{\mathbf{E}}^{i,2} = E_2 \hat{\mathbf{e_2}}, \tag{5.34}$$

when transmitting.

Note that the polarizability tensor is independent of the location of the scatterer, so this condition that the two antennas create orthogonally polarized electric fields is only required to hold at one point under the antennas. By placing the scatterer at that location, one obtains that the response on the 2 antenna when the 1 antenna transmits is

$$V_{bi,21} = -\frac{j\omega Z \left(\epsilon E_2 \hat{\mathbf{e_2}} \cdot \underline{\alpha_\mathbf{e}} \cdot E_1 \hat{\mathbf{e_1}}\right)}{2V_{inc}}. \tag{5.35}$$

Writing the $\underline{\alpha_\mathbf{e}}$ tensor in the $\hat{\mathbf{e_1}}, \hat{\mathbf{e_2}}, \hat{\mathbf{e_3}}$ basis,

$$\underline{\alpha_\mathbf{e}} = \sum_{i,j} \alpha_{ij} \hat{\mathbf{e_i}} \hat{\mathbf{e_j}}, \tag{5.36}$$

and substituting into (5.35), one obtains

$$V_{bi,21} = -\frac{j\omega\epsilon Z E_2 E_1 \alpha_{21}}{2V_{inc}}. \tag{5.37}$$

Now suppose the 2 antenna transmits and the 1 antenna receives. Evaluating the received voltage directly gives

$$V_{bi,12} = -\frac{j\omega\epsilon Z E_1 E_2 \alpha_{12}}{2V_{inc}}. \tag{5.38}$$

By reciprocity, $V_{bi,12} = V_{bi,21}$. Equating (5.37) with (5.38) gives that $\alpha_{12} = \alpha_{21}$. Similar arguments would show that $\alpha_{23} = \alpha_{32}$ and $\alpha_{31} = \alpha_{13}$. This implies that the matrix corresponding to this tensor is symmetric. A very similar argument could be made to show that the $\underline{\alpha_\mathbf{m}}$ tensor is also symmetric.

While very few general statements about tensors are required for this section, one is that this property of symmetry is independent of the chosen coordinate system. This is shown below in the special case of orthonormal systems, because this is all that is required. Suppose the components of some tensor are symmetric in the orthonormal coordinate system $\hat{\mathbf{e_1}}, \hat{\mathbf{e_2}}, \hat{\mathbf{e_3}}$. Next, suppose a coordinate transform is given to this basis from the basis $\hat{\mathbf{f_1}}, \hat{\mathbf{f_2}}, \hat{\mathbf{f_3}}$ by

$$\hat{\mathbf{e_i}} = \sum_j A_{ij} \hat{\mathbf{f_j}}. \tag{5.39}$$

Next, suppose some tensor has component form S_{ij} in the $\hat{\mathbf{e_k}}$ basis as

$$\underline{\alpha} = \sum_{ij} \alpha_{ij} \hat{\mathbf{e_i}} \hat{\mathbf{e_j}}. \tag{5.40}$$

Substituting (5.39) into (5.40) gives

$$\underline{\alpha} = \sum_{ij} \alpha_{ij} \sum_k A_{ik} \hat{\mathbf{f_k}} \sum_l A_{jl} \hat{\mathbf{f_l}} = \sum_{ijkl} \alpha_{ij} A_{ik} A_{jl} \hat{\mathbf{f_k}} \hat{\mathbf{f_l}}. \tag{5.41}$$

Next, suppose the tensor has components α'_{ij} in the $\hat{\mathbf{f_k}}$ basis,

$$\underline{\alpha} = \sum_{ij} \alpha'_{ij} \hat{\mathbf{f_i}} \hat{\mathbf{f_j}}. \tag{5.42}$$

Equating the two representations, (5.42) and (5.41),

$$\sum_{ijkl} \alpha_{ij} A_{ik} A_{jl} \hat{\mathbf{f_k}} \hat{\mathbf{f_l}} = \sum_{ij} \alpha'_{ij} \hat{\mathbf{f_i}} \hat{\mathbf{f_j}}. \tag{5.43}$$

Dotting each side of the equation on the left by $\hat{\mathbf{f_m}}$ and on the right by $\hat{\mathbf{f_n}}$ yields

$$\begin{aligned} \hat{\mathbf{f_m}} \cdot \left(\sum_{ij} \alpha'_{ij} \hat{\mathbf{f_i}} \hat{\mathbf{f_j}} \right) \cdot \hat{\mathbf{f_n}} &= \hat{\mathbf{f_m}} \cdot \left(\sum_{ijkl} \alpha_{ij} A_{ik} A_{jl} \hat{\mathbf{f_k}} \hat{\mathbf{f_l}} \right) \cdot \hat{\mathbf{f_n}} \\ \Rightarrow \sum_{ij} \alpha'_{ij} \delta_{mi} \delta_{jn} &= \sum_{ijkl} \alpha_{ij} A_{ik} A_{jl} \delta_{mk} \delta_{ln} \\ \Rightarrow \alpha'_{mn} &= \sum_{ij} \alpha_{ij} A_{im} A_{jn}, \end{aligned} \tag{5.44}$$

where δ_{ij} is the Kronecker delta, zero for $i \neq j$ and 1 otherwise. One can now write an expression for the transpose, α'_{nm},

$$\alpha'_{nm} = \sum_{ij} \alpha_{ij} A_{in} A_{jm} = \sum_{ij} \alpha_{ji} A_{jn} A_{im} = \sum_{ij} \alpha_{ji} A_{im} A_{jn}. \tag{5.45}$$

If the original matrix, α_{ij} is symmetric, then this expression simplifies to α'_{mn} by (5.44),

$$\alpha'_{nm} = \sum_{ij} \alpha_{ji} A_{im} A_{jn} = \sum_{ij} \alpha_{ij} A_{im} A_{jn} = \alpha'_{mn}, \tag{5.46}$$

showing that the property of being symmetric is independent of the coordinate system (at least among orthonormal coordinate systems).

5.4.2 Rotational Symmetry

In this section, it is shown that the symmetric tensor from the previous subsection may be reduced even further when the small scatterer has a rotational symmetry. The argument used is very similar to that given in Section 4.7 except it will provide a simpler answer using the fact that the matrix is symmetric. While the argument is shown for the electric polarizability tensor here, one could make the same argument for the magnetic polarizability tensor.

Consider a transformation tensor that rotates vectors about the $\hat{\mathbf{e}}$ axis. When viewed in the plane of rotation, a vector is rotated by an angle of θ. The rotation transformation can be represented by a tensor, $\underline{\mathbf{R}_\theta}$. One can choose an orthonormal basis such that $\hat{\mathbf{e_3}} = \hat{\mathbf{e}}$. In this basis, the components of the transformation will be a rotation matrix about $\hat{\mathbf{e_3}}$ and will take the form,

$$R_\theta = \begin{pmatrix} \cos(\theta) & -\sin(\theta) & 0 \\ \sin(\theta) & \cos(\theta) & 0 \\ 0 & 0 & 1 \end{pmatrix}. \tag{5.47}$$

Now, suppose a polarizability tensor, $\underline{\alpha}$ describes some scatterer. If an incident field of $\vec{\mathbf{E}}^i$ is applied on the scatterer, some moment, $\vec{\mathbf{p}}$, is induced, satisfying

$$\epsilon \underline{\alpha} \cdot \vec{\mathbf{E}}^i = \vec{\mathbf{p}}. \tag{5.48}$$

Now, suppose $\underline{\alpha'}$ represents the tensor for the same scattering object except rotated by θ. Since the entire system consists of the induced dipole, the incident field, and the object, it must be true that applying a rotated incident field to the rotated scatterer must produce the same moment, but rotated. This may be written as,

$$\epsilon \underline{\alpha'} \cdot (\underline{\mathbf{R}_\theta} \cdot \vec{\mathbf{E}}^i) = \underline{\mathbf{R}_\theta} \cdot \vec{\mathbf{p}} = \underline{\mathbf{R}_\theta} \cdot \epsilon(\underline{\alpha} \cdot \vec{\mathbf{E}}^i). \tag{5.49}$$

Since the vector $\vec{\mathbf{E}}^i$ is arbitrary in this argument, and a tensor is defined entirely by its action on a vector, the two tensors on the left and right side of (5.49) must be equal,

$$\underline{\alpha'} \cdot \underline{\mathbf{R}_\theta} = \underline{\mathbf{R}_\theta} \cdot \underline{\alpha}. \tag{5.50}$$

Next, if the scatterer is invariant under the rotation described, it must be true that tensors $\underline{\alpha}$ and $\underline{\alpha'}$ are the same. This implies that the tensor $\underline{\alpha}$ must satisfy the condition

$$\underline{\alpha} \cdot \underline{\mathbf{R}_\theta} = \underline{\mathbf{R}_\theta} \cdot \underline{\alpha}. \tag{5.51}$$

Expressing the tensors in terms of the $\hat{\mathbf{e}_\mathbf{k}}$ basis defined above, α_{ij} and R^θ_{ij}, this becomes a matrix equation. Evaluating $\alpha_{ij} R^\theta_{ij}$ one obtains (noting the symmetry of the α_{ij} matrix),

$$\begin{pmatrix} \alpha_{11} & \alpha_{12} & \alpha_{13} \\ \alpha_{12} & \alpha_{22} & \alpha_{23} \\ \alpha_{13} & \alpha_{23} & \alpha_{33} \end{pmatrix} \begin{pmatrix} \cos(\theta) & -\sin(\theta) & 0 \\ \sin(\theta) & \cos(\theta) & 0 \\ 0 & 0 & 1 \end{pmatrix} =$$

$$\begin{pmatrix} \cos(\theta)\alpha_{11} + \sin(\theta)\alpha_{12} & -\sin(\theta)\alpha_{11} + \cos(\theta)\alpha_{12} & \alpha_{13} \\ \cos(\theta)\alpha_{12} + \sin(\theta)\alpha_{22} & -\sin(\theta)\alpha_{12} + \cos(\theta)\alpha_{22} & \alpha_{23} \\ \cos(\theta)\alpha_{13} + \sin(\theta)\alpha_{23} & -\sin(\theta)\alpha_{13} + \cos(\theta)\alpha_{23} & \alpha_{33} \end{pmatrix} =$$

$$\cos(\theta) \begin{pmatrix} \alpha_{11} & \alpha_{12} & 0 \\ \alpha_{12} & \alpha_{22} & 0 \\ 0 & 0 & 0 \end{pmatrix} + \sin(\theta) \begin{pmatrix} \alpha_{12} & -\alpha_{11} & 0 \\ \alpha_{22} & -\alpha_{12} & 0 \\ 0 & 0 & 0 \end{pmatrix} +$$

$$\begin{pmatrix} 0 & 0 & \alpha_{13} \\ 0 & 0 & \alpha_{23} \\ \cos(\theta)\alpha_{13} + \sin(\theta)\alpha_{23} & -\sin(\theta)\alpha_{13} + \cos(\theta)\alpha_{23} & \alpha_{33} \end{pmatrix}, \tag{5.52}$$

and

$$\begin{pmatrix} \cos(\theta) & -\sin(\theta) & 0 \\ \sin(\theta) & \cos(\theta) & 0 \\ 0 & 0 & 1 \end{pmatrix} \begin{pmatrix} \alpha_{11} & \alpha_{12} & \alpha_{13} \\ \alpha_{12} & \alpha_{22} & \alpha_{23} \\ \alpha_{13} & \alpha_{23} & \alpha_{33} \end{pmatrix} =$$

$$\begin{pmatrix} \cos(\theta)\alpha_{11} - \sin(\theta)\alpha_{12} & \cos(\theta)\alpha_{12} + -\sin(\theta)\alpha_{22} & \cos(\theta)\alpha_{13} - \sin(\theta)\alpha_{23} \\ \sin(\theta)\alpha_{11} + \cos(\theta)\alpha_{12} & \sin(\theta)\alpha_{12} + \cos(\theta)\alpha_{22} & \sin(\theta)\alpha_{13} + \cos(\theta)\alpha_{23} \\ \alpha_{13} & \alpha_{23} & \alpha_{33} \end{pmatrix} =$$

$$\cos(\theta) \begin{pmatrix} \alpha_{11} & \alpha_{12} & 0 \\ \alpha_{12} & \alpha_{22} & 0 \\ 0 & 0 & 0 \end{pmatrix} + \sin(\theta) \begin{pmatrix} -\alpha_{12} & -\alpha_{22} & 0 \\ \alpha_{11} & \alpha_{12} & 0 \\ 0 & 0 & 0 \end{pmatrix} +$$

$$\begin{pmatrix} 0 & 0 & \cos(\theta)\alpha_{13} - \sin(\theta)\alpha_{23} \\ 0 & 0 & \sin(\theta)\alpha_{23} + \cos(\theta)\alpha_{23} \\ \alpha_{13} & \alpha_{23} & \alpha_{33} \end{pmatrix}. \quad (5.53)$$

Equating (5.52) and (5.53), and subtracting $\cos(\theta)$ terms, one obtains

$$\sin(\theta) \begin{pmatrix} \alpha_{12} & -\alpha_{11} & 0 \\ \alpha_{22} & -\alpha_{12} & 0 \\ 0 & 0 & 0 \end{pmatrix} + \begin{pmatrix} 0 & 0 & \alpha_{13} \\ 0 & 0 & \alpha_{23} \\ \cos(\theta)\alpha_{13} + \sin(\theta)\alpha_{23} & -\sin(\theta)\alpha_{13} + \cos(\theta)\alpha_{23} & \alpha_{33} \end{pmatrix} =$$

$$\sin(\theta) \begin{pmatrix} -\alpha_{12} & -\alpha_{22} & 0 \\ \alpha_{11} & \alpha_{12} & 0 \\ 0 & 0 & 0 \end{pmatrix} + \begin{pmatrix} 0 & 0 & \cos(\theta)\alpha_{13} - \sin(\theta)\alpha_{23} \\ 0 & 0 & \sin(\theta)\alpha_{23} + \cos(\theta)\alpha_{23} \\ \alpha_{13} & \alpha_{23} & \alpha_{33} \end{pmatrix}. \quad (5.54)$$

Assuming $\theta \neq k\pi$ for integer k, one sees that each term on the left and right must be equal for the entire expression to be equal. This yields a 2×2 matrix equation involving $\alpha_{11}, \alpha_{12}, \alpha_{22}$ and two possible matrix-vector equations involving $\alpha_{13}, \alpha_{23}, \alpha_{33}$. Only one of the two matrix-vector equations is necessary. The other is redundant. The equations obtained are

$$\begin{pmatrix} \alpha_{12} & -\alpha_{11} \\ \alpha_{22} & -\alpha_{12} \end{pmatrix} = \begin{pmatrix} -\alpha_{12} & -\alpha_{22} \\ \alpha_{11} & \alpha_{12} \end{pmatrix}, \quad (5.55)$$

and,

$$\begin{pmatrix} \cos(\theta) & -\sin(\theta) \\ \sin(\theta) & \cos(\theta) \end{pmatrix} \begin{pmatrix} \alpha_{13} \\ \alpha_{23} \end{pmatrix} = \begin{pmatrix} \alpha_{13} \\ \alpha_{23} \end{pmatrix}. \tag{5.56}$$

From (5.55), one can see that $\alpha_{11} = \alpha_{22}$ and $\alpha_{12} = 0$. (5.56) may be re-written as

$$\begin{pmatrix} \cos(\theta) & -\sin(\theta) \\ \sin(\theta) & \cos(\theta) \end{pmatrix} \begin{pmatrix} \alpha_{13} \\ \alpha_{23} \end{pmatrix} = \begin{pmatrix} 1 & 0 \\ 0 & 1 \end{pmatrix} \begin{pmatrix} \alpha_{13} \\ \alpha_{23} \end{pmatrix}$$

$$\Rightarrow \begin{pmatrix} \cos(\theta) - 1 & -\sin(\theta) \\ \sin(\theta) & \cos(\theta) - 1 \end{pmatrix} \begin{pmatrix} \alpha_{13} \\ \alpha_{23} \end{pmatrix} = \begin{pmatrix} 0 \\ 0 \end{pmatrix}. \tag{5.57}$$

By evaluating the determinant of the matrix in (5.57) and showing it to be non-zero, one can see that the matrix has a trivial null space,

$$(\cos(\theta) - 1)^2 + \sin(\theta)^2 = \cos(\theta)^2 + \sin(\theta)^2 - 2\cos(\theta) + 1 = 2(1 - \cos(\theta)). \tag{5.58}$$

Since $\cos(\theta)$ is only equal to 1 for $\theta = k\pi$, k integer, this matrix cannot be singular. This implies $\alpha_{13} = \alpha_{23} = 0$. Writing $\alpha_{33} = \alpha_{\perp}$ and $\alpha_{11} = \alpha_{22} = \alpha_{||}$, $\underline{\alpha}$ with rotational symmetry about the vector $\hat{\mathbf{e}}$ can be written in a coordinate-free form as

$$\underline{\alpha} = \alpha_{\perp} \hat{\mathbf{e}}\hat{\mathbf{e}} + \alpha_{||}(\underline{\mathbf{I}} - \hat{\mathbf{e}}\hat{\mathbf{e}}), \tag{5.59}$$

where $\underline{\mathbf{I}}$ is the identity tensor.

5.4.3 Measured Verification

In this section, two scatterers are chosen to illustrate applications of the symmetry arguments in the previous section. These scatterers are measured in the sandbox and their results are compared with the predictions given by the small-scatterer model. In addition to the use of the symmetry relations derived in Section 5.4, the scatterers are chosen so as to restrict the possible directions of current flow by forcing certain dimensions of the scatterer to be negligibly small. By combining these techniques, each scatterer is characterized within a single unknown constant. By normalizing the measured responses with respect to the maximum value of the monostatic response, this constant can be removed,

Figure 5.9: Scatterers chosen for illustrating the symmetry properties of the polarizability matrix. On the left, a square piece of copper tape is attached to Plexiglass. The scatterer is invariant under a 90° rotation and should not conduct a significant amount of current along its thickness. In the center a square of ribbon-wire is used. The only significant direction of current flow is fixed by the direction of the wire. The nickel is included as a size comparison only. Each scatterer is a 2 cm by 2 cm square.

leaving a response for the full scan lane that can be compared directly with the results of the reciprocity model.

The two scatterers chosen in this section are shown in Fig. 5.9. The first is a square of copper tape. The thin square PEC is placed in the same configuration as that shown in Fig. 5.1 with $d = 8.8$ cm. The flat side of the tape is along the $\hat{\mathbf{z}}$ direction. This means the polarizability tensor is invariant to a 90° rotation about the $\hat{\mathbf{z}}$ axis and according to (5.59) must take the form,

$$\underline{\alpha_{\mathbf{e}}} = \alpha_{\perp}\hat{\mathbf{z}}\hat{\mathbf{z}} + \alpha_{||}(\underline{\mathbf{I}} - \hat{\mathbf{z}}\hat{\mathbf{z}}). \tag{5.60}$$

Since the thickness along the z dimension has been set negligibly small, no current should be able to flow in this direction. This implies that the term $\alpha_{\perp}$ can be set to zero. This gives the expression,

$$\underline{\alpha_{\mathbf{e}}} = \alpha_e(\hat{\mathbf{x}}\hat{\mathbf{x}} + \hat{\mathbf{y}}\hat{\mathbf{y}}), \tag{5.61}$$

where α_e is unknown. Since the only possible current loop on the scatterer would have to be in the xy plane, the only magnetic moment that could be produced is along the $\hat{\mathbf{z}}$ direction. This implies that the $\underline{\alpha_{\mathbf{m}}}$ tensor must take the form,

$$\underline{\alpha_{\mathbf{m}}} = \alpha_1\hat{\mathbf{z}}\hat{\mathbf{x}} + \alpha_2\hat{\mathbf{z}}\hat{\mathbf{y}} + \alpha_3\hat{\mathbf{z}}\hat{\mathbf{z}}. \tag{5.62}$$

Because the tensor must be symmetric, $\alpha_1 = \alpha_2 = 0$. This means the scatterer's magnetic response is entirely related to the H_z component. Because the H_z component is fairly small compared with the E_x and E_y components over the region where a significant response is obtained from the scatterer, the magnetic properties of the scatterer are ignored here. It is shown in the verification that this is not a bad approximation. With only a single unknown for the scatterer, α_e, the V_{mono} and V_{bi} scattered monostatic and bistatic voltages can be written from (5.27) and (5.28). Suppose the induced field in the ground is known for all positions when the antennas are transmitting from position $x = 0$ with field intensities, $\vec{\mathbf{E}}^{i,1}$ and $\vec{\mathbf{E}}^{i,2}$.

$$
\begin{aligned}
V_{mono}(\omega) &= -\frac{j\omega\epsilon\alpha_e Z}{2V_{inc}(\omega)} \left(E_x^{i,1}(x,z,\omega) E_x^{i,1}(x,z,\omega) + E_y^{i,1}(x,z,\omega) E_y^{i,1}(x,z,\omega) \right) \\
V_{bi}(\omega) &= -\frac{j\omega\epsilon\alpha_e Z}{2V_{inc}(\omega)} \left(E_x^{i,2}(x,z,\omega) E_x^{i,1}(x,z,\omega) + E_y^{i,2}(x,z,\omega) E_y^{i,1}(x,z,\omega) \right). \qquad (5.63)
\end{aligned}
$$

The expressions given allow two FDTD simulations to predict the response from a scatterer at any location in the ground. In the measurement situation, however, the scatterer is buried at a fixed location and the antennas are scanned over the ground. If one makes the additional assumption that the ground is homogeneous, the situation where the antennas are moved while the scatterer is stationary is equivalent to the situation of where the antennas are stationary and the scatterer moves. One can then use the FDTD simulations to calculate the full scan lane response of a fixed scatterer.

If the antennas are placed at scan location x and the scatterer is fixed at location $(0, -8.8)$ cm, the induced field in the ground is $\vec{\mathbf{E}}^{i,k}(-x, -d, \omega)$. This allows the complete scan response to be calculated as a function of time by inverse Fourier transforming (5.63) and negating the x coordinate. The response is seen and compared to a measured version of the same situation in Fig. 5.10. Considering the degree of approximation involved in assuming the homogeneity of the sand, the responses show excellent agreement. A primary feature of interest is the similarity of the monostatic response shown to Fig. 4.31 where a spherical PEC is measured. Both responses have a long dispersed pulse that occurs at later times than the initial peak seen in the bistatic response. One key difference is that

the monostatic response shown here is reduced only directly above the scatterer while the sphere shows no response at the time of the bistatic peak at all. There is not at present any explanation for this behavior, but it is shown in Section 5.6 that this is not simply because the scatterer used here has only a single axis of symmetry while the sphere has continuous rotational symmetry.

The second scatterer chosen is a square of ribbon-wire. Ribbon-wire consists of a row of thin parallel wires, so any scattered currents on the wire must go along the same direction. There is no rotational symmetry to ribbon-wire, so the general expression for a polarizability tensor must be used. The constraint that current must only point along the direction of the wires, however, constrains the tensor considerably. In particular, if $\hat{\mathbf{e_k}}$ is an orthonormal basis and the wire is pointing along the direction $\hat{\mathbf{e_1}}$ then the tensor must be of the form

$$\underline{\alpha_{\mathbf{e}}} = \alpha_{11}\hat{\mathbf{e_1}}\hat{\mathbf{e_1}} + \alpha_{12}\hat{\mathbf{e_1}}\hat{\mathbf{e_2}} + \alpha_{13}\hat{\mathbf{e_1}}\hat{\mathbf{e_3}}, \tag{5.64}$$

since otherwise currents could be induced in a direction other than $\hat{\mathbf{e_1}}$. However, this tensor is not symmetric, so the tensor must be of the form

$$\underline{\alpha_{\mathbf{e}}} = \alpha\hat{\mathbf{e_1}}\hat{\mathbf{e_1}}. \tag{5.65}$$

No significant loops of current should exist on the scatterer so $\underline{\alpha_{\mathbf{m}}} = 0$. If the scatterer is oriented so that the wires point in the $\hat{\mathbf{y}}$ direction and located at $(0, -d)$ when the antennas are placed at x, one can obtain an expression for the bistatic and monostatic radar responses. Let $\vec{\mathbf{E}}^{i,1}(x, z, \omega)$ be the field induced at the position (x, z) when a voltage wave of unity magnitude excites the transmit antenna and let $\vec{\mathbf{E}}^{i,2}(x, z, \omega)$ be the field induced at the position (x, z) under the same circumstances for the receive antenna. One then obtains,

$$V_{mono}(\omega) = -\frac{j\omega\epsilon\alpha_e Z}{2V_{inc}(\omega)} E_y^{i,1}(-x, z, \omega) E_y^{i,1}(-x, z, \omega) \tag{5.66}$$

$$V_{bi}(\omega) = -\frac{j\omega\epsilon\alpha_e Z}{2V_{inc}(\omega)} E_y^{i,2}(-x, z, \omega) E_y^{i,1}(-x, z, \omega). \tag{5.67}$$

Using these expressions and inverse Fourier transforming, one can obtain time-domain responses for each scan position of the antennas. The ribbon wire was buried in the sandbox

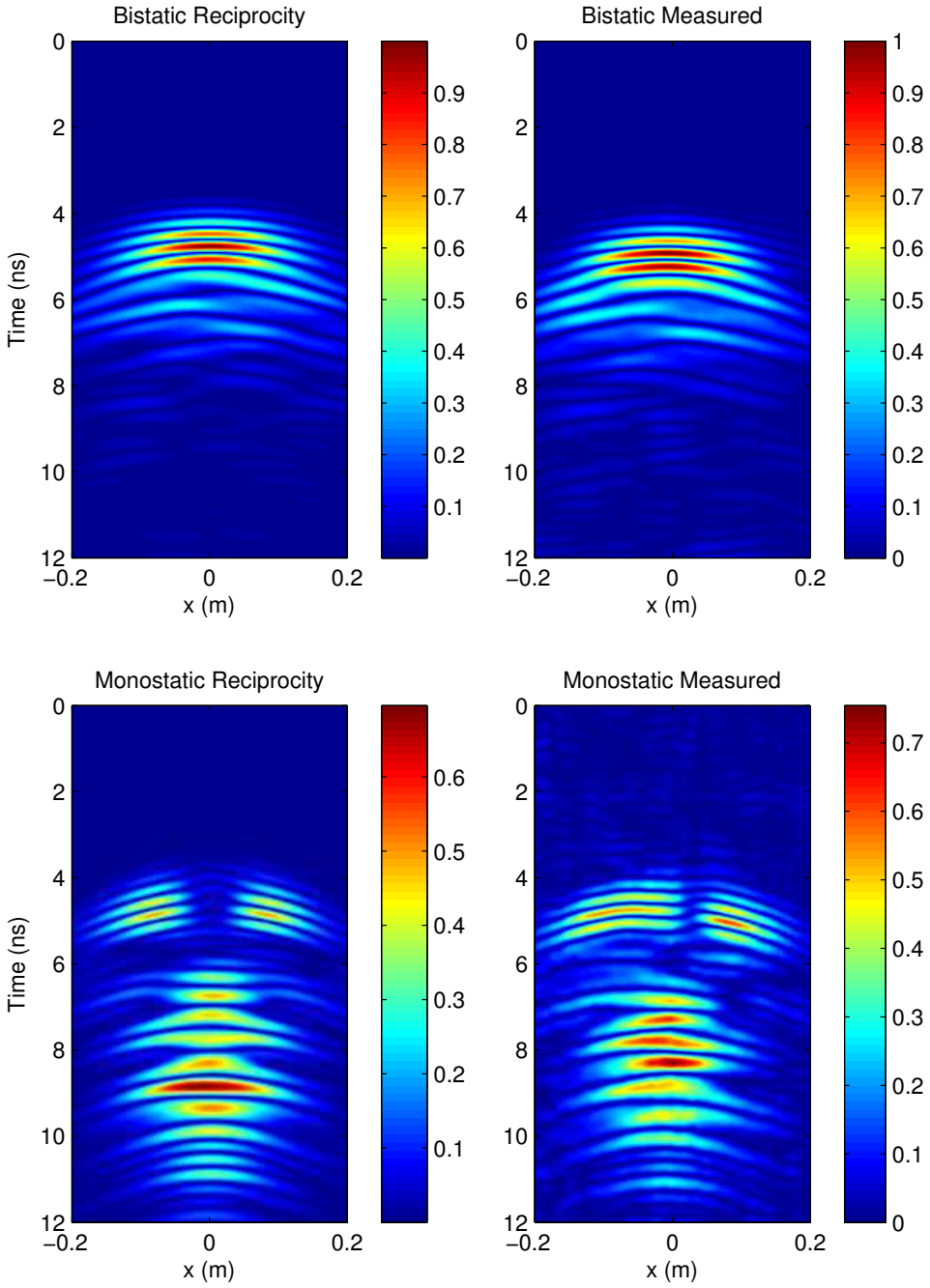

Figure 5.10: Monostatic and bistatic responses of a 2 cm by 2 cm PEC square buried 8.8 cm deep in the sand box. Comparisons are made to the small scatterer model. Responses are normalized with respect to the maximum value of the bistatic response. This removes the single unknown constant, α_e in (5.63).

at $d = 6.4$ cm. The comparison of the measurement to the reciprocity relation is shown in Fig. 5.11.

The bistatic responses shown are very similar. The monostatic responses show the same shape but differ by a constant factor. It is shown in Section 5.5 that the ratio of the monostatic to bistatic response varies extremely rapidly as a function of depth, so this may be a very difficult constant to match to measurement without a better knowledge of the position of the scatterer after burial. It should be noted that the monostatic response is much stronger than the bistatic response for an asymmetric scatterer.

5.5 Analysis of the Small-Scatterer Responses

Having verified the small scatterer model using the FDTD model and measurements, an attempt to analyze the system using the model is undertaken. Since the intensity of the response is essentially a product of the induced fields for each antenna, one should be able to make some general statements about the GPR system by viewing these field intensity products. In this section, several metrics are proposed to view the responses to asymmetric scatterers and symmetric scatterers in a normalized way. These field intensity plots are shown as the parameters of the GPR system h and ϵ_r are varied.

The first analysis plots show the response to an asymmetric scatterer with a scattering tensor of the form $\hat{\mathbf{y}}\hat{\mathbf{y}}$. The response to a scatterer of the form $\hat{\mathbf{x}}\hat{\mathbf{x}}$ is not significantly different over the operating band. These responses are normalized with respect to the maximum value seen in a given trend, and this normalization is specific to the trend being shown in a particular series. The intensities of the monostatic response and bistatic response, I_{mono} and I_{bi}, are,

$$I_{mono}(x, z, f, \epsilon_r, h) = \left| E_y^{i,1}(x, z, f, \epsilon_r, h) E_y^{i,1}(x, z, f, \epsilon_r, h) \right| \tag{5.68}$$

$$I_{bi}(x, z, f, \epsilon_r, h) = \left| E_y^{i,2}(x, z, f, \epsilon_r, h) E_y^{i,1}(x, z, f, \epsilon_r, h) \right|, \tag{5.69}$$

where h, x and z are defined in Fig. 5.1, and f is the frequency.

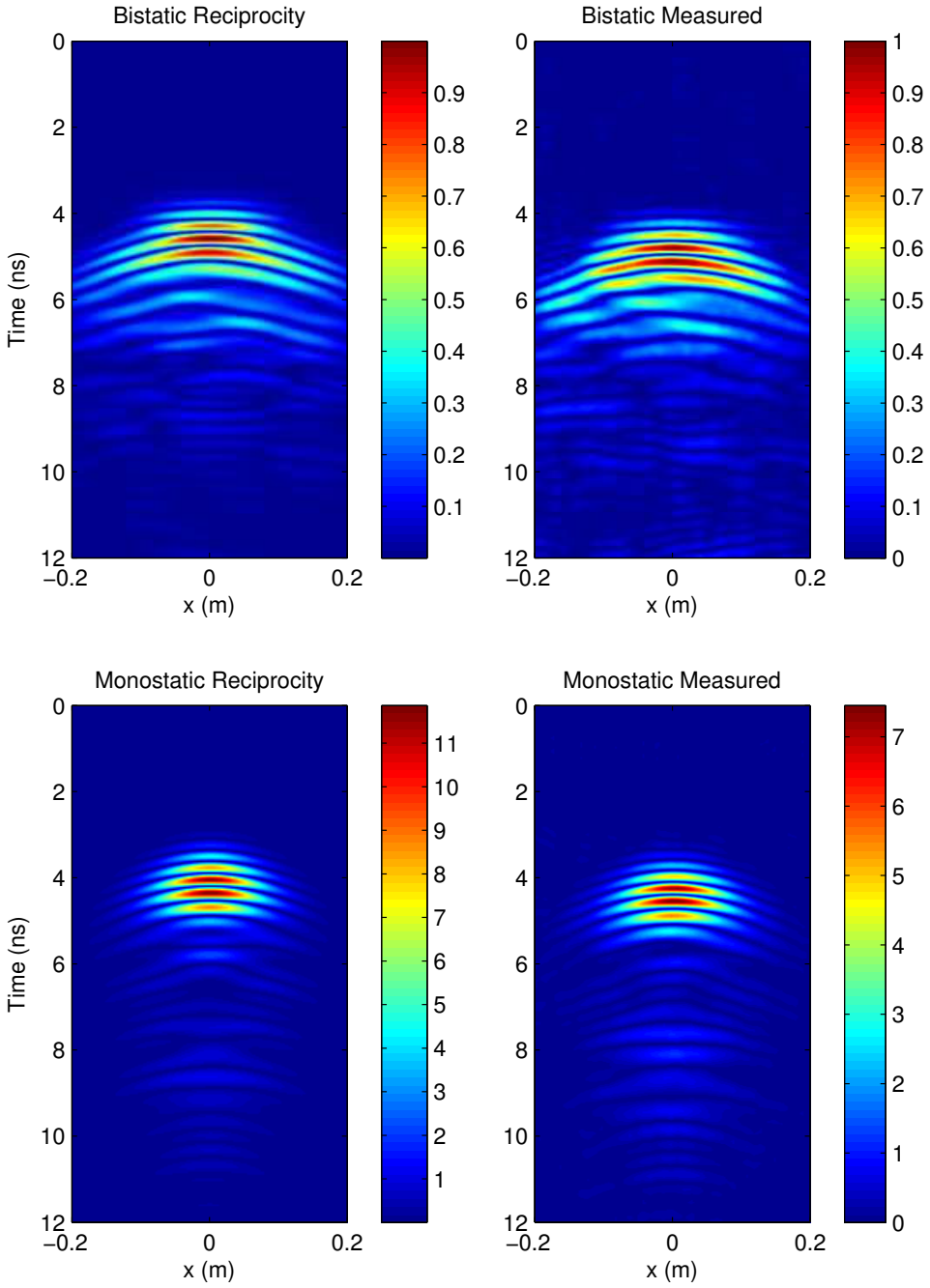

Figure 5.11: Monostatic and bistatic responses of a 2 cm by 2 cm piece of ribbon wire buried 6.4 cm deep in the sand box. Comparisons are made to the small scatterer model. Responses are normalized with respect to the maximum value of the bistatic response. This removes the single unknown constant, α_e in (5.67).

5.5.1 Dielectric Constant and Beam Narrowing

To study the effect of the dielectric constant for the ground on the responses to linear targets, a metric was proposed where the height of the antennas above the ground was held fixed,

$$I^{\epsilon_r}_{mono}(x,z,f,\epsilon_r) = \frac{I_{mono}(x,z,f,\epsilon_r,5.5\text{cm})}{\max\limits_{\{z<0,x,\epsilon_r\}} I_{mono}(x,z,f,\epsilon_r,5.5\text{cm})}$$
$$I^{\epsilon_r}_{bi}(x,z,f,\epsilon_r) = \frac{I_{bi}(x,z,f,\epsilon_r,5.5\text{cm})}{\max\limits_{\{z<0,x,\epsilon_r\}} I_{mono}(x,z,f,\epsilon_r,5.5\text{cm})}. \tag{5.70}$$

A plot of $I^{\epsilon_r}_{mono}$ is shown in Fig. 5.14 and $I^{\epsilon_r}_{bi}$ is shown in Fig. 5.15.

The plots show one frequency below the operating region and three frequencies in the operating region of the antenna. The monostatic responses are easier to interpret than the bistatic responses, since they are just the square norm of the field intensity. Looking at these, the main effect that can be seen is that the dielectric constant causes the main beam to become narrower. This effect is consistent with how rays transmitting into a half-space from different angles would behave inside the half-space. At higher dielectric values the rays would tend to concentrate toward the center by Snell's law. This effect has its counterpart in the bistatic responses. Whereas the monostatic response is the square of the field intensity, the bistatic is the product of the two intensities related to the T and R antennas. As such, as the two cones for the antennas become narrower, the intersection becomes less wide and lower in intensity. A diagram of this behavior is shown in Fig. 5.12. This accounts for the shape seen in the bistatic patterns as the dielectric constant increases.

A second important feature of the plots shown is that the bistatic response is in general much smaller than the monostatic response. By viewing the bistatic response as the intersection of two patterns, it is clear that sufficiently far away from the antennas the bistatic and monostatic responses should be nearly the same magnitude, however, for the depths in this study, this depth has not been reached. The antennas used are fairly close to one another, so it may be the case that to find scatterers in this region, less than 30 cm below the ground, these antennas must be tilted toward one another for use in the bistatic mode. Since tilting the antennas toward one another would be very difficult in the structured

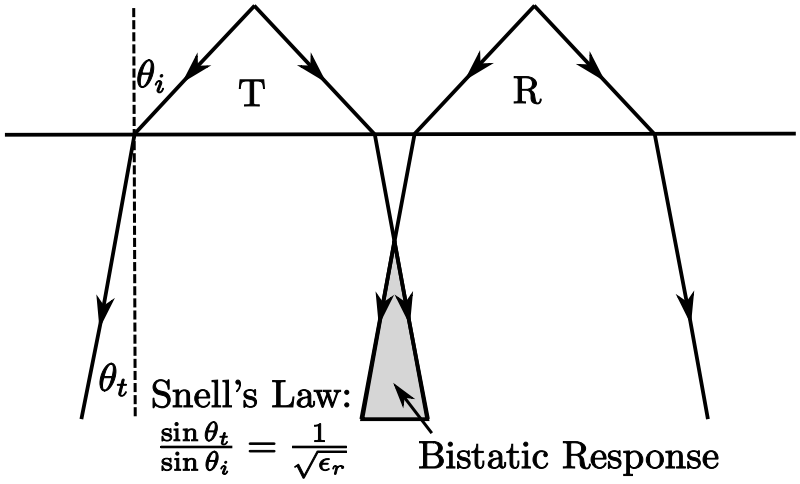

Figure 5.12: A geometric optics approximation that could explain the effect of the dielectric on the beam width seen. Snell's law predicts that rays transmitted into the half-space will propagate nearer to perpendicular to the air-ground interface as ϵ_r increases.

FDTD mesh, exploring the idea further is deemed outside the scope of the thesis.

5.5.2 Distance from Ground and Rapid Field Reduction

In this section, a similar metric to (5.70) is constructed in order to compare the GPR responses for a $\hat{\mathbf{y}}\hat{\mathbf{y}}$ scatterer as the distance of the antennas from the ground is varied. The only difference is the normalization,

$$I^h_{mono}(x,z,f,h) = \frac{I_{mono}(x,z,f,2.35,h)}{\max\limits_{\{z<0,x,h\}} I_{mono}(x,z,f,2.35,h)}$$
$$I^h_{bi}(x,z,f,h) = \frac{I_{bi}(x,z,f,2.35,h)}{\max\limits_{\{z<0,x,h\}} I_{mono}(x,z,f,2.35,h)}. \tag{5.71}$$

Graphs were constructed using the metric in (5.71) for various frequencies and heights. The bistatic response is shown in Fig. 5.16 and the monostatic response is shown in Fig. 5.17.

The immediate conclusion is that closer antennas detect better. Ignoring this, it is interesting to note that the bistatic responses increase in intensity about 5-10 dB over the 8 cm height variation shown, while the maximum monostatic responses vary much more rapidly by 15-20 dB. While not entirely obvious from Fig. 5.17, the detection region is much more concentrated very near the surface for closer antennas. A better illustration of this fact can be seen by taking a cross-section of each graph directly below the T antenna

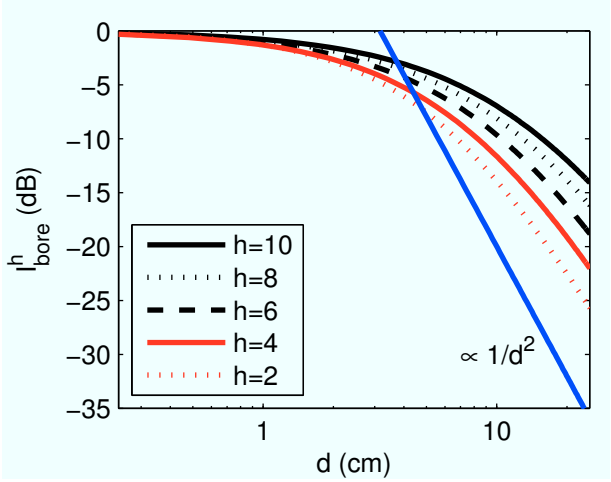

Figure 5.13: I^h_{bore} is shown for a number of heights at the fixed frequency of 1.19 GHz. This frequency is chosen because it is within the operating band of the antenna. It can be seen that the antenna configurations that are closest to the ground show the fastest decrease in intensity with the depth of the target. A curve of $1/d^2$ is shown to compare the slopes of the curves.

and plotting each response normalized to its own maximum value. This is taken for a single frequency and referred to as I^h_{bore}. This is defined to be

$$I^h_{bore}(z,h) = \frac{I^h_{mono}(0 \text{ cm}, z, 1.19 \text{ GHz}, 2.35, h)}{\max\limits_z I^h_{mono}(0 \text{ cm}, z, 1.19 \text{ GHz}, 2.35, h)}. \tag{5.72}$$

A graph of I^h_{bore} is shown for various h in Fig. 5.13. Here it can be seen that the most rapid decrease from the maximum value (0 dB) occurs for the lowest heights. For reference, a line proportional to $1/d^2$ is shown. If fields in the ground were to decay as $1/r$, where r is the distance from the antenna, then this $1/d^2$ line would have the same slope as responses shown on a log-log plot. The fact that none of the curves reach a point where $1/d^2$ decay occurs suggests that they have not reached the far-field.

The data suggests that a monostatic antenna would be much more sensitive to clutter at the surface of the ground than a bistatic antenna would be. In addition, the closer the antennas come to the ground surface, the more this would be the case. Finally, the closest heights show that even the bistatic antenna begins to have intensity peaks very near the surface of the ground.

5.5.3 Rejection of Symmetric Scatterers and the Ground

In this section, a metric is defined that relates to the discussion about circular polarization in the ground near the antennas. Circular polarization is typically defined in the far-field by stating that the electric and magnetic field vectors rotate about the propagation vector. The propagation vector is the direction of maximal phase change for the electric and magnetic fields [4]. In the far-field, the phase variation with position of the fields is related only to the distance from the antenna. However, in the near-field of the antenna, while the propagation vector could be defined in terms of the phase variation, it is not clear that the phase variation of the electric and magnetic fields are related, so the propagation vector concept is not useful. While the electric and magnetic fields may rotate about some axis, this axis may have no relation to the direction of maximal phase change for either the electric or magnetic field.

Because defining circular polarization is problematic in the near-field, a simple approach is to look at a property that is attributed to circular polarization and study that property instead, ignoring the question of whether it is related to circular polarization. Two such properties have been discussed earlier in the context of a GPR system. First, a linear scatterer can be rotated about the axis of CP without changing the magnitude of the response. Second, a symmetric scatterer will show no response to a CP wave. In this section, the ability of a monostatic radar configuration to reject a symmetric scatterer is studied in the presence of the ground. A metric, $I^{\epsilon_r}_{reject}$, is defined as the ratio of the monostatic response for a symmetric scatterer to the intensity of the fields in the ground.

$$I^{\epsilon_r}_{reject} = \frac{\left|\left(\vec{\mathbf{E}}^{i,1}\right)\cdot\left(\vec{\mathbf{E}}^{i,1}\right)\right|}{\left(\vec{\mathbf{E}}^{i,1}\right)^{*}\cdot\left(\vec{\mathbf{E}}^{i,1}\right)}, \tag{5.73}$$

where $*$ applies a complex conjugate to each component of the vector. This metric is undefined when the field is zero, but is also not of interest in these cases. The choice of the metric's definition is related to its value for two extremes of the electric field. If the electric field oscillates but does not change direction, it is similar to a linearly polarized wave and

[4] The propagation vector is the gradient of the phase function within a sign factor determined by the choice of Fourier transform.

the metric will evaluate to one. If the electric field rotates in some plane, it is similar to a circularly polarized wave and the metric will evaluate to zero. This is shown below.

When the metric (5.73) is evaluated for a linear electric field, $\vec{\mathbf{E}}^{i,1}$ can be written in the form $E\hat{\mathbf{e}}$, where $\hat{\mathbf{e}}$ is some real vector. The metric reduces to

$$I^{\epsilon_r}_{reject} = \frac{|E\hat{\mathbf{e}} \cdot E\hat{\mathbf{e}}|}{E^*\hat{\mathbf{e}} \cdot E\hat{\mathbf{e}}} = 1. \tag{5.74}$$

When the metric is evaluated for a circulating electric field, it must rotate about some fixed vector, $\hat{\mathbf{e_1}}$. An orthonormal basis can be constructed, $\hat{\mathbf{e_1}}, \hat{\mathbf{e_2}}, \hat{\mathbf{e_3}}$, so that the field can be expressed

$$\vec{\mathbf{E}}^i = E(\hat{\mathbf{e_2}} \pm j\hat{\mathbf{e_3}}) \tag{5.75}$$

Inserting this into the metric, (5.73), one obtains

$$I^{\epsilon_r}_{reject} = \frac{\left|E^2(\hat{\mathbf{e_2}} \pm j\hat{\mathbf{e_3}}) \cdot (\hat{\mathbf{e_2}} \pm j\hat{\mathbf{e_3}})\right|}{|E^2(\hat{\mathbf{e_2}} \mp j\hat{\mathbf{e_3}}) \cdot (\hat{\mathbf{e_2}} \pm \hat{\mathbf{e_3}})|} = 0. \tag{5.76}$$

While these statements are useful in interpreting the metric, the converse of the second statement is the most important for interpreting the graphs in this section. Below it is shown that a zero on the rejection graph indicates a region where the electric field circulates.

To show this, break the field into its real and imaginary parts

$$\vec{\mathbf{E}}^i = \vec{\mathbf{E_r}} + j\vec{\mathbf{E_i}}, \tag{5.77}$$

where $\vec{\mathbf{E_r}}$ and $\vec{\mathbf{E_i}}$ are both real vectors. If the metric (5.73) is zero, then, since the field is assumed to be non-zero, it must be true that

$$\vec{\mathbf{E}}^i \cdot \vec{\mathbf{E}}^i = 0 \tag{5.78}$$

$$\Rightarrow \vec{\mathbf{E_r}} \cdot \vec{\mathbf{E_r}} - \vec{\mathbf{E_i}} \cdot \vec{\mathbf{E_i}} + 2j\vec{\mathbf{E_r}} \cdot \vec{\mathbf{E_i}} = 0. \tag{5.79}$$

Equating the real and imaginary parts of (5.79), one obtains the two equations,

$$\vec{\mathbf{E_r}} \cdot \vec{\mathbf{E_i}} = 0 \tag{5.80}$$

$$\left|\vec{\mathbf{E_r}}\right| = \left|\vec{\mathbf{E_i}}\right|. \tag{5.81}$$

Since the fields are non-zero, neither $\vec{\mathbf{E}}_\mathbf{r}$ nor $\vec{\mathbf{E}}_\mathbf{i}$ can be a zero vector. Defining,

$$E = \left|\vec{\mathbf{E}}_\mathbf{r}\right| \tag{5.82}$$

$$\vec{\mathbf{e_2}} = \frac{\vec{\mathbf{E}}_\mathbf{r}}{E} \tag{5.83}$$

$$\vec{\mathbf{e_3}} = \frac{\vec{\mathbf{E}}_\mathbf{i}}{E} \tag{5.84}$$

$$\vec{\mathbf{e_1}} = \vec{\mathbf{e_2}} \times \vec{\mathbf{e_3}}, \tag{5.85}$$

one can substitute these definitions into (5.77) to obtain,

$$\vec{\mathbf{E}}^i = E(\vec{\mathbf{e_2}} + j\vec{\mathbf{e_3}}), \tag{5.86}$$

in the orthonormal basis $\vec{\mathbf{e_1}}, \vec{\mathbf{e_2}}, \vec{\mathbf{e_3}}$. This is (5.75).

A graph of $I^{\epsilon_r}_{reject}$ is shown for a number of ϵ_r at a fixed height of $h = 5.5$ cm in Fig. 5.18. Two key points can be taken from the graph. First, there is a clear region of rejection that takes up some angular segment in front of the antennas. This segment shows much better rejection for higher frequencies than lower ones. Second, the angular width of rejection is seen to decrease as the dielectric constant increases. This is a similar behavior to that seen in Fig. 5.15. The overall conclusion is that it is fair to say rejection occurs in the near-field, and it seems to even occur very close to the antennas. It can be seen, though, that the rejection is not as strong at lower frequencies. Comparing these results to time-domain data obtained for a symmetric scatterer in Section 5.4, one sees that this may be related to the late-time radiation that occurs directly above the scatterer. This radiation appears to consist of lower frequency content than the thin sharp pulse that occurs initially. This idea is explored more fully in Section 5.6.

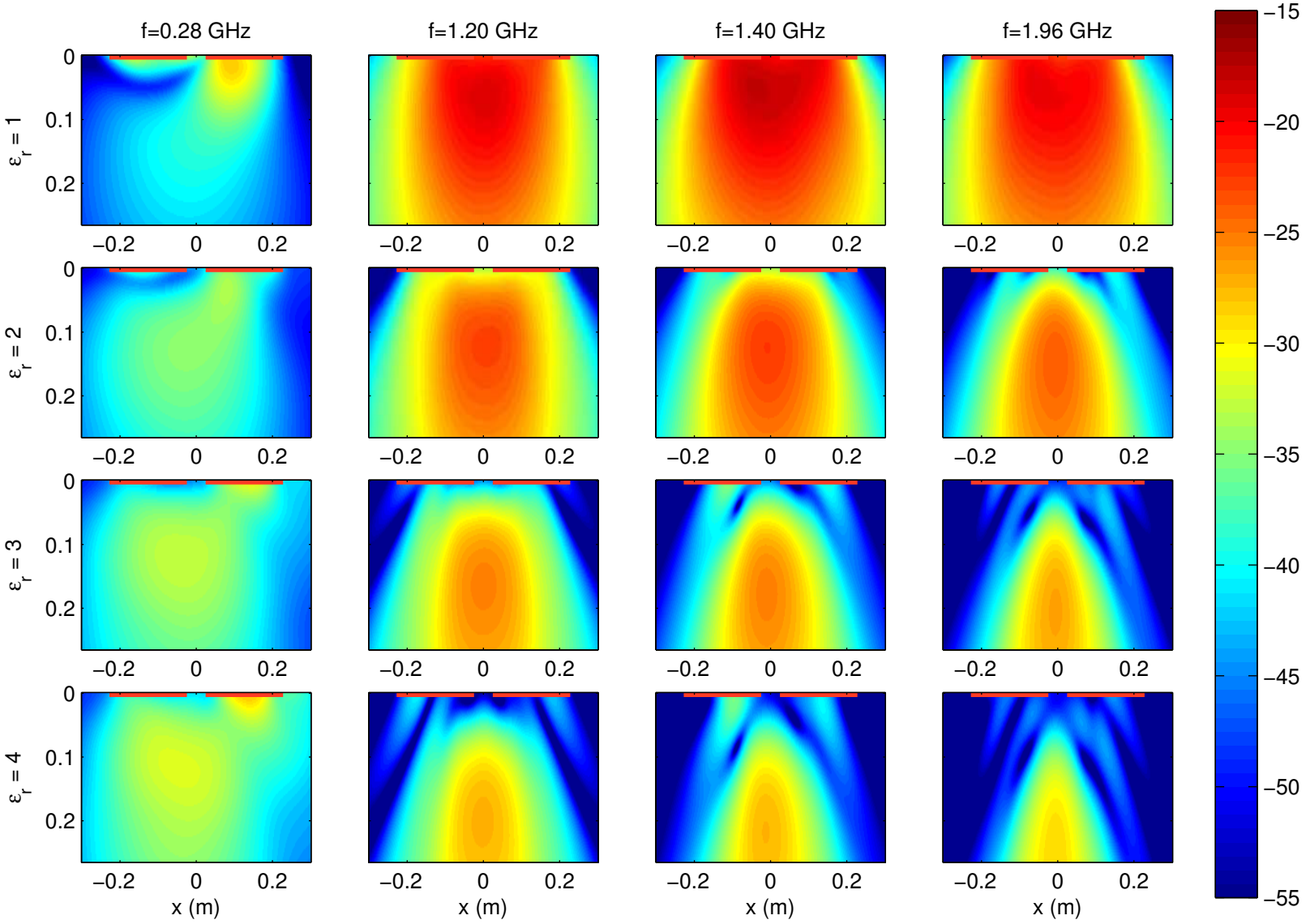

Figure 5.14: The metric $I_{bi}^{\epsilon_r}$ is shown for a number of frequencies and dielectric constants.

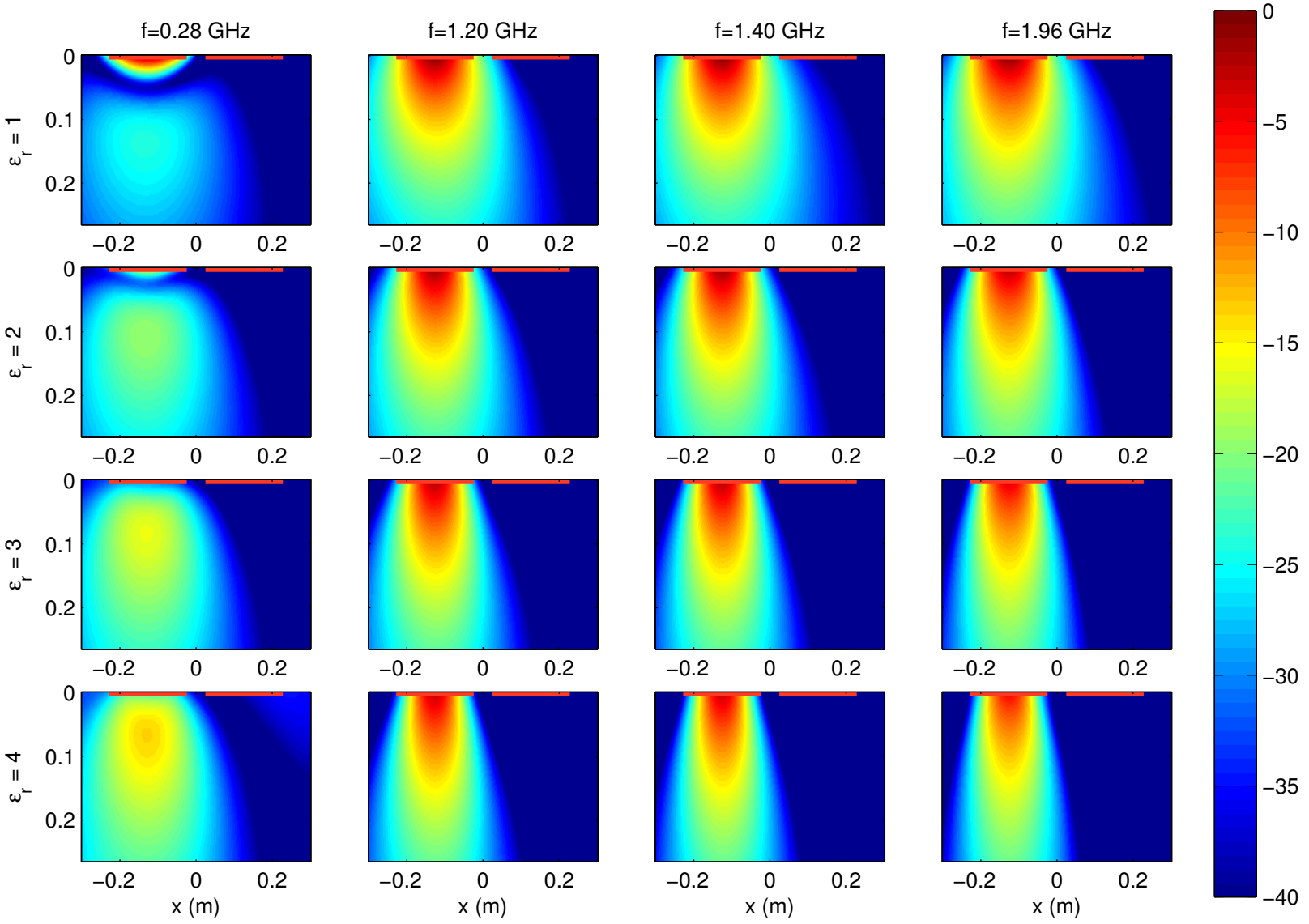

Figure 5.15: The metric $I^{\epsilon_r}_{mono}$ is shown for a number of frequencies and dielectric constants.

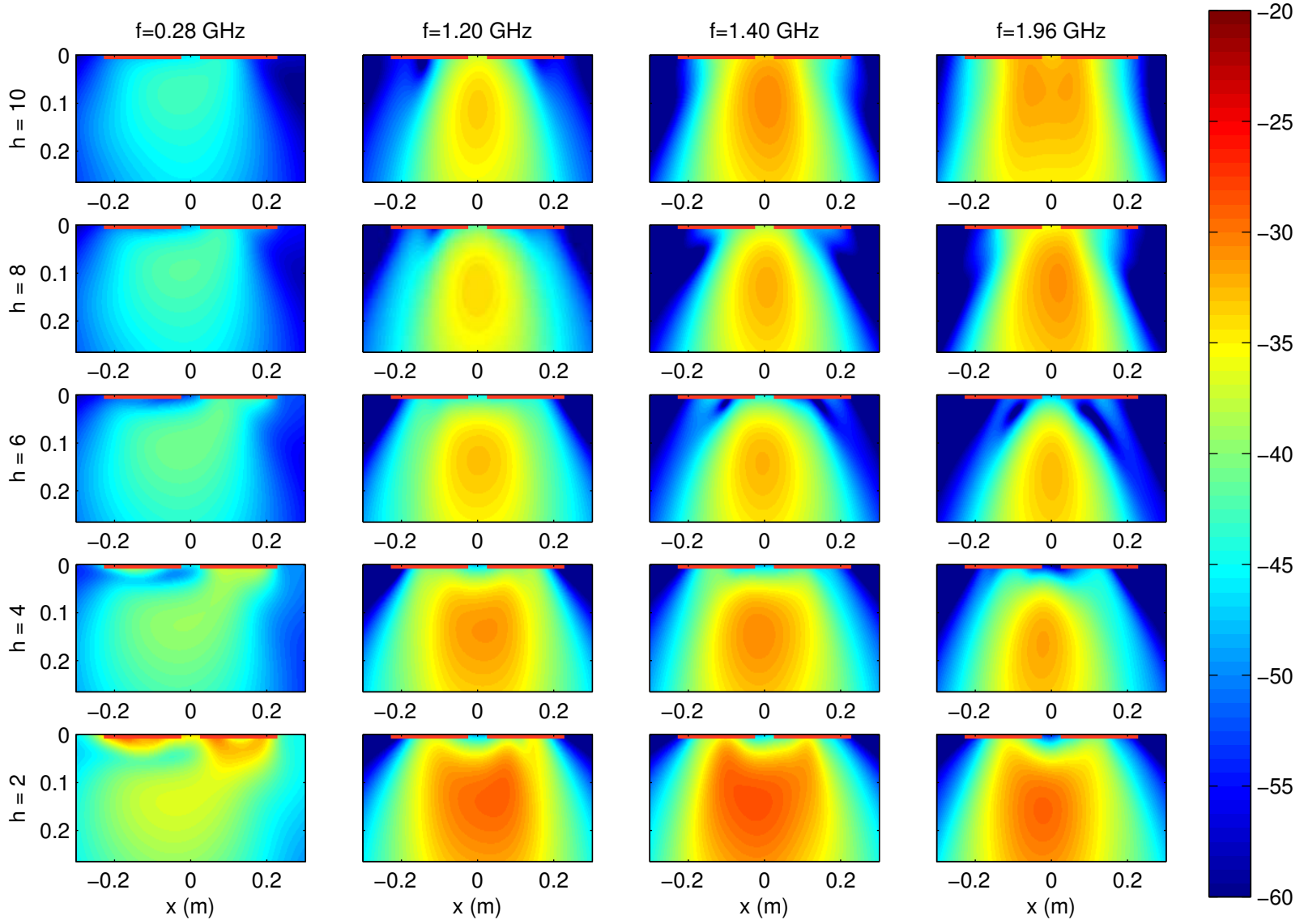

Figure 5.16: The metric I_{bi}^{h} is shown for a number of frequencies and heights.

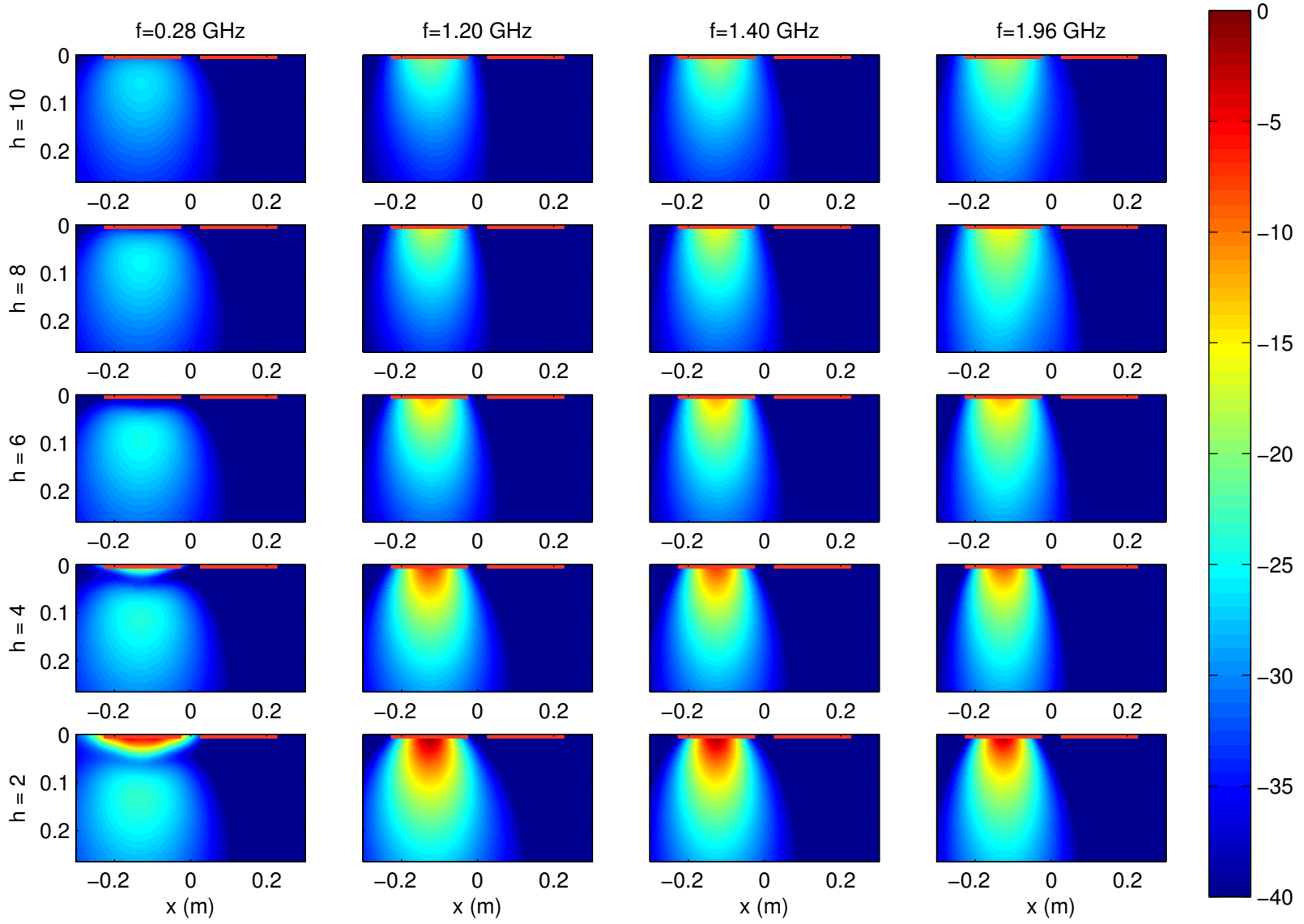

Figure 5.17: The metric I^h_{mono} is shown for a number of frequencies and heights.

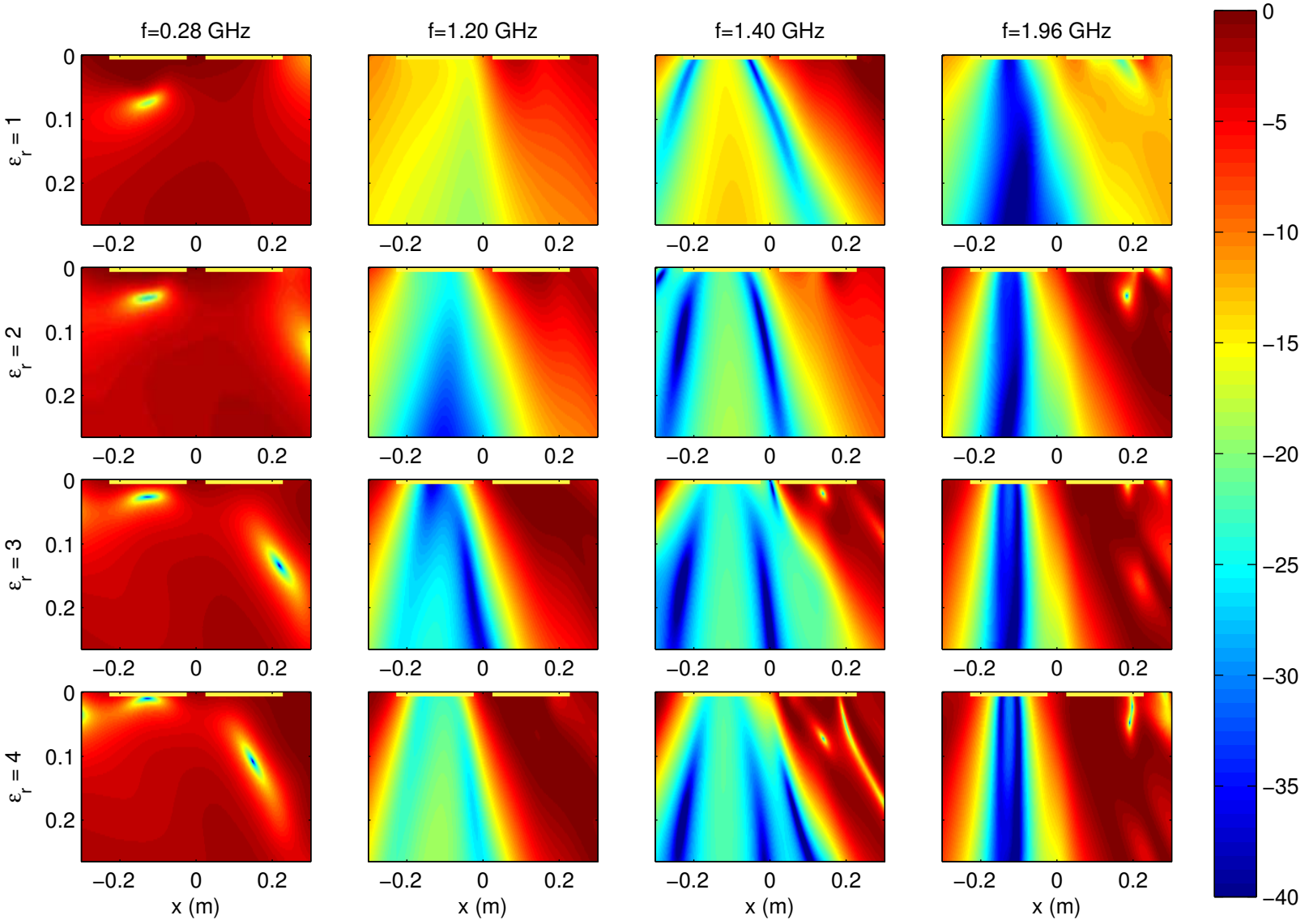

Figure 5.18: The metric $I^{\epsilon_r}_{reject}$ is shown for a number of frequencies and dielectric constants.

5.6 Late-time Symmetric-Scatterer Responses in Monostatic Data

In the monostatic results shown in Fig. 5.10, it can be seen that a scatterer with an xy symmetry has an initial response that is rejected directly above the scatterer and a late-time response that is most visible directly above the scatterer. Both responses are of a comparable magnitude to the bistatic response, so understanding the cause of this response could be important in applications where it is necessary to discriminate between symmetric and asymmetric targets. In the previous section, it was shown that the reason for this response's size compared to the bistatic response is primarily due to the fact that the monostatic response is so much stronger than the bistatic response in general. In this section, the cause of the late-time response is traced to the behavior of the spiral element and is shown to be related to its outer truncation. The monostatic response for a symmetric scatterer at some depth d takes the form given by (5.63),

$$V_{mono}(\omega) = -\frac{j\omega\epsilon\alpha_e Z}{2V_{inc}(\omega)}\left(E_x^{i,1}(0,-d,\omega)E_x^{i,1}(0,-d,\omega) + E_y^{i,1}(0,-d,\omega)E_y^{i,1}(0,-d,\omega)\right). \quad (5.87)$$

This is a sum of the responses from a y and x oriented dipole, both of which take the form

$$V_{mono}^{x,y}(\omega) = -\frac{j\omega\epsilon\alpha_e Z}{2V_{inc}}\left(E_{x,y}^{i,1}(0,-d,\omega)E_{x,y}^{i,1}(0,-d,\omega)\right). \quad (5.88)$$

These responses are inverse Fourier transformed using the modulated Gaussian pulse in (4.17). The time-domain response is shown in Fig. 5.19 along with the sum for the case of $d = 8.8$ cm used in Fig. 5.10. The responses, $V_{mono}^{x,y}$, consist of initial pulses that are in antiphase and a late-time region that is in phase. This suggests that the late-time response is always a feature of the scattering from an object, it is just usually overwhelmed by the intensity of the initial scattered response. Only when the initial scattered response is rejected, as with V_{mono}, does the secondary response become prominent enough to be noticeable.

Further decomposition of the responses shown in (5.88) can be made by considering the effect of each portion on the inverse Fourier transform. In particular, consider one of the responses, x or y. The transfer function between V_{inc} and this field has an impulse response of $e_{x,y}(t)$ and the modulated Gaussian pulse used has the form $v_{inc}(t)$. One can then write

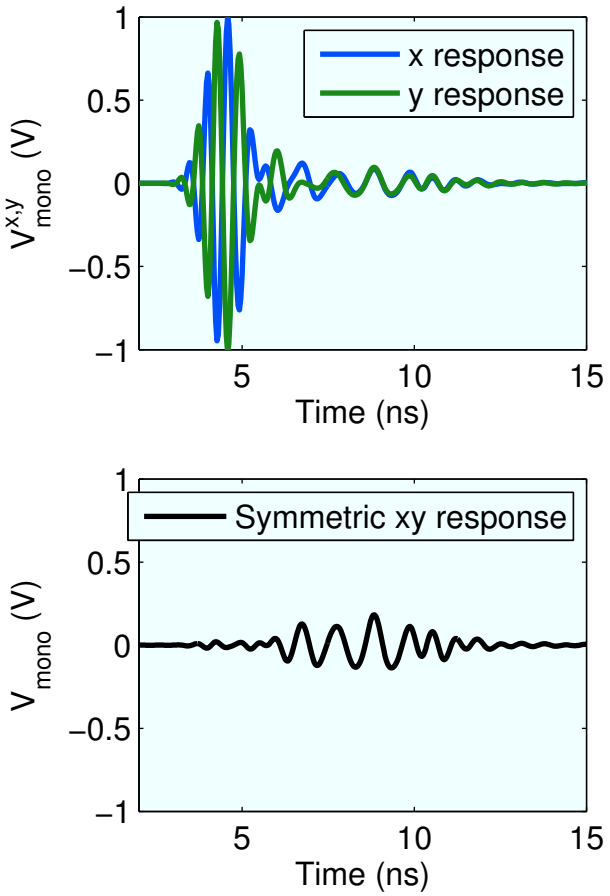

Figure 5.19: The response to a symmetric scatterer is the sum of the response to an x-oriented dipole and a y-oriented dipole. Each is shown above and the sum below would be the response of the symmetric scatterer. This is only known within a constant factor, so all responses here are normalized with respect to the largest value of the x response.

the time-domain form, $v_{mono}^{x,y}(t)$ as

$$v_{mono}^{x,y}(t) = -\frac{\epsilon\alpha_e Z}{2}\left(\frac{d}{dt}e_{x,y}(t) * e_{x,y}(t) * v_{inc}(t)\right). \tag{5.89}$$

The transfer function from the incident voltage to the monostatic response is the convolution of the field induced by an impulse with its own derivative. By looking at the individual fields $e_{x,y}(t)$ it may be possible to ascertain why the signals initially cancel and later add. In Fig. 5.20, the fields,

$$e_{x,y}(t) * v_{inc}(t), \tag{5.90}$$

are shown. A modulated Gaussian excitation is chosen for $v_{inc}(t)$ with the form

$$\begin{aligned} v_{inc}(t) &= \cos\left(2\pi f_{mod}(t-t_d)\right) e^{\left(\frac{t-t_d}{\tau}\right)^2} V \\ f_{mod} &= 1.4 \text{ GHz} \\ \tau &= 0.8 \text{ ns} \\ t_d &= 2 \text{ ns}, \end{aligned} \tag{5.91}$$

where τ has been increased from its value of 0.5 ns in (4.17) in order to allow the phase-relationship between the x and y fields to be more clearly visible.

The fields, like the monostatic response, consist of two regions. The first is the main pulse from 2 ns to 5 ns and it can be seen that here the x component lags the y component by 90 degrees. This is most easily observed by noting that the maxima and minima of one component occur at the zeros of the other. The second spans from 7 ns to 11 ns and in this region, the y component lags the x component by 90 degrees. If the components were interpreted as they would be in the far-field, it could be said that directly below the antennas the waves propagate in the $-\hat{\mathbf{z}}$ direction and the initial pulse is RHCP while the late-time wave is LHCP.

In this context, it is much more clear why the secondary pulse is visible in the monostatic response. An antenna that radiates RHCP will reject LHCP incoming waves and receive RHCP waves. If the antenna transmits an initial large pulse of RHCP then a smaller pulse of LHCP, a symmetric scatterer will reflect back radiation that is initially LHCP and then

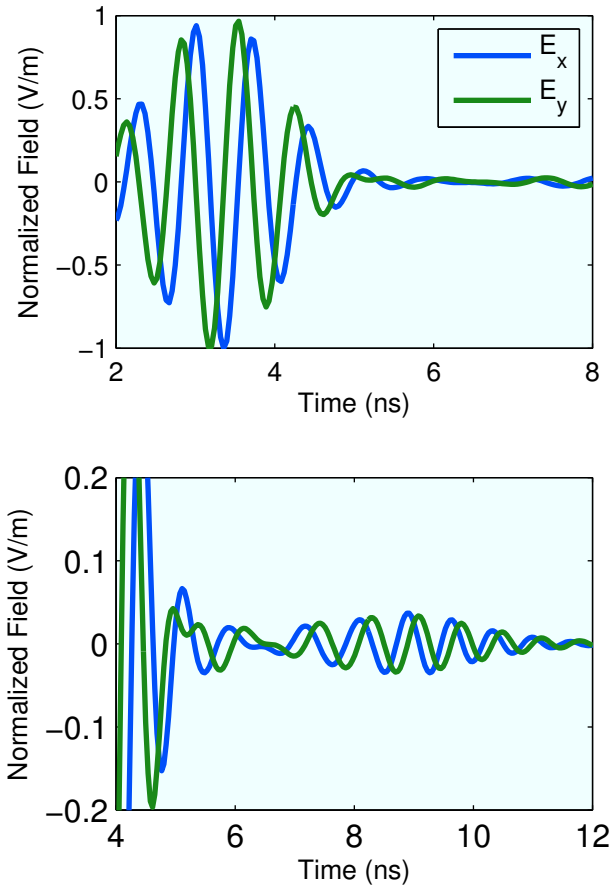

Figure 5.20: The fields directly in front of the transmitting antenna 8.8 cm into the ground when the antennas are $h = 5.5$ cm above the ground. The transmit antenna used here is right-hand circularly polarized. If the fields were interpreted in the far-field, the propagation vector would be $-\hat{\mathbf{z}}$, meaning the early-time response would represent an RHCP wave while the late-time response would represent an LHCP wave.

later RHCP. The initial received pulse of LHCP will be rejected by the antenna while the late-time RHCP pulse will be received properly. By reciprocity considerations, the initial large LHCP pulse will be received by the antenna also, it will simply be delayed and reduced in magnitude.

There are a number of reasons that the antenna in the GPR system could emit a late-time pulse because the large number of components in the system allow for many sources of a reflection. To narrow down the possibilities, components are removed from the system. The simplified system consists of a single transmit element with no absorbing can. The ground has been removed by setting $\epsilon_r = 1$, but the geometry is still like that shown in Fig. 5.1. The field from the isolated spiral element, as modeled in FDTD, is shown in Fig. 5.21. The field is shown at 14.3 cm away from the spiral plane (this is equivalent to $h = 5.5$ cm, $d = 8.8$ cm, and $\epsilon_r = 1$). The pulse (5.91) is used as the excitation of the antenna. Fig. 5.21, like Fig. 5.20, shows an initial RHCP and a late-time LHCP type field.

With a simplified model showing this behavior, it was found that the late-time response could be partially controlled either by removing low-frequency content from the spiral's excitation pulse or by increasing the outer truncation radius of the spiral. Both of these solutions are consistent with the notion that the second wave is caused by currents reflected at the spiral arms because the active region for that frequency does not radiate all power out of the wave prior to truncation. If this is the case, a possible improvement that does not involve increasing the size of the antenna is to apply resistive loading at the edges of the antenna. In Fig. 5.22, the predicted monostatic response is shown for a y oriented scatterer and a scatterer that is symmetric in the xy plane. In the top frame, this is shown for the spiral element used in this work, and in the bottom frame it is shown for the same spiral but with $R_{out} = 29.2$ cm and a substrate with radius $R = 30.5$ cm. It can be seen that the late-time reflection of the symmetric scatterer is reduced considerably by increasing R_{out}.

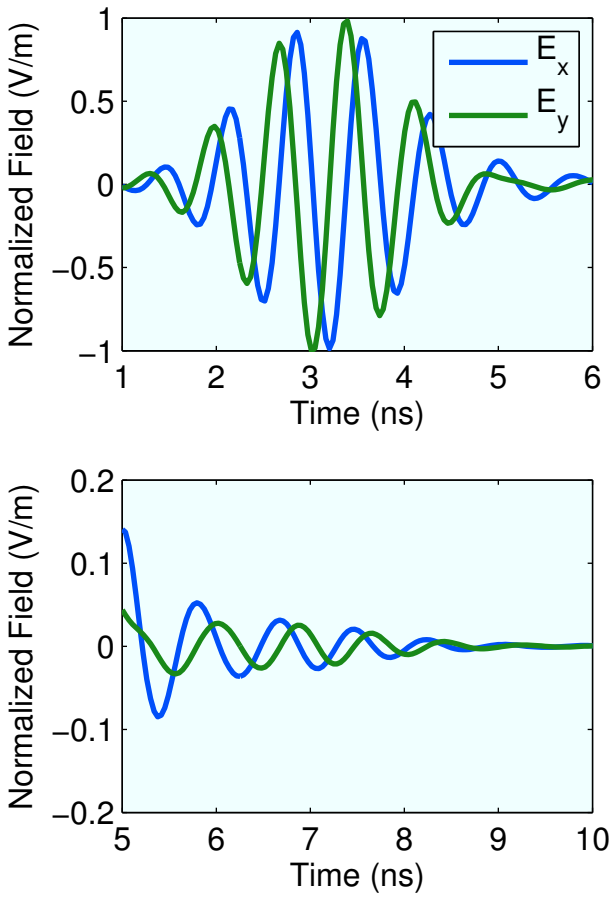

Figure 5.21: The normalized fields seen directly in front of a transmitting element 14.3 cm away. The pulse consists of two regions, one where the fields resemble an RHCP wave and a later portion where they resemble an LHCP wave.

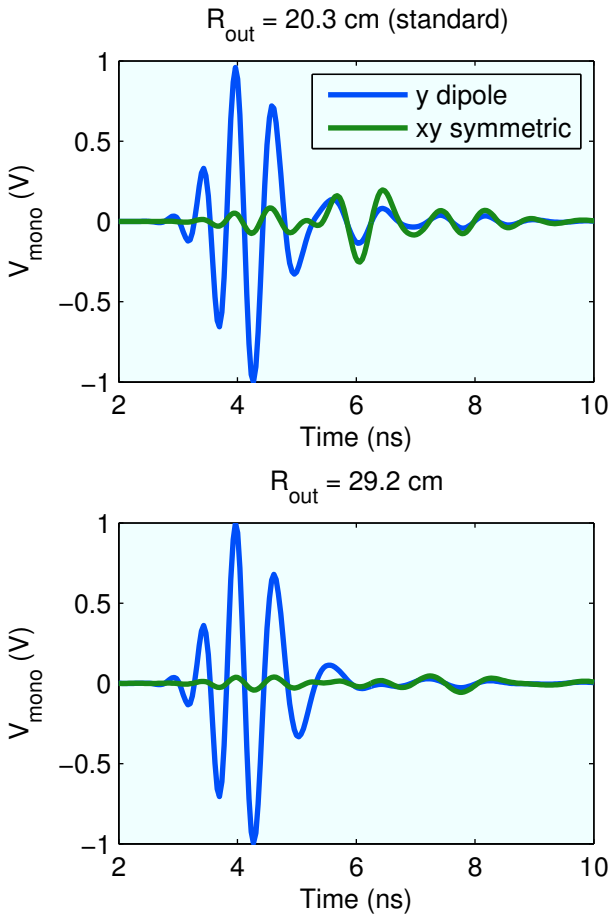

Figure 5.22: Monostatic responses for an isolated spiral element interacting with a y oriented dipole and a scatterer that is symmetric in the xy plane. It can be seen that the larger radius spiral has a better rejection of the symmetric scatterer than the small radius.

CHAPTER VI

GPR CHARACTERIZATION USING THE PLANE-WAVE SPECTRUM

This chapter details an improved method for calculating the plane wave spectrum (PWS) for an antenna in free-space. This technique was developed in order to use the PWS of an antenna in free-space to predict the fields in the ground when it radiates over a half-space of dielectric. With some approximation, this would allow a single PWS to be used to calculate the fields for antennas at any height above the ground and for any dielectric value for the ground using a single FDTD simulation. In addition, the PWS of an antenna could be used itself for analytical purposes.

Unfortunately the applicability of this method is limited for a problem where a large antenna radiates near a half-space. While the PWS can calculate the fields induced in a low-contrast ground, in a high-contrast ground, the fields can become inaccurate. The cause is the interaction between the antenna and the ground at the surface. Multiple reflections between the antenna and the ground can cause the current distribution on the antenna to change from its distribution operating in free-space. It was found that the spiral antenna shows currents that change significantly for all but a dielectric constant value of the ground very near unity. Because this restriction would limit the analysis of the spiral system considerably, the alternative method of using the FDTD model to calculate the fields in the ground directly was used in Chapter 5. Despite its limitations, the PWS is frequently used to study antennas with a low scattering cross-section, and the techniques developed in this chapter would be of use in other GPR projects.

In this chapter, a technique for reducing the truncation error present in PWS calculations is presented. The technique uses a far-field pattern for the antenna, which could be measured or calculated from a numerical model. In this work, a near-field-to-far-field transform is used to obtain the far-field pattern. It is shown that the technique reduces the truncation

error in the PWS and a rate of convergence for the $\mathcal{L}^2$ norm of the truncation error is provided. Finally, an application of the method to the prediction of the fields in a half space for a low scattering cross-section antenna (the resistive dipole) is provided.

6.1 Motivation

The angular spectrum of plane waves or the plane wave spectrum is a representation of an electromagnetic field in a sourceless homogeneous region in terms of a distribution of propagating and evanescent plane waves. The method was formalized as a general procedure by Clemmow in [63]. Early applications of the PWS focused on techniques for extracting information about the far-field pattern of an antenna from near-field data [64, 65]. The method was later used extensively by Kerns to handle more general scattering problems as well as probe compensation for pattern measurements [66].

One natural application of the PWS is the ground penetrating radar (GPR) problem. Here, the earth is typically modeled as a material half-space below the antenna. Because the interaction of a plane wave with a half-space is dictated by the Fresnel coefficients, the field under the ground may be approximately determined when the spectrum above the ground is known. This method is only exact when the radiating antenna is electrically small such as in [67], but is still a useful approximation when the antenna-ground interaction is expected to have multiple reflections [68, 69].

An area of interest in the GPR community has been the effect of the evanescent portion of the spectrum on the GPR system [70]. In order to obtain some insight into this effect, the ability to accurately calculate the complete plane wave spectrum of an antenna is necessary. Techniques for calculating the plane wave spectrum of an antenna have received considerable attention in the literature because the calculation is an important first step in obtaining the far-field pattern of an antenna in a near-field measurement facility. An extensive review of the literature on the near-field measurement process is available in [71].

To calculate the PWS, one obtains samples of the electric field over some portion of a plane in front of the antenna of interest. These samples make up a frame of data that is sometimes pretreated [72], and then sent through a fast Fourier transform (FFT) to

obtain the PWS. Because most near-field measurement facilities are for electrically large, and consequently very directive antennas, there is often not a problem with the truncation of the fields at the edges of the frame. However, as pointed out in an error analysis by Newell [73], for less directive antennas, a truncation error exists in the PWS for any finite frame size. Bucci and Migliore address this truncation error problem by using the measured near-fields to extrapolate onto a larger frame than can be measured in a facility [74]. In a more recent work, the truncation error in the PWS of an aperture antenna is removed by an iterative approach that enforces the condition that the field outside of the aperture must be zero at the aperture plane [75].

In this chapter, a method for pretreating a frame of data obtained from a numerical simulation is proposed that reduces the truncation error in the calculated PWS. An outline of the method follows: first, an approximate expression for the field outside of the frame is obtained using a near-field-to-far-field transform. This expression is then subtracted from the frame of data to obtain a reduced frame. This reduced frame is then put through an FFT. The transform of the reduced frame will have significantly less truncation error because of the more continuous transition to zero at the frame's edge. Finally, the exact Fourier transform of the portion that was removed is added back to the frame in the spatial frequency domain to obtain the complete transform.

The chapter begins with a brief description of the PWS. Next, the Hertzian dipole is used as an example of a non-directional antenna to demonstrate that the FFT method will not resolve the truncation error even for extremely large frame sizes. The method proposed to reduce the truncation error is described in detail. To illustrate the effect of the method, the PWS of a Hertzian dipole is calculated using both methods and compared against the analytical solution. Next, an error analysis is provided that shows that the method can be used to significantly reduce the truncation error in a transform at the expense of a controlled introduction of aliasing error. Finally, the method is applied to a resistively loaded dipole that is simulated using the finite difference time-domain (FDTD) method. The PWS for the antenna is shown and used to calculate the fields below ground. Finally, it is shown that the proposed method predicts the fields transmitted underground when the antenna is

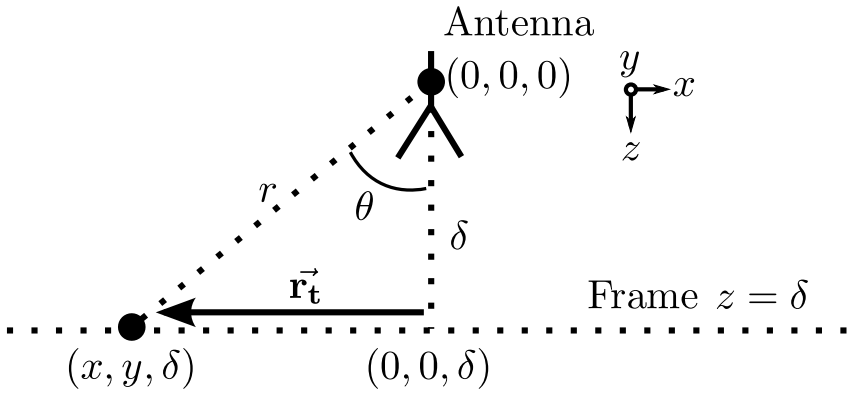

Figure 6.1: Geometry of an antenna under test when calculating a PWS.

placed nearby better than a standard windowed FFT.

6.2 Definition of the Plane-wave Spectrum

In this section, the plane wave spectrum is defined using a notation similar to that used in [76]. Consider the antenna shown in Fig. 6.1. Here an antenna radiates at an angular frequency of ω, and is located in the half-space $z < \delta$. The region $z > \delta$ contains no sources, and consists of some stratified media, which for the purposes of this chapter will mean either free-space or a half-space of a constant dielectric. The electric field at a point on the plane $z = \delta$ has a harmonic variation in time of $e^{j\omega t}$. This variation is suppressed here and the field is written $\vec{\mathbf{E}}_\delta(\vec{\mathbf{r}}_t)$, where $\vec{\mathbf{r}}_t = (x, y)$. The plane wave spectral method defines a transform between the field on the plane $z = \delta$, $\vec{\mathbf{E}}_\delta(\vec{\mathbf{r}}_t)$, and a distribution of plane waves, $\vec{\mathbf{F}}_\delta(\vec{\mathbf{k}}_t)$, using the Fourier transform pair, $\mathcal{F}^{\pm}\{\cdot\}$,

$$\vec{\mathbf{F}}_\delta(\vec{\mathbf{k}}_t) = \mathcal{F}^{+}\left\{\vec{\mathbf{E}}_\delta\right\} = \int\int \vec{\mathbf{E}}_\delta(\vec{\mathbf{r}}_t) e^{j\vec{\mathbf{k}}_t\cdot\vec{\mathbf{r}}_t} d\vec{\mathbf{r}}_t \text{ Vm}, \tag{6.1}$$

$$\vec{\mathbf{E}}_\delta(\vec{\mathbf{r}}_t) = \mathcal{F}^{-}\left\{\vec{\mathbf{F}}_\delta\right\} = \frac{1}{4\pi^2}\int\int \vec{\mathbf{F}}_\delta(\vec{\mathbf{k}}_t) e^{-j\vec{\mathbf{k}}_t\cdot\vec{\mathbf{r}}_t} d\vec{\mathbf{k}}_t \text{ V/m}, \tag{6.2}$$

where $\vec{\mathbf{k}}_t = (k_x, k_y)$. When the region $z > \delta$ consists of stratified media, a PWS at some plane $z = \delta_1$ can be propagated to another plane $z = \delta_2$ when $\delta_1, \delta_2 \geq \delta$. This propagator is closely related to those used to translate a field distribution in a transmission line to a different position in the line. In a homogeneous region, this propagator is

$$\vec{\mathbf{F}}_{\delta_2}(\vec{\mathbf{k}}_t) = \vec{\mathbf{F}}_{\delta_1}(\vec{\mathbf{k}}_t) e^{-jk_z(\delta_2-\delta_1)}, \tag{6.3}$$

where k_z is defined by the dispersion relation,

$$\vec{\mathbf{k}}_t \cdot \vec{\mathbf{k}}_t + k_z^2 = k^2. \tag{6.4}$$

When the plane $z = \delta$ is in a region with permittivity ϵ_r, $k = \sqrt{\epsilon_r} k_0 = \sqrt{\epsilon_r}\omega/c_0$ and c_0 is the speed of light in free space. The dispersion relation requires a choice of branch-cut to solve for k_z. This is determined by the sign convention used. For $e^{j\omega t}$ time variations, the chosen k_z is:

$$\begin{aligned} k_z = &\quad \sqrt{k^2 - k_t^2} \quad \text{when } k_t^2 \leq k_0^2 \\ k_z = &\quad -j\sqrt{k_t^2 - k^2} \quad \text{when } k_t^2 > k_0^2. \end{aligned} \tag{6.5}$$

When the first condition holds, k_z is real and the plane wave is propagating. When the second condition holds, k_z is imaginary and the plane wave is evanescent. The branch-cut chosen sets the condition that as $z \to \infty$, which is equivalent to $\delta_2 \to \infty$ in (6.3), each plane wave component remains finite in amplitude. Because of this, it should be noted that the PWS representation can only be valid in the half of the space that is sourceless, while in the other half the evanescent components become unbounded in amplitude.

An additional condition is imposed on the PWS in order to allow it to be fully defined by only two of its three vector components. This condition is,

$$(\vec{\mathbf{k}}_t + k_z \hat{\mathbf{z}}) \cdot \vec{\mathbf{F}}_\delta(\vec{\mathbf{k}}_t) = 0. \tag{6.6}$$

For a propagating plane-wave, condition (6.6) constrains the vector $\vec{\mathbf{F}}_\delta(\vec{\mathbf{k}}_t)$ to the plane transverse to the propagation direction. In general, (6.6) restricts $\vec{\mathbf{F}}_\delta(\vec{\mathbf{k}}_t)$ to a two-dimensional subspace that varies with $\vec{\mathbf{k}}_t$. Because of this, it is common to define the plane wave spectrum by choosing some basis for this subspace and referring to the coefficients of $\vec{\mathbf{F}}_\delta$ in that basis as the plane-wave spectrum. At present there are two main bases in use. In the work of [66] and [67], where the focus is on the use of the PWS for scattering and transmission problems, a basis that simplifies the use of the Fresnel coefficients is used. In [59] and [63], as well as in this work, the F_z component is solved using (6.6) to write $\vec{\mathbf{F}}_\delta$ in terms of its x

and y components:

$$F_z(\vec{\mathbf{k}}_t) = -\frac{k_x}{k_z}F_x(\vec{\mathbf{k}}_t) - \frac{k_y}{k_z}F_y(\vec{\mathbf{k}}_t) \tag{6.7}$$

$$\vec{\mathbf{F}}_\delta(\vec{\mathbf{k}}_t) = F_x(\vec{\mathbf{k}}_t)(\hat{\mathbf{x}} - \frac{k_x}{k_z}\hat{\mathbf{z}}) + F_y(\vec{\mathbf{k}}_t)(\hat{\mathbf{y}} - \frac{k_y}{k_z}\hat{\mathbf{z}}). \tag{6.8}$$

This basis choice will make the majority of the chapter more succinct at the expense of the final section, where the Fresnel coefficients are used.

The components F_x and F_y of $\vec{\mathbf{F}}_\delta$, $\vec{\mathbf{F}}^t_\delta$, relate to the tangential $\vec{\mathbf{E}}_\delta$ components, $\vec{\mathbf{E}}_t$, by a two dimensional Fourier transform, as seen in (6.1). Because of this, it is common to use uniform samples of $\vec{\mathbf{E}}_t$ spaced Δ apart and the FFT algorithm to calculate samples of $\vec{\mathbf{F}}_\delta$. The FFT method is discussed extensively in [77].

Since the PWS will be almost band-limited for a frame of data sufficiently far away from the antenna, the sampling cell size, Δ, can generally be chosen small enough to show no aliasing in the transform [76]. However, when this method is applied to an antenna that is not particularly directive, the assumption that the frame of data is spatially limited will not be true. When this assumption is not true, the transform has an error that is referred to as truncation error in [73]. This error can be controlled by windowing the frame of data, but this technique will not remove it completely. As pointed out in the conclusion of Yaghjian's paper [71], when the antenna pattern is non-zero in the xy-plane, the error induced by truncating the frame at some distance from the origin may not tend to zero as the frame size goes to infinity.

Correcting the truncation errors caused by non-directional antennas is the primary subject of this chapter. The Hertzian dipole is used as a test case to illustrate the effect of the proposed method on these errors. This is chosen because the field of a Hertzian dipole is known analytically in space, and because the PWS of the antenna can be calculated analytically. In the examples shown in this chapter for a Hertzian dipole, a fixed frequency of 1 GHz is chosen. By the scaling principle, however, the results given may be extended to different frequencies.

If the Hertzian dipole is modeled as a current distribution $\vec{\mathbf{J}}(\vec{\mathbf{r}}) = I\Delta_l\hat{\mathbf{y}}\delta(\vec{\mathbf{r}})$ A/m^2 where $\delta(\cdot)$ is the Dirac delta distribution, I is the current in the dipole, and Δ_l is the length of the

dipole, then the electric field induced may be expressed in terms of the standard spherical coordinates (r, θ, ϕ) where r is the distance from the origin, θ is the elevation, and ϕ is the azimuth, in the form

$$\begin{aligned}\vec{\mathbf{E}}(r,\theta,\phi) =& \frac{-jI\Delta_l e^{-jk_0 r}}{4\pi\epsilon_0\omega r^3}\left[(1+jk_0 r)\right. \\ &\times\left(2\sin\theta\sin\phi\hat{\mathbf{r}} - \cos\theta\sin\phi\hat{\theta} - \cos\phi\hat{\phi}\right) \\ &\left.-k_0^2 r^2\left(\cos\theta\sin\phi\hat{\theta} + \cos\phi\hat{\phi}\right)\right] \text{ V/m},\end{aligned} \tag{6.9}$$

as in [59] 7.22 for example. Here ϵ_0 is the permittivity of free space.

The PWS of the Hertzian dipole may be derived analytically [67]. In the basis used here, the resulting expression is

$$\begin{aligned}\vec{\mathbf{F}}_\delta(\vec{\mathbf{k}}_t) = \frac{I\Delta_l\eta_0}{2k_0k_z}&\left(k_xk_y\left(\hat{\mathbf{x}} - \frac{k_x}{k_z}\hat{\mathbf{z}}\right) - \right. \\ &\left.(k_0^2 - k_y^2)\left(\hat{\mathbf{y}} - \frac{k_y}{k_z}\hat{\mathbf{z}}\right)\right)e^{-jk_z\delta} \text{ Vm}.\end{aligned} \tag{6.10}$$

where η_0 is the impedance of free space.

The PWS of the Hertzian dipole is shown in Fig. 6.3 for $\delta = 5$ cm, and $I\delta_l = 1$ Am. One thing to note that is not shown explicitly in the contour plots is that the spectra F_x and F_y diverge near the circle $k_t^2 = k_x^2 + k_y^2 = k_0^2$, where $k_z = 0$. It can be seen in the plots that the largest values of the distributions are there. In Fig. 6.4, cross-sections of the contour plots in Fig. 6.3 are shown along with windowed FFTs (WFFT) for frame sizes from $2\lambda \times 2\lambda$ to $16\lambda \times 16\lambda$, where λ is the free-space wavelength. These FFTs are obtained from samples of the Hertzian dipole field as calculated by (6.9). The cross-sections shown in Fig. 6.4 are the red lines in Fig. 6.3. The FFT was taken using a Kaiser window, defined as

$$w^n = \begin{cases} \frac{I_0\left[\beta(1-(\frac{n}{N/2})^2\right]}{I_0(\beta)} & -N/2 \le n \le N/2, \\ 0 & \text{otherwise}, \end{cases} \tag{6.11}$$

where $I_0(\cdot)$ is a modified Bessel function and $\beta = 3.87$. The Kaiser window is shown for various β in Fig. 6.2.

It is seen in Fig. 6.4 that even for extremely large frame sizes there is a significant difference near $k_t = k_0$, where $k_z = 0$. For the 1 GHz values shown, the pole occurs at

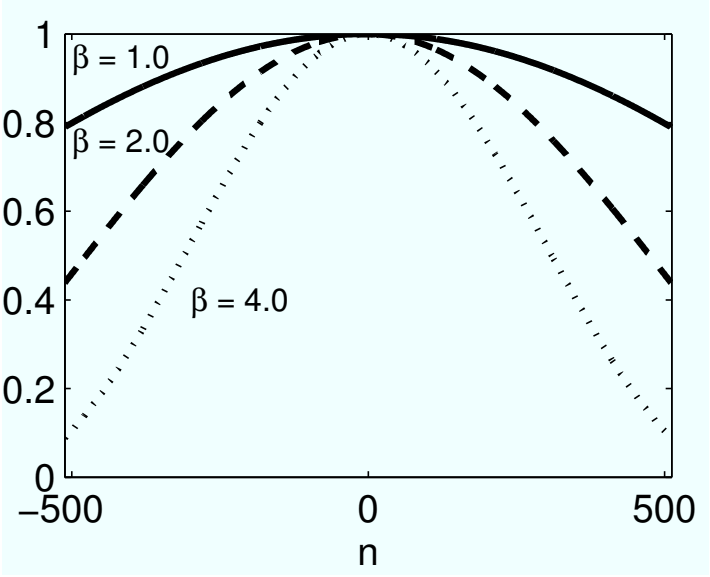

Figure 6.2: The Kaiser window is shown for three values of β. Here $N = 512$.

$k_t = k_0 = 21.01$. Because the coefficients in (6.10) actually diverge near this circle, there will always be a significant difference for a finite frame size.

6.3 Removing the Far-Field Asymptote

Because the portion of a transformed frame that is windowed to zero is the cause of the errors near $k_t = k_0$ in the PWS of a non-directional antenna, it is reasonable to expect that accounting for this part of the field could improve the transforms. If the frame truncates beyond $|x| > R$ and $|y| > R$, and $R >> \delta$, a simple approximation for the field at some point, $\vec{\mathbf{E}}_\delta(\vec{\mathbf{r}}_t)$, is the far-field radiation at that point. If (r_t, ϕ) are the standard polar coordinates on the xy-plane, this far-field radiation is

$$\vec{\mathbf{E}}_\delta(\vec{\mathbf{r}}_t) \approx \vec{\mathbf{E}}^r(\pi/2, \phi)\frac{e^{-jk_0 r_t}}{r_t}, \tag{6.12}$$

where $\vec{\mathbf{E}}^r(\theta, \phi)$ is the portion of the far field radiated in the direction (θ, ϕ).

Most numerical methods provide some method to calculate the radiated field $\vec{\mathbf{E}}^r(\theta, \phi)$ of a transmitting antenna. For example, in the finite-difference time-domain method, one may use the method proposed in [36]. The field at the edge of the frame will converge asymptotically to this value as the frame size increases. Define $\vec{\mathbf{A}}_1(r_t, \phi)$ to be the part of $\vec{\mathbf{E}}^r(\pi/2, \phi)e^{-jk_0 r_t}/r_t$ that is tangent to the xy-plane. Prior to transforming the tangential

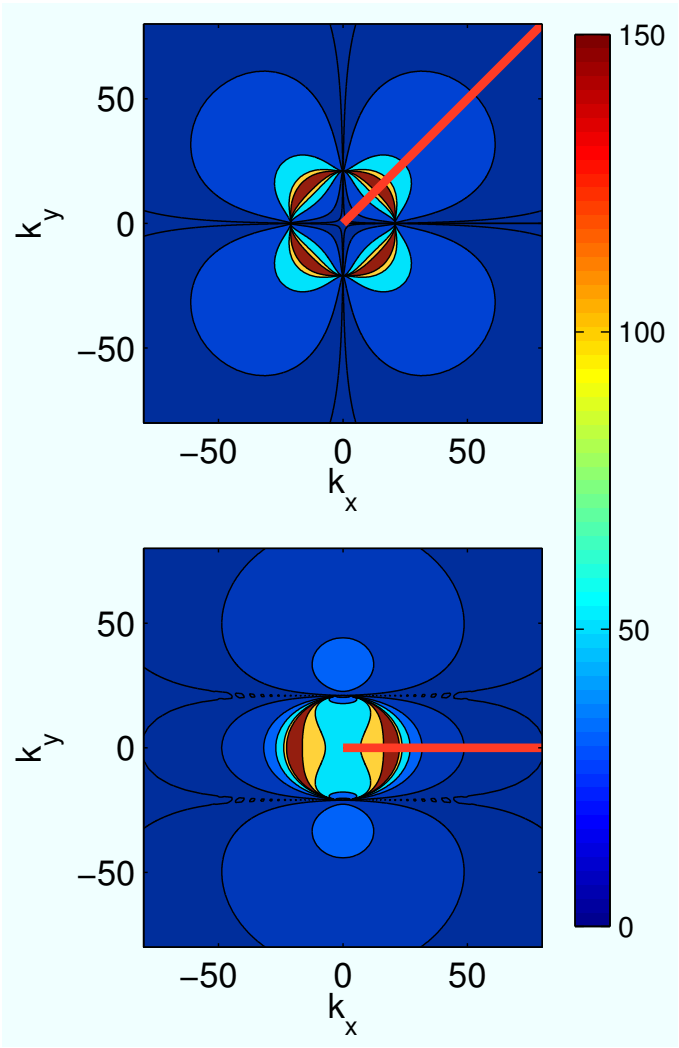

Figure 6.3: Plane wave spectral components of a Hertzian dipole at 1GHz with $\delta = 5$ cm, $F_x(k_x, k_y)$ (top) and $F_y(k_x, k_y)$ (bottom). The red line is the cross-section that is used in the following figures.

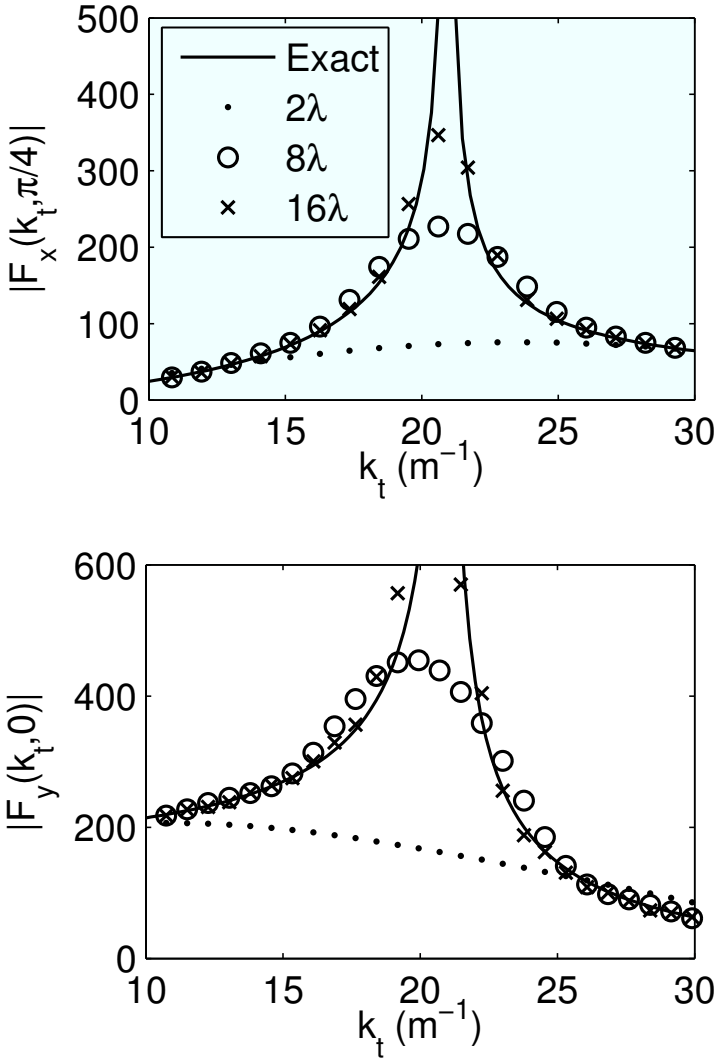

Figure 6.4: Plane wave spectral component cross-sections of a Hertzian dipole at 1GHz with $\delta = 5$ cm are shown calculated by the WFFT method for various frame sizes and compared to the analytical solution.

field, $\vec{\mathbf{E}}_t$, remove this asymptote to obtain

$$\vec{\mathbf{E}}'_t(\vec{\mathbf{r}}_t) = \vec{\mathbf{E}}_t(\vec{\mathbf{r}}_t) - \vec{\mathbf{A}}_1(r_t, \phi). \tag{6.13}$$

One may use the linearity of the Fourier transform to obtain the transform of $\vec{\mathbf{E}}_t$ by

$$\vec{\mathbf{F}}^t_\delta = \mathcal{F}^+\left\{\vec{\mathbf{E}}_t\right\} = \mathcal{F}^+\left\{\vec{\mathbf{E}}'_t\right\} + \mathcal{F}^+\left\{\vec{\mathbf{A}}_1(r_t, \phi)\right\}. \tag{6.14}$$

Additionally, if the field $\vec{\mathbf{E}}'_t$ were spatially-limited and band-limited, samples of its Fourier transform could be calculated using an FFT and samples of $\mathcal{F}^+\left\{\vec{\mathbf{A}}_1\right\}$ would be known if its full transform were known analytically. This would allow the transform to be computed in two portions, one part using the FFT algorithm on a finite frame, and the other part analytically over the full frame.

In reality, the new frame $\vec{\mathbf{E}}'_t$ will be neither spatially-limited nor band-limited. However, the magnitude of the field at the edge of the frame will converge to zero an order of magnitude faster than it did originally. This reduction will significantly reduce the truncation error. Unfortunately, the introduction of the asymptote, $\vec{\mathbf{A}}_1(r_t, \phi)$, will also introduce a singularity into the field near $r_t = 0$ that creates a large amount of high frequency content and leads to aliasing.

One way to reduce the truncation error, while not introducing a significant amount of aliasing error is to add back a second asymptote to the frame that accounts for the divergent behavior of the first asymptote near $r_t = 0$. If the second asymptote decays to zero quickly as $r_t \to \infty$, the truncation error reduction from the first asymptote will be unchanged. A simple candidate for this asymptote is

$$\vec{\mathbf{A}}_2(r_t, \phi) = \vec{\mathbf{A}}_1(r_t, \phi)e^{-\gamma r_t}, \tag{6.15}$$

where γ is some positive real number. The difference $\vec{\mathbf{A}}_1 - \vec{\mathbf{A}}_2$ may be shown to tend to a finite value of $\vec{\mathbf{E}}^r(\pi/2, \phi)\gamma$ for each ϕ as $r_t \to 0$ using L'Hospital's rule. While still not continuous at $r_t = 0$, this situation is vastly preferable to the previous singular behavior, and the size of the discontinuity may be controlled by the parameter γ.

Therefore, the field may be adjusted to form

$$\vec{\mathbf{E}}''_t(\vec{\mathbf{r}}_t) = \vec{\mathbf{E}}_t(\vec{\mathbf{r}}_t) - \vec{\mathbf{A}}_1(r_t, \phi) + \vec{\mathbf{A}}_2(r_t, \phi), \tag{6.16}$$

and the transform may be calculated as

$$\mathcal{F}^+\left\{\vec{\mathbf{E}}_t\right\} = \mathcal{F}^+\left\{\vec{\mathbf{E}}_t''\right\} + \mathcal{F}^+\left\{\vec{\mathbf{A}}_1(r_t,\phi) - \vec{\mathbf{A}}_2(r_t,\phi)\right\}. \tag{6.17}$$

In this form, it will be shown that an improvement over the WFFT may be obtained. Again, $\mathcal{F}^+\left\{\vec{\mathbf{E}}_t''\right\}$ is approximated with an FFT. To calculate $\mathcal{F}^+\left\{\vec{\mathbf{A}}_1 - \vec{\mathbf{A}}_2\right\}$, an analytical expression for $\vec{\mathbf{E}}^r(\pi/2,\phi)$ is required. Because this function has period 2π in ϕ, it can be approximated by a Fourier series. Typically, this Fourier series can be truncated to a small number of terms. In the work for this chapter, which included calculating the PWS of an equiangular spiral, a resistive dipole, a resistive vee, and a Hertzian dipole, the series never required more than sixteen terms. Suppose the series is truncated at some even N terms, then write

$$\vec{\mathbf{A}}_1(r_t,\phi) = \sum_{n=-N/2}^{N/2-1} c_n \frac{e^{jn\phi}e^{-jk_0 r_t}}{r_t}\hat{\phi}. \tag{6.18}$$

Note that the $\hat{\theta}$ component of the radiated field may be ignored because only the electric fields tangential to the xy-plane contribute to the PWS.

One may then use the linearity of the Fourier transform to calculate $\mathcal{F}^+\left\{\vec{\mathbf{A}}_1\right\}$ or $\mathcal{F}^+\left\{\vec{\mathbf{A}}_2\right\}$ by calculating the integrals

$$F_x^n(\vec{\mathbf{k}}_t) = \int\int \frac{e^{jn\phi}e^{-sr_t}e^{j\vec{\mathbf{k}}_t\cdot\vec{\mathbf{r}}_t}}{r_t}\hat{\phi}\cdot\hat{\mathbf{x}}\,d\vec{\mathbf{r}}_t, \tag{6.19}$$

$$F_y^n(\vec{\mathbf{k}}_t) = \int\int \frac{e^{jn\phi}e^{-sr_t}e^{j\vec{\mathbf{k}}_t\cdot\vec{\mathbf{r}}_t}}{r_t}\hat{\phi}\cdot\hat{\mathbf{y}}\,d\vec{\mathbf{r}}_t, \tag{6.20}$$

where $s = jk_0$ for $\vec{\mathbf{A}}_1$, and $s = jk_0 + \gamma$ for $\vec{\mathbf{A}}_2$. Combining (6.18), (6.19), and (6.20) gives

$$\mathcal{F}^+\left\{\vec{\mathbf{A}}_1\right\}(\vec{\mathbf{k}}_t) = \sum_{n=-N/2}^{N/2-1} c_n \left(F_x^n(\vec{\mathbf{k}}_t)\hat{\mathbf{x}} + F_y^n(\vec{\mathbf{k}}_t)\hat{\mathbf{y}}\right)\Big|_{s=jk_0}, \tag{6.21}$$

and the same transform for $\vec{\mathbf{A}}_2$ with $s = jk_0 + \gamma$.

The integrals (6.19) and (6.20) may be calculated analytically. Interested readers are referred to the appendix in section A.1 for details. The resulting functions are given below. The results are given in polar coordinates (k_t,ξ) in the (k_x,k_y) plane, where $k_t = \sqrt{k_x^2+k_y^2}$ and $\xi = \arccos(k_x/k_t)$. The form given below is amenable to computation.

$$
\begin{aligned}
\mathcal{C}_B =& \frac{s}{k_t} \\
\mathcal{C}_C =& \sqrt{1+\mathcal{C}_B^2} \qquad\qquad \text{where } -\pi/2 < \arg \mathcal{C}_C \leq \pi/2 \\
\mathcal{C}_E =& e^{j\xi} \\
\mathcal{C}_M =& \frac{j}{\mathcal{C}_B + \mathcal{C}_C} \\
\mathcal{C}_F =& \frac{\pi}{k_t \mathcal{C}_C}
\end{aligned} \tag{6.22}
$$

$$
F_x^n = j\mathcal{C}_F(\mathcal{C}_E^{n+1}\mathcal{C}_M^{|n+1|} - \mathcal{C}_E^{n-1}\mathcal{C}_M^{|n-1|}) \tag{6.23}
$$

$$
F_y^n = \mathcal{C}_F(\mathcal{C}_E^{n+1}\mathcal{C}_M^{|n+1|} + \mathcal{C}_E^{n-1}\mathcal{C}_M^{|n-1|}). \tag{6.24}
$$

As presented, the method does not require the evaluation of any special functions and consists only of a complex exponential and a complex square root for equations (6.22), which are all evaluated independently of n. Only (6.23) and (6.24) depend on n, and these contain only integer powers, which may be computed very efficiently with the proper implementation.

The method suggested was applied to the Hertzian dipole frame used in Fig. 6.4. Here, the size of the frame was 4λ by 4λ. In Fig. 6.5, the magnitude of the tangential field, $|\vec{\mathbf{E}}_t(\vec{\mathbf{r}}_t)|$, of the Hertzian dipole is shown in the top subplot. In the middle subplot, the field $|\vec{\mathbf{E}}'_t(\vec{\mathbf{r}}_t)|$ of (6.13) is plotted, where the asymptote $\vec{\mathbf{A}}_1$ has been removed. It should be noted that the magnitude of the field near the edge of the frame has been reduced in some places by more than 12 dB (a factor of four). Unfortunately, a significant increase in the field magnitude near the center of the frame may also be observed in this subplot, and the field actually diverges at the center of the frame. As stated above, this creates a significant aliasing error in the transformed frame.

In the bottom subplot of Fig. 6.5, the frame $|\vec{\mathbf{E}}''_t(\vec{\mathbf{r}}_t)|$, from (6.16), is shown. Here, the asymptote $\vec{\mathbf{A}}_1 - \vec{\mathbf{A}}_2$ has been removed. In this frame one can see approximately the same reduction in the magnitude of the field at the edge of the frame as in the middle frame with essentially the same behavior near the center as the top frame.

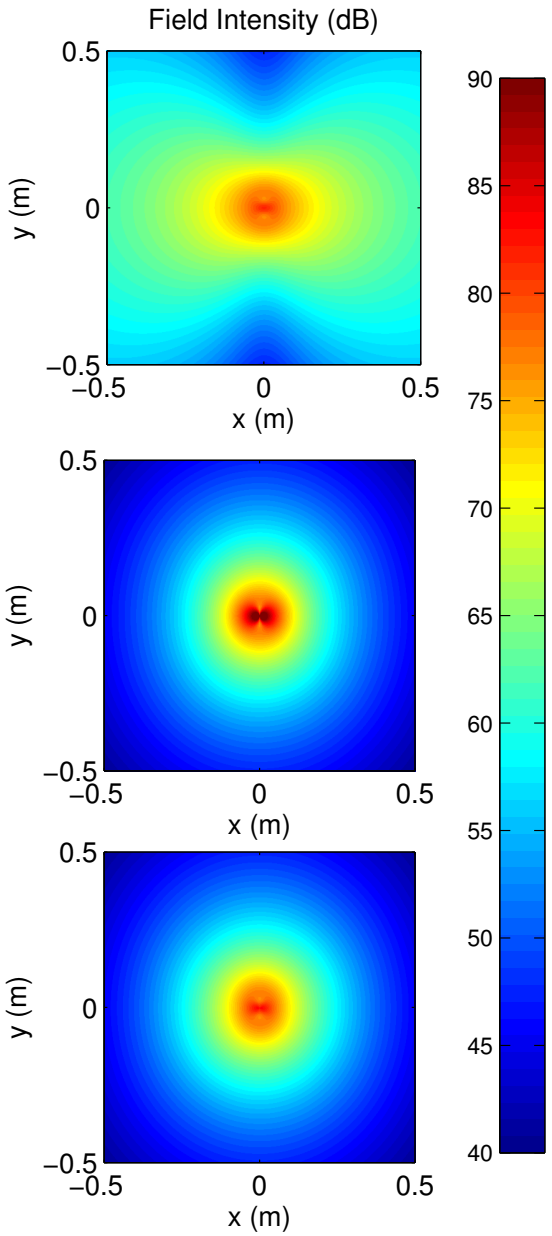

Figure 6.5: $|\vec{\mathbf{E}}_t(\vec{\mathbf{r}}_t)|$ for the Hertzian dipole at 1 GHz and $\delta = 5$ cm. The field is shown first with a rectangular window (top), then with the asymptote $\vec{\mathbf{A}}_1(r_t, \phi)$ removed (middle), and finally with the asymptote $\vec{\mathbf{A}}_2(r_t, \phi)$ added back.

Using the frame of data $\vec{\mathbf{E}}_t''(\vec{\mathbf{r}}_t)$, a windowed FFT is performed. The resulting frame of PWS samples is then adjusted by adding the analytical transform of the asymptote $\vec{\mathbf{A}}_1 - \vec{\mathbf{A}}_2$. Upon completion, the frame is a new approximation to the PWS that incorporates the behavior of the antenna on the truncated portion of the frame. In Fig. 6.6, a frame size of 4λ by 4λ is used for the WFFT method and the proposed method. These are compared with the analytical solution over the same cross-sections used in Fig. 6.4.

The error between the WFFT solution and the proposed method is plotted over the entire (k_x, k_y) plane in Fig. 6.7. In both transforms, a Kaiser window is used with $\beta = 3.87$, which is chosen as a compromise to attempt to resolve the peaks well without introducing too much error from the transition to zero. In the proposed method, the parameter γ was chosen to be 3.0. It is clear that the error near the poles has been reduced significantly. In the WFFT frame, the error exceeds 200 units near the poles, but does not significantly exceed 10 units in the proposed method. Additionally, the truncation error introduced by the window's transition to zero, which appears as a ripple near the lines $k_x = 0$ and $k_y = 0$, is much smaller and reduces faster than the WFFT.

6.4 Error Analysis

As stated earlier, the FFT calculates samples of a Fourier transform when the frame of data is band-limited and spatially-limited. When the band-limited assumption is not satisfied, an aliasing error is present in the transform. When the spatially-limited assumption is not satisfied, a truncation error is present in the transform. The removal of the asymptote in Section 6.3 reduces the magnitude of the field values that are truncated out of the frame, which reduces the truncation error. This is done at the expense of an aliasing error caused by the behavior of the asymptote near the center of the frame at $r_t = 0$. In this section, the error introduced by the proposed method is analyzed. To illustrate the results of the analysis, the Hertzian dipole from the previous section, sampled at $\delta = 5$ cm, is used as a reference case.

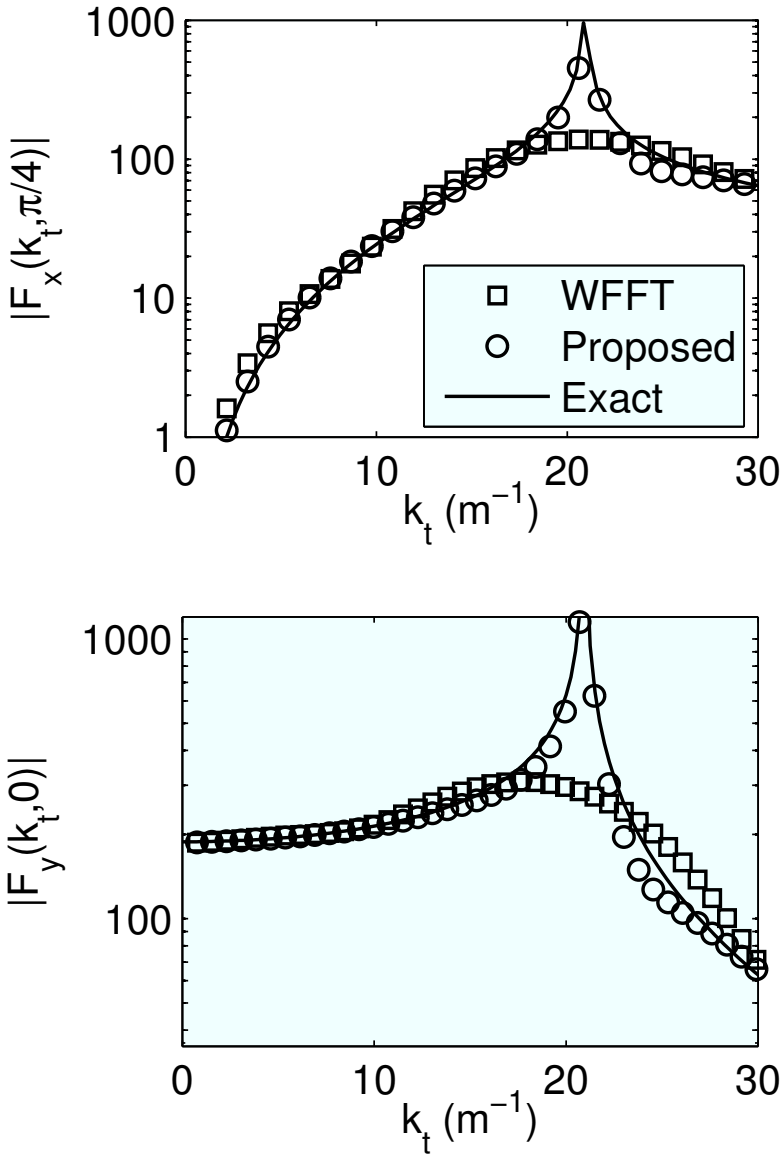

Figure 6.6: Cross-sections of the PWS for the analytical solution, the WFFT approximation, and the proposed method using the same window. Here, $\delta = 5$ cm, $\beta = 3.87$, and $\gamma = 3.0$.

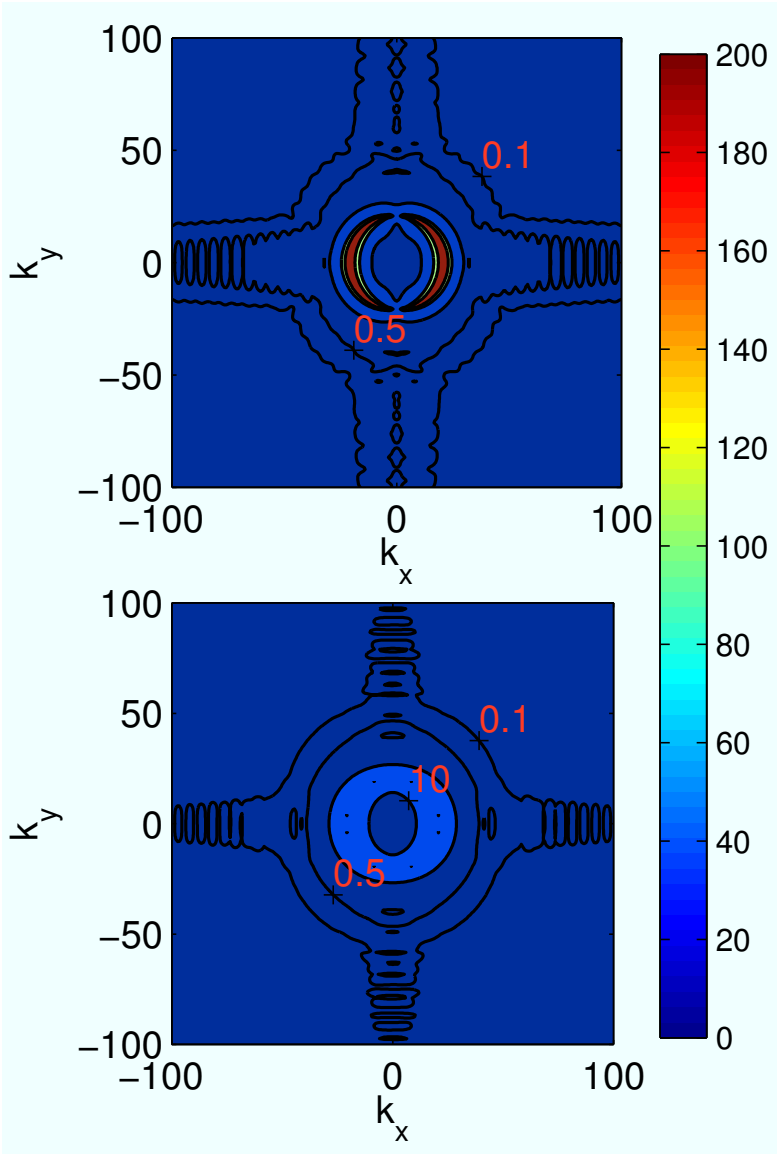

Figure 6.7: Error in the PWS as approximated by the WFFT with no asymptotic removal (above) and with the proposed method (below).

6.4.1 Truncation Error

As stated above, the truncation error in the PWS is related to the portion of the field that is outside of the sampled frame of data. This error can be analyzed independently of the aliasing error by ignoring that the data is sampled. Suppose that $\vec{\mathbf{F}}_\delta$ is the actual PWS of a frame at $z = \delta$ for some antenna. Let $\vec{\mathbf{F}}_\delta^R$ be the approximation to this PWS obtained by multiplying the field by the window $w_R(x, y)$. The window w_R has support on the set $[-R, R] \times [-R, R]$.

To quantify the error, a vector $\mathcal{L}^2$ norm, $|\cdot|_V$, for $\vec{\mathbf{F}}_\delta$ is introduced

$$\begin{aligned} \left|\vec{\mathbf{F}}_\delta\right|_V^2 &= \int\int_{\mathbf{R}^2} \left|\vec{\mathbf{F}}_\delta^t(\vec{\mathbf{r}}_t)\right|^2 d\vec{\mathbf{r}}_t \\ &= |F_x|_{\mathcal{L}^2}^2 + |F_y|_{\mathcal{L}^2}^2 \,, \end{aligned} \tag{6.25}$$

The error between $\vec{\mathbf{F}}_\delta$ and $\vec{\mathbf{F}}_\delta^R$ may be written,

$$\% \text{ Error} = 100 \times \frac{\left|\vec{\mathbf{F}}_\delta - \vec{\mathbf{F}}_\delta^R\right|_V}{\left|\vec{\mathbf{F}}_\delta\right|_V}. \tag{6.26}$$

One may relate this error to the size of the fields truncated out of the frame. Below, the error in F_x is related to the error in E_x

$$\begin{aligned} \left|F_x - F_x^R\right|_{\mathcal{L}^2} &= \left|\mathcal{F}^+\left\{E_x\right\} - \mathcal{F}^+\left\{E_x w_R\right\}\right|_{\mathcal{L}^2} \\ &= \left|\mathcal{F}^+\left\{E_x\left(1 - w_R\right)\right\}\right|_{\mathcal{L}^2} \\ &= (2\pi)^2 \left|E_x\left(1 - w_R\right)\right|_{\mathcal{L}^2} \,, \end{aligned} \tag{6.27}$$

where Parseval's relation was used in the last line. It can be shown that after removing the asymptote $\vec{\mathbf{A}}_1 - \vec{\mathbf{A}}_2$, the right side of (6.27) is $O\left(1/R\right)$ for a rectangular window with the given support. It can also be shown that the error in F_y is $O(1/R)$. The details of this calculation are shown in section A.2.1. These bounds cannot be obtained without removing the asymptote unless the antenna is very directional.

This error may be approximated when samples of $\vec{\mathbf{F}}_\delta$ and $\vec{\mathbf{F}}_\delta^R$ are known using a sum in place of the integrals. The truncation error was computed for a set of frame sizes. In Fig. 6.8, the Hertzian dipole case is used to illustrate the trends in the error. For a frame size $W_\lambda = 2R/\lambda$ wavelengths square, samples were taken and transformed using the proposed method, and the WFFT. The error is calculated using (6.26).

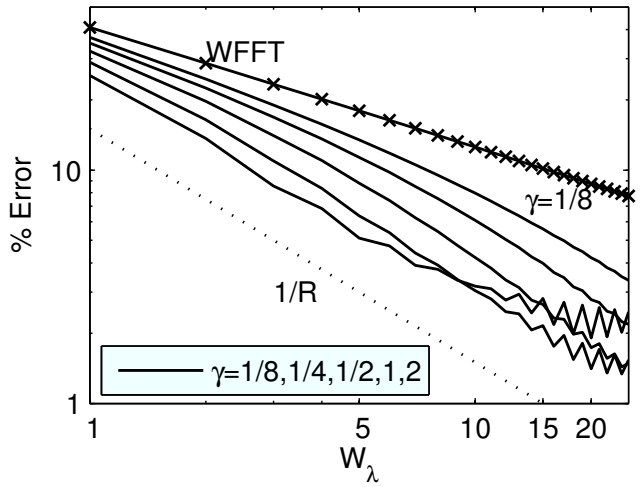

Figure 6.8: Error in PWS approximation for WFFT and the proposed method with various values of γ as a function of frame size. Here values of γ range from 1/8 to 2 from top to bottom on the left side of the figure.

In Fig. 6.8 an additional dotted line has been inserted to show $1/R$ decay. One thing to note here is that the WFFT norm does decrease, but not as fast as $1/R$. In fact, it goes as $1/\sqrt{R}$ for the Hertzian dipole but no argument is available that this is true in general. It can be seen that for small frames, the smallest γ values tend to show the same slope as the WFFT. In this region, r_t is sufficiently small that the $e^{-\gamma r_t}$ term in $\vec{\mathbf{A}}_2$ is nearly unity, causing the total asymptote to have less effect. As this term decays exponentially, each plot tends toward the slope of the $1/R$ decay. When the truncation error gets sufficiently low at the far right of the plot, an error floor is reached that appears as an oscillation in the error around a constant value. This floor relates to the aliasing error and is discussed further in the next subsection.

It may also be useful to see the shape of the truncation error itself. In Fig. 6.9, the magnitude of F_y is shown near the peak in the transform. It can be seen that the effect of increasing the γ parameter is to better resolve the transform near $k_t = k_0$. Since setting γ to zero sets the $\vec{\mathbf{A}}_1 - \vec{\mathbf{A}}_2$ asymptote to zero, one may expect that extremely small γ begin to converge to the WFFT solution.

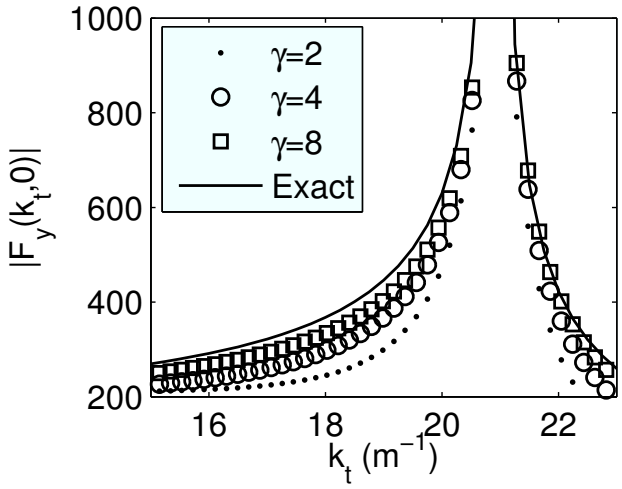

Figure 6.9: Effect of the γ parameter on error. As γ tends to zero, the effect of the asymptote is negated, causing error near the poles. γ should be set so that the lossy term is negligible at the edge of the frame. These errors are shown on a linear scale for γ values of 2,4, and 8.

6.4.2 Aliasing Error

The aliasing error is also affected by the proposed method because the asymptote that is removed from the frame of data is not band-limited. In this section, the aliasing error is analyzed and its relation to the parameters involved in the method is shown. An upper bound on the aliasing error was not achieved as it was for the truncation error. If the windowing is ignored for a moment, the aliasing error can be analyzed separately. The aliasing introduced by the method is the difference between the FFT approximation of $\mathcal{F}^+\left\{\vec{\mathbf{A}}_1 - \vec{\mathbf{A}}_2\right\}$ and the actual Fourier transform. The relation between these two transforms is discussed in [77]. The FFT approximation will be called $\hat{\mathbf{B}}(\vec{\mathbf{k}}_t)$ and the Fourier transform itself will be called $\vec{\mathbf{B}}(\vec{\mathbf{k}}_t)$. The aliasing error is

$$\hat{\mathbf{B}}(\vec{\mathbf{k}}_t) - \vec{\mathbf{B}}(\vec{\mathbf{k}}_t) = \sum_{k,l\neq 0} \vec{\mathbf{B}}\left(\vec{\mathbf{k}}_t + (k\hat{x} + l\hat{y})\frac{2\pi}{\Delta}\right), \quad \text{where } k_t < \frac{\pi}{\Delta}. \tag{6.28}$$

In other words, the aliasing error is a sum of the transforms, $\vec{\mathbf{B}}$, evaluated at different $\vec{\mathbf{k}}_t$ where $k_t > \pi/\Delta$. Consider the expressions for $\vec{\mathbf{B}}$ given in (6.22-6.24). $\vec{\mathbf{B}}$ is a sum of terms of the form $\mathcal{C}_E^n\left(\mathcal{C}_F\mathcal{C}_M^n - \mathcal{C}'_F\mathcal{C}'^n_M\right)$ where $\mathcal{C}_F$ and $\mathcal{C}_M$ are evaluated for $s = jk_0$ while $\mathcal{C}'_F$ and $\mathcal{C}'_M$ are evaluated for $s = jk_0 + \gamma$. Because the only ξ dependence in these terms is in

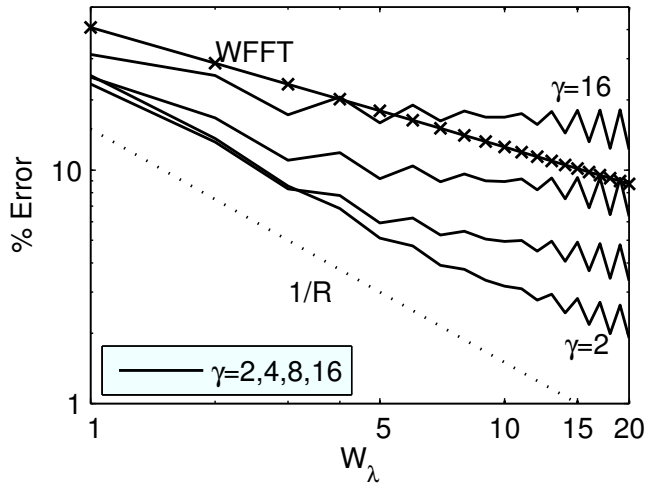

Figure 6.10: Error in PWS approximation for WFFT and asymptotic method with various values of γ as a function of frame size. Here values of γ range from 2 to 16 from bottom to top. The dotted line is the curve $1/W_\lambda$ and is intended for reference.

$\mathcal{C}_E$, and $|\mathcal{C}_E| = 1$, the magnitude is independent of ξ. The error from each term in (6.28) could be approximated by obtaining a bound for $|\mathcal{C}'_F\mathcal{C}'^n_M - \mathcal{C}_F\mathcal{C}^n_M|$. This can be done and the details are shown in appendix A.2.2. The resulting bound is

$$|\mathcal{C}'_F\mathcal{C}'^n_M - \mathcal{C}_F\mathcal{C}^n_M| \leq \frac{n\pi\gamma}{k_t^2} + O\left(\frac{1}{k_t^3}\right). \tag{6.29}$$

At the edge of the frame, this means

$$|\mathcal{C}'_F\mathcal{C}'^n_M - \mathcal{C}_F\mathcal{C}^n_M| \leq \frac{n\gamma\Delta^2}{\pi} + O(\Delta^3). \tag{6.30}$$

If the error in (6.28) converges for some $\vec{\mathbf{k}}_t$, it will have the same $\gamma\Delta^2$ dependence. However, this convergence itself is not proven here. The aliasing error in all transforms seen so far has been both finite and insignificant if γ is chosen small enough. The trends noted also show themselves in the test case of the Hertzian dipole. For example, for very large γ one expects more aliasing error. In Fig. 6.10, unproductively large γ are chosen to show the nature of the aliasing error. Here, like Fig. 6.8, the aliasing error appears only when the truncation error goes below a certain threshold. One can also see that the aliasing error remains roughly constant as W_λ increases. Also, each time γ is halved, the aliasing error roughly halves as well as would be expected from (6.30).

Additionally, the aliasing error can be seen to go as the square of the cell size. In Fig. 6.11, the values of the PWS are shown in the same cross-section used in Fig. 6.9 except the

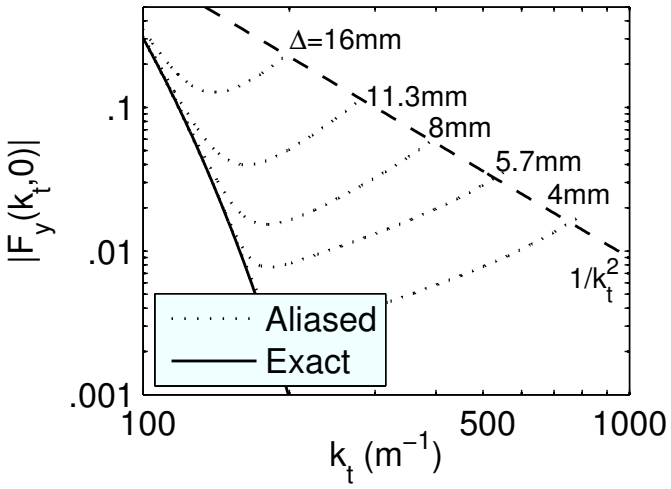

Figure 6.11: Effect of the sampling cell size on the aliasing error. $|F_y|$ rapidly approaches zero near the edge of the frame. The approximations, shown as dotted lines, consequently show the aliasing error. Here the dashed line shows a $1/k_t^2$ decay so as to compare against (6.29). The agreement is reasonably good over the majority of cell sizes. The minor disagreement for smaller Δ values may be attributed to interference from other aliases or errors unrelated to those introduced by the transform.

k_t axis is extended to the edge of the frame. When viewing Fig. 6.11, it should be kept in mind that the maximum k_t on the frame is a function of Δ. Near the edge, the exact PWS has a value very close to zero. The non-zero values seen in the PWS approximations can be attributed to aliasing from the nearest neighbor. It can be seen that the aliasing error at the edge of the frame matches the curve $1/k_t^2$ reasonably well.

6.4.3 Conclusions on Error

The preceding discussion demonstrates that the error in the transform may be reduced below that in the WFFT transform if γ and Δ are chosen appropriately. In general, the effect will be more pronounced when a large frame of data is available. The guideline for Δ would be to make it as small as is computationally feasible for the problem. The guideline for γ is less clear cut. The optimal γ is a function of the size of the frame of data that is available. When γ is chosen too large, aliasing error predominates. When γ is chosen too small the asymptote is reduced to zero and has no effect on the truncation error. A general guideline is to use the smallest γ that makes the term $e^{-\gamma r_t}$ small compared to unity when r_t is near the edge of the frame. When implemented properly, it is not difficult to try a

number of γ for a given frame.

One factor that is not addressed here is the type of window used. For example in the truncation error subsection above, the only error shown due to truncation is the resolution of the pole. In reality, there are two errors caused by the window. The first is the lost resolution at the pole and the second is a ripple introduced along the lines $k_x = 0$ and $k_y = 0$ that may be seen in Fig. 6.7. This ripple can be reduced significantly by the use of a smooth window. If a sharp window is used, one can resolve the pole better at the expense of introducing more of the rippled error. This type of trade-off is discussed in [78].

6.5 Calculating the PWS of a Resistively Loaded Dipole using FDTD

All PWS calculations shown in previous sections have used a Hertzian dipole. This antenna was chosen because of the known analytical solutions (6.9) and (6.10). The known PWS allowed errors to be calculated for the method. The known field values allowed the errors to be attributed only to the method itself, and not some numerical artifact in the calculation of the fields used. However, special properties of the Hertzian dipole may make the proposed method appear to be less general than it is.

In this section, the method is applied to an antenna modeled using the FDTD method. Here, a resistively loaded dipole is modeled in free-space. Its PWS is calculated using the windowed FFT and the proposed method. Since there is not a known analytical solution to compare the results against, the two versions of the PWS are used to predict the field at some point off of the frame of sampled data and compared against the FDTD result at that point. One way to do this would be to calculate the PWS at some frame $z = \delta$, then use (6.3) and an inversion to calculate the field on some other frame $z = \delta'$ where $\delta' > \delta$. For directional antennas, this would be feasible because the PWS of such an antenna does not have singularities near the circle $k_t = k_0$. However, for non-directional antennas, these singularities do exist. When these are properly represented in the samples of the PWS, one obtains a frame of data that cannot be inverted using a standard FFT. The FFT of such a frame exhibits a behavior that is dual to aliasing, where the reconstructed signal has support that extends beyond the frame of data. Aliased versions of the signal then interfere

with the field. Because of this problem, this verification technique was abandoned in the course of this work.

An alternative method is to calculate the PWS in free-space, and then use this PWS to calculate the field inside of a half-space of dielectric, a model for the ground. The details of this procedure are discussed below. This method is closer to the intention of this research and has an additional advantage. The act of passing the PWS into a dielectric half-space has the effect of reducing its singular behavior near $k_t = k_0$. The method has the disadvantage that it is not exact, even if the PWS calculation works flawlessly. This is because an approximation is required to calculate the field underground. When the antenna is placed near a half-space of dielectric, the PWS transmitted into the ground has a large contribution that is from the PWS in free-space, but it also contains additional terms that relate to currents on the antenna that are induced by the reflection from the half-space. Because this second portion cannot be accounted for, the method will work best for an antenna that has a low scattering cross-section and for a ground with a low permittivity. For our demonstration we use $\epsilon_r = 2.0$, which is close to that of dry sand.

The resistive dipole was chosen because it radiates a compact pulse and because it has a small scattering cross-section. Both of these properties make it attractive for use in a ground-penetrating radar system. Additionally, the resistive dipole is a non-directional antenna, which makes the calculation of its PWS a good illustration of how the method handles truncation errors. The antenna uses a Wu-King resistivity profile that was implemented in the FDTD model using solid blocks of conductive material [79]. The geometry of the dipole is shown in Fig. 6.12. The antenna was modeled once in free-space and again with a half-space of dielectric present. In the free-space case, a frame of data was taken 2 cm away from the plane containing the center line of the dipole. In the simulation that included the half-space, a frame of data was taken 10 cm from the center line of the dipole, which is inside the half-space. Since the FDTD method provides a solution as a function of time, an additional step of using the FFT along the time dimension for each point in the frames was necessary prior to calculating a PWS. The frame of data taken in free-space was used to calculate the PWS of the resistive dipole. The PWS obtained is shown in Fig.

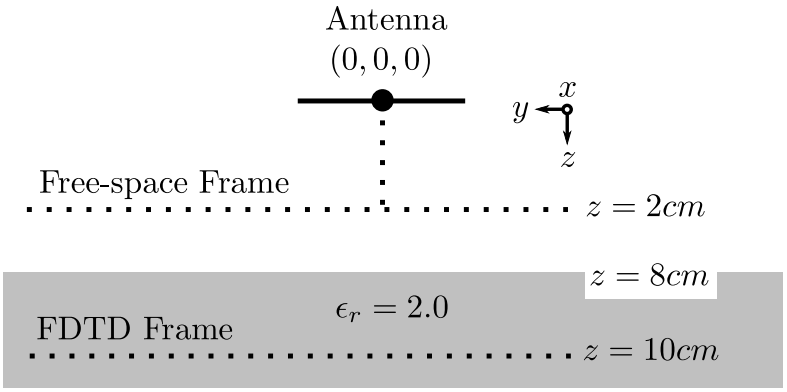

Figure 6.12: Geometry of the resistive dipole and the geometry of the dipole radiating over the half-space.

6.13.

The calculated PWS was then used to predict the field under ground. This was done in three steps. First, the PWS was shifted to $z = 8$ cm, where the half-space was located. Next, the Fresnel coefficients were used to calculate the portion of the PWS that was transmitted into the ground. Finally, the PWS was shifted to $z = 10$ cm, where the field calculated by the FDTD method is known. To shift the field, the transform in (6.3) was used.

The use of the Fresnel coefficients to transmit the PWS into the half-space is typically not formulated in the basis used in this chapter. The coefficients can be seen in an alternative basis in [67]. Let k_1, k_2 be the wave numbers in air and in the dielectric, respectively. Let $k_{z,1}, k_{z,2}$ be the k_z components in air and the dielectric respectively. Let ψ be the angle $\arccos(k_x/k_t)$. The transmission coefficients may then be written

$$T_\perp = \frac{2k_{z,1}}{k_{z,1} + k_{z,2}} \tag{6.31}$$

$$T_\parallel = \frac{2k_1^2 k_{z,2}}{k_1^2 k_{z,2} + k_2^2 k_{z,1}} \tag{6.32}$$

$$\begin{pmatrix} F_x^t \\ F_y^t \end{pmatrix} = \left[T_\perp \begin{pmatrix} \sin^2\psi & -\cos\psi\sin\psi \\ -\cos\psi\sin\psi & \cos^2\psi \end{pmatrix} + T_\parallel \begin{pmatrix} \cos^2\psi & \cos\psi\sin\psi \\ \cos\psi\sin\psi & \sin^2\psi \end{pmatrix} \right] \begin{pmatrix} F_x \\ F_y \end{pmatrix}, \tag{6.33}$$

where F_x, F_y are the PWS in free-space and F_x^t, F_y^t are the PWS in the dielectric half-space.

After these steps were performed on the PWS calculated in free-space, it was inverted to

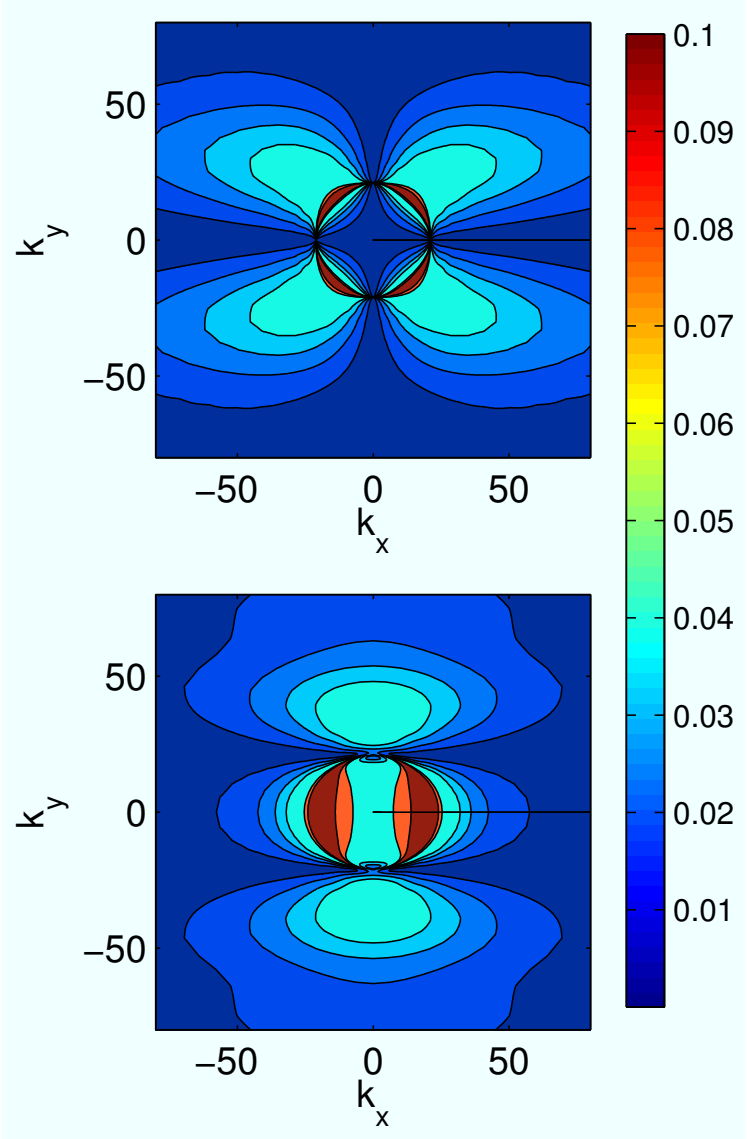

Figure 6.13: Plane-wave spectrum of a resistively loaded dipole as calculated by the proposed method: $F_x(k_x, k_y)$ (top) and $F_y(k_x, k_y)$ (bottom).

fields using the FFT. These fields were compared against the fields obtained underground in the FDTD simulation. The magnitude of the tangential field, $\vec{\mathbf{E}}_t$, is shown in the top subfigure of Fig. 6.14, as calculated by the FDTD method. The following subfigures show the magnitude of the error in the tangential fields between the proposed method and FDTD, and between a standard windowed FFT and FDTD. It should be noted that only the tangential components are compared because the E_z component is not located on the xy-plane in the FDTD method. It can be seen in the figures that the error in the directions $\hat{x}$ and $-\hat{x}$ is significantly reduced using the proposed method. The remaining errors are in directions where there exists a null in the pattern for the loaded dipole, $\hat{y}$ and $-\hat{y}$. The largest error in the prediction using the proposed method is in the center of the frame. This is where the field values have the largest magnitude. Some of this error may relate to multiple reflections between the antenna and the ground.

6.6 Conclusions on the PWS

The method proposed has been shown to reduce the truncation error associated with a windowed FFT when calculating an approximation to the PWS. While the method introduces an aliasing error into the PWS approximation, this error is generally small and can be controlled by the two parameters, γ and Δ. The test case of the Hertzian dipole was used to demonstrate the relationships between the parameters of the method and the errors introduced. Additionally, an analysis of the error was used to argue that these relationships will hold true for a general antenna. Finally, the method was used on a more complicated antenna, the resistively loaded dipole, to calculate the PWS and use it to estimate the fields under ground. It was shown that the proposed method predicts the fields more accurately than the windowed FFT alone.

The work leaves open several questions and applications for future contributions. First, the asymptotes used in the method could be improved upon. A properly chosen asymptote that remains continuous near the center of the frame could significantly reduce the aliasing error introduced. In addition, if an asymptote was obtained that reduced the magnitude $|\vec{\mathbf{E}}''_t|$ at a faster rate than $O(1/r_t^2)$, this could decrease the truncation error significantly.

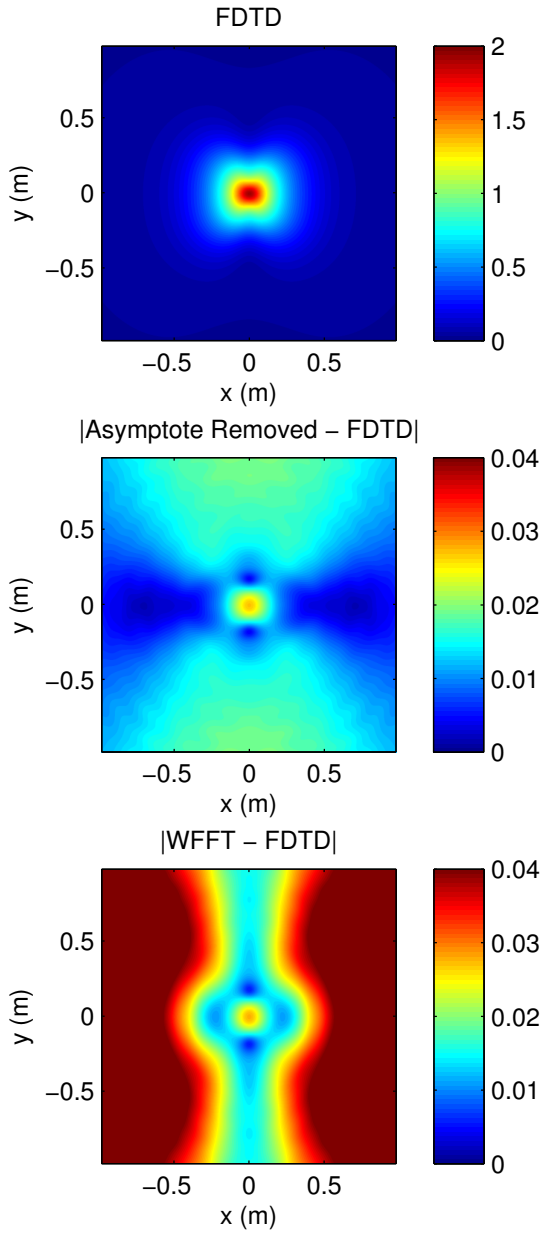

Figure 6.14: Inverted fields underground according to the FDTD method (top), the error in the proposed method (middle), and the error in the WFFT method (bottom).

Second, in some applications it is required that the PWS be inverted in free-space. As mentioned in the chapter, the samples of the PWS that include the singularity make it impossible to use a traditional FFT to invert the spectrum. Instead, the divergent portion of the spectrum must be inverted separately. Future work could focus on inverting the divergent portion of the spectrum analytically or using an adaptive integration scheme like that proposed in [80]. Finally, the ability to easily calculate the PWS of various antennas that are used in ground penetrating radar systems should help to answer certain questions about the role of evanescent waves in GPR detection, such as those raised in [70].

CHAPTER VII

CONCLUSIONS

In this thesis, a numerical model of a spiral-based GPR system was constructed and verified against a prototype system. The spiral element itself and later the GPR system are analyzed parametrically to obtain a better understanding of the relationships between the geometry chosen and the performance. Throughout the work, an attempt is made to balance numerical simulation with measurement, and theory with numerical simulation in order to maintain a good degree of confidence in the results described.

In Chapter 1, the notion of a frequency-independent antenna is presented and the argument that the spiral antenna is a frequency-independent antenna is provided. References to the use of the spiral antenna in detection systems suggest that one frequent feature of interest for the antenna is its inherent circular polarization.

In Chapter 2, the finite-difference time-domain method is described briefly and the use of the ballooned mesh for the spiral antenna is explained. The initial prototype spiral antennas are shown and the comparison between the numerical method and the measurements show good agreement.

In Chapter 3, the numerical model described in Chapter 2 is used to perform a comprehensive study of the spiral element. First, the behavior of the spiral element over its operating-band region is discussed. A design graph to relate the dielectric substrate used to the characteristic impedance of the antenna is given and the essential features of the boresight gain are described and related to simple models. Next, the frequencies of the operating band are described and related to the geometry of the antenna.

Chapter 4 describes the process of extending the numerical model of the spiral element to a numerical model of a full GPR system and the verifications necessary to do so. This involves the characterization of the material properties of the absorber used for the spiral and the new method of feeding the antennas that does not require the use of an uncharacterized

balun. The system is used in a sand box with different types of scatterers buried in it and the radar responses are matched to FDTD data. It is shown that the dispersion present in the responses can be removed by a physical model of the antenna. It is also shown that the responses obtained are a strong function of the geometry of the scatterer and a simple argument that the antennas should reject symmetric scatterers is described and shown to be only partially true.

In Chapter 5, the complete GPR system is analyzed. Because the full-system model has a very long run time, a technique was developed to allow fewer runs to be used to characterize the response to a scatterer. This technique used the assumption that the scatterer interacting with the antennas was small. After verifying the technique, the effect on the radar responses of the distance of the spiral antennas to the ground and the dielectric constant of the ground was studied parametrically. It was shown that small symmetric scatterers are rejected by the monostatic antenna system and that this is true well into the near field. The response of the monostatic system, however, seems to be separated into two distinct regions in time. The initial pulse is rejected directly over the scatterer and occurs at roughly the same time as the bistatic response, while the late-time response is not rejected. This late-time portion is shown to be caused by a secondary radiation that has the opposite circular polarization from the initial radiation.

Finally, in Chapter 6, a method for improving the calculation of the plane-wave spectrum is presented. The plane-wave spectrum is a technique often used to describe GPR systems because the plane-wave basis has a well-defined interaction with a half-space. One difficulty in calculating the plane-wave spectrum is the necessity of taking a Fourier transform of the field data. Because many antennas are non-directional, the FFT used in the Fourier transform calculation is often windowed. This windowing adds an error called truncation error to the spectrum calculated. The technique described makes use of the known behavior of the fields outside of the window to correct for some of the truncation error introduced.

APPENDIX A

ADDITIONAL CALCULATIONS FOR THE PWS METHOD

A.1 Fourier Transforming the Asymptotes

In this section, the missing steps between (6.19) and (6.23) are shown. The steps between (6.20) and (6.24) parallel these steps exactly. The integral in (6.19) may be simplified by introducing polar coordinates for the variables k_x and k_y as well as the variables x and y. If (k_x, k_y) is transformed to polar coordinates (k_t, ξ) and (x, y) is transformed to polar coordinates (r_t, ϕ), (6.19) becomes

$$-\int_0^\infty \int_0^{2\pi} e^{jn\phi} e^{-sr_t} \sin\phi e^{jk_t r_t \cos(\phi-\xi)} d\phi dr_t. \tag{A.1}$$

If Euler's identity is applied to the $\sin\phi$ term, the integral may be re-written

$$-\int_0^\infty \int_0^{2\pi} e^{-sr_t} \left(\frac{e^{j(n+1)\phi} - e^{j(n-1)\phi}}{2j} \right) e^{jk_t r_t \cos(\phi-\xi)} d\phi dr_t. \tag{A.2}$$

Introducing the notation,

$$\mathcal{I}_n = \int_0^{2\pi} e^{jn\phi} e^{jk_t r_t \cos(\phi-\xi)} d\phi, \tag{A.3}$$

(A.2) is the integral,

$$-\int_0^\infty e^{-sr_t} \frac{\mathcal{I}_{n+1} - \mathcal{I}_{n-1}}{2j} dr_t. \tag{A.4}$$

To evaluate $\mathcal{I}_n$, begin by making the substitution $\phi' = \phi - \xi$.

$$\begin{aligned} \mathcal{I}_n &= \int_{-\xi}^{2\pi-\xi} e^{jn(\phi'+\xi)} e^{jk_t r_t cos(\phi')} d\phi' \\ &= e^{jn\xi} \int_{-\xi}^{2\pi-\xi} e^{jn\phi} e^{jk_t r_t cos(\phi)} d\phi. \end{aligned} \tag{A.5}$$

Noting that the integrand has period 2π in ϕ, the period may be shifted to $[-\pi, \pi]$ without affecting the integral. Furthermore, Euler's identity may be employed again to expand out

the complex exponentials to obtain

$$\begin{aligned}\mathcal{I}_n = e^{jn\xi}\Bigg[&\int_{-\pi}^{\pi} \cos(n\phi)\cos(k_t r_t \cos\phi)d\phi \\ &- \int_{-\pi}^{\pi} \sin(n\phi)\sin(k_t r_t \cos\phi)d\phi \\ &+ j\int_{-\pi}^{\pi} \cos(n\phi)\sin(k_t r_t \cos\phi)d\phi \\ &+ j\int_{-\pi}^{\pi} \sin(n\phi)\cos(k_t r_t \cos\phi)d\phi\Bigg].\end{aligned} \tag{A.6}$$

The symmetry of each integrand in (A.6) from top to bottom is even, odd, even, and odd. Each odd integral will have no contribution to the sum. Each even integral may be written as twice the integral over the region $[0, \pi]$. Applying this and using Euler's identity again to simplify, one obtains

$$\mathcal{I}_n = 2e^{jn\xi}\int_0^{\pi} \cos(n\phi)e^{jk_t r_t \cos\phi}d\phi. \tag{A.7}$$

This integral relates to a Bessel function as may be seen from [81] 9.1.21.

$$\mathcal{I}_n = 2\pi e^{jn\xi} j^n J_n(k_t r_t), \tag{A.8}$$

where $J_n(\cdot)$ is a Bessel function of the first kind. Returning to (A.4), one obtains:

$$\begin{aligned}&-\frac{2\pi e^{j(n+1)\xi} j^{n+1}}{2j}\int_0^{\infty} e^{-sr_t}J_{n+1}(k_t r_t)dr_t \\ &+\frac{2\pi e^{j(n-1)\xi} j^{n-1}}{2j}\int_0^{\infty} e^{-sr_t}J_{n-1}(k_t r_t)dr_t.\end{aligned} \tag{A.9}$$

Introducing the notation,

$$\mathcal{I}'_n = \int_0^{\infty} e^{-sr_t}J_n(k_t r_t)dr_t, \tag{A.10}$$

(A.9) may be written as

$$F_x^n = j\pi(j^{n+1}e^{j(n+1)\xi}\mathcal{I}'_{n+1} - j^{n-1}e^{j(n-1)\xi}\mathcal{I}'_{n-1}). \tag{A.11}$$

The integral $\mathcal{I}'_n$ is the Laplace transform of a Bessel function. Its transform is given in [82] table 17.3 as

$$\int_0^{\infty} J_n(k_t r_t)e^{-sr_t}dr_t = k_t^n(s + (s^2 + k_t^2)^{\frac{1}{2}})^{-n}(s^2 + k_t^2)^{-\frac{1}{2}}, \tag{A.12}$$

for $n > -1$ and s with real part greater than zero. Using the substitutions in (6.22), this may be written

$$\int_0^\infty J_n(k_t r_t) e^{-s r_t} dr_t = \left[(\mathcal{C}_B + \mathcal{C}_C)^n k_t \mathcal{C}_C \right]^{-1}. \tag{A.13}$$

It may be noted that the result is not valid for a purely imaginary s, even though it is required for $s = jk_0$. The transform for purely imaginary s may be derived from [82] 6.671 using Euler's identity, and these forms may be shown to be equal to (A.12) when the branch cut is chosen such that $\sqrt{x}$ has an argument in $(-\pi/2, \pi/2]$. This form will be valid everywhere except when $k_t = k_0$, where the form diverges.

The fact that the expression (A.13) is only valid for $n > -1$ must be dealt with before re-writing the final integral. Since for any Bessel function and integer $n > 0$, $J_{-n}(z) = J_n(z)(-1)^n$ by [81] 9.1.5, one may write for arbitrary integer n, $J_n(z) = p_n^n J_{|n|}(z)$ where p_n is 1 for $n \geq 0$, else -1. By rearranging terms one may then write the general expression for $\mathcal{I}'_n$ as,

$$\mathcal{I}'_n = \int_0^\infty J_n(k_t r_t) e^{-s r_t} dr_t = \int_0^\infty p_n^n J_{|n|}(k_t r_t) e^{-s r_t} dr_t \tag{A.14}$$

$$= p_n^n \left((\mathcal{C}_B + \mathcal{C}_C)^{|n|} k_t \mathcal{C}_C \right)^{-1} = \left[[p_n(\mathcal{C}_B + \mathcal{C}_C)]^{|n|} k_t \mathcal{C}_C \right]^{-1}, \tag{A.15}$$

where in the last line, the fact that $p_n^n = p_n^{-n} = p_n^{|n|}$ has been used.

Returning now to (A.11), we write

$$F_x^n = j\pi \left(Z_{n+1} - Z_{n-1} \right), \tag{A.16}$$

where,

$$Z_n = j^n \mathcal{C}_E^n \left[[p_n(\mathcal{C}_B + \mathcal{C}_C)]^{|n|} k_t \mathcal{C}_C \right]^{-1}. \tag{A.17}$$

This may be simplified as

$$\begin{aligned} Z_n &= \frac{\mathcal{C}_E^n}{k_t \mathcal{C}_C} j^n \left[p_n(\mathcal{C}_B + \mathcal{C}_C) \right]^{-|n|} \\ &= \frac{\mathcal{C}_E^n}{k_t \mathcal{C}_C} (p_n j)^{|n|} \left[p_n(\mathcal{C}_B + \mathcal{C}_C) \right]^{-|n|}, \\ &= \frac{\mathcal{C}_E^n}{k_t \mathcal{C}_C} \left(\frac{j}{\mathcal{C}_B + \mathcal{C}_C} \right)^{|n|} = \frac{\mathcal{C}_E^n \mathcal{C}_M^{|n|}}{k_t \mathcal{C}_C} \end{aligned} \tag{A.18}$$

where the fact that $j^n = (p_n j)^{|n|}$ was used. In this form, F_x^n, may be written in its final form by substituting (A.18) into (A.16) to obtain (6.23). The expression for F_y^n may be derived by repeating the above steps but using $\cos\phi$ in place of $-\sin\phi$.

A.2 Error Analyses

A.2.1 Truncation Error

In this section, it is shown that the truncation error introduced by a rectangular window with support $[-R, R] \times [-R, R]$ on a frame of data with its far-field asymptote removed goes as $O(1/R)$. It is first noted that when w_R is a rectangular window,

$$|E_x(1 - w_R)|_{\mathcal{L}^2} \leq |E_x(r_t, \phi)u(r_t - R)|_{\mathcal{L}^2}\,, \tag{A.19}$$

where $u(\cdot)$ is the Heaviside step function and (r_t, ϕ) are polar coordinates. In this section, it will be shown that $\left|\vec{\mathbf{E}}_t''(r_t, \phi)\right|$ decays as $O(1/r_t^2)$. Then it will be shown that this decay rate implies that (A.19) decays as $O(1/R)$.

To begin, consider the field, $\vec{\mathbf{E}}_\delta$. In all situations of interest, the radiating currents are contained inside some closed surface that is inside the region $z < \delta$. In this situation the electric field outside of the surface can be represented in terms of a series of vector spherical harmonics [83]. The exact form of this expansion is not necessary for our purposes, but its existence is. Since all currents are inside a surface in the region $z < \delta$, the field on the plane, $z = \delta$, must be expressible in terms of outward propagating waves. The radial dependence of vector harmonics that are outward propagating is written in terms of the spherical Hankel functions of the second type for our $e^{j\omega t}$ time dependence. These functions are typically written as $h_n^{(2)}(k_0 r)$, and have a finite expansion in terms of functions of the form $e^{-jk_0 r}/r^n$ [81] 10.1.17. If terms of common $1/r^n$ dependence are grouped together, we may write the field on our frame as:

$$\vec{\mathbf{E}}_\delta(x, y) = \vec{\mathbf{M}}_1(\theta, \phi)\frac{e^{-jk_0 r}}{r} + \vec{\mathbf{M}}_2(\theta, \phi)\frac{e^{-jk_0 r}}{r^2} + O\left(\frac{1}{r^3}\right), \tag{A.20}$$

where we have written explicitly the terms of $1/r$ and $1/r^2$ dependence, but grouped all orders of $1/r^3$ or greater in the final term. In doing so, we defined the function $\vec{\mathbf{M}}_1(\theta, \phi)$, which is the pattern of the antenna, $\vec{\mathbf{E}}^r(\theta, \phi)$, and $\vec{\mathbf{M}}_2(\theta, \phi)$, which is the largest order term

remaining when the $1/r$ term is removed. Let $\vec{\mathbf{M}}_1^t$ and $\vec{\mathbf{M}}_2^t$ represent the portions of $\vec{\mathbf{M}}_1$ and $\vec{\mathbf{M}}_2$ that are tangent to the xy-plane. It is not necessary to know these functions, but some assumptions about smoothness and boundedness will be taken for granted in the following argument.

The notion of the method proposed is to approximately remove the term $\vec{\mathbf{M}}_1^t(\theta,\phi)e^{-jk_0r}/r$ from the portion of the field that is tangent to the xy-plane prior to taking the FFT by subtracting the asymptote $\vec{\mathbf{A}}_1(r_t,\phi) = \vec{\mathbf{M}}_1^t(\pi/2,\phi)e^{-jk_0r_t}/r_t$. It may be noted that the asymptote $\vec{\mathbf{A}}_1(r_t,\phi)$ is approximated with a finite Fourier series. For the moment, it will be assumed that the pattern is sufficiently smooth that this approximation is exact. One may then bound the field at the edge of the frame using the expansion in (A.20) and the triangle inequality to obtain

$$\begin{aligned}\left|\vec{\mathbf{E}}_t''(x,y)\right| &= \left|\vec{\mathbf{E}}_t(x,y) - \vec{\mathbf{A}}_1(x,y) + \vec{\mathbf{A}}_2(x,y)\right| \\ &\leq \left|\vec{\mathbf{M}}_1^t(\theta,\phi)\frac{e^{-jk_0r}}{r} - \vec{\mathbf{M}}_1^t(\pi/2,\phi)\frac{e^{-jk_0r_t}}{r_t}\right| + \left|\vec{\mathbf{M}}_1^t(\pi/2,\phi)\right|\frac{e^{-\gamma r_t}}{r_t} \\ &\quad + \left|\vec{\mathbf{M}}_2^t(\theta,\phi)\right|\frac{1}{r^2} + O\left(\frac{1}{r^3}\right). \quad \text{(A.21)}\end{aligned}$$

Since $1/r^n \leq 1/r_t^n$ for $n > 0$, to show that $\left|\vec{\mathbf{E}}_t''\right|$ goes as $O(1/r_t^2)$, it is sufficient to show that the term

$$\left|\vec{\mathbf{M}}_1(\theta,\phi)\frac{e^{-jk_0r}}{r} - \vec{\mathbf{M}}_1(\pi/2,\phi)\frac{e^{-jk_0r_t}}{r_t}\right|, \quad \text{(A.22)}$$

goes as $O(1/r_t^2)$. First, the triangle inequality is used to separate (A.22) into two pieces:

$$\begin{aligned}&\left|\vec{\mathbf{M}}_1^t(\theta,\phi)\frac{e^{-jk_0r}}{r} - \vec{\mathbf{M}}_1^t(\pi/2,\phi)\frac{e^{-jk_0r_t}}{r_t}\right| = \\ &\quad \left|\vec{\mathbf{M}}_1^t(\theta,\phi)\frac{e^{-jk_0r}}{r} - \vec{\mathbf{M}}_1^t(\pi/2,\phi)\frac{e^{-jk_0r}}{r} + \vec{\mathbf{M}}_1^t(\pi/2,\phi)\frac{e^{-jk_0r}}{r} - \vec{\mathbf{M}}_1^t(\pi/2,\phi)\frac{e^{-jk_0r_t}}{r_t}\right| \\ &\quad \leq \left|\vec{\mathbf{M}}_1^t(\theta,\phi) - \vec{\mathbf{M}}_1^t(\pi/2,\phi)\right|\frac{1}{r} + \left|\vec{\mathbf{M}}_1^t(\pi/2,\phi)\right|\left|\frac{e^{-jk_0r}}{r} - \frac{e^{-jk_0r_t}}{r_t}\right|. \quad \text{(A.23)}\end{aligned}$$

The second term on the right hand side of (A.23) is treated by splitting it into contributions using the triangle inequality as above. The $\left|\vec{\mathbf{M}}_1^t(\pi/2,\phi)\right|$ portion will be ignored for the

moment.

$$\left|\frac{e^{-jk_0r}}{r}-\frac{e^{-jk_0r_t}}{r_t}\right|\leq\left|\frac{e^{-jk_0r}-e^{-jk_0r_t}}{r}\right|+\left|\frac{1}{r}-\frac{1}{r_t}\right|\left|e^{-jk_0r_t}\right|. \tag{A.24}$$

The second term on the right hand side of (A.24) may be written as

$$\left|\frac{1}{\sqrt{r_t^2+\delta^2}}-\frac{1}{r_t}\right|=\frac{1}{r_t}\left|\frac{1}{\sqrt{1+(\delta/r_t)^2}}-1\right|. \tag{A.25}$$

Making the substitution $v=1/r_t$ and expanding a Taylor series near $v=0$ one obtains,

$$\begin{aligned}\left|\frac{1}{\sqrt{1+(\delta/r_t)^2}}-1\right|&=\left|\frac{1}{\sqrt{1+(\delta v)^2}}-1\right|\\&=\left|1+0v+O(v^2)-1\right|.\end{aligned} \tag{A.26}$$

In other words,

$$\left|\frac{1}{r}-\frac{1}{r_t}\right|=O\left(\frac{1}{r_t^3}\right). \tag{A.27}$$

The exponential portion of the first term in (A.24) is

$$\left|e^{-jk_0r}-e^{-jk_0r_t}\right|=\left|1-e^{-jk_0(r_t-r)}\right|. \tag{A.28}$$

The remaining exponential term may be re-written using the substitution $v=1/r_t$ as well, giving

$$\begin{aligned}e^{-jk_0(r_t-\sqrt{\delta^2+r_t^2})}&=e^{-jk_0(v^{-1}-\sqrt{\delta^2+v^{-2}})}\\&=e^{-jk_0v^{-1}(1-\sqrt{1+(\delta v)^2})}.\end{aligned} \tag{A.29}$$

This expression is defined for all $v\neq 0$ and is analytic in a region near $v=0$ that excludes 0. The limit as $v\to 0$ is defined and converges to 1. By the Riemann extension theorem [84], the function can be extended to,

$$g(v)=\begin{cases}e^{-jk_0v^{-1}(1-\sqrt{1+(\delta v)^2})} & \text{when } 0<|v|<1\\ 1 & \text{v} = 0\end{cases}, \tag{A.30}$$

analytically, meaning a Taylor expansion exists near $v=0$. This expansion is

$$\begin{aligned}g(v)&=1+g'(0)v+O\left(v^2\right)\\&=1+\left(\lim_{v\to 0}g'(v)\right)v+O\left(v^2\right),\end{aligned} \tag{A.31}$$

where the fact that $g'(v)$ is continuous near $v = 0$ has been used. One may evaluate $g'(0)$ as,

$$\begin{aligned} g'(0) &= \lim_{v\to 0} e^{-jk_0 v^{-1}(1-\sqrt{1+(\delta v)^2})} \\ &\quad \times \left[-jk_0\left[\frac{\sqrt{1+(\delta v)^2}-1}{v^2} - \frac{\delta^2}{\sqrt{1+(\delta v)^2}}\right]\right]. \\ &= \frac{1}{2}jk_0\delta^2 \end{aligned} \tag{A.32}$$

This gives,

$$\begin{aligned} \left|\frac{e^{-jk_0 r} - e^{-jk_0 r_t}}{r}\right| &\leq \frac{1}{r}\left|1 - \left(1 + \frac{jk_0\delta^2}{2r})\right)\right| + O\left(1/r^3\right) \\ &= \frac{k_0\delta^2}{2r^2} + O\left(\frac{1}{r^3}\right). \end{aligned} \tag{A.33}$$

Combining (A.33) and (A.27), one may re-write (A.24) to obtain,

$$\left|\frac{e^{-jk_0 r}}{r} - \frac{e^{-jk_0 r_t}}{r_t}\right| \leq \frac{k_0\delta^2}{2r_t^2} + O\left(\frac{1}{r_t^3}\right). \tag{A.34}$$

The first term on the right hand side of (A.23) can be rewritten with the substitution $v = 1/r$ to obtain

$$\left|\vec{\mathbf{M}}_1^t(\theta,\phi) - \vec{\mathbf{M}}_1^t(\pi/2,\phi)\right|\frac{1}{r} = v^2\left|\frac{\vec{\mathbf{M}}_1^t(\theta,\phi) - \vec{\mathbf{M}}_1^t(\pi/2,\phi)}{v}\right|. \tag{A.35}$$

Next, from the geometry described in Fig. 6.1,

$$\begin{aligned} \theta = \arcsin\left(\frac{r_t}{r}\right) &= \arcsin\left(\frac{\sqrt{r^2-\delta^2}}{r}\right) \\ &= \arcsin\left(\sqrt{1-(\delta v)^2}\right), \end{aligned} \tag{A.36}$$

where the branch of the $\arcsin(\cdot)$ is chosen so that $\theta(0) = \pi/2$. To obtain a Taylor expansion at $v = 0$ will require the derivative of $\theta(v)$ at $v = 0$. For v near but not equal to v, the chain rule may be applied to obtain

$$\begin{aligned} \frac{d\theta(v)}{dv} &= \frac{d(\arcsin(\sqrt{1-(\delta v)^2}))}{d(\sqrt{1-(\delta v)^2})} \cdot \frac{d(\sqrt{1-(\delta v)^2})}{dv} \\ &= \frac{1}{\delta v} \cdot \frac{-\delta^2 v}{\sqrt{1-(\delta v)^2}}. \end{aligned} \tag{A.37}$$

Using a similar extension argument to that used for $g(\cdot)$ above, the limit as $v \to 0$ may be taken to be $\theta'(0)$. To obtain an approximation for (A.35), some continuity on $\vec{\mathbf{M}}_1^t$ is

required also. A Taylor expansion at $v = 0$ gives,

$$\begin{aligned}\frac{\vec{\mathbf{M}}_1^t(\theta(v),\phi) - \vec{\mathbf{M}}_1^t(\theta(0),\phi)}{v} &= \left.\frac{\partial \vec{\mathbf{M}}_1^t}{\partial v}\right|_{v=0} + O(v) \\ &= \frac{\partial \vec{\mathbf{M}}_1^t(\pi/2,\phi)}{\partial \theta}(-\delta) + O\left(\frac{1}{r}\right),\end{aligned} \tag{A.38}$$

where the chain rule was used in the second line.

Combining (A.38) and (A.34) into (A.23), then (A.21), one obtains

$$\begin{aligned}\left|\vec{\mathbf{E}}_t''(x,y)\right| \leq \frac{1}{r_t^2}\Bigg(&\left|\frac{\partial \vec{\mathbf{M}}_1(\pi/2,\phi)}{\partial \theta}\right|\delta \\ &+ \left|\vec{\mathbf{M}}_1(\pi/2,\phi)\right|\frac{k_0\delta^2}{2} + \left|\vec{\mathbf{M}}_2(\theta,\phi)\right|\Bigg) \\ &+ \left|\vec{\mathbf{M}}_1(\pi/2,\phi)\right|\frac{e^{-\gamma r_t}}{r_t} + O\left(\frac{1}{r_t^3}\right).\end{aligned} \tag{A.39}$$

The inequality (A.39) is interesting by itself, as it shows the separate contributions to the error. The first term represents the assumption that the pattern is smooth near $\theta = \pi/2$. The second term represents the assumption that $e^{-jk_0 r}/r \approx e^{-jk_0 r_t}/r_t$. The third term represents near-field quantities, and the fourth term represents the error from the $\vec{\mathbf{A}}_2$ asymptote.

To bound the truncation error, the only term with any r_t dependence to be concerned with is

$$\frac{1}{r_t^2}\left|\vec{\mathbf{M}}_2(\theta,\phi)\right| \leq \frac{1}{r_t^2}\max_\theta \left|\vec{\mathbf{M}}_2(\theta,\phi)\right|. \tag{A.40}$$

Combining (A.39) and (A.40) the field may be bound by defining for each ϕ the real valued function $f(\phi)$. Write (A.39) as,

$$\left|\vec{\mathbf{E}}_t''(x,y)\right| \leq \frac{f(\phi)}{r_t^2} + O\left(\frac{1}{r_t^3}\right). \tag{A.41}$$

Then one may calculate the norm of $E_x u(r_t - R)$ in a region where $e^{-\gamma r_t}$ is sufficiently small by neglecting the order $1/r_t^3$ contributions to obtain

$$\begin{aligned}|E_x u(r_t - R)|_{\mathcal{L}^2}^2 \lessapprox &\int_R^\infty \int_0^{2\pi} \frac{|f(\phi)|^2}{r_t^4} r_t dr_t d\phi \\ &= \int_0^{2\pi} |f(\phi)|^2 d\phi \frac{1}{2R^2} \propto \frac{1}{R^2}\end{aligned} \tag{A.42}$$

$$|E_x\left(1-w_R\right)|_{\mathcal{L}^2} = O\left(\frac{1}{R}\right). \tag{A.43}$$

Since the same could be said of $|E_y\left(1-w_R\right)|$, it is shown then that $\left|\vec{\mathbf{F}}_\delta - \vec{\mathbf{F}}_\delta^R\right| = O(1/R)$.

A.2.2 Aliasing Error

In this section, (6.30) is shown. Beginning with

$$\begin{aligned}|\mathcal{C}'_F\mathcal{C}_E^n\mathcal{C}'^n_M - \mathcal{C}_F\mathcal{C}_E^n\mathcal{C}_M^n| = \\ \frac{\pi}{k_t}\left|\left(\frac{1}{\left(\mathcal{C}'_B+\sqrt{1+\mathcal{C}'^2_B}\right)^n\sqrt{1+\mathcal{C}'^2_B}}\right)\right. \\ \left. -\left(\frac{1}{\left(\mathcal{C}_B+\sqrt{1+\mathcal{C}_B^2}\right)^n\sqrt{1+\mathcal{C}_B^2}}\right)\right|,\end{aligned} \tag{A.44}$$

where the primes denote $s = jk_0+\gamma$ and the lack of primes denote $s = jk_0$. Define the function

$$f(s) = \left(s+(1+s^2)^{\frac{1}{2}}\right)^{-n}(1+s^2)^{-\frac{1}{2}}. \tag{A.45}$$

Then

$$\begin{aligned}|\mathcal{C}'_F\mathcal{C}_E^n\mathcal{C}'^n_M - \mathcal{C}_F\mathcal{C}_E^n\mathcal{C}_M^n| &= \frac{\pi}{k_t}\left|f\left(\frac{jk_0+\gamma}{k_t}\right) - f\left(\frac{jk_0}{k_t}\right)\right| \\ &= \frac{\pi}{k_t}\left|f'\left(\frac{jk_0}{k_t}\right)\frac{\gamma}{k_t} + O\left(\frac{1}{k_t^2}\right)\right|.\end{aligned} \tag{A.46}$$

Additionally, since in general $k_t >> k_0$, use the expansion

$$f'\left(\frac{jk_0}{k_t}\right) = f'(0) + O\left(\frac{1}{k_t}\right), \tag{A.47}$$

which makes

$$|\mathcal{C}'_F\mathcal{C}_E^n\mathcal{C}'^n_M - \mathcal{C}_F\mathcal{C}_E^n\mathcal{C}_M^n| = \frac{\pi}{k_t}\left|f'(0)\frac{\gamma}{k_t} + O\left(\frac{1}{k_t^2}\right)\right|. \tag{A.48}$$

f is differentiated below to give

$$\begin{aligned} f'(s) &= -\frac{1}{2}(1+s^2)^{-\frac{3}{2}}2s(s+(1+s^2)^{\frac{1}{2}})^{-n} \\ &\quad + -n(s+(1+s^2)^{1/2})^{-(n+1)}(1+s(1+s^2)^{-\frac{1}{2}}) \\ &\quad \times (1+s^2)^{-\frac{1}{2}} \end{aligned} \tag{A.49}$$

$$f'(0) = -n. \tag{A.50}$$

Then, (A.48) becomes

$$|\mathcal{C}'_F\mathcal{C}_E^n\mathcal{C}_M'^n - \mathcal{C}_F\mathcal{C}_E^n\mathcal{C}_M^n| \leq \frac{n\pi\gamma}{k_t^2} + O\left(\frac{1}{k_t^3}\right). \tag{A.51}$$

REFERENCES

[1] J. D. Dyson, "The Equiangular Spiral Antenna," *IRE Trans. Antennas Propagat.*, vol. AP-7, pp. 181–187, 1959.

[2] V. H. Rumsey, *Frequency Independent Antennas*, ser. Electrical Science, H. G. Booker and N. DeClaris, Eds. Academic Press, 1966.

[3] J.D. Dyson, R. Bawer, P.E. Mayes, and J.I. Wolfe, "A note on the difference between equiangular and archimedes spiral antennas (correspondence)," *IEEE Trans. Microwave Theory Tech.*, vol. 9, pp. 203–205, 1961.

[4] J. D. Dyson, "The Equiangular Spiral Antenna," Ph.D. dissertation, Univ. Illinois, Urbana, Illinois, 1957.

[5] R. H. DuHamel and J. P. Scherer, *Antenna Engineering Handbook*, 3rd ed. McGraw-Hill, 1993, ch. 14.

[6] S. R. Laxpati and R. Mittra, "Current Distribution on a Two-arm Thin-wire Planar Equiangular Spiral Antenna," *Electronics Letters*, vol. 1, pp. 213–215, 1965.

[7] Y. S. Yeh and K. K. Mei, "Theory of Conical Equiangular-Spiral Antennas Part I - Numerical Technique," *IEEE Trans. Antennas Propagat.*, vol. 15, pp. 634–639, 1967.

[8] J. A. Kaiser, "The archimedean two-wire spiral antenna," *IRE Trans. Antennas Propagat.*, vol. 8, pp. 312–323, 1960.

[9] R. G. Corzine and J. A. Mosko, *Four-Arm Spiral Antennas*. Artech House, 1990.

[10] N. Padros et al., "Comparative study of high-performance GPS receiving antenna designs," *IEEE Trans. Antennas Propagat.*, vol. 45, pp. 698–706, 1997.

[11] W. Clark, J. Ralston, et al., "The Measured Effect of Soils on Ground Penetrating Radar Antenna Resolution," in *Tenth International Conference on Ground Penetrating Radar*, Delft, The Netherlands, june 2004, pp. 125–128.

[12] D. Daniels, *Ground Penetrating Radar*. Inspec/IEE, 2004.

[13] W. L. Curtis, "Spiral Antennas," *IRE Trans. Antennas Propagat.*, vol. AP-8, pp. 298–306, 1960.

[14] B. R. Cheo and V. H. Rumsey, "A Solution to the Frequency-Independent Antenna Problem," *IRE Trans. Antennas Propagat.*, vol. AP-9, pp. 527–534, 1967.

[15] R. Sivan-Sussman, "Various modes of the equiangular spiral antenna," *IRE Trans. Antennas Propagat.*, vol. 11, pp. 533–539, 1963.

[16] R. Bawer and J. J. Wolfe, "The spiral antenna," *IRE Trans. Antennas Propagat.*, vol. AP-8, pp. 84–95, 1960.

[17] J. J. Wolfe and R. Bawer, "Designing printed-circuit spiral antennas," *Electronics*, vol. 34, 1961.

[18] W. Weir et al., "Driving-point-impedance measurement and balun design for spiral antennas," Stanford Research Institute, Tech. Rep., 1972.

[19] H. G. Booker, "Slot aerials and their relation to complementary wire aerials (Babinet's Principle)," *J. IEE*, vol. 93, pp. 620–626, 1946.

[20] K. K. Mei, "On the Integral Equations of Thin Wire Antennas," *IRE Trans. Antennas Propagat.*, vol. 13, pp. 374–378, 1965.

[21] C. Penney and R. Luebbers, "Input impedance, radiation pattern, and radar cross section of spiral antennas using FDTD," *IEEE Trans. Antennas Propagat.*, vol. 42, pp. 1328–1332, 1994.

[22] S. M. Wentworth and S. M. Rao, "Analysis of Equiangular Spiral Antennas," *Int. J. Microwave Mill.*, vol. 6, pp. 92–98, 1996.

[23] C. Fumeaux, D. Baumann, and R. Vahldieck, "Finite-Volume Time-Domain Analysis of a Cavity-Backed Archimedean Spiral Antenna," *IEEE Trans. Antennas Propagat.*, vol. 54, pp. 844–851, 2006.

[24] J. H. Wang and V. K. Tripp, "Design of Multioctave Spiral-Mode Microstrip Antennas," *IEEE Trans. Antennas Propagat.*, vol. 39, pp. 332–335, 1991.

[25] H. Nakano, et al., "A Spiral Antenna Backed by a Conducting Plane Reflector," *IEEE Trans. Antennas Propagat.*, vol. 34, pp. 791–796, 1986.

[26] H. Nakano, K. Kikkawa, Y. Iitsuka, and J. Yamauchi, "Equiangular Spiral Antenna Backed by a Shallow Cavity With Absorbing Strips," *IEEE Trans. Antennas Propagat.*, vol. 56, pp. 2742–2747, 2008.

[27] H. Nakano et al., "Low-Profile Equiangular Spiral Antenna Backed by an EBG Reflector," *IEEE Trans. Antennas Propagat.*, vol. 57, pp. 1309–1318, 2009.

[28] M. Phelan, H. Su, and J. Vetri, "Near Field Analysis of a Wideband Log-Spiral Antenna for 1-2GHz GPR," *IEEE Canadian Conference on Elect. and Comp. Engineering*, vol. 1, pp. 336–341, 2002.

[29] D. Paolino, M. Neel, and C. Franck, "Reduced Size Spiral Antenna Design Using Dielectric Overlay Loading for Use in Ground-Penetrating Radar and Design of Alternative Antennas Using Vivaldi Radiators," *Proc. SPIE*, vol. 4742, pp. 218–229, 2002.

[30] P. Lacko, C. Franck, M. Johnson, J. Ralston, M. Bradley, and B. McCummins, "Archimedean and log-spiral antenna comparison," *Proc. SPIE*, vol. 4742, pp. 230–236, 2002.

[31] M. Bradley, T. Witten, M. Duncan, and B. McCummins, "Anti-tank and side-attack mine detection with a forward-looking GPR," *Proc. SPIE*, vol. 5415, pp. 421–432, 2004.

[32] J. Thaysen, K. B. Jakobsen, and H.-R. Lenler-Eriksen, "Wideband Cavity Backed Spiral Antenna for Stepped Frequency Ground Penetrating Radar," *IEEE Symp. Antennas Propagat.*, vol. 1B, pp. 418–421, 2005.

[33] D. J. Gunton et al., "Ground Probing Radar Method and Apparatus," US Patent 4 967 199, 1990.

[34] W. Steinway et al., "Computerized Tomography Using Radar," US Patent 7 312 742 B2, 2007.

[35] S. Cole et al., "Moving-Entity Detection," US Patent 7 345 618 B1, 2008.

[36] A. Taflove and S. C. Hagness, *Computational Electrodynamics*, 3rd ed. Artech House, 2000.

[37] K. S. Yee, "Numerical solution of initial boundary value problems involving maxwell's equations," *IEEE Trans. Antennas Propagat.*, vol. 14, pp. 302–307, 1966.

[38] S. Dey and R. Mittra, "A locally conformal finite-difference time-domain (fdtd) algorithm for modeling three-dimensional perfectly conducting objects," *IEEE Trans. Antennas Propagat.*, vol. 7, pp. 273–275, 1997.

[39] T. Xiao and Q. H. Liu, "Enlarged cells for the conformal fdtd method to avoid the time step reduction," *IEEE Trans. Antennas Propagat.*, vol. 14, pp. 551–553, 2004.

[40] B. Q. Gao and O. P. Gandhi, "An expanding grid algorithm for the finite-difference time-domain method," *IEEE Trans. Antennas Propagat.*, vol. 34, pp. 277–283, 1992.

[41] M. Kuzuoglu and R. Mittra, "Frequency dependence of the constitutive parameters of causal perfectly matched anisotropic absorbers," *IEEE Trans. Antennas Propagat.*, vol. 6, pp. 447–449, 1996.

[42] J. A. Roden and S. D. Gedney, "Convolutional PML (CPML): An Efficient FDTD Implementation of the CFS-PML for Arbitrary Media," *Microwave Optical Tech. Lett.*, vol. 27, pp. 334–339, 2000.

[43] R. J. Luebbers and H. S. Langdon, "A simple feed model that reduces time steps needed for fdtd antenna and microstrip calculations," *IEEE Trans. Antennas Propagat.*, vol. 44, pp. 1000–1005, 1996.

[44] W. Kruppa and K. F. Sodomsky, "An Explicit Solution for the Scattering Parameters of a Linear Two-Port Measured with an Imperfect Test Set," *IEEE Trans. Microwave Theory Tech.*, vol. 19, pp. 122–123, 1971.

[45] C. A. Balanis, *Antenna Theory.* Wiley, 1982.

[46] T. Iwasaki, A. P. Freundorfer, and K. Iizuka, "A unidirectional semi-circle spiral antenna for subsurface radars," *IEEE Trans. Electromagn. Compat.*, vol. 36, pp. 1–6, 1994.

[47] J. A. Huffman and T. Cencich, "Modal Impedances of Planar, Non-Complementary, N-fold Symmetric Antenna Structures," *IEEE Antennas Propagat. Mag.*, vol. 47, pp. 110–116, 2005.

[48] R. S. Elliott, *Antenna Theory and Design.* Wiley-Interscience, 2003.

[49] B. Kramer, M. Lee, C. Chen and J. Volakis, "Design and performance of an ultrawideband ceramic-loaded slot spiral," *IEEE Trans. Antennas Propagat.*, vol. 53, pp. 2193–2199, 2005.

[50] D. E. Bockelman and W. R. Eisenstadt, "Combined Differential and Common-Mode Scattering Parameters: Theory and Simulation," *IEEE Trans. Microwave Theory Tech.*, vol. 43, pp. 1530–1539, 1995.

[51] J. Baker-Jarvis et. al., *Transmission/Reflection and Short-Circuit Line Methods for Measuring Permittivity and Permeability.* U. S. Government Printing Office, 1993.

[52] D. Rytting, "Advances in microwave error correcting techniques," in *Hewlett-Packard, RF & MW Symp.*, 1987.

[53] D. Pozar, *Microwave Engineering.* Wiley, 1998.

[54] T. P. Montoya, "Vee dipole antennas for use in short-pulse ground-penetrating radars," Ph.D. dissertation, Georgia Institute of Technology, 1998.

[55] T. W. Hertel and G. S. Smith, "On the Dispersive Properties of the Conical Spiral Antenna and Its Use for Pulsed Radiation," *IEEE Trans. Antennas Propagat.*, vol. 51, pp. 1426–1433, 2003.

[56] C. Baum, "Interaction Note 476: SEM Backscattering," Air Force Weapons Laboratory, Tech. Rep., 1989.

[57] R. Azaro, S. Caorsi, and M. Pastorino, "On the Relationship For the Monostatic Modulated Fundamental Scattering Technique," *Microwave and Optical Letters*, vol. 38, pp. 187–190, 2003.

[58] C. E. Baum, *Detection and Identification of Visually Obscured Targets.* Taylor and Francis, 1999.

[59] G. S. Smith, *An Introduction to Classical Electromagnetic Radiation.* Cambridge, 1997.

[60] C. A. Balanis, *Advanced Engineering Electromagnetics.* Wiley, 1989.

[61] J. C. Kolecki, "An Introduction to Tensors for Students of Physics and Engineering," Glenn Research Center, Tech. Rep., 2002. [Online]. Available: http://www.grc.nasa.gov/WWW/K-12/Numbers/Math/documents/Tensors_TM2002211716.pdf [Nov. 2009].

[62] J. H. Vleck, F. Bloch, and M. Hamermesh, "Theory of Radar Reflection from Wires or Thin Metallic Strips," *J. Appl. Phys.*, vol. 18, pp. 274–94, 1947.

[63] P. C. Clemmow, *The Plane Wave Spectrum Representation of Electromagnetic Fields.* Oxford University Press, 1966.

[64] H. G. Booker and P. C. Clemmow, "The concept of an angular spectrum of plane waves and its relation to that of a polar diagram and aperture distribution," *Proc. IEE*, vol. 97, pp. 343–351, 1958.

[65] J. Brown, "A theoretical analysis of some errors in aerial measurements," *Proc. IEE*, vol. 105C, pp. 343–351, 1958.

[66] D. M. Kerns, *Plane-Wave Scattering-Matrix Theory of Antennas and Antenna-Antenna Interactions.* U.S. Government Printing Office, 1981.

[67] G. S. Smith, "Directive properties of antennas for transmission into a material half space," *IEEE Trans. Antennas Propagat.*, vol. 32, pp. 232–246, 1984.

[68] D. A. Hill, "Electromagnetic scattering by buried objects of low contrast," *IEEE Trans. Geosci. Remote Sensing*, vol. 26, pp. 195–203, 1988.

[69] P. Meincke and T. B. Hansen, "Plane-wave characterization of antennas close to a planar interface," *IEEE Trans. Geosci. Remote Sensing*, vol. 42, pp. 1222–1232, 2004.

[70] G. S. Smith and L. E. R. Petersson, "On the use of evanescent electromagnetic waves in the detection and identification of objects buried in lossy soil," *IEEE Trans. Antennas Propagat.*, vol. 48, pp. 1295–1300, 2000.

[71] A. Yaghjian, "An overview of near-field antenna measurements," *IEEE Trans. Antennas Propagat.*, vol. 34, pp. 30–45, 1986.

[72] E. Joy and D. E. Paris, "Spatial sampling and filtering in near-field measurements," *IEEE Trans. Antennas Propagat.*, vol. 20, pp. 253–261, 1972.

[73] A. C. Newell, "Error analysis techniques for planar near-field measurements," *IEEE Trans. Antennas Propagat.*, vol. 36, pp. 754–768, 1988.

[74] O. M. Bucci and M. D. Migliore, "A new method for avoiding the truncation error in near-field antenna measurements," *IEEE Trans. Antennas Propagat.*, vol. 54, pp. 2940–2952, 2006.

[75] E. Martini, O. Breinberg, and S. Maci, "Reduction of truncation errors in planar near-field aperture antenna measurements using the gerchberg-papoulis algorithm," *IEEE Trans. Antennas Propagat.*, vol. 56, no. 11, pp. 3485–3493, 2008.

[76] J. H. Wang, "An examination of the theory and practices of planar near-field measurement," *IEEE Trans. Antennas Propagat.*, vol. 36, pp. 746–753, 1988.

[77] A. V. Oppenheim and R. W. Schafer, *Discrete-Time Signal Processing.* Prentice-Hall, Inc., 1989.

[78] F. J. Harris, "On the use of windows for harmonic analysis with the discrete fourier transform," *Proc. IEEE*, vol. 66, pp. 51–83, 1978.

[79] T. T. Wu and R. P. King, "The cylindrical antenna with nonreflecting resistive loading," *IEEE Trans. Antennas Propagat.*, vol. 13, no. 3, pp. 369–373, 1965.

[80] R. Streich and J. van der Kruk, "Accurate imaging of multicomponent gpr data based on exact radiation patterns," *IEEE Trans. Geosci. Remote Sensing*, vol. 45, no. 1, pp. 93–103, 2007.

[81] M. Abramowitz and I. Stegun, *Handbook of Mathematical Functions.* Dover, 1965.

[82] I. S. Gradshteyn and I. M. Ryzhik, *Tables of Integrals, Series, and Products*, 5th ed. Academic Press, 1965.

[83] C. Bohren and D. R. Huffman, *Absorption and Scattering of Light by Small Particles.* John Wiley and Sons, Inc., 1983.

[84] R. Narasimhan and Y. Nievergelt, *Complex Analysis in One Variable.* Birkhauser, 2001.

VITA

Mike McFadden received the B.S.E.E. and M.S.E.C.E. degrees from the Georgia Institute of Technology in 2004 and 2006 respectively. He was employed as a graduate research assistant at the Georgia Institute of Technology from 2005 to 2009. His research interests include antenna design and numerical modeling.